Studies of scintillator-based muon triggers in CMS

Von der Fakultät für Mathematik, Informatik und Naturwissenschaften
der RWTH Aachen University zur Erlangung des akademischen Grades
eines Doktors der Naturwissenschaften genehmigte Dissertation

vorgelegt von

Florian Scheuch, M.Sc. RWTH

aus Dorsten

Berichter: Univ.-Prof. Dr. Thomas Hebbeker
Priv.-Doz. Dr. Oliver Pooth

Tag der mündlichen Prüfung 16.03.2017

“The imagination of nature is far, far greater than the imagination of man.”

(Richard Feynman, 1955)

Abstract

The CMS experiment at the LHC will face challenges due to upgrades and improvements of the LHC in future. Especially, the upgrade towards the high luminosity LHC in 2025 with a foreseen center of mass energy of 14 TeV, an instantaneous luminosity of $O(10^{35}cm^{-2}s^{-1})$ and the concurrent aging of and radiation damage to the detectors will have an impact on the fast CMS trigger system and the CMS sub-detectors. Especially, the impact on the CMS muon system - and more particular on the drift tube (DT) system - is of vital interest.

In order to respond to these challenges the performance of the DT system as part of the L1 muon trigger and the use of a scintillator-based muon trigger as supportive detector are analyzed in this thesis.
First, the concept of such a scintillator-based muon trigger, the Muon Track fast Tag (MTT), as support for the DT trigger system, is presented. The conducted related R&D is described. Exploiting the similarity of the MTT concept and the existing hadron outer calorimeter (HO), studies are presented that evaluate the impact of the challenges on the L1 Trigger as well as the potential of the HO detector as a possible response to these challenges. It is shown that the HO detector can be of help in case of DT detector failures and it is able to improve the muon recognition of the DT detector in the L1 Trigger. The reduction of L1 muon ambiguities with the HO detector is found to be not feasible.
The results, that were obtained using HO, are extrapolated towards the MTT concept. The MTT concept is rated as valuable backup solution that, however, will not increase the benefit above the HO detector in the presented application scenarios.

After a summary of the performed analyses, the conclusion is drawn, that the HO detector should be included into the L1 Trigger decision. The initiated upgrade process of the HO integration into the L1 muon trigger, that was motivated by these studies, is presented. The preceding upgrade of HO with silicon-photomultipliers and the corresponding commissioning are described. The thesis concludes with the presentation of first HO signals that are now received in the upgraded L1 muon trigger hardware component.

Kurzzusammenfassung

Das CMS Experiment am LHC Beschleuniger steht vor großen Herausforderungen durch zukünftige Erweiterungen des Beschleunigers. Besonders der Ausbau zum High Luminosity LHC bis 2025 mit einer geplanten Schwerpunktsenergie von 14 TeV bei einer instantanen Luminosität von (10^{35}cm^{-2}s^{-1}), sowie die mit der Zeit einhergehenden Alters- und Strahlenschäden werden einen Einfluss auf das schnelle Triggersystem und die einzelnen Detektoren des CMS Experiments haben. Besonders hervorzuheben ist die Bedeutung für das CMS Myon System und das darin enthaltene Drift Tube (DT) System.

Um den genannten Herausforderungen zu begegnen wurden in dieser Arbeit die Leistungsfähigkeit des DT Systems als Teil des L1 Myon Triggers und die Verwendung eines szintillator-basierten Myon Triggers als Unterstützung des DT Systems untersucht.
Zu Beginn wird das Konzept eines solchen szintillator-basierten Myon Triggers, des Muon Track fast Tag (MTT), sowie die diesbezügliche Forschung und Entwicklung vorgestellt. Die Ähnlichkeit des MTT Konzepts zum bestehenden Hadron Outer Kalorimeter (HO) wird in den anschließend präsentierten Studien verwendet, welche den Einfluss der genannten Herausforderungen auf den L1 Trigger und die Fähigkeit des HO Detektors diesen zu begegnen untersuchen. Es wird gezeigt, dass das HO System dem DT System Hilfe bei Detektorausfällen leisten kann. Des Weiteren wird die Fähigkeit des HO Systems die Myonerkennung des DT Detektors im L1 Trigger zu verbessern herausgestellt. Eine Verwendung von HO zur Reduzierung von Myonambiguitäten wird verneint.
Die Analyse des Zusammenspiels von HO und DT System wird dazu verwendet Aussagen über das MTT Konzept zu treffen. MTT zeigt sich als gutes Backup-System. Allerdings kann MTT den in dieser Arbeit untersuchten Herausforderungen nicht besser begegnen als das bestehende HO System.

Nach der Zusammenfassung der durchgeführten Analysen wird die Schlussfolgerung gezogen, dass der HO Detektor in die L1 Trigger Entscheidung eingebunden werden soll. Der durch diese Studien vorangebrachte Upgradeprozess der Integration des HO Systems in den L1 Myon Trigger wird anschließend präsentiert. Ebenso wird das dazu notwendige Upgrade des HO mit Silizium-Photomultipliern und die entsprechenden Abnahmetests beschrieben. Die Arbeit schließt mit der Präsentation der ersten HO Signale, welche nun in der neuen L1 Myon Trigger Hardware empfangen werden.

Contents

Chapter 1

Introduction

The Large Hadron Collider (LHC) is the largest particle accelerator for proton-proton, proton-lead, and lead-lead collisions in the world (see figure 1.1 for a drawing of the accelerator complex). During the first run (end 2009 – begin 2013) the LHC reached a center of mass energy of 8 TeV and a maximum instantaneous luminosity of $7.7\frac{\text{Hz}}{\text{nb}}$ for proton-proton collisions delivered at the Compact Muon Solenoid (CMS) experiment, one of the four main experiments of the LHC and subject of this thesis. Proton-proton bunches crossed every 50 ns during this run.
The measurement of the Higgs-Boson has been the greatest discovery made by CMS and ATLAS during this first run [2], [3]. Also searches on super-symmetry [4] and other beyond standard model (BSM) physics have been performed.
After a major upgrade phase of the LHC and the CMS detector, a second run started in 2015 which will last until 2018. The proton-proton collision center of mass energy was increased to 13 TeV. By increasing the bunch-crossing rate to 40 MHz and improving the beam focus, a maximum instantaneous luminosity of $15\frac{\text{Hz}}{\text{nb}}$ has been reached. Consequently, the instantaneous luminosity increased by a factor of 2 with respect to the first run. The integrated luminosity recorded by CMS reached 38.27 fb^{-1} during 2016. A plot of the recorded luminosity versus time is shown in figure 1.2.
During the very successful second run, on the one hand, the Higgs-Boson properties have been measured more precisely, on the other hand searches for BSM physics continued (e.g. heavy [6] or very narrow resonances [7]) and allow for strong constraints of a wide range of BSM scenarios.

The precise measurement of leptons is crucial for many of these searches and analyses. For example, the decay of the Higgs-Boson into four leptons ($H \rightarrow ZZ \rightarrow llll$) is very important for precise measurements of the Higgs-Boson's properties. This so-

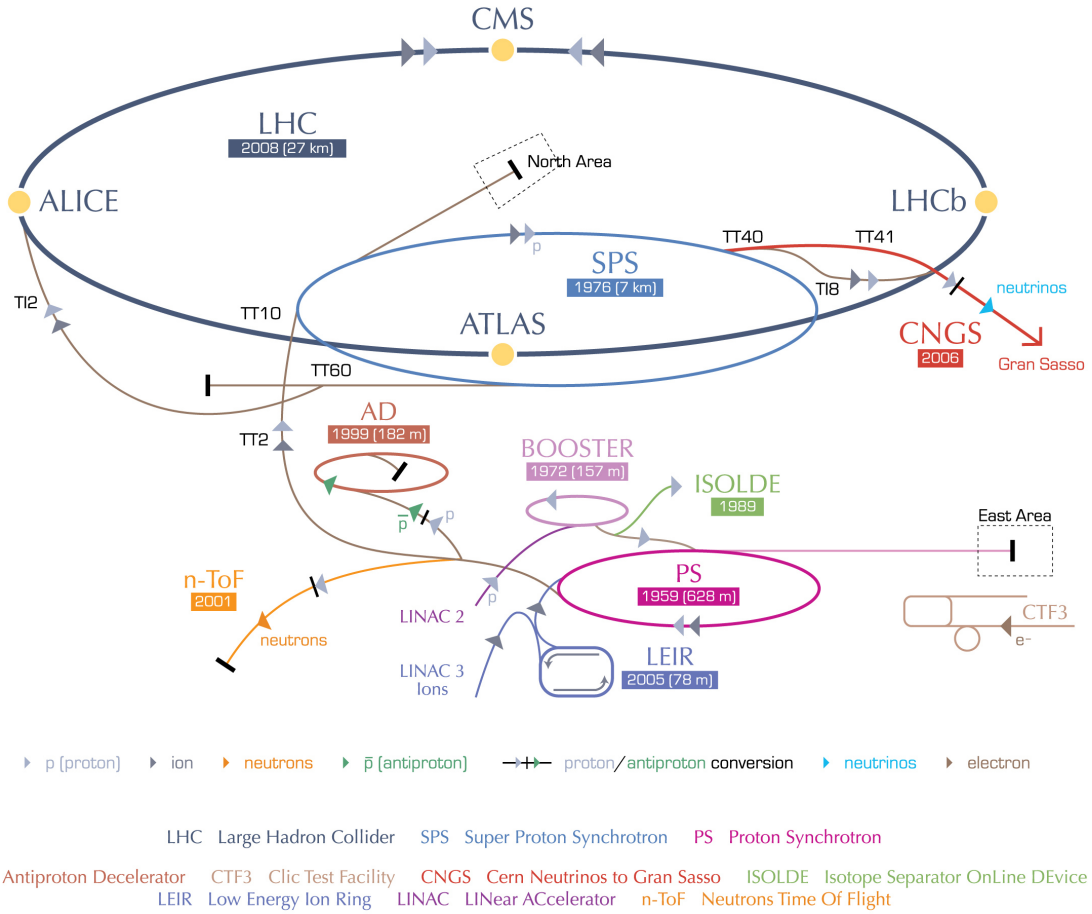

Figure 1.1: Drawing of the LHC accelerator complex [1]. Proton beams are injected at the LINAC 2. After a first acceleration in the BOOSTER, the protons are fed into the PS in order to gain more energy. After a further energy increase in the SPS, the protons are directed to the LHC for the final energy boost.

called “Golden Channel” has a very clean signature due to the capability of the CMS detector to fully detect electrons and muons with a high precision [8] and a well known background [9].
Many BSM searches also look into lepton final states [10]. In order to explore these undiscovered fields of particle physics, an accurate particle recognition (i.e. muons) goes hand in hand with an increase of luminosity to gain enough statistics.
This increase of instantaneous luminosity, as well as an increase of the center of mass energy to 14 TeV is foreseen in 2025. By that year, the LHC is planned to be upgraded to a high luminosity version (HL-LHC). The HL-LHC is expected to deliver an integrated luminosity of 3000 fb^{-1} by 2035 [11]. The LHC will be equipped with new cutting edge superconducting magnets that provide a magnetic field of up to 12 T compared to 8.3 T nowadays. Also the cavities have to be upgraded, as well as the vacuum and cryogenics system [12].
But not only the LHC faces challenges due to the planned upgrades. The increase of

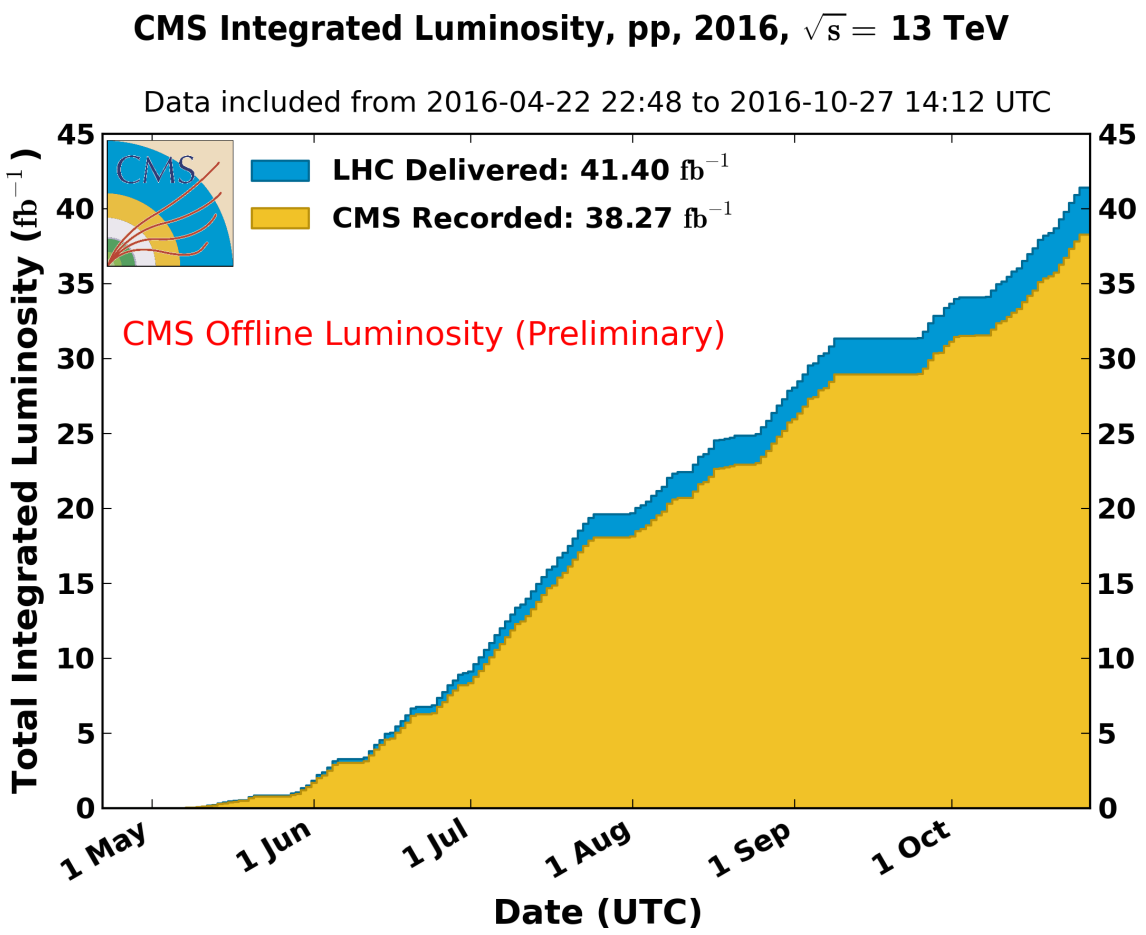

Figure 1.2: Delivered and recorded integrated luminosity versus time at the CMS detector in 2016 [5].

luminosity will result in a high number of pile-up interactions[1]). In turn, the resulting high number of secondary particles will challenge the detector systems of CMS. The tracker system, for example, has to measure a very high density of tracks with up to 10000 tracks during a single bunch-crossing [13]. But also the other detector systems, such as the muon system, will have to adapt to the high number of primary vertices (~ 140).

Together with the detector systems also the trigger system, that is responsible for a fast preselection of the recorded events, will experience an increased workload. The display of a simulated event with 200 pile-up interactions, that visualizes the high amount of particles in the detector, is shown in figure 1.3. A zoomed view into the interaction region is shown in figure 1.4.

In order to deal with these challenges, the concept of a scintillator-based fast muon trigger has been explored, that can improve both, the muon detector system as well as the trigger. The trigger system has to be able to efficiently measure the passage of a

[1] Occurrence of separate proton-proton interactions during the same bunch-crossing.

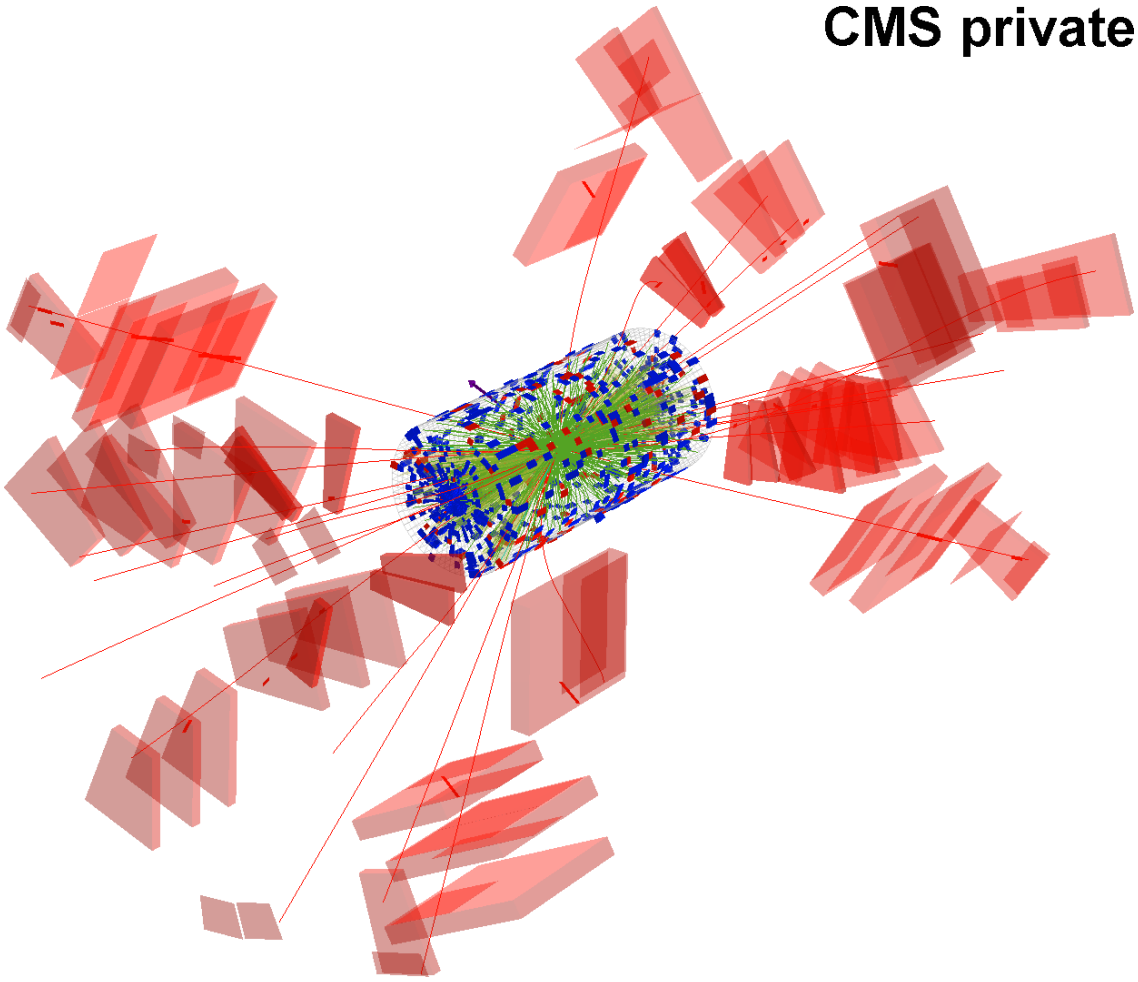

Figure 1.3: A typical event display of a simulated event with 200 pile-up interactions at one bunch-crossing. The red lines are muon tracks that traverse the muon system (red volumes). The green lines are tracks measured in the tracker, that is represented by the cylinder. Calorimetric measurements are shown as red and blue colors projected to the outside of the tracker.

minimum ionizing particle (MIP) every 25 ns which corresponds to the bunch-crossing rate of 40 MHz.
In the next chapter, the CMS detector and its subsystems - particularly the hadron outer (HO) system, a scintillator based calorimeter tail-catcher - are introduced (chapter 2). Afterwards, the evolution of a concept for a fast muon trigger, the Muon Track fast Tag (MTT) and its development are discussed (chapter 3), leading to the current challenges that can be counteracted by an MTT detector. Exploiting the similarity of HO and the MTT concept, the introduced challenges - muon ambiguities (chapter 4), muon system failures (chapter 5) and muon system inefficiencies (chapter 6) - are analyzed for their impact on the fast Level 1 (L1) muon trigger. The application of HO and the MTT concept to solve these challenges is discussed in each chapter subsequently. Utilizing the

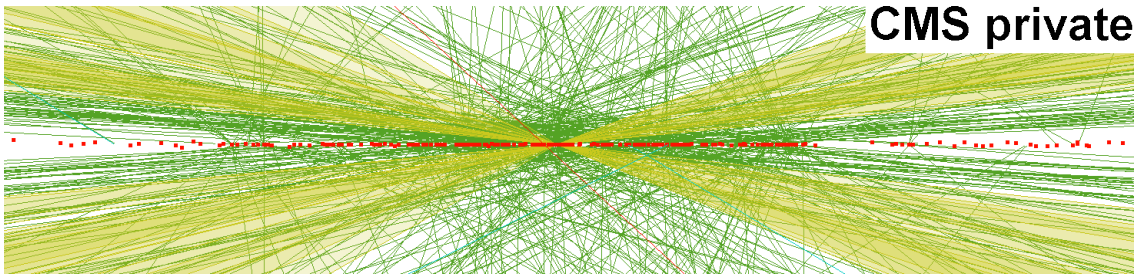

Figure 1.4: View in the ρ-Z-plane on an event display of a simulated event with 200 pile-up interactions at one bunch-crossing. The red dots are reconstructed primary vertices. The green lines are tracks measured in the tracker. Yellow areas illustrate jets.

analysis results, the conclusion is drawn, that the implementation of the HO system into the muon trigger can be of great help (chapter 7). The resulting implementation of the HO system into the muon trigger system is then described, as well as the performed preparatory and technical works (chapter 8).
The last chapter will summarize the impact of scintillator-based muon triggers in CMS in the current detector environment, and the trigger upgrade work that is motivated by this thesis (chapter 9).

Chapter 2

The Compact Muon Solenoid at the Large Hadron Collider

The Compact Muon Solenoid (CMS) experiment is a multi-purpose particle detector at the Large Hadron Collider (LHC) at the CERN facility in Geneva, Switzerland. This chapter outlines the main facts about the experiment and the particle accelerator. Also all important concepts of the detector are introduced that are crucial for the understanding of this thesis.

2.1 The Large Hadron Collider

The Large Hadron Collider (LHC) is a circular particle accelerator for protons and lead ions. It is located in the border region between Switzerland and France near Geneva at the European Organization for Nuclear Research (CERN) facility. It is the replacement of the former Large Electron-Positron Collider (LEP) that collided electrons and positrons at a maximum center of mass energy of 209 GeV between 1989 and 2000 [14]. For further information about the LHC refer to the LHC design report [15] and to [16].
The LEP was replaced by the LHC which both had and have the same length of approximately 27 km. Different to the LEP, the LHC accelerates protons and heavy ions which results in a much less energy loss by synchrotron radiation $\Delta E_{\text{synch.}}$ [17] as it decreases by

$$\Delta E_{\text{synch.}} \propto \frac{1}{m_0^4} \tag{2.1}$$

per time unit with the particle mass m_0 [18]. The reduced synchrotron radiation allows for much higher center of mass energies with a design energy of 14 TeV for protons.

Currently 13 TeV have been achieved. The design luminosity of $10^{34}\text{cm}^{-2}\text{s}^{-1}$ [15] has been first reached in June 2016 and will be increased further. The average number of pile-up interactions per bunch-crossing was 27 in June 2016. O(50) pile-up interactions are expected till 2022. The bunch-crossing rate was 20 MHz in the years 2011-2012. Afterwards, it was increased to 40 MHz, the design frequency. A clock signal provided to all experiments at the LHC has exactly this frequency. It is referred to as LHC clock.

Four main experiments measure the particles created during collisions in the collider:

- The Compact Muon Solenoid (CMS) is one of the two multi-purpose detectors at the LHC. It has a very strong magnetic field that allows for a high precision momentum resolution in the tracker. The CMS detector is explained in more detail in the next section.
- ATLAS is the second of the two multi-purpose detectors at the LHC. It is the largest particle detector in the world utilizing two different superconducting toroid magnets and one solenoid [19].
- ALICE (A Large Ion Collider Experiment) is specialized for the heavy ion runs of the LHC [20].
- LHCb (LHC beauty) is concentrating on the measurement of hadrons containing a bottom or a charm quark. Due to the fact that a pair of b-hadrons is mainly produced in the same forward direction, LHCb has been built as a single arm forward spectrometer [21].

The particle interactions produced by the LHC lead to various new observations in the attached detectors. For example, the CMS and the ATLAS collaboration were able to detect the Higgs-Boson in 2012 [2].

2.2 The Compact Muon Solenoid (CMS)

As this thesis concentrates on the CMS detector systems, this detector will be discussed more precisely. The discussion focuses on the items that have to be known in order to follow the presented analyses. For more detailed information about the CMS experiment please refer to [22] and [23]. A sketch of the CMS detector is shown in figure 2.1.

The CMS experiment is located at the LHC ring at the exact opposite side of ATLAS. The weight of 14000 tons exceeds the weight of the ATLAS experiment by a factor of 2. With a height of 15 m and a length of 24 m it is relatively compact. The detector layout consists of layers of sub-systems that are stacked around the interaction point in the barrel region. The open sides of the layers are covered by a special endcap detector system. The barrel region is divided into five detector wheels. These wheels are counted as yoke barrel (YB) 2-, 1-, 0, 1 and 2. Moving the wheels during accelerator

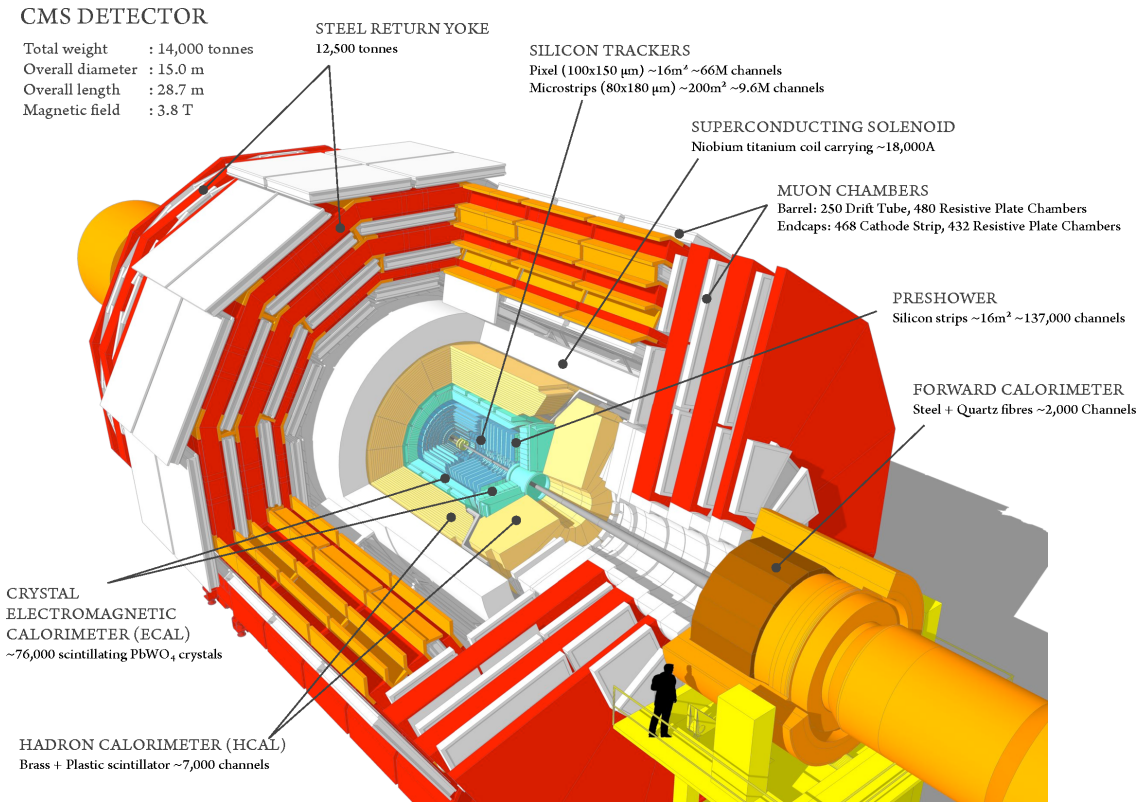

Figure 2.1: Cutaway sketch of the CMS detector [24]. The concentric cylinder shaped sub-detectors around the gray colored beam axis are part of the barrel region. The detector disks, that close the cylinder, are part of the endcap region.

shutdowns allows to reach all detector components in the barrel region.

After the introduction of the CMS coordinate system in section 2.2.1, the sub-systems of the barrel region are introduced from the center to the outside. The endcap detectors of the muon system are also explained in section 2.2.6.

2.2.1 CMS coordinate system

In order to define directions within the CMS detector, a particular coordinate system is used.
It is a Cartesian coordinate system with the origin at the targeted interaction point[1]. This point is also defined as the center of CMS. The x-axis points to the center of the LHC. The y-axis is pointing vertically upwards. The z-axis points into the direction of the particle beam such that the coordinate system is right-handed. The angle in the x-y-plane relative to the y-axis is called ϕ. The angle of the y-z-plane relative to the

[1]The real interaction points are positioned around the targeted interaction point due to the finite size of the proton bunches.

z-axis is θ.
The θ value is commonly expressed as pseudo-rapidity

$$\eta = -\ln\left(\tan\left(\frac{\theta}{2}\right)\right). \tag{2.2}$$

The pseudo-rapidity therefore defines the angle between a line and the beam axis in the y-z-plane. The particle flux originating from hadron-hadron-collisions is about the same for every η interval. A sketch of the CMS coordinate system is shown in figure 2.2. A view of CMS with different marked η values is shown in figure 2.3.
CMS is divided into 12 sectors in ϕ. Sector one is thereby the sector at $\phi = 0$. Thus,

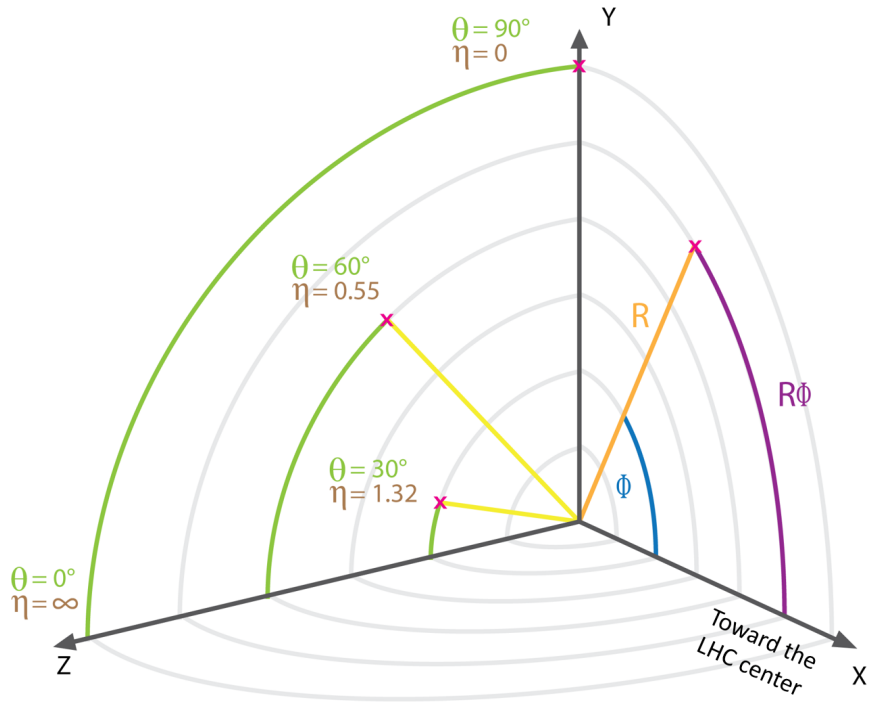

Figure 2.2: Sketch of the CMS coordinate system [25].

each sector has the size of 30°.
The barrel region is at $|\eta| < 0.8$. The so-called overlap region between barrel and endcap is at $0.8 < |\eta| < 1.2$. The endcap region starts at $1.2 < |\eta|$.

Distances in the detector are often calculated as difference in η and ϕ. The distance ΔR is defined as

$$\Delta R = \sqrt{(\Delta\phi)^2 + (\Delta\eta)^2}. \tag{2.3}$$

2.2.2 Tracker

The innermost layer of the CMS detector is the tracker system. It consists of two different components. The closest detector system near the interaction point is a pixel de-

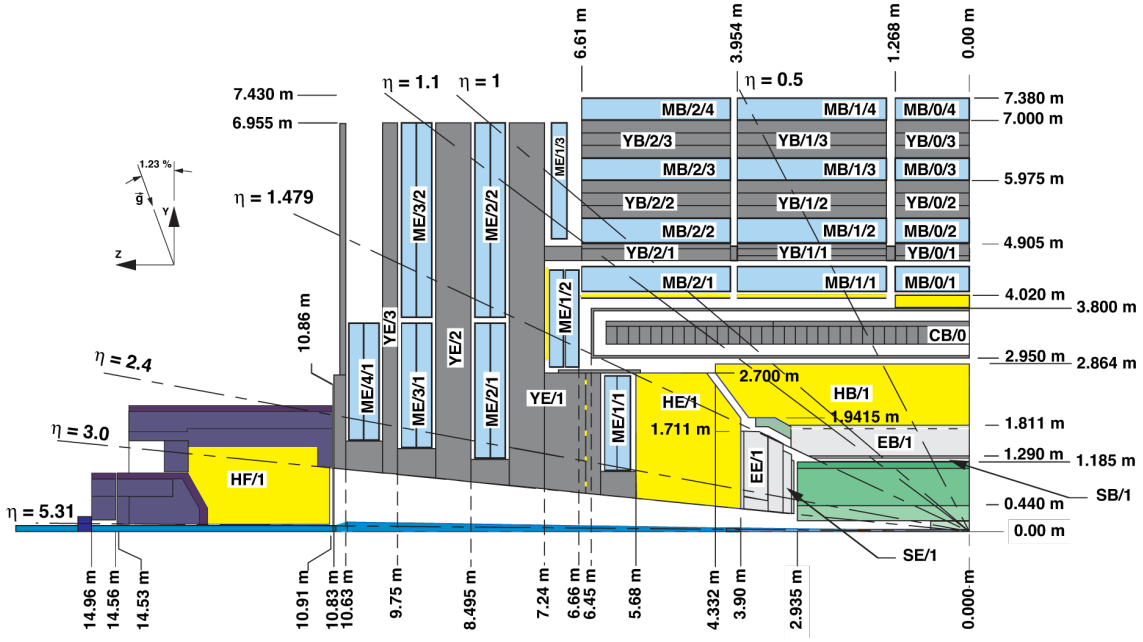

Figure 2.3: Sketch of the CMS in the y-z-plane [26]. Different values of η have been marked. The different sub-systems are explained in the next sections.

tector. The second system is a strip detector. Both detector systems are semiconductor-based devices designed as concentric cylinders around the interaction region. The high amount of channels (66 million pixels + 10 million strips) allows for a primary vertex reconstruction precision of O(10–100 μm) in all three dimensions. The exact value depends on the number of outgoing tracks [27]. A vertex resolution plot is shown in figure 2.4. It is not possible to read-out the whole tracker system at every LHC clock cycle. Thus, the tracker cannot be used in a trigger system that operates at these frequencies.
The high particle flux in the tracker system creates a significant amount of radiation damage. The track density will reach $4 \cdot 10^8 \text{cm}^{-2}\text{s}^{-1}$ at 2 cm distance from the interaction point [27]. This radiation damage is higher than expected, since the LHC already exceeded its design luminosity in the year 2016. Thus, an upgrade and exchange of the pixel detector is performed during the LHC shutdown in 2016/2017. The new pixel detector does not only contain less inactive material, allowing for more precise measurements, but has also an additional active layer. The newly designed pixel detector will allow to have a full coverage at $|\eta| < 2.5$ (compared to $|\eta| < 1.5$ before) and will be almost fully efficient at a luminosity of up to $2 \cdot 10^{34} \text{cm}^{-2}\text{s}^{-1}$ [29].

As the LHC will be upgraded to a high luminosity LHC (HL-LHC) between 2022 and 2025, the entire tracker will again be upgraded in order to cope with the further increased luminosity. Due to this upgrade, the readout capability will be increased, allowing the tracker's strip detector information to be used in the trigger system, that works at a rate of 40 MHz [29].

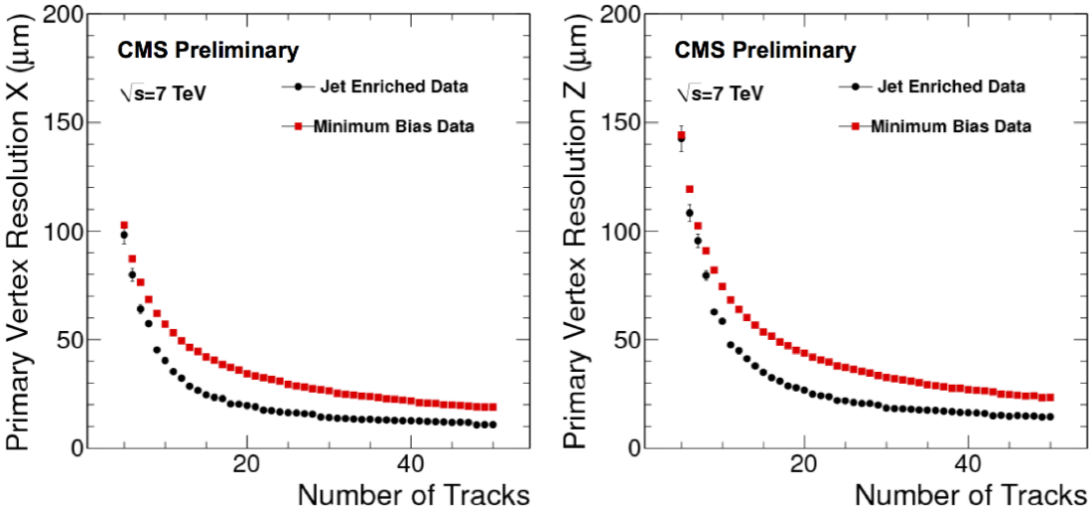

Figure 2.4: Resolution of the primary vertex in the transverse plane (left) and along the beam-line (right) depending on the number of used tracks for reconstruction [28]. Vertices with assigned jets are more precise than those from minimum bias events.

2.2.3 Electromagnetic Calorimeter

The next layer is the electromagnetic calorimeter (ECal) [30]. It can measure the energy of photons and electrons/positrons as long as they are completely stopped within the ECal. The ECal is divided into two regions. The ECal in the barrel region is called ECal-Barrel (EB), and ECal-Endcap (EE) in the endcap region, respectively. The EB is placed concentrically around the interaction region. The active material of the ECal consists of lead tungsten crystals (PbWO4). These crystals have a very high density ($\rho = 8.3 \frac{\text{kg}}{\text{dm}^3}$), but are highly transparent and scintillating [31]. This material therefore allows for a continuous energy measurement of all the deposited energy. Furthermore, lead tungsten crystals are quite radiation resistant. The ECal has a thickness of 26 X_0 (electron radiation length) in the barrel region.
The calorimeter is divided into so-called calorimeter towers in which the deposited energy is measured. In the barrel region a single calorimeter tower has the size of $\Delta\eta \cdot \Delta\phi = 0.087 \cdot 0.087$.

2.2.4 Hadronic Calorimeter

In principle, the ECal is also able to measure hadronic showers. But as for hadronic showers the size of the ECal would have to be much larger in order to completely stop the shower, a second calorimeter was placed directly behind the ECal. The hadronic calorimeter (HCal) is a sampling calorimeter utilizing brass as absorber material[2] and organic scintillator tiles for readout [32]. The scintillator type was selected to be

[2]Over one million shell casements from the Russian Navy used in World War II were melted and used for parts of the brass absorber. A perfect example of how to make “swords to plowshares”.

long-term stable and to have an acceptable radiation hardness [33]. The hadronic calorimeter consists of four components: The hadron barrel (HB) and the hadron outer (HO) detectors are placed in the barrel region. The hadron endcap (HE) and the hadron forward (HF) detectors are placed outside the barrel region in forward direction ($|\eta| > 1.2$).
The HB detector has a thickness of 7.2 – 11.0 hadronic interaction lengths depending on the exact position in CMS. The hadronic interaction length is the distance that a hadron can propagate through the material without making an interaction with a probability of $1/e \approx 37$ %. The size and position of the HCal calorimeter towers match those of the ECal. In order to also measure high energetic jets, that are not fully absorbed within the HB, the hadron outer (HO) system was installed as a so called tail catcher.

2.2.4.1 Hadron Outer Calorimeter

The HO is located in the barrel region directly behind the CMS solenoid [34]. It consists of 2730 scintillating tiles of BC-408 [35] with a thickness of 1.0 cm [36] each. The tile size is $\Delta\eta \cdot \Delta\phi = 0.087 \cdot 0.087$ [34]. The tiles match the calorimeters towers (see section 2.2.3). A picture of an HO tile is shown in figure 2.5.
In the center wheel of the CMS barrel region (YB 0), a second scintillator layer behind the first layer of the return iron yoke is installed. These two separated scintillator tiles

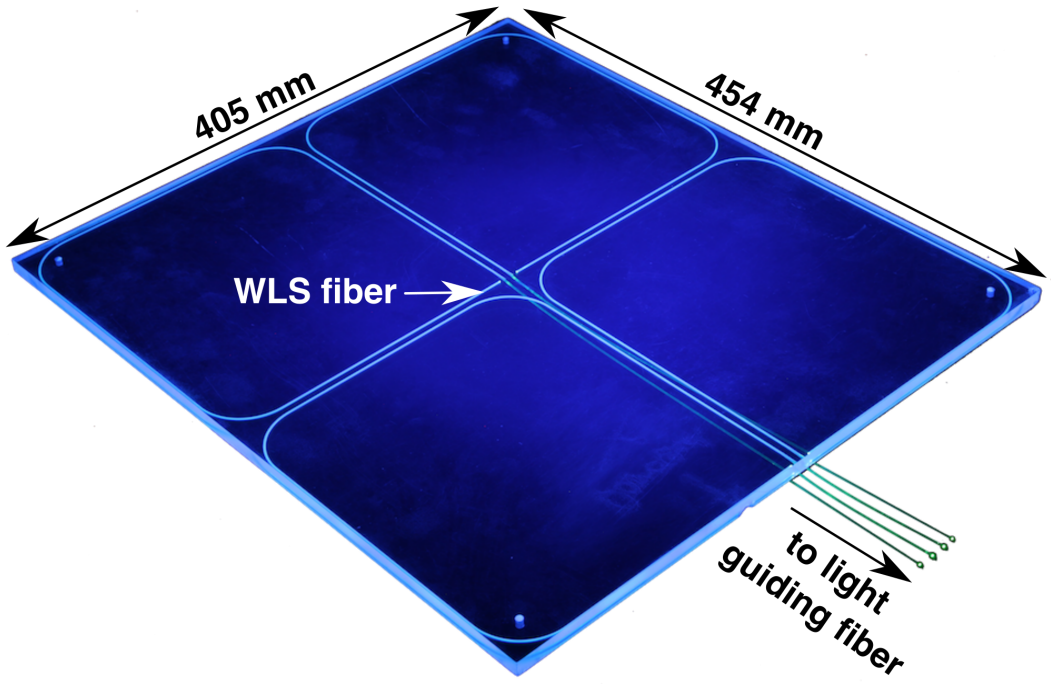

Figure 2.5: Picture of an HO tile. The four wavelength-shifting fibers are directed to light guiding fibers.

allow for an improved energy measurement as well as a reduction of noise induced by thermal neutrons. A picture of the HO position relative to the rest of the calorimeter system is shown in figure 2.6.

The use of the solenoid as additional absorber allows for an extension of the maximum

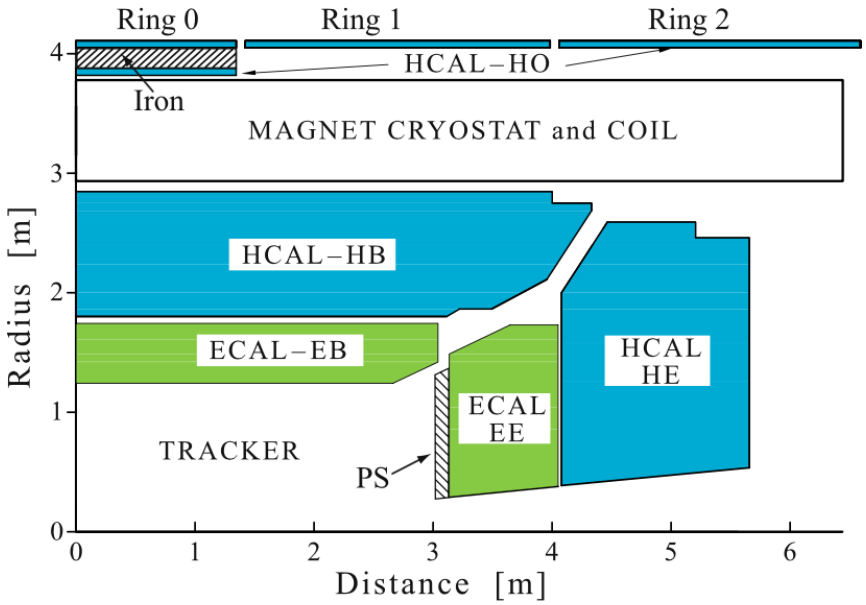

Figure 2.6: Position of the hadron outer calorimeter (HO) in the CMS detector [34]. The HO has two scintillator layers in wheel 0 (called Ring 0).

contained hadronic interaction lengths in the calorimeter system. A plot of the material budget of the calorimeter subsystems in terms of hadronic interaction lengths is shown in figure 2.7.

A concept of a muon trigger similar to HO was discussed since 2007. The resulting detector concept that could be used instead of the HO system is described in section 3. Since the HO system plays a key role in this thesis, its technical design and the HO tile counting system are described in detail now.

Technical design Each HO tile has four wavelength shifting fibers (WLS) embedded. Each WLS fiber is positioned in a sigma shape groove in a quarter of each tile. The light from the WLS fiber is then guided with a clear light transmitting fiber to silicon photo-multipliers (SiPMs). The signal of one calorimeter tower is thereby directed to one SiPM. The light guiding fibers are directly mounted to the SiPMs surface in all wheels but wheel 0. In wheel 0 the fibers are mounted in front of a light mixer that is placed upon the SiPM (see section 8.3 for further details). Up to 18 SiPMs are located on the optical decoder unit (ODU) that are mounted in the readout-module (RM) which are located behind the first muon station (see section 2.2.6 for the position of the muon stations) on the readout-box (RBX). One RBX mounts three to four RMs.

HO used hybrid photo-detectors instead of SiPMs during CMS startup. However, they showed to be noisy and have a photon detection efficiency degrading with time [37].

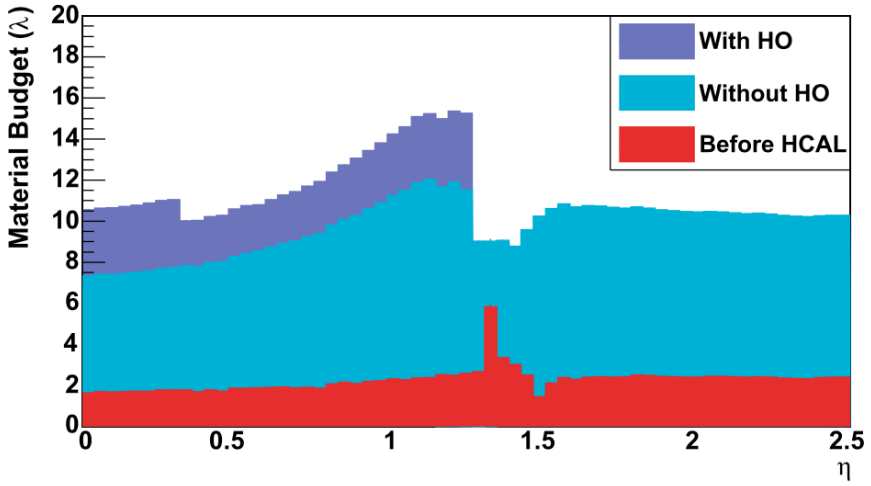

Figure 2.7: Material budget of the CMS calorimeter material [34] as a function of the pseudo-rapidity η. The extension of the calorimeter system with HO allows for additional 2–3 interaction lengths in the calorimeter measurement.

For the upgrade process towards SiPM readout please refer to section 8.2 and 8.3.
The SiPM signals are digitized by a QiE 8 [38] in 25 ns steps and transmitted out of the service cavern[3]. The QiE is also located in the RM. The digitized information from three SiPMs is transmitted via one optical fiber. Eight of these fibers are integrated into one data cable. The setup in the experimental cavern is shown in figure 2.8
In the service cavern the data cables are split again and rearranged such that eight clear fibers - each containing the data from three HO tiles - are combined in one cable. The processing of this digitized data is then done in the HCal trigger and readout cards (HTR). 14 HTR cards are operated in one of the four HO VME crates in the service cavern. Two of those cards are used for calibration only. Each HTR card has two input channels (called top and bottom).
The data of every tile is processed in the HTR card. Ten so-called time slices are integrated to a charge value. In case of an external trigger signal, all integrated HO charge values are routed to the data concentrator card (DCC). The DCC then transmits the HO information to the data acquisition.
Additionally, these charge values are sent out as HO trigger primitives (HO TPs). The upgrade and technicality of the HO TP deployment is explained in chapter 8.

HO tile counting In order to count HO tiles it is not appropriate to use the η and ϕ position since their values are floating numbers binned in steps of 0.087. Therefore, the tiles are counted in integer coordinates called iϕ and iη. This counting is more easy to handle. Starting from the center of CMS in wheel 0, the tiles are counted in iη. Tiles in negative wheel sides have the values $-15 \leq i\eta \leq -1$. Tiles in positive wheel

[3]The service cavern is close to the experimental cavern that houses the CMS detector. The service cavern houses trigger and data acquisition electronics and is always accessible, also during LHC runs.

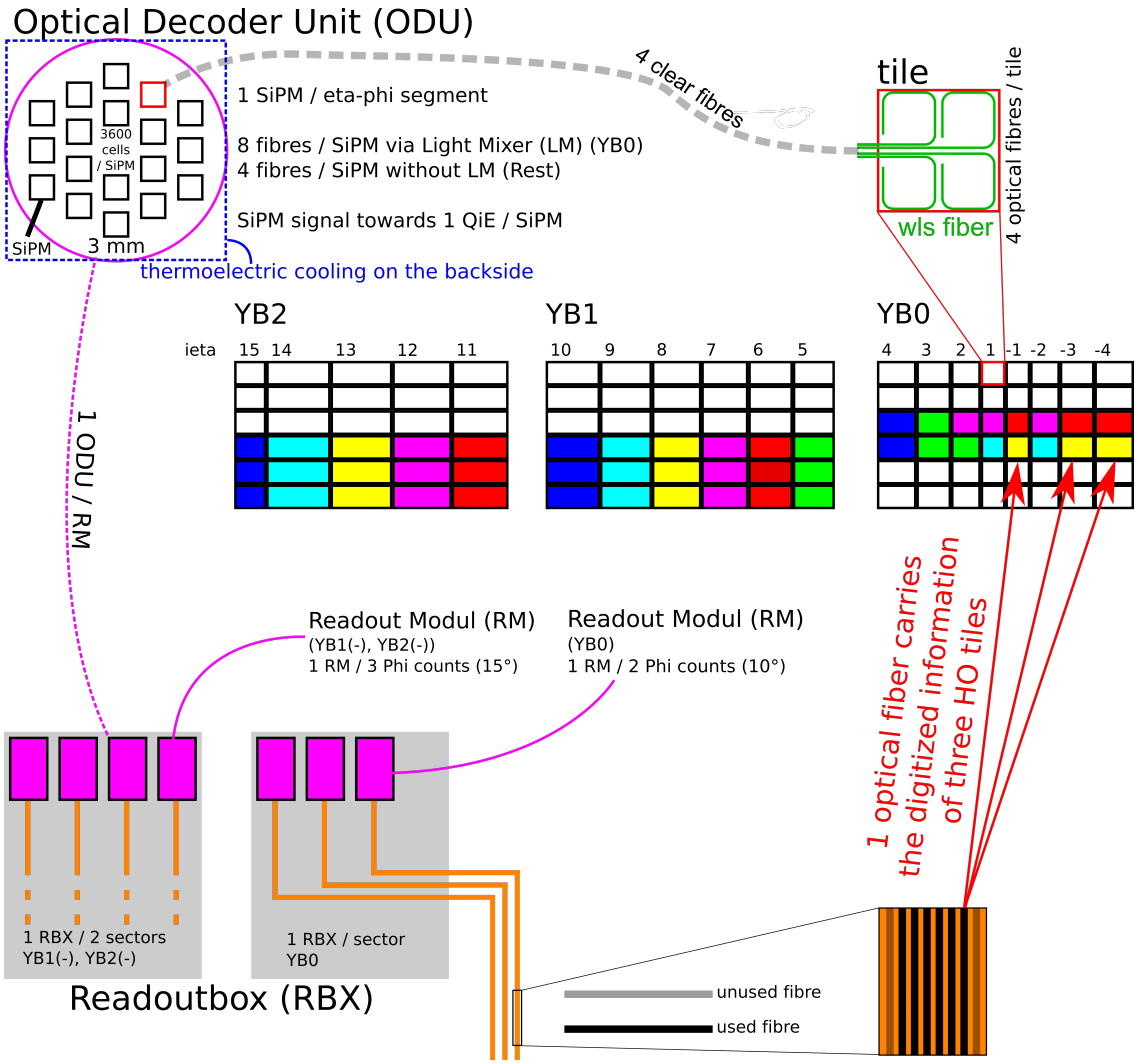

Figure 2.8: HO readout layout in the experimental cavern. The information of the three HO tiles with the same color within a wheel are transmitted via one optical fiber to the service cavern. The pattern is repeated in the white-colored tiles.

sides consequently have the numbers $1 \leq i\eta \leq 15$. A tile at $i\eta = 0$ does not exist since HO has no central tile.
The counting of the $i\phi$ variable starts at $\phi = 0$ and is counted up to 72 in the mathematical positive direction of rotation.
An illustration of the $i\eta$ and $i\phi$ counting of HO is shown in figure 2.9.

2.2.5 Solenoid

Except for HO, the calorimeter system in the barrel region is surrounded by the superconducting solenoid. A map of the magnetic field induced by the solenoid is shown

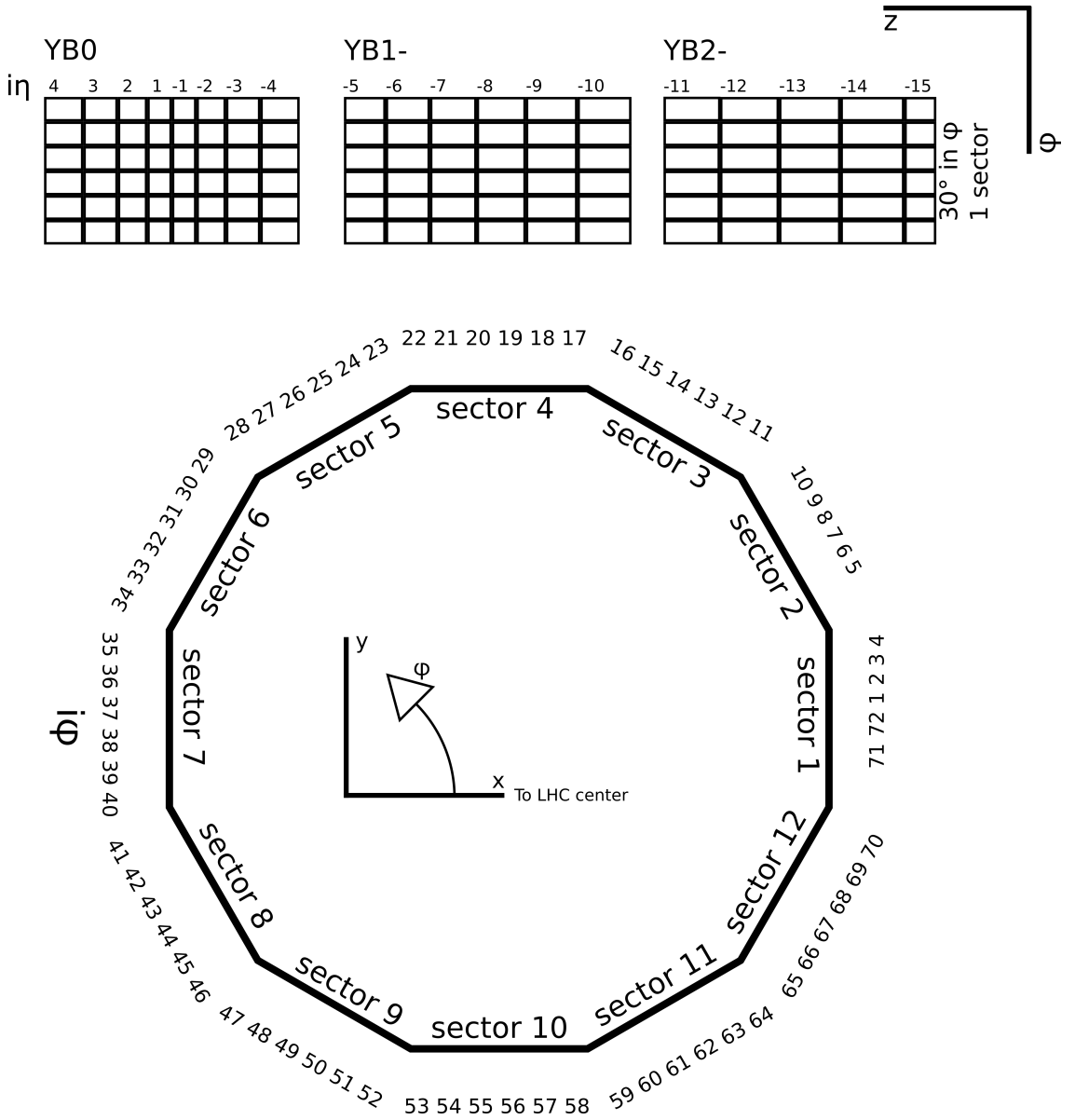

Figure 2.9: Tile counting of the HO tiles in iη and iϕ. The tiles in wheel YB 2 and YB 1 are counted accordingly.

in figure 2.10. The B-field inside the solenoid is very homogeneous at a magnetic flux density of 3.8 T. The solenoid is cooled with liquid helium allowing for an inducing current of 18160 A.
The field outside the magnet is returned via the iron return yokes. Three yokes alternate with stations of the muon system. Due to the return yokes, the magnetic field outside the solenoid and yokes is low ($B < 0.2$ T).

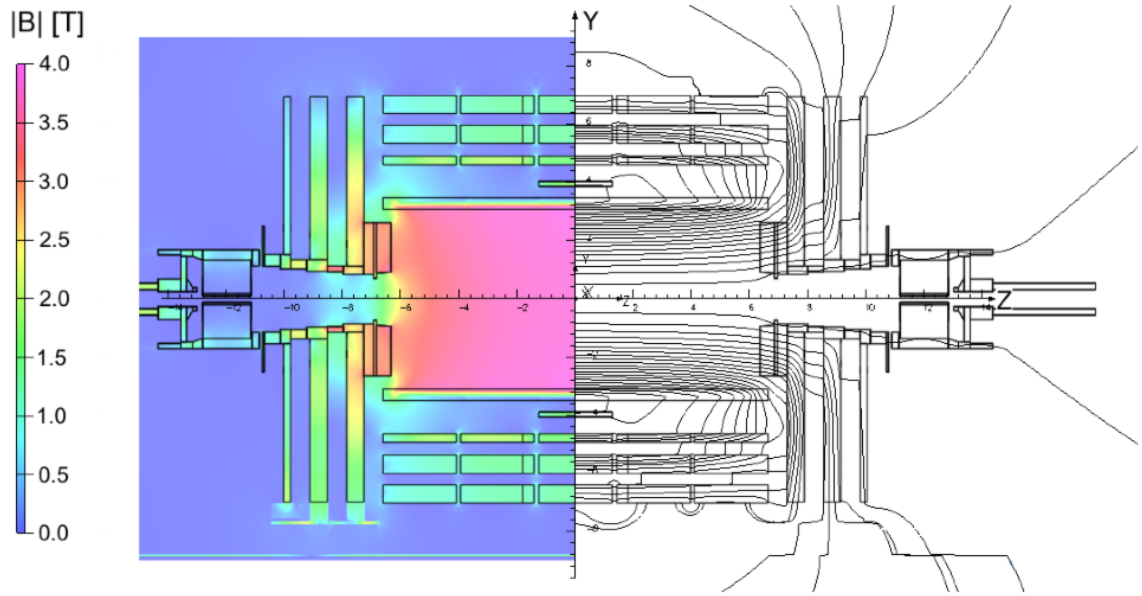

Figure 2.10: y-z-plane of the simulated magnetic field in CMS [39]. The left hand side shows the magnetic flux density. The right hand side shows the field lines.

2.2.6 Muon system

The outer most detector system is specialized for muon measurement. This muon system - located behind the HO system - consists of three independent systems:

- The drift tube system (DT) is located in the barrel region (see section 2.2.6.1).
- The resistive plate chamber system (RPC) is located in the barrel region as well as in the endcap region (see section 2.2.6.2).
- The cathode strip chamber system (CSC) is only installed in the endcap region (see section 2.2.6.3).

The three muon systems are explained in the next sections in more detail. The description contains the information that is crucial for an understanding of the analyses in this thesis. A very detailed picture including many technicalities can be found in the technical design report of the muon system [40].
The DT and RPC systems are positioned in four stations in the barrel region. The stations are counted MB 1-4 starting with the station nearest to the interaction point. As described above, the iron return segments are located between the stations. A high p_T muon will have an almost straight track. Due to the fact, that the gaps of the muon system between different wheels are at a fixed z position, they are at different η positions for different stations. The track projection for straight tracks in the muon system is shown in figure 2.11. The graphic allows to see the muon system gaps that a straight muon track will hit. In this projection a straight muon track is a line parallel to the y-axis.

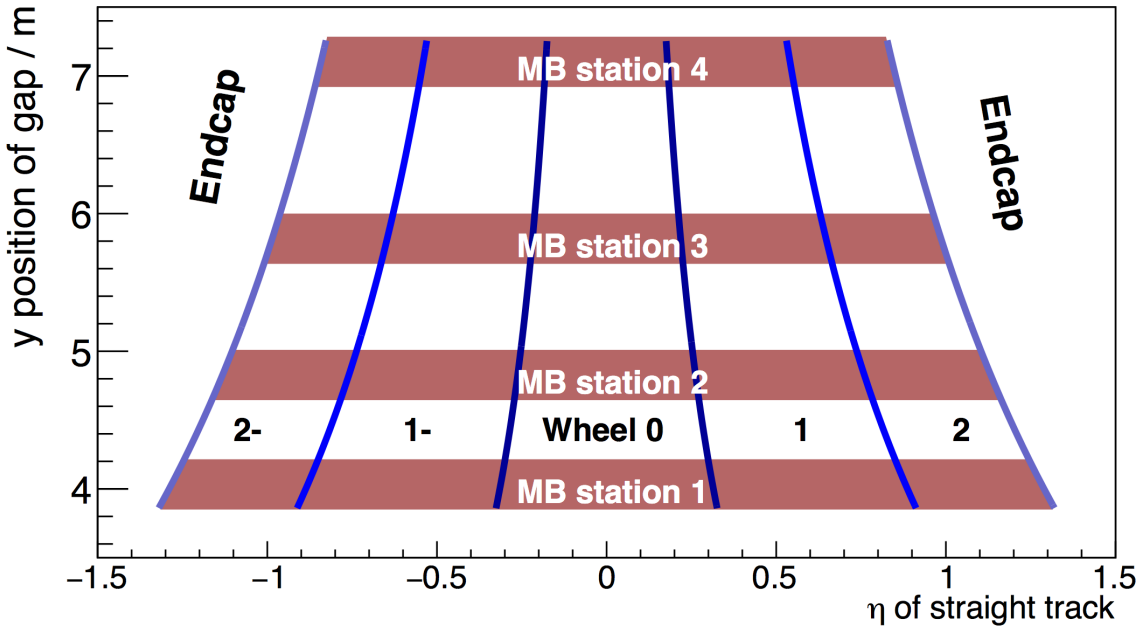

Figure 2.11: y projection of the muon chambers (MB station 1–4). A straight muon track has a fixed η value on the x-axis. This plot allows to easily see which MBs are hit by a muon with a straight track. The blue lines mark the wheel borders.

2.2.6.1 Drift-Tubes

The drift tube system (DT) of the CMS detector consists of a large number of drift tube cells. A single cell has an area of 13 mm · 40 mm and a length of 2.5 m. At this length a conducting wire is centrally stretched. The cell uses an argon-carbon dioxide gas mixture and a high voltage supply O(kV) to create charge avalanches. The maximum drift time is 400 ns with a single cell resolution of 260 μm [41]. A sketch of a DT cell and its electrical field is shown in figure 2.12.

Four layers of cells are stacked to one so-called superlayer. Depending on their orientation, the super layers are called η- and ϕ-superlayer. Thereby, superlayers with a fine ϕ resolution are called ϕ-superlayer, and for η correspondingly.
The muon stations 1–3 contain two ϕ- and one η-superlayer. The muon station 4 has only two ϕ-superlayers. The ϕ-superlayers measure the muon track in the bending projection. A complete station can obtain a spatial track resolution of 100 μm.

Trigger algorithm As already mentioned, CMS uses a dedicated trigger system in order to reduce the number of events that have to be processed. The DT system plays a prominent role in this trigger. In order to contribute to the CMS trigger, the data in the DT system is processed in several steps.
In a first step, the bunch and track identifier (BTI) tries to find four or three cells in a superlayer that have registered a signal from a traversing muon. The timing and position of the muon in the cells are aligned by solving a system of linear equations [40]. The

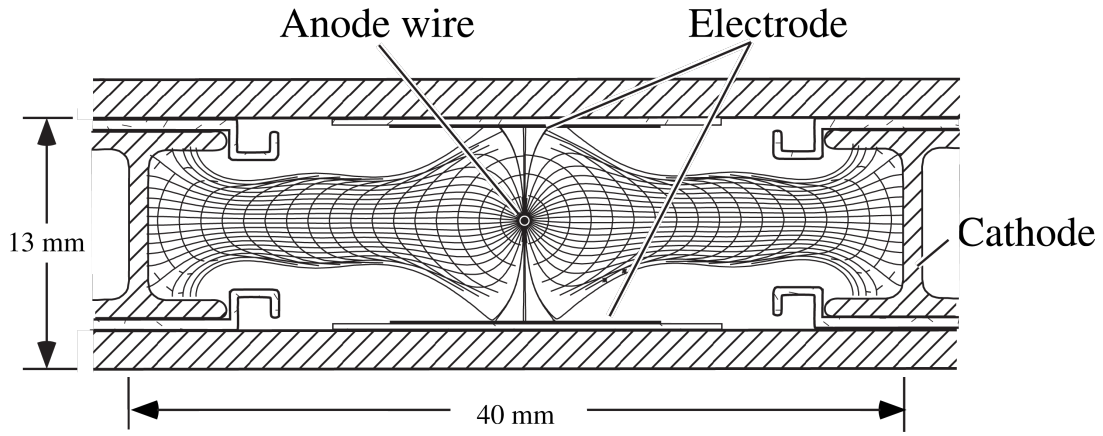

Figure 2.12: Draft of a single DT cell and its electrical field [40]. The DT cell has a size of 2.5 m in the direction along the wire. The drift lines and isochrones are also shown for a typical applied bias voltage.

results are timing and angle information of a track of three or four DT cells. The local BTI tracks of the two ϕ-superlayers in a certain station are then combined in the track correlator (TRACO). The TRACO picks the BTI track of the superlayer that is closer to the interaction point and checks the second superlayer for a BTI track in a search window of $\phi_{\text{search}} = \pm 55^\circ$ [42]. If a corresponding BTI track is found, the TRACO creates a trigger primitive (TP). The TP contains information of the muon entrance point in the muon station, the muon's angular direction and the muon timing. The TRACO information is available for the η- and ϕ-superlayer separately. The TRACO can output one track information (η and ϕ) per bunch-crossing. If more than one combination of BTI tracks is possible, the two TPs with the highest quality (the highest number of hit DT cells) are sent out. The second TP is then transmitted during the next bunch-crossing. A schematic of the TRACO function is shown in figure 2.13.

The TPs are then further used depending on the muon trigger layout. In the original legacy trigger, the Track Sorter (TS) collects all TPs within a station. These TPs are then directed from the TS into sector collector (SC), that collects the data of the whole sector. This collected data is then forwarded to the DT track finder (DTTF). TPs are combined to DTTF tracks there. The DTTF uses a 3-step scheme to build tracks [43]. For every pair of distinct muon stations (i.e. MB 1 and MB2 or MB 3 and MB 4) a track segment is calculated by matching the DT TP of the inner station to a DT TP of the next outer station using a matching cone. These track segments are combined to tracks in a next step. Up to two muon tracks in a sector in a given wheel are created by combining the track segments. If more than two tracks are possible, the tracks with the highest quality (i.e. most hit DT cells) and the highest transverse momentum are selected. In a last step, the physical values of η, ϕ, and p_T are assigned to the matched tracks.
After the track assignment, the four muon tracks with the highest quality and transverse momentum are filtered and forwarded to the global muon trigger (see section 2.3.1).

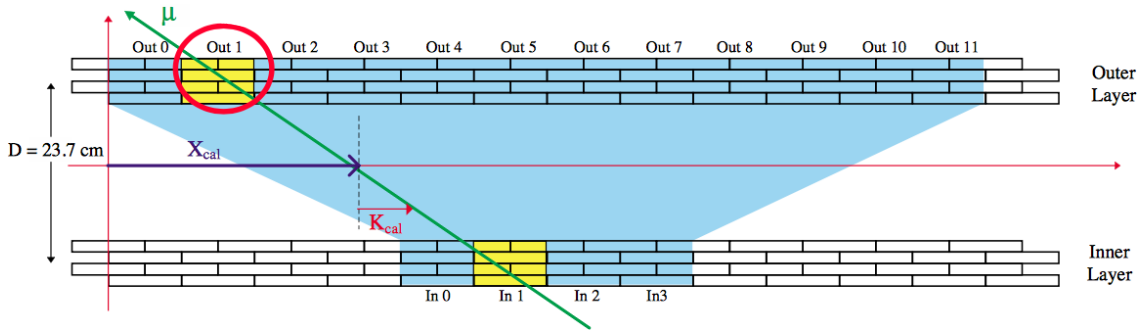

Figure 2.13: Sketch of the TRACO [42]. The TRACO uses the lower BTI track and matches it to the upper BTI track. The values X_{cal} and K_{cal} are values used for internal computation. Using these values the entrance position and muon direction are calculated. For further information on this calculation refer to [42].

2.2.6.2 Resistive-Plate-Chambers

The RPC system equips the CMS detector with double gap resistive plate chambers in the barrel and endcap region. The RPCs are also located in the four stations in the barrel region that also contain the DT system. The muon stations 1 and 2 contain two RPCs. The muon stations 3 and 4 contain only one RPC.
Due to the very precise timing measurement, RPC can achieve a timing resolution of 3 ns compared to 5 ns of the DT system. However, the spatial single hit and track resolution is worse compared to the DT system with a Gaussian width of about 8 mm in the barrel region [44]. Besides of the reduced spatial resolution, the RPC system is a fully redundant muon measurement system [45]. Thus, the RPC also transmits four muon candidates in the barrel region to the global muon legacy trigger.
The increasing luminosity will be a future challenge for the RPC system since it will increase the noise rate. Also the reduction of SF_6 gas usage due to environment protection contributes to an increased noise rate since SF_6 is an electron catching gas [46].

2.2.6.3 Cathode-Strip-Chambers

Cathode-Strip-Chambers (CSC) are also used in the endcap region as muon detection system. The particular challenge in the forward region is the uneven and in some areas strong magnetic field (i.e. 3 T in the first CSC station) and the high particle flux. The CSC system has three to four chambers for muon measurement. Each chamber contains six planes in order to allow for a precise track measurement. The design timing resolution is 6 ns [39].
The CSC system also creates up to four muon candidates that are fed into the global muon trigger.

2.3 Trigger system

As stated above, the LHC collides proton-proton bunches every 25 ns translating to 40 million bunch-crossings (also called events) per second. Each bunch-crossing can result in O(10 – 50) proton-proton interactions (pile-up). The high rate of events does not allow for a complete record of all data taken during these events. In order to reduce the number of events, that are recorded, a two-stage trigger system has been installed [47]. The requirements for this trigger system are very tight. On the one hand, the trigger has to reduce the data to a manageable amount. On the other hand, the trigger must not discard events containing important physics processes. As additional constraint, the full detector information can currently only be buffered for 3.5 μs. A first trigger decision has to be done within this latency time.
The two-stage trigger system thereby allows for a very fast discard of less interesting events in a first step (Level-1-Trigger, L1). Interesting events can be further analyzed and sorted in the next higher trigger stage (High-Level-Trigger, HLT).
This trigger chain allows to reduce the number of recorded events from 40 million per second to about 100 – 1000 per second [48].

2.3.1 The Level-1-Trigger

The L1-Trigger is processed on dedicated hardware. Currently, only the information of the muon system and the calorimeter system is considered since the readout of the tracker at a rate of 40 MHz is impossible.
A sketch of the L1-Trigger chain is shown in figure 2.14.
The two main trigger parts, the muon trigger and the calorimeter trigger, work separately. The calorimeter trigger uses the information of ECal and HCal regionally to create energy information called trigger primitive [49]. These trigger primitives are used by the regional calorimeter trigger, that creates basic jet information locally. On the one hand, this information is used by the muon trigger to define the isolation of muons. On the other hand, the local information is used by the global calorimeter trigger to generate information about jet topologies and missing transverse energy for the global L1-Trigger.
The muon trigger was changed in 2016. Before, DT, RPC, and CSC created muon candidates independently. DT and CSC created up to four candidates each. Thereby, DT used information of the CSC system in the overlap region and vice versa. The RPC system created up to eight muon candidates - up to four candidates in the endcap and in the barrel region each. These up to 16 muon candidates were forwarded to the global muon trigger, which sorted them and used the four muons with the highest measured transverse momentum and measurement quality. These muons were forwarded to the global L1-Trigger. They are referred to as L1 muons.
The global trigger inspects the event topology and checks if certain criteria are fulfilled. Typical trigger criteria are certain particles above a particular p_T threshold or a missing transverse energy value threshold and combinations of those. The exact criteria depend on the used look up table (called trigger menu). These menus are adapted for

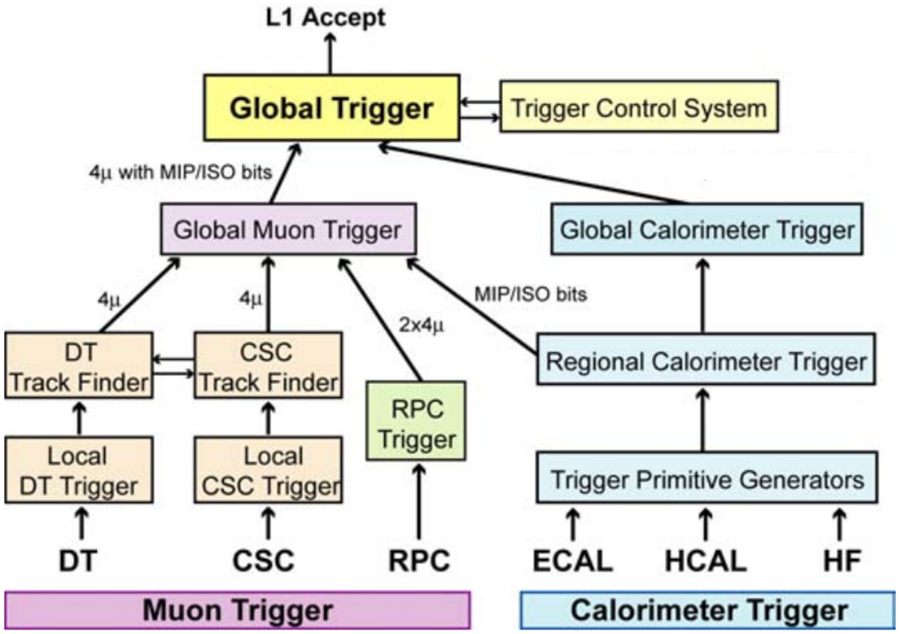

Figure 2.14: Schematic of the L1 legacy trigger chain till 2015 [23]. The information is processed from the bottom up. All steps are realized on dedicated hardware. The muon trigger has changed afterwards, combining DT, RPC, and HO information at the stage of the DT Track Finder (see figure 2.15).

the different run conditions of the LHC.
The individual criteria may be prescaled. Events fulfilling a prescaled criterion are only accepted with a certain probability. The probabilities for the prescaled criteria are also listed in the trigger menu.
If the event passes one or more of these criteria, the L1-Trigger will issue an L1 accept. The event data is then forwarded to the High-Level-Trigger. The L1-Trigger typically issues an L1 accept with a rate of O(100 kHz).

2.3.1.1 Upgraded muon trigger

As the luminosity and thus the particle flux is expected to increase, the muon trigger was upgraded. This upgrade is currently (end of 2016) ongoing. The upgraded muon trigger combines the information of DT and RPC in the barrel region, DT, RPC, and CSC in the overlap region and CSC and RPC in the endcap region to create the muon candidates. The earlier merging of detector data allows for a more efficient muon detection as well as a shorter trigger latency compared to the legacy trigger [50]. The design of the upgraded muon trigger is shown in figure 2.15.
The upgraded muon trigger electronics uses μTCA technology instead of VME [51]. Therefore, the global muon trigger and the global trigger are referred to as micro triggers.
The hardware component that combines DT and RPC data in the barrel region is called

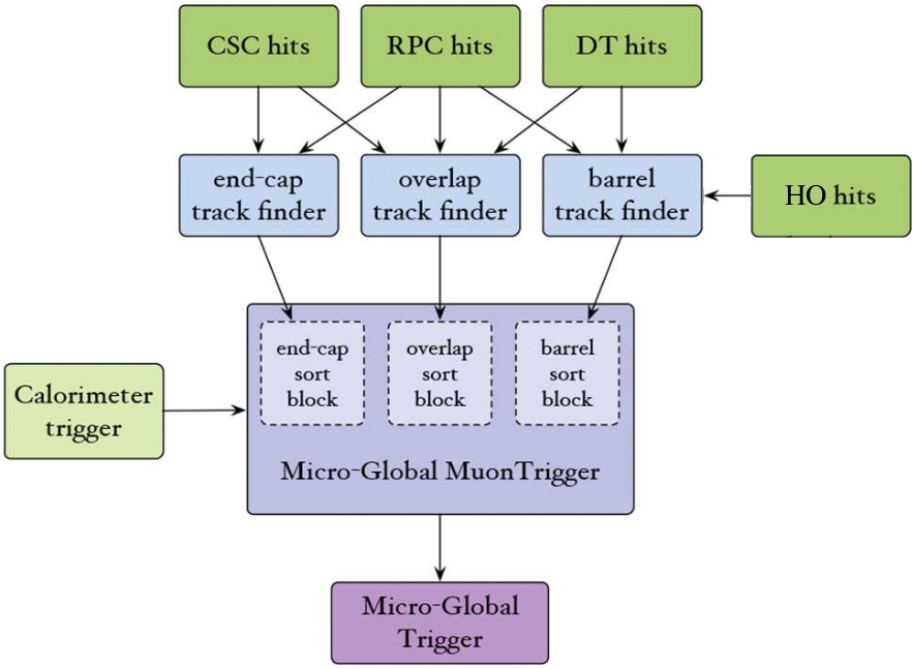

Figure 2.15: Schematic of the upgraded muon trigger [50]. Data is processed from the top down. The detector data is merged for the barrel, overlap, and endcap region. The μ-Global Muon Trigger includes calorimeter data for isolation assignment. The combination of muon candidates from every subsystem can be omitted, resulting in a shorter trigger latency. The μ prefix refers to the newly used μTCA technology. All steps are processed on dedicated hardware.

TwinMux. The TwinMux is able to include information of the HO system if a minimum ionizing particle traversed a particular HO tile (MIP information). In order to justify the effort of an HO data inclusion, the resulting benefit had to be proven. The corresponding analyses are presented in the chapters 5 and 6.
When the micro global trigger accepts the event, the event data is forwarded to the High-Level-Trigger.

2.3.2 The High-Level-Trigger

The High-Level-Trigger (HLT) is the second step of the CMS trigger system. After an L1 accept the full event data is directed to a server farm on the CMS site. The events are processed on many single core computers running the same reconstruction software that is used for a full offline event reconstruction. The online software only uses different parameters and seeds from the L1-Trigger for a faster analysis of the events. Different to the L1-Trigger, the HLT is able to use tracker data. This allows to match muon tracks from the muon system with tracker tracks, resulting in a finer p_T resolution. The HLT therefore uses the muon system information, matches it to the tracks in

the tracker and performs a track fit afterwards [52]. The HLT takes 100 ms – 500 ms to create a trigger decision. The event rate is thereby reduced to about 100 Hz – 1000 Hz. The L1-Trigger and the HLT will face challenges in the future due to an increase of the LHC luminosity.

2.4 LHC and CMS prospects

After the first data taking period - referred to as phase 1, an increase of luminosity is planned. The so-called high luminosity LHC (HL-LHC) will reach an instantaneous luminosity of up to $5 \cdot 10^{34}\text{cm}^{-2}\text{s}^{-1}$. Starting from 2025, the integrated luminosity will accumulate to 2500 fb^{-1} till 2035. As far as a detector environment is simulated in conditions of 2023 in this thesis it is due to the fact that the starting date was postponed from 2023 in former plannings. A plot of the planned luminosities and a rough estimate on the shutdown times is shown in figure 2.16.

During the long shutdown 3 (LS 3) the LHC will be upgraded to the HL-LHC, which

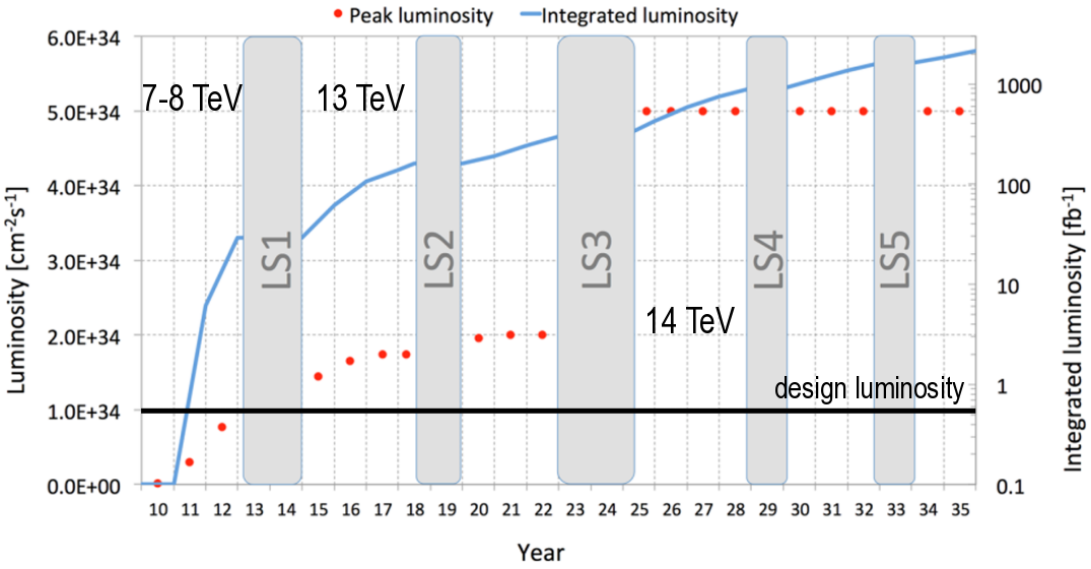

Figure 2.16: Planned peak and integrated luminosity of the LHC over time as of 2015 [53]. The slots for the long shutdowns (LS) show the current planning. The year is referring to 20xx.

is visible by the peak luminosity increase. The period after LS 3 is referred to as phase 2.

Due to the increased instantaneous luminosity, the maximum number of proton-proton interactions within one event can increase to $N_{\text{pile-up}} > 200$ [29]. This high number of interactions will create a high load in all CMS sub-detectors. Furthermore, the detectors will degrade over time due to aging and radiation damage.

The combination of data from different sub-detectors in early trigger stages becomes more vital due to these challenges. Therefore, a fast muon trigger concept has been

developed in order to allow for a combination of a muon tag from an independent detector with the muon track data from the muon system. The aspects and challenges of this concept are presented in the next chapter.

Chapter 3

The concept of a fast muon trigger

The Muon-Track-fast-Tag (MTT) is a concept of a fast scintillator-based muon detector with silicon-photomultiplier (SiPM) readout for application in the high luminosity LHC (HL-LHC). MTT is a complement of the existing muon chambers in the CMS detector. In 2007 this concept did first arise and was developed from there on. Thereby, the applications of this detector-concept have changed corresponding to the evolving design and function of the CMS subsystems.
In the following sections the concept and technical constraints of the MTT will be presented. The evolution of the concept and the current status will be discussed.

3.1 The original idea

This section describes the original MTT concept in 2007. The field of application changed during the last years. For a description of the current applications refer to section 3.3.
In 2007 the MTT was first presented by a group of the INFN Bologna [54]. Studies showed, that for the planned high LHC luminosity of $L = 10^{35}$ cm^{-2}s^{-1} the trigger rate of the muon system will increase above the rate that can be handled by the current L1 trigger (for detailed information about the L1 trigger please refer to section 2.3.1). The trigger rate for muons was planned to be kept at the same 10 kHz as in the current CMS trigger. This can for example be achieved by a larger p_T threshold. But as shown in figure 3.1, the trigger rate cannot be reduced by increasing the p_T trigger threshold due to low energetic muons that are mismeasured as high energetic muons by the muon system when using information from the muon system only. Taking into account the information of the tracker system, the rate of mismeasurement can be significantly reduced. The matching of tracker and muon system information reduces the number

of mismeasured muons by an order of magnitude for muons with a $p_T > 25$ GeV. Thus, a combination of muon system and tracker in the L1 trigger can keep the trigger's ability to reduce the event acceptance frequency using a muon p_T threshold.

The technical development in 2007 suggested that the trigger would not be able to be

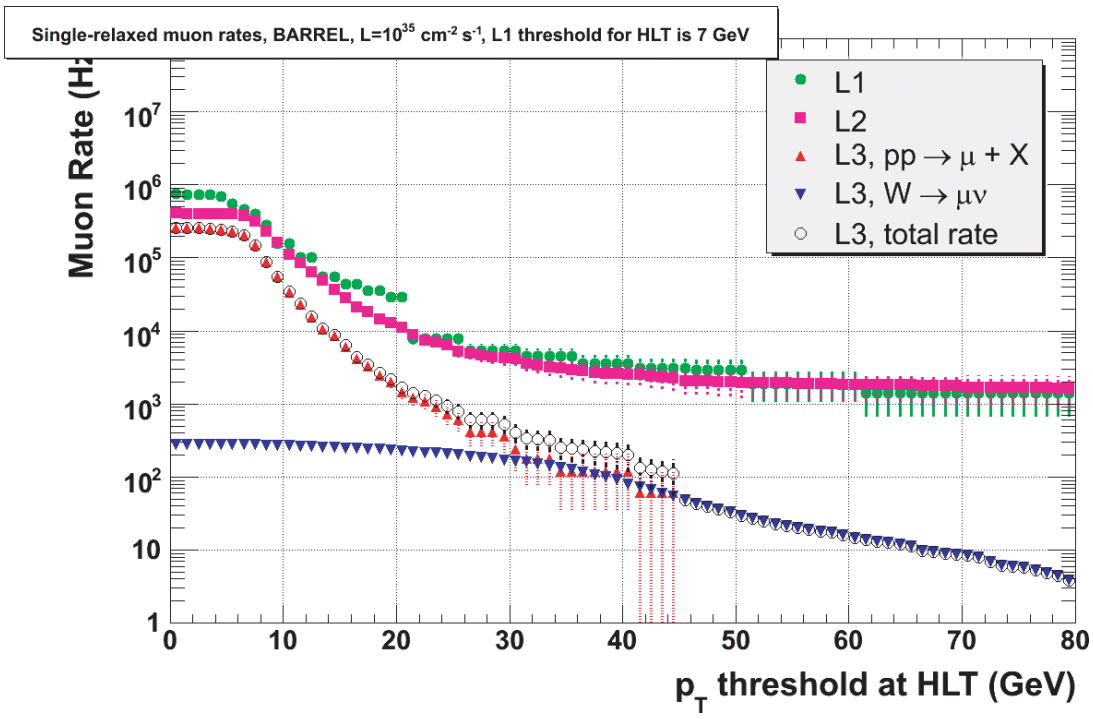

Figure 3.1: Muon trigger rate as a function of the applied p_T threshold [54]. L1 denotes the L1-Trigger. L2 takes into account the full drift time data of the drift tubes. L3 uses a combination of muon system and tracker data in order to improve the p_T resolution. It can clearly be seen that the muon rate in the combined L3 trigger is reduced by one order of magnitude with respect to the L2 and L1 triggers.

fully read out every collision (i.e. every 25 ns) and within the trigger latency of 3.2 μs. The trigger times of the DT system, the global muon trigger and the global trigger are shown in table 3.1.

To solve this problem a partial readout of the tracker system was proposed, based on regions of interest that are read out in the tracker. These regions of interest are defined as a region with a muon in the muon system above a certain p_T-threshold. With this approach the data to be read out from the tracker system could have been reduced to a manageable amount.

In order to achieve a fast readout of the tracker's region of interest, a fast track trigger, referred to as Muon-Track-fast-Tag (MTT), was needed. The potential position was right behind the solenoid in front of the muon system. A particular design was not proposed. Nevertheless, an upgraded resistive plate chamber system (RPC) was deemed possible.

Trigger Sub-System	Latency
DT drift time	18 bx
DT BTI and TRACO	13 bx
Sector collector	43 bx
Transmission to GMT	7 bx
Global muon trigger	10 bx
Global trigger	12 bx
Link to detector	24 bx
Sum	127 bx

Table 3.1: Latency of the DT system and the L1 trigger as of 2015 [43]. One bunchcrossing (bx) is 25 ns.

3.1.1 Geometrical resolution

A geometrical calculation yields an estimator for the needed resolution of the MTT. The needed segmentation can be obtained by calculating the curvature of two oppositely charged muons originating from the vertex with a track direction difference of $\Delta\phi = 45°$

$$\frac{r}{\mathrm{m}} = \frac{p_T/\mathrm{GeV}}{0.3 \cdot B/\mathrm{T}} \tag{3.1}$$

with the track radius r, the muon momentum p_T, and the B-field B and calculating the intersection of these tracks with the MTT directly in front of muon station 1 (see figure 3.2).

Assuming a minimum p_T acceptance for this method of 10 GeV, for a region of interest of 45 ° in the ϕ plane the ϕ segmentation of the MTT is allowed to be 15 ° at maximum. For a tracker layer segmentation of 15°, the region of interest has the size of three tracker layer sectors. 15° in ϕ correspond to $1/24$ of the whole radius.
Therefore, the maximum allowed size of one MTT-module in ϕ ($N_{\mathrm{sectors}} = 24$) at a position directly in front of muon station 1 ($r = 3.85$ m) is

$$\frac{2 \cdot \phi \cdot r}{N_{\mathrm{sectors}}} \approx 1.0 \text{ m}. \tag{3.2}$$

The proposed MTT segmentation in η was half a wheel. Thus, the MTT's η-segmentation is $(1.28 - 1.34)$ m depending on the particular wheel. This translates to a size of the region of interest in x at the position of the tracker (i.e. $r = 80$ cm) of 36 cm.

3.1.2 Timing requirements

At the time of the first proposal for an MTT system the expected trigger latency was 3.2 μs with a bunch spacing of 25 ns. Within the latency time the MTT system has to

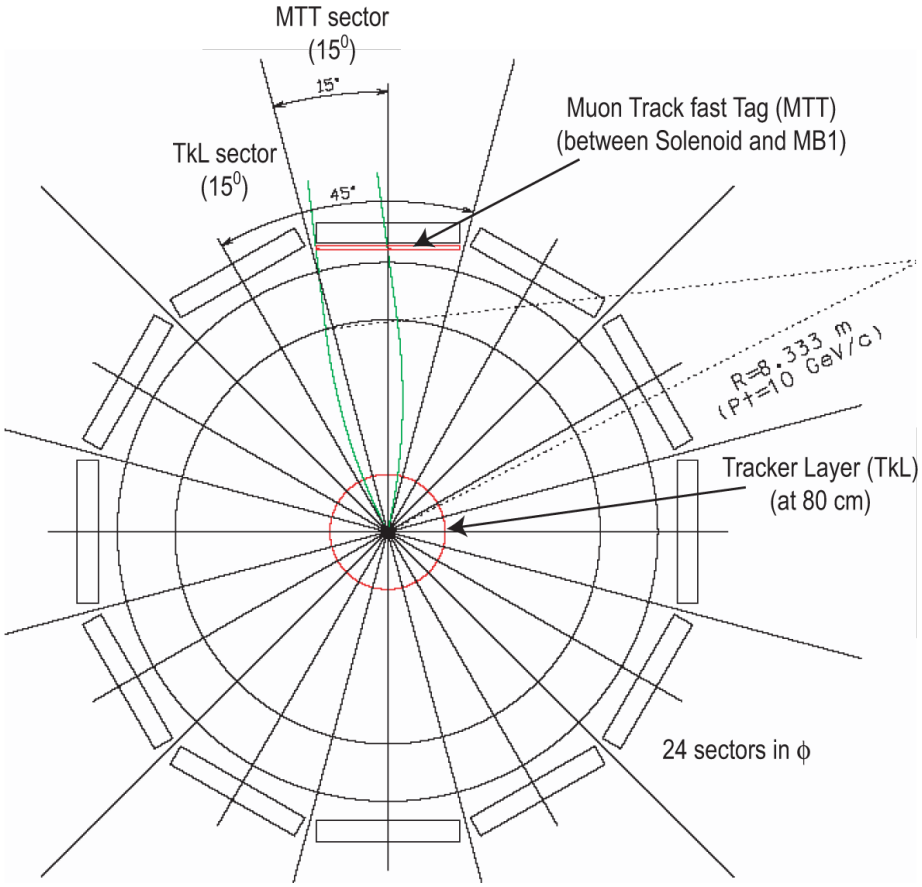

Figure 3.2: Sketch of the calculation procedure for the maximally allowed MTT segmentation in the ϕ-r-plane [54]. The tracker layer (TkL) sectors and the MTT sectors have a size of 15° in ϕ. The curvature of the muon track with $p_T = 10$ GeV is calculated via formula 3.1. R denotes the track bending radius.

define the region of interest and communicate it to the tracker system. The tracker has to read out the data in the region of interest. This data has to be combined with the data of the muon system and then to be processed in the muon and L1 trigger. RPC and DT data was planned to be available 73 and 74 bunchcrossings after the collision (i.e. after 1.825 μs and 1.850 μs) [40] in the global muon trigger. Taking into account the readout of the tracker part and transmission delays, the available time for the MTT to produce the muon tag is very short (O(100 ns)).

3.2 MTT development

As stated above, at the time of the first proposal the design and detector type of the MTT was not specified. In 2008 the group of the III. Physics Institute A of RWTH Aachen University joined the MTT group bringing up the idea of a scintillator-based muon

detector with silicon-photomultiplier (SiPM) readout [55]. The III. Physics Institute B of RWTH Aachen University also joined later on [56].

3.2.1 Prototype development

The idea is to use a fast scintillator and SiPMs with fast readout electronics to detect signals of minimum ionizing particles that traverse the MTT. SiPMs are semiconductor-based photo-detectors consisting of parallel Geiger mode avalanche photo-diodes. They have a small size (O(few mm^2)), are B-field resistent, and very fast with a typical time resolution of O(1 ns) [57]. A lot of prototype development has been conducted since 2008. The development concentrated on various fields of the potential MTT detector. These fields are presented in the following sections.

3.2.1.1 Geometrical layout

The decision on how large a single scintillator tile has to be in the MTT detector is a trade-off between the complexity and the resolution of the system [58]. A small tile size results in a large amount of transferred data and expensive readout electronics. Too large scintillator tiles could limit the potential of the detector. During the detector development tiles with a size of $10 \cdot 10$ cm^2 were investigated. Nonetheless, a larger tile size of $35 \cdot 35$ cm^2 has also been investigated [59][60]. The final size will be also depending on the exact physics application. A picture of an MTT module prototype with $10 \cdot 10$ cm^2 and $35 \cdot 35$ cm^2 is shown in figure 3.3.

The designated type of light readout is depending on the final tile size. For small modules (i.e. $10 \cdot 10$ cm^2) the direct readout would be preferred due to a more homogeneous light collection [61]. But with growing tile size the indirect readout via wavelength-shifting fibers (WLS) allows for a better collection of light [62] [59].

3.2.1.2 Reflective coating of the scintillator

To reflect the light that is produced by a muon in the scintillator and thus avoid light losses, a good reflective coating had to be found. The research concentrated on various types of coating (i.e. white ink, Tyvek, aluminum foil, PTFE). Several key conclusions could be drawn during the studies.

- An air gap between scintillator and coating is necessary in order to preserve total reflection. [62]
- The coating has to resist physical stress during preparation of the detector. Therefore, aluminum foil is not handy. [63]
- PTFE and Tyvek show a very good diffuse reflection and are stable and proper to handle. [59][63]

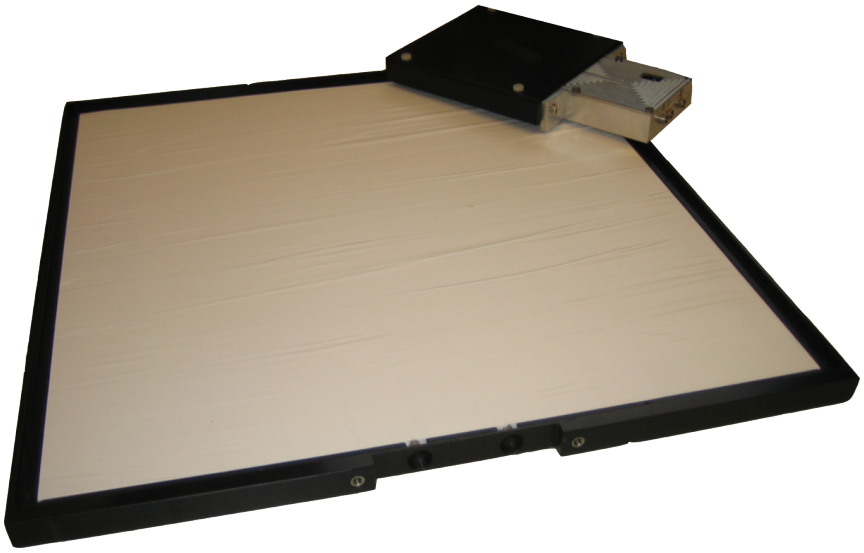

Figure 3.3: A picture of two MTT prototypes with direct SiPM readout [59]. The scintillator of the larger module has a size of $35 \cdot 35$ cm^2. The scintillator of the smaller module is as large as $10 \cdot 10$ cm^2. Both scintillators have a thickness of 1 cm. The case of the small module is closed. The large module is opened and has no electronics attached. The wrapping with white PTFE tape is clearly visible.

3.2.1.3 Type of SiPM

The investigation on the properties of SiPMs and the consequences for the MTT detector were committed with very high effort. To make a statement about the best SiPM type for an MTT detector, the properties of SiPMs had to be studied in detail. Due to the very dynamic improvements of SiPMs over the last years, the exact SiPM properties were subject to fast changes. The key aspects of an SiPM are their geometric properties, their temperature dependence of the dark current [64] and the required bias voltage [65] as well as the parameters of crosstalk and afterpulsing and photon detection efficiency [66]. Detailed measurements and simulations of the electrical characteristics have also been performed [67] [68].
In summary, the latest generation of SiPMs comply with the requirements for an MTT detector in terms of noise and efficiency [59]. The size of the SiPM used for a readout of the MTT module should be $3 \cdot 3$ mm^2 or above rather than $1 \cdot 1$ mm^2 with a cell pitch of 50 μm in order to collect much light to distinguish between signal and noise with a signal purity of 99,9 % for muon detection with an efficiency of 99,5 % [59].
A particular SiPM manufacturer is not pointed out, since nowadays several producers offer SiPMs with the required specifications.

3.2.2 CMSSW simulation of MTT

During the prototype development a coarse model of the MTT detector was included into the CMS software framework (CMSSW) for simulation purposes [58][60]. With these simulations a first estimate on the MTT behavior within CMS was performed. The material properties of the scintillator are that of BC-404 [69], a very fast organic scintillator. Instead of an electronic response, the energy deposition in the scintillator was used as variable for muon detection. Thus, the simulation does not include electronics. The tile size was chosen to

$$\Delta d_\eta \cdot \Delta d_\phi = (10.2 - 10.9) \cdot 25.2 \text{ cm}^2 \tag{3.3}$$

with the distances Δd in the directions η and ϕ depending on the η-position within CMS. The long side of the detector is placed in ϕ-direction. Accordingly, the detector segmentation in the simulation is significantly finer compared to the calculations in the first MTT proposal (see section 3.1.1). The thickness of the scintillator is 10 mm. Using simulations of about 10000 events each including 100 and 200 pile-up interactions and no specific trigger on the event, the signal-to-background-ratio (S/B) and muon-detection-efficiency (ϵ) were calculated. For these events the best threshold for energy loss in the MTT scintillator of 2.0 MeV results in a S/B of $\sim$ 12 with an efficiency of 90 %.[58]. The simulated energy deposition distribution in MTT for events with 100 and 200 pile-up interactions is shown in figure 3.4.

The increase of pile-up does not lead to a dramatic reduction of detection capability

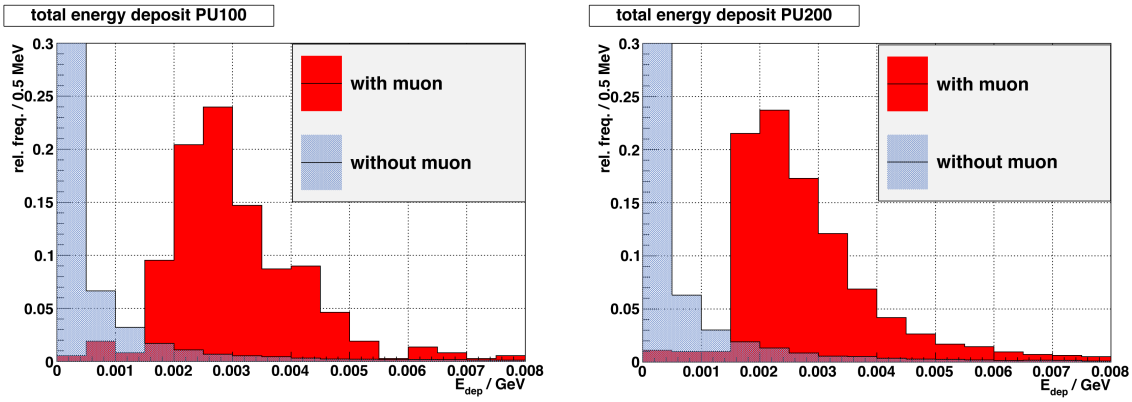

Figure 3.4: Simulated relative energy deposition in MTT in events with 100 and 200 pile-up interactions for MTT tiles with and without passing muon [58]. The distribution for tiles without passing muon is the noise distribution.

of the MTT system. This is a very important result with respect to the plans of the HL-LHC.

The main issue revealed by this simulation is the placing of MTT between solenoid and muon system. The space in this region is limited due to the presence of the hadron outer calorimeter system (HO). Furthermore, some space needs to be left to allow for detector movements. So the MTT detector would have to be very thin (O(5 mm)). An

exchange of HO with MTT would yield more space O(2.5 cm) for the MTT detector components. The simulated position of MTT in CMS is shown in figure 3.5.

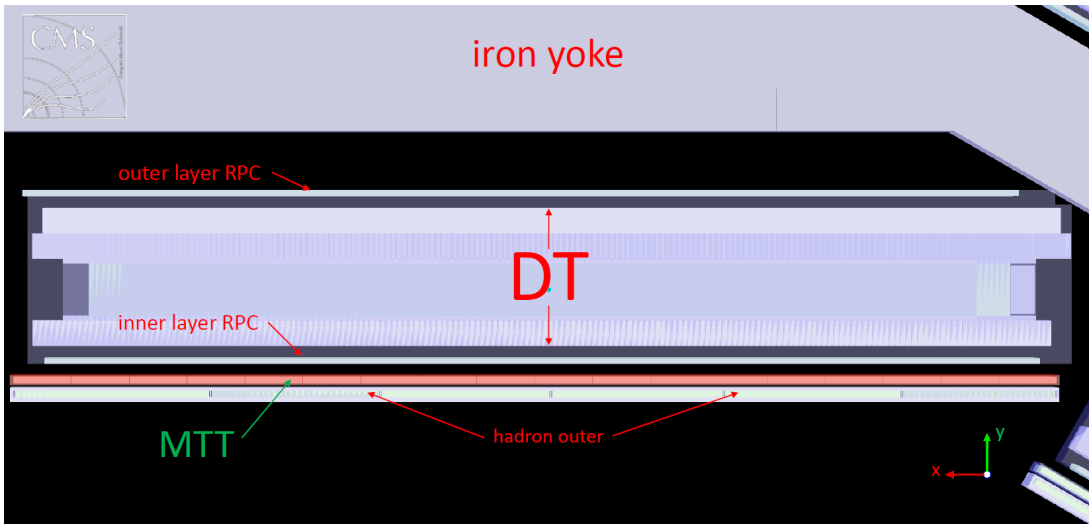

Figure 3.5: A screenshot of the MTT detector in the CMSSW simulation. MTT is placed right behind the existing HO detector and in front of the muon station. The space between HO and muon system is very constrained [60].

3.2.3 Cost estimation for an MTT detector

Due to constant new developments and unknown specs of the MTT concept only a coarse cost estimation is possible. This estimation is done for an MTT detector with $10 \cdot 10$ cm^2 tile size and is based on estimated large quantity prices for the detector components (scintillator, SiPM, electronics) as well as the manufacturing. The sales discount for large quantities is very hard to estimate. Here, the discount is estimated to be 70% at the end of the calculation.
At the position right behind the solenoid the area that needs to be covered is 320 m^2. This results in a need for about 32000 tiles with a tile size of $10 \cdot 10$ cm^2.
This would result in a total cost for the MTT setup of O(5 million) EUR taking into account the large quantity discount. For comparison, the hadron outer system was estimated with 4 million CHF in the technical design report [70] in 1997.

3.3 Present MTT application focus

Summarizing, an extensive MTT prototype development was conducted at RWTH Aachen University. The scintillator layout was tested for $10 \cdot 10$ cm^2 and $35 \cdot 35$ cm^2 tile sizes, a detailed SiPM measurement and analysis was performed and the principle of use was demonstrated in the CMSSW simulation framework.

In parallel to these developments, the upgrade plans for the CMS detector evolved, leading to new prospects for the MTT detector concept.
Compared to the former planning, the trigger latency of the L1-Trigger will increase to 12.5 μs. In coincidence with an upgrade of the tracker system it will be possible to use the full tracker information in the L1-Trigger decision without the need to define a region of interest with an external detector [53].
Due to this development the original application of a dedicated MTT detector became less interesting. The decreased funding for the CMS detector currently does not allow for a complete replacing of HO by a new MTT detector. Refer to section 3.2.3 for a rough cost estimation.
The focus of the MTT concept was therefore changed with respect to the state of the CMS phase II upgrade technical proposal [53]. The new focus of the application of a scintillator-based fast muon trigger in the muon system was investigated widely. Main aspects are presented and the corresponding analyses are referenced in the next sections.

3.3.1 Muon ambiguities

The DT muon detector has a layout of long drift tubes in ϕ and η direction. The tubes of both directions are placed perpendicular to each other. If a muon traverses the detector, the muon position can be determined by finding the intersection of the drift tubes in ϕ and η orientation that measured the muon.
In the case of two muons traversing the same DT station at the same time, four groups of drift tubes could measure muons leading to ambiguities (see figure 3.6). The detector cannot distinguish if two, three or four muons passed the detector.
An MTT detector with tiles significantly shorter than the drift tube's length can reduce these ambiguities. In the described case (see figure 3.6) the MTT detector is able to solve the ambiguity completely if the muon's distance is larger than the MTT-tile size. The potential of MTT in muon ambiguity reduction and the impact of muon ambiguities on the L1-Trigger is discussed in chapter 4.

3.3.2 Muon system inefficiencies

The muon system will suffer from inefficiencies due to aging and radiation damage. The dimension of this loss is hard to estimate. Especially the detector performance decrease due to aging is hardly measurable. However, including currently planned repairs the degradation of the DT system is expected to reach 28 % of the drift tubes and 20 % of the RPCs in 2029 after 1500 fb^{-1} delivered luminosity [71]. In this case, 28 % of the DT channels are expected to be inoperative due to a complete malfunction or a high measurement efficiency loss.
This degradation can lead to significant inefficiencies in the muon system. The impact of this degradation was extensively analyzed for reconstructed muons [71]. DT failure scenarios and the impact on the L1 muon trigger system are discussed in chapter 5. Also the redundancy potential of an MTT like system is discussed there.

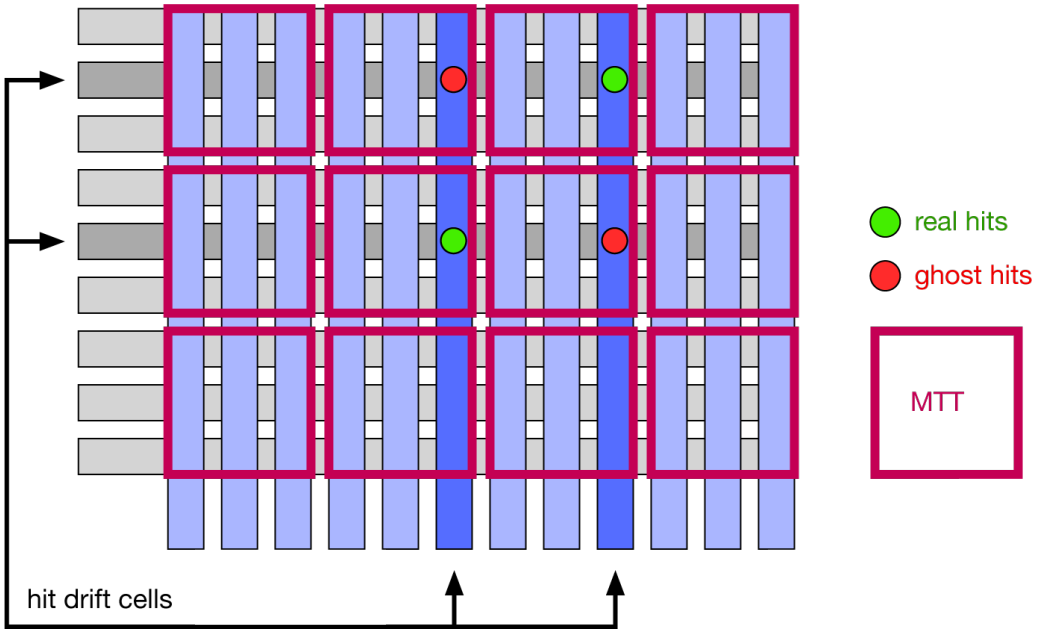

Figure 3.6: Origin of potential muon ambiguities [60]. Two muons traverse the DT detector at the same time. Accordingly, two superlayers of drift tubes (drift cells) in η and ϕ orientation each detect a signal. The reconstruction of the muon paths is ambiguous in this case. The schematic MTT module can solve the ambiguity due to its finite coverage in both DT directions.

The additional information of an MTT detector with a fine granularity can help to compensate for these inefficiencies.

3.3.3 Muon timing measurement

MTT is designed to be a fast and efficient muon detector. Therefore, the timing resolution of this system could be used to support the timing measurements of the muon system. The expected timing resolutions of the muon subsystems are shown in table 3.2. With a typical timing resolution of O(1 ns) for scintillator detectors with SiPM

Subsystem	DT	RPC	CSC
Design timing resolution	5 ns	3 ns	6 ns

Table 3.2: Design timing resolution of all three muon sub-detectors [39] for 2009. The timing resolution is expected to stay stable during the detector upgrades.

readout [72] the gain from this approach is expected to be small. Though, the timing resolution of the muon sub-systems could decrease with higher pile-up due to mismatches between the detector segments.

3.4 Use of HO as MTT-like detector system

The hadron outer calorimeter (HO) is a scintillator-based detector, now with SiPM readout, quite similar to the MTT concept. For further details of the HO system refer to section 2.2.4.1.
A comparison of the HO system and the concept of an MTT detector reveals the ability to gain experience from the HO system for the MTT concept (see table 3.3). The basic

System	MTT concept	HO detector
Scintillator type	BC404	Bicron BC408
Scintillator area ($\Delta d_\eta \cdot \Delta d_\phi$)	$10 \cdot 10$ cm$^2 - 35 \cdot 35$ cm^2	$(26-40) \cdot (33-63)$ cm^2
Scintillator thickness	$0.5 - 1.0$ cm	1.0 cm
SiPM size	$3 \cdot 3$ mm^2, 50/100 μm pitch	$3 \cdot 3$ mm^2, 50 μm pitch
Readout type	WLS fiber	WLS & clear fiber

Table 3.3: Comparison of existing HO system [34][73] and the MTT concept.

structure of both detectors is very much alike. Thus, it is reasonable to use the existing HO system for analyses and to extrapolate the outcome to a possible MTT system.
Consequently, the studies of the MTT's capability to resolve or compensate L1 muon ambiguities, drift-tube failures, and current muon system inefficiencies are discussed using HO as sample detector in the following chapters.

3.5 Summary

A concept of a fast muon trigger has been introduced. Different fields of application and the resulting prototype development were described. However, the focus of the MTT detector application changed during the prototype development. As the CMS muon system will face challenges due to a higher luminosity and pile-up, a new application that uses a fast muon trigger in order to support the muon DT system has been obtained.
The use of HO for an analysis of these aspects has been justified due to the similarity of HO and the MTT concept. A fast muon trigger support in case of muon ambiguities, DT system failure scenarios and muon system inefficiencies is investigated in the next chapters.

Chapter 4

Muon ambiguity studies

As discussed in the previous chapter, a fast muon trigger can support the muon system in its trigger decisions. The capability of the HO (section 2.2.4.1) and the MTT concept (chapter 3) in reducing muon ambiguities is investigated in this chapter. Muon ambiguities are the measurement of two or more muons if only one muon is physically present. These ambiguities are also called ghosts. An example sketch of an L1 muon ambiguity is shown in figure 4.1.

For example, it is possible that a single muon is traversing two different wheels. If the

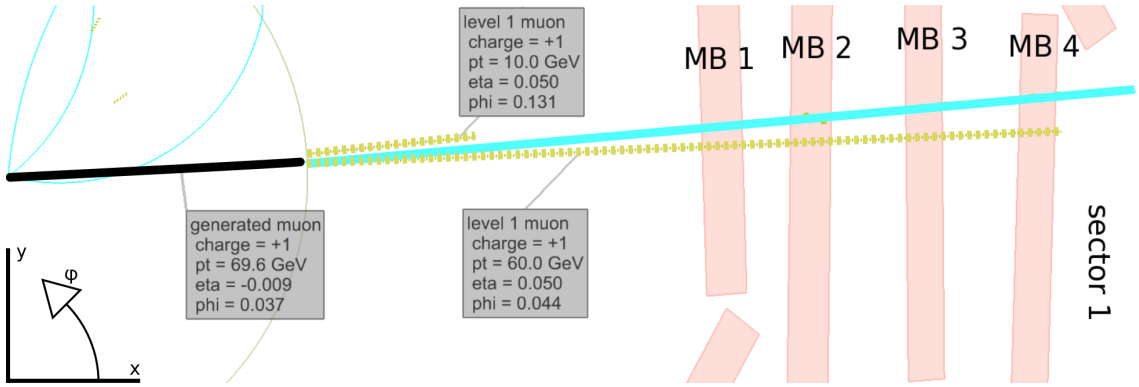

Figure 4.1: Example sketch of an L1 muon ambiguity in the ϕ projection of the CMS detector. Only one generated muon is present. However, the Level-1 trigger creates two L1 muons with slightly different directions and different muon momentum.

matching of the muon tracks from both wheels fails, the resulting measurement could yield two instead of one muon. These ambiguities are also possible at sector borders.

Furthermore, non-muonic particles could be misidentified as muons and could contribute to muon mismeasurements. As the pile-up will increase during the LHC runtime, this effect is expected to worsen.
If these ambiguities occur with a high frequency in the L1-Trigger, the trigger can exceed its bandwidth. Additionally, the respective L1-Trigger is compromised. Therefore, the occurrence of muon ambiguities has to be well understood in the L1-Trigger. Especially, the rate of occurrence has to be investigated.
In order to investigate the impact of muon ambiguities on the L1-Trigger, several analyses with an increasing number of pile-up interactions are presented. As starting point, single muon gun simulations without pile-up were analyzed. After the presentation of these results, an analysis of data from 2015 including pile-up is introduced. Although, the instantaneous luminosity is not as high as it is planned for phase 2, the center of mass energy of 13 TeV is almost compatible with the design energy of 14 TeV.
Finally, the investigation is closed with an analysis of simulations including pile-up in a phase 2 LHC environment (referred to as 2023 conditions or HL-LHC environment). The simulation of events in the expected environment of the HL-LHC is very important due to the high pile-up expectations. Using

$$\mu = \frac{\sigma_{\text{inel}} \cdot \mathscr{L}}{n_b \cdot f_r} \tag{4.1}$$

with the inelastic cross section $\sigma_{\text{inel}} = 81 \pm 3$ mb, the delivered luminosity $\mathscr{L} = 5 \cdot 10^{34}$ cm^{-2} s^{-1}, the number of colliding bunches $n_b = 2808$ and the revolution frequency $f_r = 11230$ Hz, yields a mean pile-up of $\mu = 128 \pm 5$ [74]. More than 12 % of the collisions will have 140 and more pile-up events. The increased pile-up causes a higher occupancy of the muon system. This will directly translate to a higher number of muon ambiguities.
With the investigation results the capability of HO and MTT to distinguish between a physical muon and a ghost track is discussed and a conclusion on the impact on the MTT concept is drawn (see section 4.3).

4.1 Single-muon gun simulations

To gain a clean picture about the impact of muon ambiguities, at first single-muon gun samples without pile-up were investigated. All presented samples contain one half positively and one half negatively charged muons. The simulations were produced using `CMSSW_6_2_0_SLHC28_patch1` simulating the detector at the HL-LHC. The samples were produced with the `GeometryExtended2023`[1]. The simulation includes an upgraded tracker system as it is foreseen for phase 2 detector operation. Furthermore, two layers of gas electron multiplier systems (GEM) [75] are simulated in the forward region ($1.6 < |\eta| < 2.2$). Two planned additional RPC detector layers [76] are also

[1] https://twiki.cern.ch/twiki/bin/view/CMSPublic/SWGuideUpgradeGeom#Extended2023 (called October 5th, 2016)

simulated in this forward region. The simulated L1 trigger chain is still the legacy trigger chain (see section 2.3.1). The impact of the upgraded muon trigger is addressed in the next section. It is however expected to be small.
The single muon gun allows to compare the generator information with the information of the resulting L1 muons. Since each event contains nothing but one generated muon, the number of measured L1 muons can be directly translated into information about ambiguities. If more than one L1 muon is found, the event contains an ambiguity.
Even though the event contains one muon only, a matching of the L1 muon to the reconstructed muon was done in a large cone of $\Delta R < 0.5$, in order to distinguish background L1 muons that occur due to detector noise at a completely different position. However, no L1 muon outside the matching cone was observed in all performed single muon gun simulations. This fulfills the expectation, since the muon system should not create L1 muons without any measurement in the corresponding detector part.

4.1.1 η and ϕ distribution

The η and ϕ distributions of muon ambiguities can yield if the detector topology leads to accumulations of ambiguities at certain positions. In order to gain these η and ϕ distributions of the L1 muon ambiguities, a single muon gun sample was created with a flat transverse momentum spectrum of 5 GeV $< p_T <$ 100 GeV. The muons are flatly distributed in η and ϕ. The η values range from $-0.8 < \eta < 0.8$ to cover the whole barrel region. The whole sample contains 300000 events with exactly one muon per event.
As described before, the matching is intrinsically present.
In a first step, the number of L1 muons within the events was counted. The histogram with the number of L1 muons in all events is shown in figure 4.2.
A L1 muon ambiguity occurred in events with two or more L1 muons. 1097 events (0.37 %) contained two L1 muons. Only one event had three L1 muons. In 5192 events (1.73 %) the L1 muon identification failed. This will be addressed in chapter 6 where a study on the L1 detection efficiency is presented.
In a second step, the η and ϕ directions of the generated muon in events with an ambiguity are filled into histograms. Consequently, the two histograms contain 1098 entries each. The plots are shown in figure 4.3.
Obviously, the number of L1 muon ambiguities is increased for larger absolute η directions. For larger η values the muons have a higher probability to cross two wheels. The muon track is created for each wheel separately in the L1-Trigger and then matched to each other (see also section 2.2.6.1). If this matching fails, the tracks of both wheels can yield a L1 muon and thus result in an ambiguity.
The local L1 muon ambiguity rate increase in ϕ direction, at the gaps between two sectors in the detector, can be explained similarly. The muon tracks in ϕ direction are created for each sector separately, too. If the merging of these tracks between adjacent sectors fails, the two tracks can seed an L1 muon each resulting in an ambiguity.
An improvement due to the upgraded muon trigger (see section 2.3.1.1) is not ex-

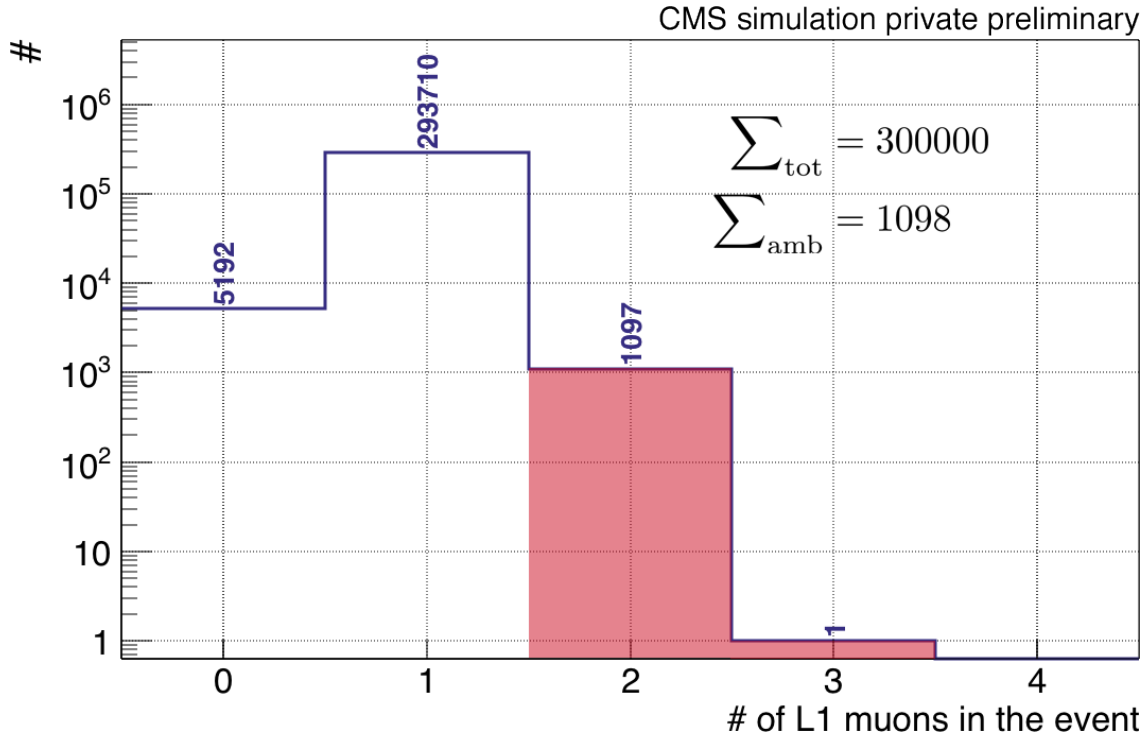

Figure 4.2: The number of L1 muons in 300000 events of a single muon gun with a muon momentum of 5 GeV $< p_T <$ 100 GeV. One L1 muon is expected. Therefore, events with two or more L1 muons are events with L1 muon ambiguity (1098 events). Events without L1 muon are events with an L1 muon measurement inefficiency (5192 events).

pected. The information of DT and RPC is combined in each wheel and sector separately. A matching of the resulting tracks between wheels and sectors, that is susceptive to muon ambiguities, has to be still done.
Even though the accumulations occur, the local increase of the number of L1 muon ambiguities is at a factor of ~ 5 between minima within a sector and maxima at sector gaps. The muon ambiguities thus affect the whole barrel region.
Therefore, it is reliable to examine the impact of all L1 muon ambiguities on the L1-Trigger and not to examine the local hot spots. Especially, since the increase of the L1-Trigger rate is not depending on the exact L1 muon's position.
The topological behavior of L1 muon ambiguities is understood. As a next step the behavior depending on the muon momentum is investigated.

4.1.2 Muon momentum dependence

An investigation of the L1 muon ambiguity rate depending on the transverse muon momentum can give information on the impact of an increase in the energy of the LHC on the L1 muon ambiguities.
Therefore, single muon gun samples with a fixed transverse muon momentum $p_T = (10,$

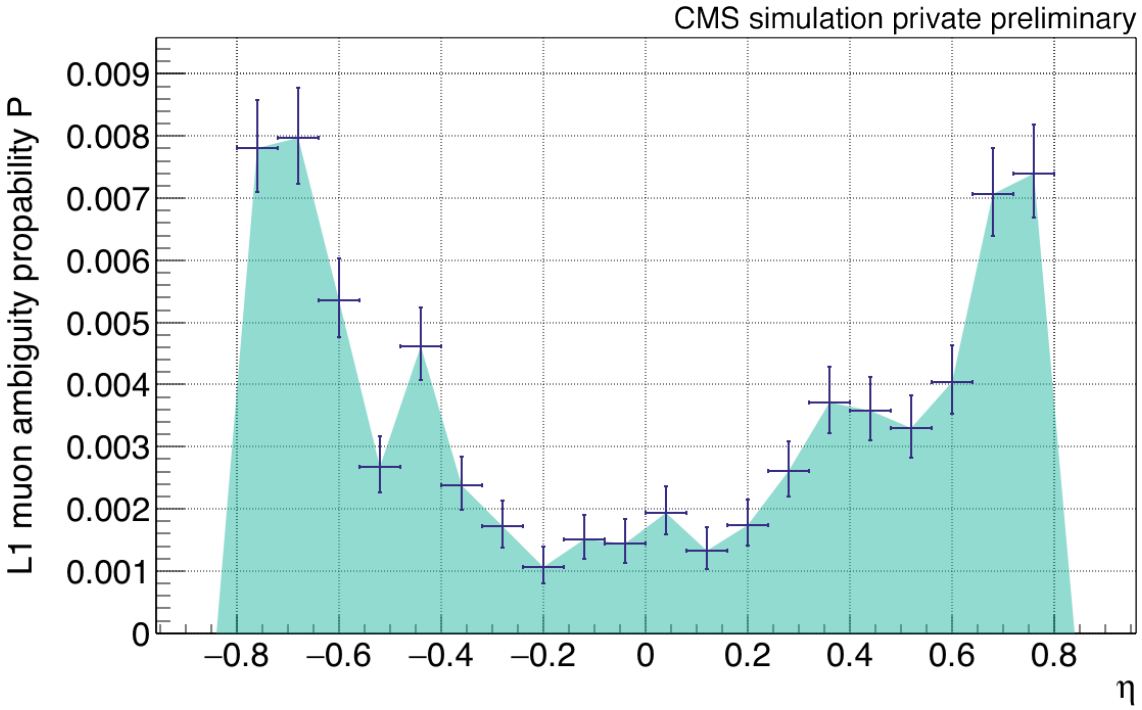

(a)

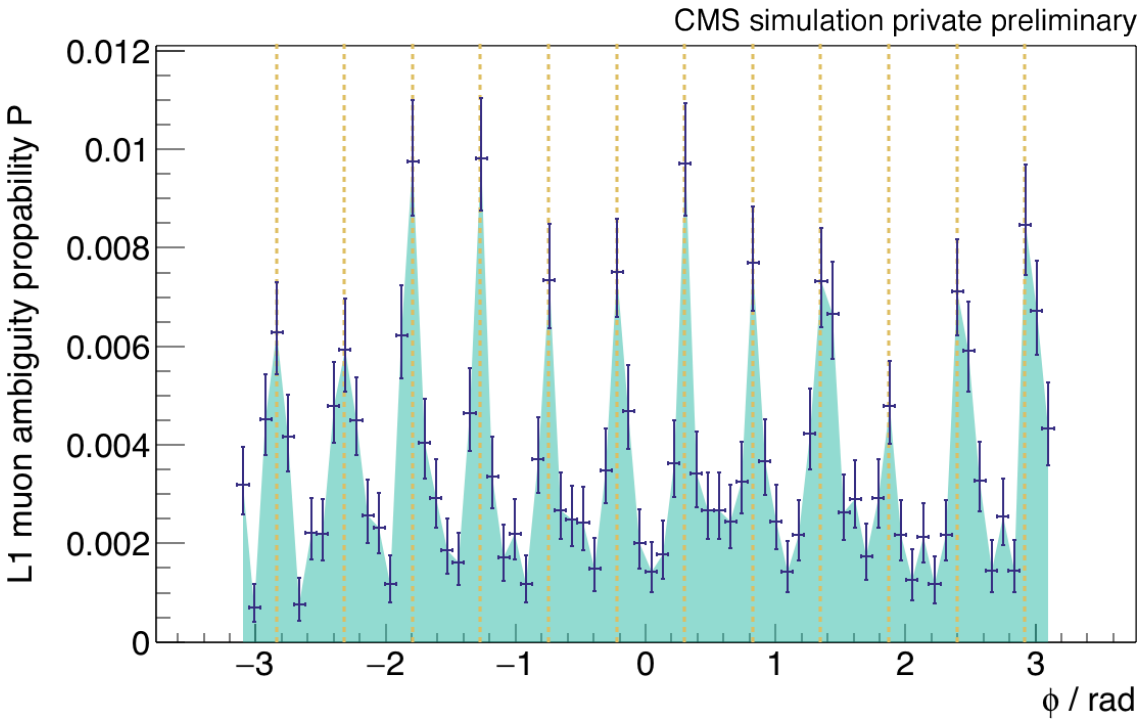

(b)

Figure 4.3: η and ϕ spectra of the generated muon in the events with L1 muon ambiguity. The uncertainty are statistical uncertainties. The yellow dashed lines show the position of the sector borders in the ϕ view.

30, 100, 300, 1000) GeV were produced. As in the sample presented before, the gun covers the full ϕ coordinate space as well as -0.8 $< \eta <$ 0.8. Each sample for a certain muon momentum contains 50000 muons.
The number of L1 muon ambiguities is again determined by counting the number of events with two or more L1 muons. The resulting L1 muon ambiguities are shown in table 4.1.

The number of L1 muon ambiguities increases with the muon momentum. Plotting

	Events with muon ambiguities	
Transverse muon momentum p_T / GeV	Number	% compared to all events
10	165	0.33 ± 0.03
30	145	0.29 ± 0.02
100	220	0.44 ± 0.03
300	441	0.88 ± 0.04
1000	1020	2.04 ± 0.06

Table 4.1: Number of L1 muon ambiguities for different muon momenta. The uncertainties are statistical uncertainties.

the data points reveals an almost linear behavior. Fitting a polynomial of order one results in the ambiguity probability

$$P(p_T) = a \cdot p_T + b \tag{4.2}$$

with $a = (0.26 \pm 0.02)$ GeV^{-1} and $b = (1.81 \pm 0.06) \cdot 10^{-3}$. The $\frac{\chi^2}{\text{NDF}}$ is $\frac{8.2}{3.0} = 2.7$ resulting from a fit taking into account the statistical counting uncertainties, showing that the behavior of the data points is not exactly linear. However, the fit can be used as estimator for the increase of the muon ambiguity rate. The fit result is shown in figure 4.4.

Nonetheless, the increase of the muon ambiguity rate with larger muon momenta does not imply an impact on the L1-Trigger rate.
The L1-Trigger accepts the event if one or more trigger criteria are fulfilled (see section 2.3.1). The transverse momentum of a single muon that exceeds an unprescaled trigger criterion and therefore can initiate the L1-Trigger accept is in the order of 20 GeV. A muon ambiguity for a muon with a transverse momentum above that trigger value will not result in an additional L1 accept, since the accept is already given by the single muon trigger. While the ambiguous L1 muon candidate is still forwarded to the high level trigger (HLT, see section 2.3.2) as seed, resulting in a higher HLT processing time for the event, the ambiguity is likely to be discarded in the HLT since the tracker information is available.
Therefore, the impact of muon ambiguities has to be inspected for muons with a transverse momentum in the range of the single muon trigger threshold.

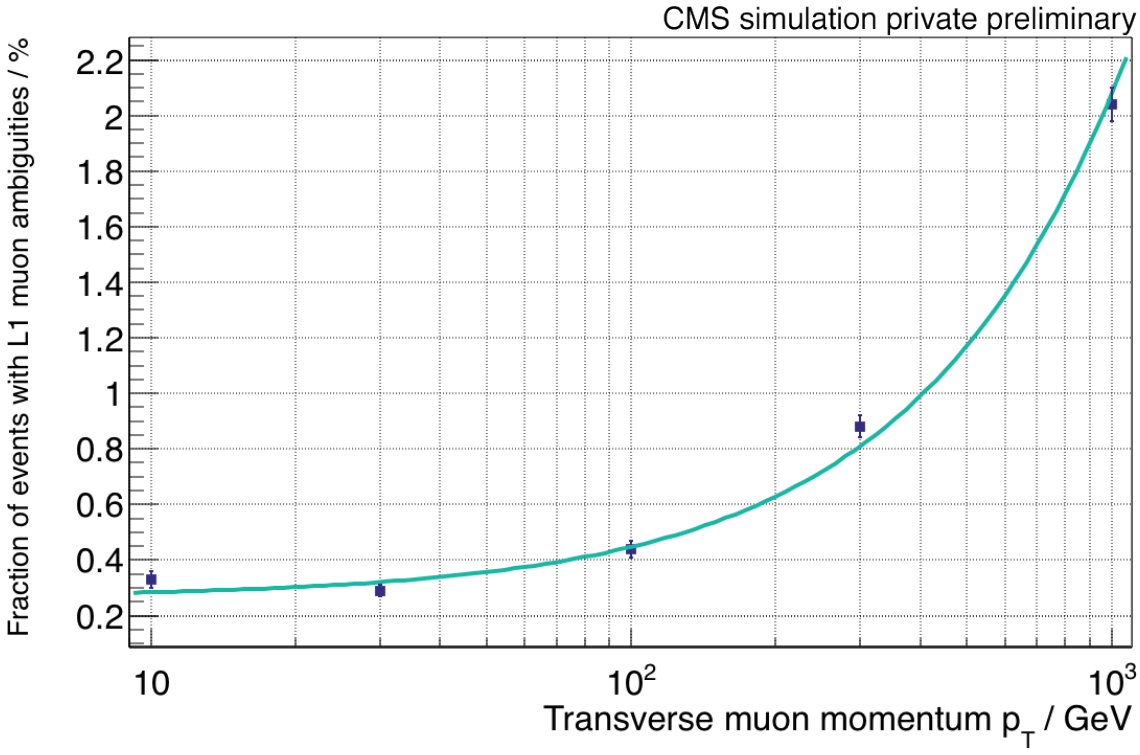

Figure 4.4: p_T dependence of the L1 muon ambiguity rate in a simulated sample with a single muon gun. The curve is a linear fit to the data points.

4.1.3 L1-Trigger rate impact

In order to gain a picture of L1 muon ambiguity's impact on the L1-Trigger rate, 500000 events of a single muon gun were produced. The single muon gun had a flat momentum spectrum of 10 GeV $< p_T <$ 40 GeV. The muon direction spectrum again ranges from -0.8 $< \eta <$ 0.8 and $-\pi < \phi < \pi$.
If two ore more L1 muons can be matched to the generated muon, the event is assumed to contain an ambiguity.
Different trigger thresholds are tested for the single and double muon L1-Trigger. Their order of magnitude is similar to the current trigger thresholds used in 2016 and are expected to stay at similar values in future LHC runs [77].
Only, if the measured transverse momentum of any L1 muon in the event is too low to exceed the L1 single muon trigger threshold and at least two L1 muons in the event exceed the trigger threshold of the double muon trigger, the event would be additionally triggered.
A table of the investigated trigger thresholds and the absolute and relative number of additionally triggered events is shown in table 4.2.
As expected, the number of additionally triggered events is smaller for smaller differences between the single and double muon trigger threshold. However, the number is very small even for this tuned parameter set of the muon momentum thresholds.
An influence of the muon momentum spectrum on the number of additionally triggered

Trigger thresholds		No. of additionally triggered events	
Single muon / GeV	Double muon / GeV	Absolute	Relative
25	10	11	$(2.2 \pm 0.7) \cdot 10^{-5}$
20	10	8	$(1.6 \pm 0.6) \cdot 10^{-5}$
25	15	8	$(1.6 \pm 0.6) \cdot 10^{-5}$
20	15	2	$(0.4 \pm 0.3) \cdot 10^{-5}$

Table 4.2: Assumed trigger thresholds for the single and double muon trigger with the resulting number of additional L1 accepts due to L1 muon ambiguity. The uncertainties are statistical uncertainties.

events is expected if many ambiguous L1 muons have a higher transverse momentum than the correctly measured L1 muon. In this case a steeply falling transverse muon momentum spectrum with a high number of low p_T muons ($p_T <\sim 15$ GeV) will result in a higher number of additionally triggered events, since an ambiguity with a mismeasured high p_T value can exceed the single muon trigger threshold. In order to test for this phenomena, the fraction of the p_T values of the correctly measured L1 muon ($p_{T_{\text{L1 muon}}}$) and the ambiguous L1 muon ($p_{T_{\text{ambiguity}}}$) is plotted (see figure 4.5). The L1 muon with the p_T value that is closest to the p_T value of the generated muon in the event is considered to be the correctly measured muon ($p_{T_{\text{L1 muon}}}$). The fraction

$$f = \frac{p_{T_{\text{ambiguity}}}}{p_{T_{\text{L1 muon}}}} \tag{4.3}$$

is entered into the histogram. If more than one ambiguous L1 muon is present in the event, the fractions are calculated for each ambiguous L1 muon. 2.7 % of the muon ambiguities have a measured transverse muon momentum that is larger than the measured L1 muon momentum of the correct L1 muon (see figure 4.5). The local maxima within the distribution result from the binning of the p_T values in the L1 trigger. Muon ambiguities strongly tend to have a smaller muon momentum than the correctly measured L1 muon. The impact of different muon momentum spectra is therefore expected to be small.

Muon ambiguities will thus not be a problem in the L1 muon trigger for single muons. But the number of muon ambiguities has still to be investigated for events that contain pile-up. Therefore, a pile-up simulation as well as a data analysis have been performed (see sections 4.2.2 and 4.2.1).
The granularity of an HO-/MTT-like muon trigger that is necessary to reject the additional L1 accepts, has been investigated, too.
The positions of the muons creating a false L1 accept were observed. A geometrical calculation yields whether the muons would hit two different tiles of the HO/MTT module. The calculation showed that for none of the additionally observed L1 accepts a granularity of $\Delta\eta \cdot \Delta\phi = 0.087 \cdot 0.087$ is sufficient to distinguish the position of the

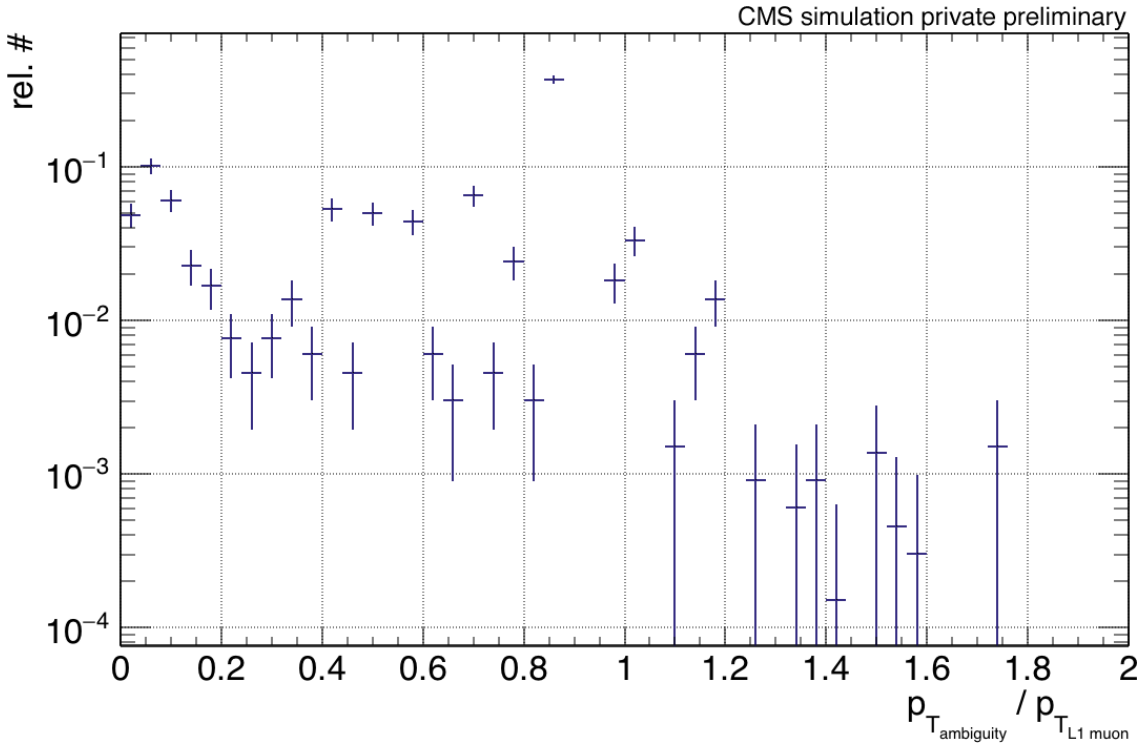

Figure 4.5: Fraction of the p_T values of the correctly measured L1 muon ($p_{T_{\text{L1 muon}}}$) and the L1 muon ambiguity ($p_{T_{\text{ambiguity}}}$). The ambiguous L1 muon has a higher measured p_T value than the correctly measured L1 muon if the fraction is larger than 1.

involved L1 muons.
A look into the position of the L1 muons leading to an additional L1 accept reveals that their position is the same within the binning of the L1 muon coordinates (binned in $\Delta\eta \cdot \Delta\phi = 0.044 \cdot 0.044$). Thus a smaller tile size (e.g. tile size of MTT) can not lead to a better rejection of L1 accepts that are induced by L1 muon ambiguities.

4.2 Analysis of event containing pile-up

Up to this point, the ambiguity phenomena were investigated using a single muon gun. In order to verify these numbers, an analysis of a sample including real pile-up interactions has to be performed. Utilizing a pile-up sample allows for a determination of the influence of pile-up on the number of L1 muon ambiguities.
In a first step, a data set from 2015 has been used that contains a mean pile-up of 10. In a second step, the number of pile-up interactions within the events was further increased by utilizing a simulated sample in an HL-LHC environment with a mean pile-up of 140. Both samples use the legacy trigger.

4.2.1 Data analysis for Run 2015D

The used sample for the first step is a subset of data taken in the last data taking period of 2015 (called 2015D). The set contains 502495 events with a reconstructed $Z \rightarrow \mu\mu$ decay including pile-up. It was filtered by checking if a $Z \rightarrow \mu\mu$ decay is present using a predefined skimmer[2].
The skimming criterion is

$$M_{\text{inv}}(\mu_1, \mu_2) > 30 \text{ GeV}. \tag{4.4}$$

One muon (μ_1) has to fulfill the following criteria:

- $p_T > 10$ GeV
- $\left|\eta_\mu\right| < 2.4$
- μ_1 has to be measured in the muon system and in the tracker.
- $|\texttt{innerTrack().dxy}| < 2$ cm

Another muon (μ_2) has to have a transverse momentum of $p_T > 20$ GeV only.
The η and number of pile-up distributions are shown in figure 4.6.
The η distribution shows a decrease to higher pseudo-rapidities η. This topology is due to the lower number of generated Z bosons at these directions [78]. Furthermore, the distribution shows a decrease at the wheel gap between the wheels 0 and 1±. The detector has a reduced reconstruction efficiency at these gaps.
The average mean pile-up is 10.3, which is expected considering formula 4.1 and the instantaneous luminosity in Run 2015D of $\sim 5 \cdot 10^{33} \text{s}^{-1}\text{cm}^{-2}$ [79]. The distribution shows the expected behavior. In each event the L1 muons are matched to the reconstructed global muons. The matching is valid if the direction of the global muon and the L1 muon at the interaction point differs by $\Delta R < 0.2$. The matching cone is much tighter compared to the analysis of the single muon gun samples (see section 4.1). A matching cone of $\Delta R < 0.5$ would not be sufficient to discriminate other muons in a pile-up sample. For comparison, the resolution of the L1 muons in η and ϕ is 0.043. Furthermore, the relative transverse momentum difference δp_T must be

$$\delta p_T = \left| \frac{p_{T_{\text{RECO}}} - p_{T_{\text{L1}}}}{p_{T_{\text{RECO}}}} \right| < 0.5 \tag{4.5}$$

with the transverse muon momentum of the reconstructed muon $p_{T_{\text{RECO}}}$ and of the L1 muon $p_{T_{\text{L1}}}$. The number of L1 muons within the matching cone is counted. In order to avoid a double counting due to a second reconstructed muon within the matching cone that is assigned to a second L1 muon, the number of additional reconstructed muons within the matching cone is subtracted. The principle of the counting is visualized in figure 4.7.
If two or more L1 muons are matched to a single global muon, an ambiguity occurred.

[2] https://github.com/lpernie/cmssw-1/blob/CMSSW_7_6_X/DPGAnalysis/Skims/python/ZMuSkim_cff.py (called November 8, 2016)

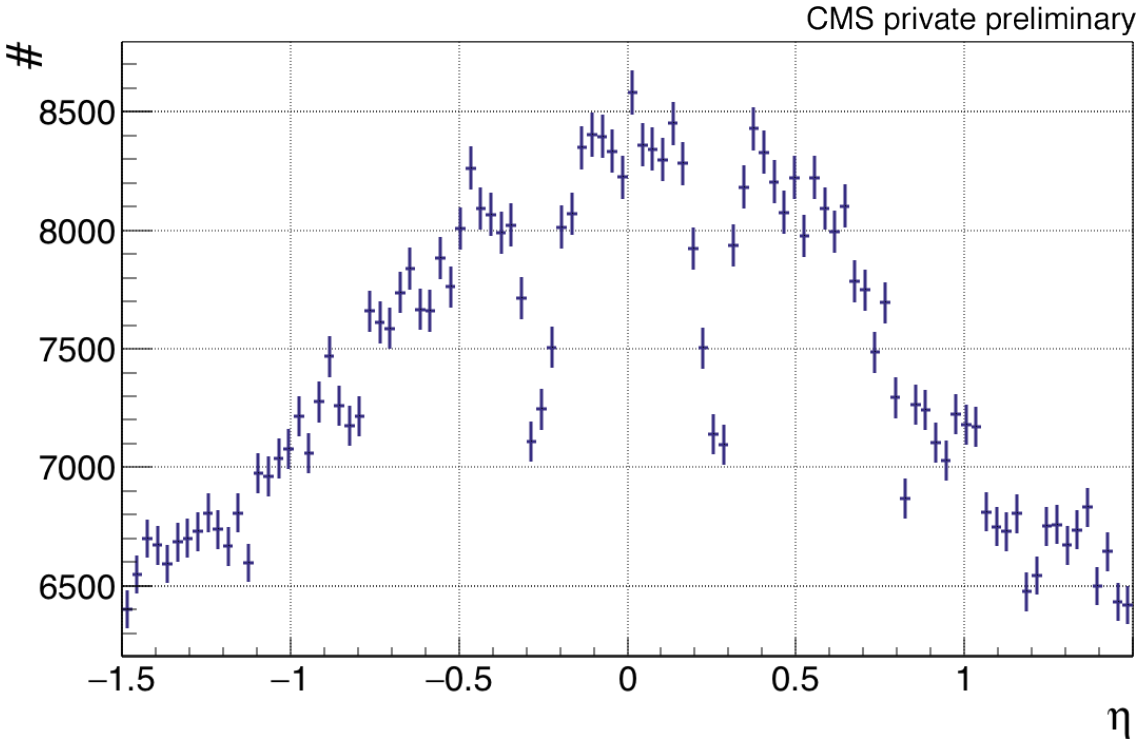

(a) η distribution of all global muons in the events.

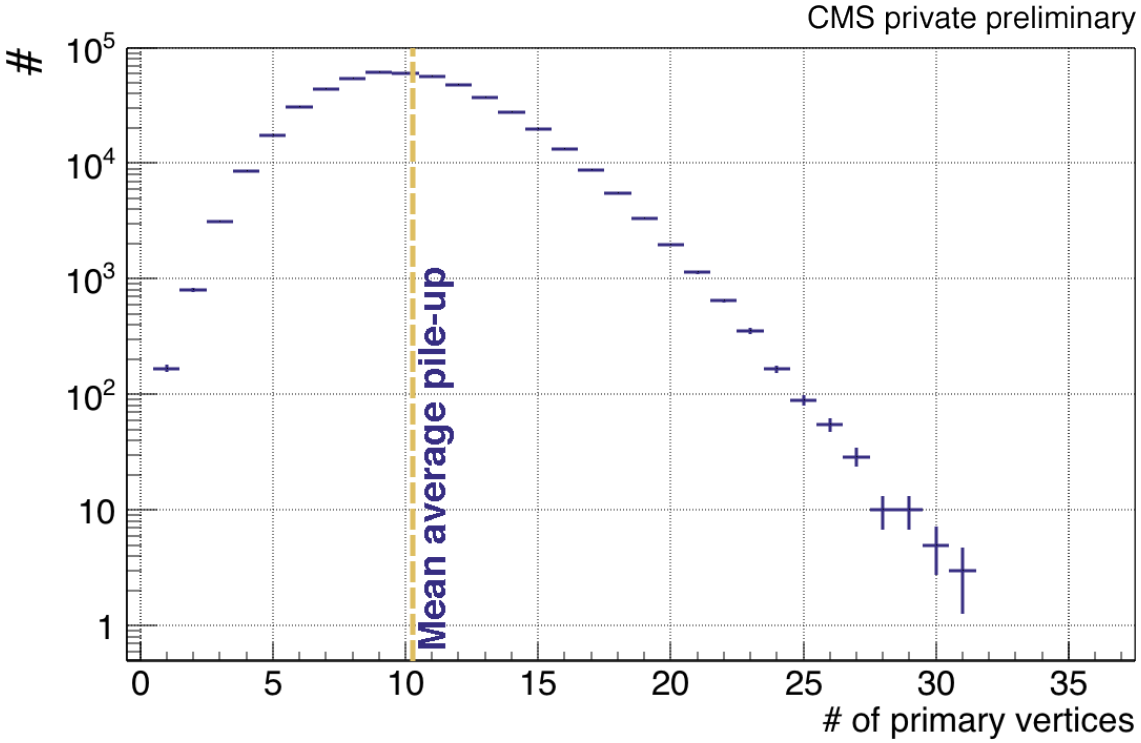

(b) Number of reconstructed primary vertices per event.

Figure 4.6: Pseudo-rapidity η distribution of all global muons within the events and distribution of the number of pile-up (number of reconstructed primary vertices).

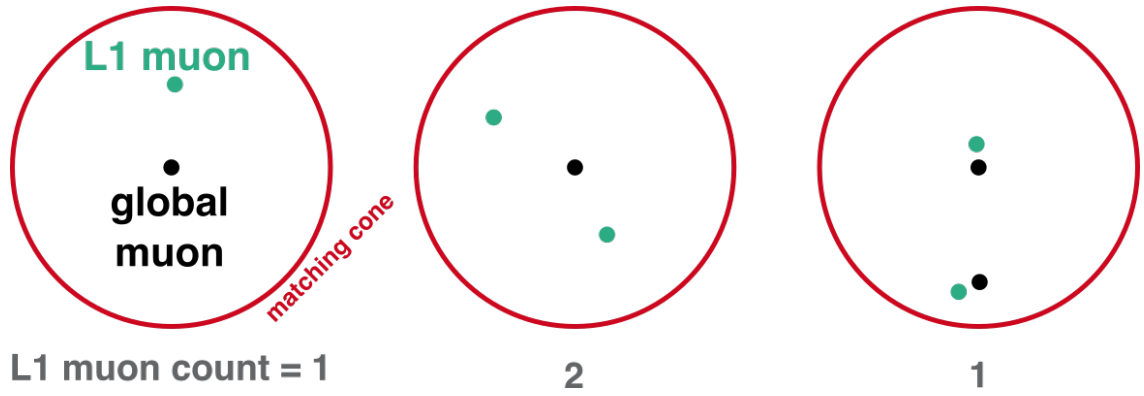

Figure 4.7: The principle of L1 muon counting during matching of reconstructed global muons (black) to L1 muons (green). If another reconstructed muon is within the matching cone, a second L1 muon will not be counted.

4.2.1.1 Results

The number of L1 muons matched to the reconstructed global muons is shown in figure 4.8. The distribution reveals:

- Most of the reconstructed global muons have exactly one matching L1 muon (84.2 %).
- 13.6 % of the global muons do not have a matching L1 muon. The L1 muon recognition is known to be not fully efficient (see also chapter 6). The missing matching L1 muon does not necessarily origin from an inefficient detector. Only four L1 muons are produced by the global muon trigger even if the detector measured more muons in the L1-Trigger.
- 2.2 % show an ambiguity at L1.
- Less than 0.1 % of the global muons have three or more L1 muons associated.

The number of L1 muon ambiguities (2.3 %) is larger compared to those of the single muon gun sample (0.4 %). On the one hand, the muon system's occupancy is larger compared to an event with a single muon without pile-up. On the other hand, the simulation can underestimate the muon ambiguity rate. Furthermore, no generator information is present in the sample. Thus, unreconstructed muons can contribute to the ambiguity rate, if they still create a L1 muon.
However, the number of L1 muon ambiguities is still very small. In combination with the discussed prerequisites for an L1-Trigger overload (see section 4.1.3) the muon ambiguity rate does not have a significant impact on the L1-Trigger rate.

The topology of the L1 muon ambiguities was also investigated and compared to the single muon gun sample's ambiguity topology. The η and ϕ distributions of the muon

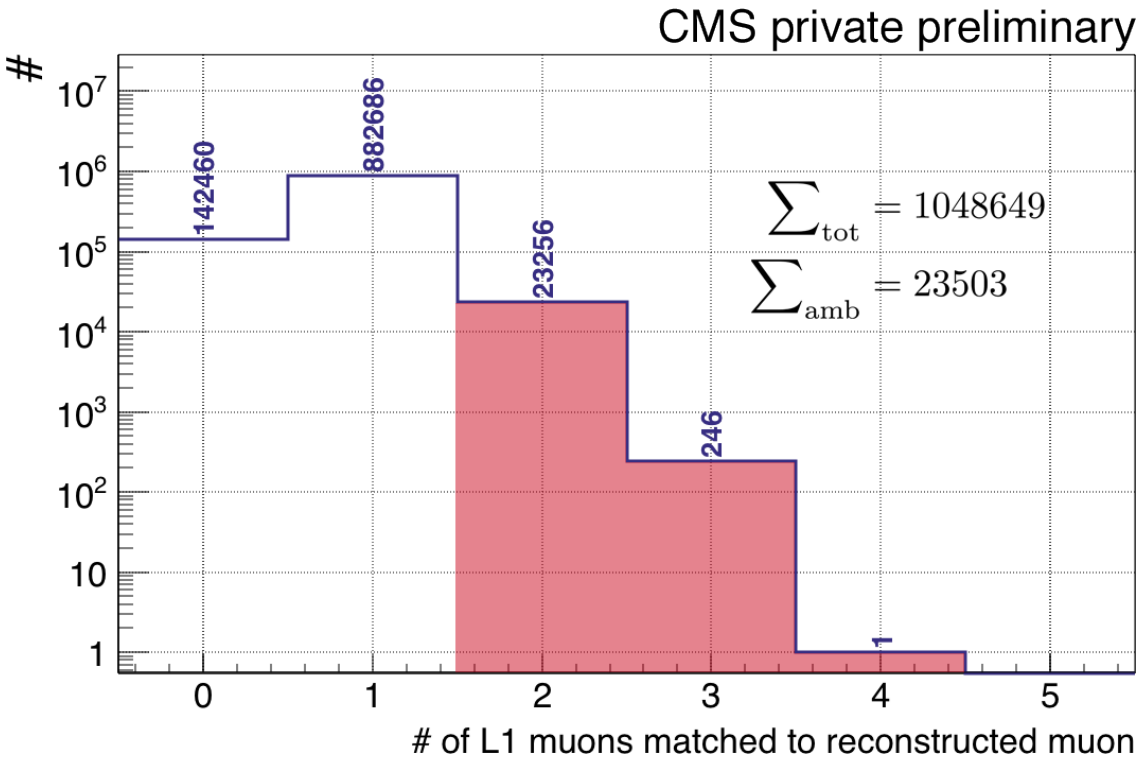

Figure 4.8: Distribution of L1 muons per global muon. One L1 muon is expected per global muon. Therefore, global muons with two or more L1 muons are muons with L1 muon ambiguity (2.3 %).

ambiguities are shown in figure 4.9.

The ϕ view reveals the higher chance of L1 muon ambiguities in the sector gaps. The distribution matches the distribution of the single muon gun sample qualitatively. Even though the binning in both distributions (figure 4.9b and 4.3b) is the same, the relative values for the local muon ambiguity rate cannot be compared. The significantly larger statistics in the data sample allow for a better resolution of the peaks at the sector borders resulting in higher local values.

The increase of muon ambiguities towards the endcap regions is also visible in the η view originating from the data sample. In the region of $-0.2 < \eta < 0.2$, the distribution is not symmetric towards $\eta = 0$ as it is expected. The asymmetry can result from the supply chimneys in the detector. At these regions the muon system is not equipped. The muon system itself was certified good in the sample.

4.2.2 Simulation analysis with 2023 conditions

In addition to the 2015 data sample, a simulated sample in a 2023 detector environment has been investigated.

Each event in the sample contains a QCD event with a parton center of mass energy of 15 GeV – 3 TeV. The center of mass energy distribution is steeply falling. An average

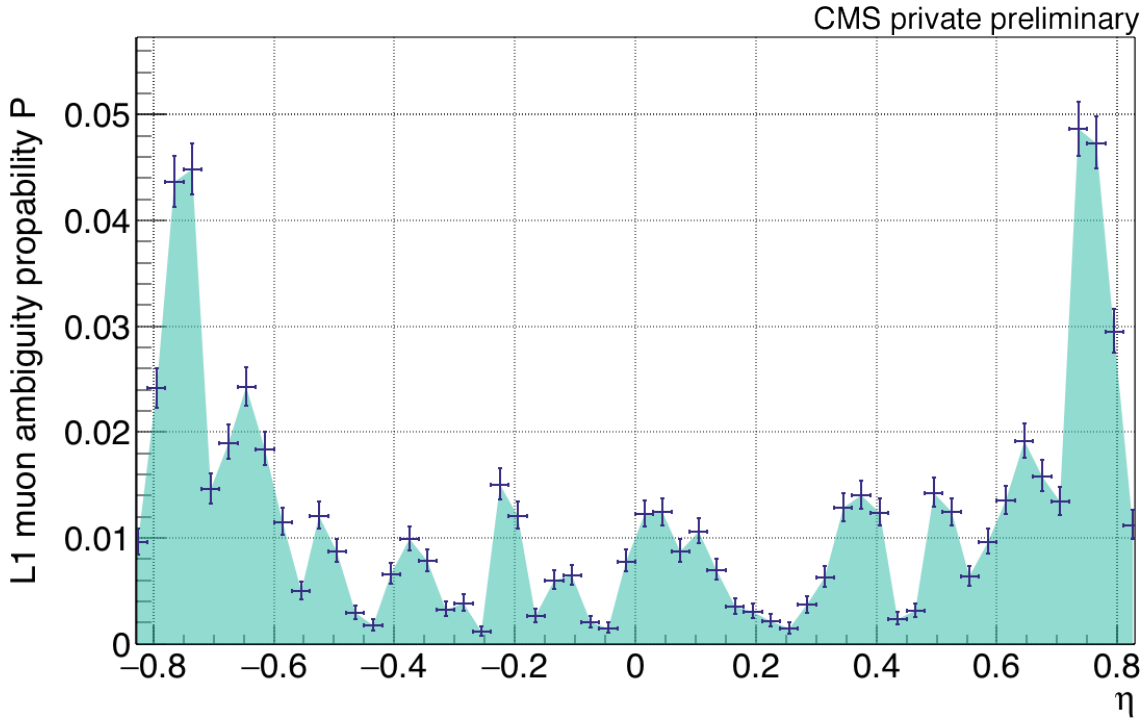

(a)

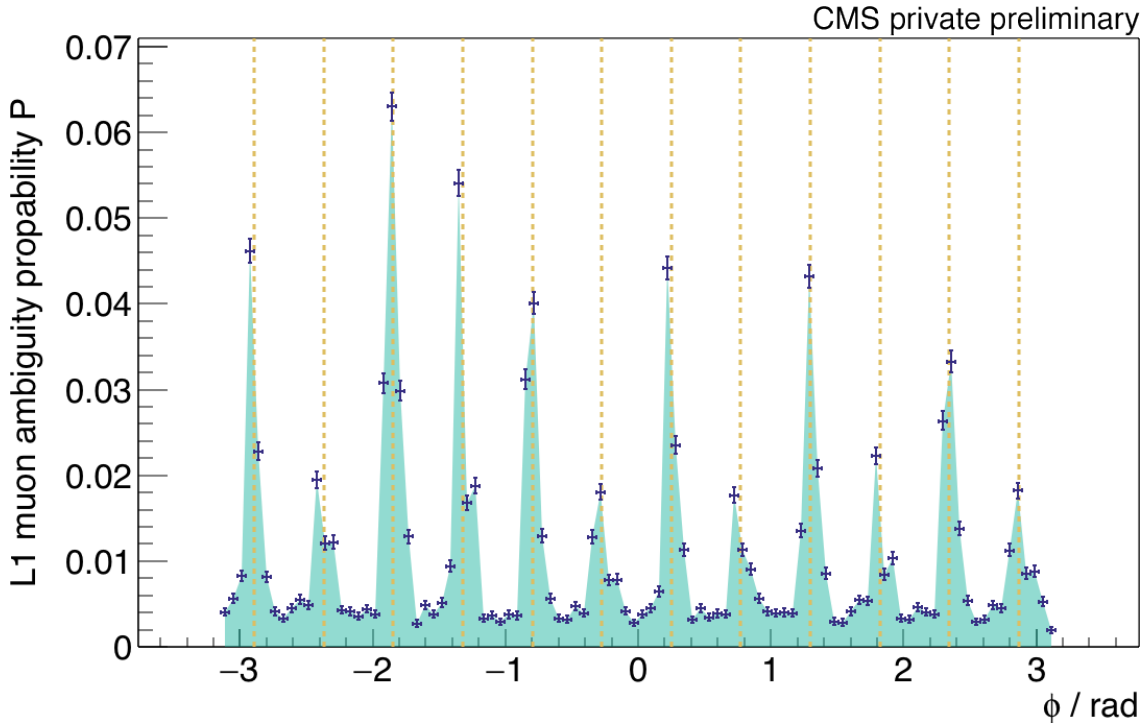

(b)

Figure 4.9: η and ϕ spectra of the reconstructed global muons with associated L1 muon ambiguity. The uncertainty bars represent the statistical uncertainties. The yellow dashed lines show the position of the sector borders in the ϕ view.

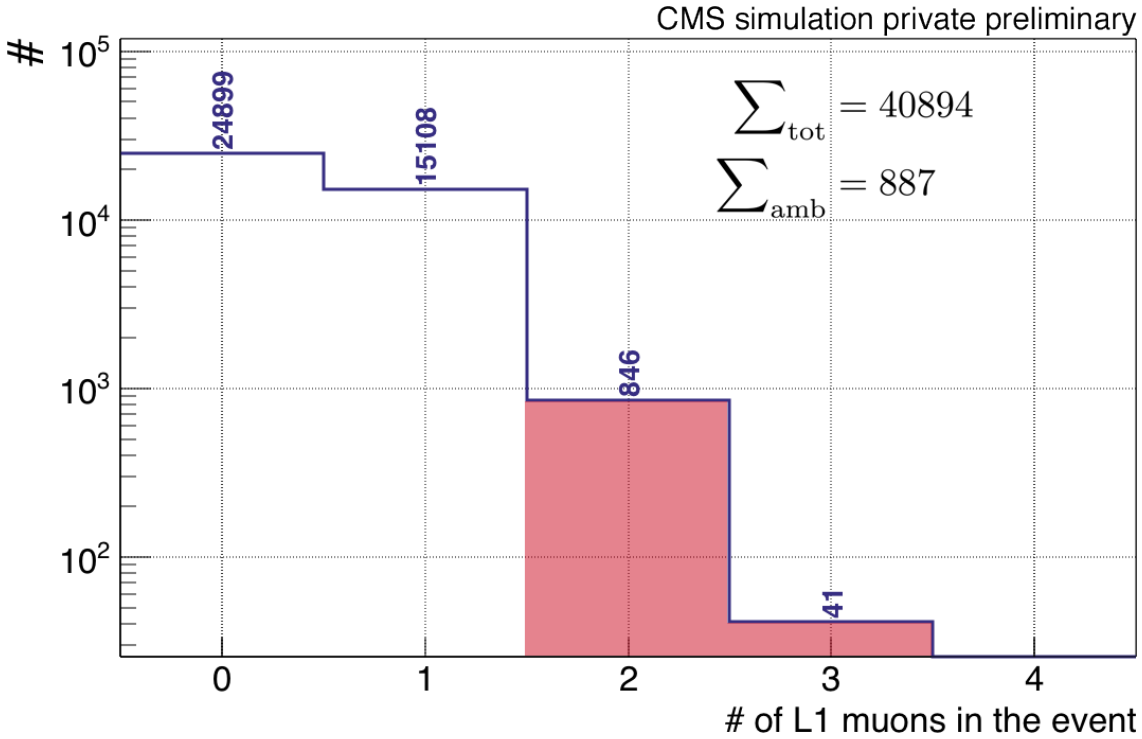

Figure 4.10: The number of L1 muons matched to global muons. One L1 muon is expected per global muon. Therefore global muons with two or more L1 muons are muons with L1 muon ambiguity (2.2 %).

number of 140 pile-up interactions per event is mixed into the sample. The sample contains 10500 events.
When mixing pile-up to the event, the generator information of the pile-up particles is lost. Therefore, the information of the reconstruction is used instead of the generator information. This also allows for a better comparison to the 2015 data sample results. For an investigation on the precision of reconstructed muon data compared to the generator information please refer to section 5.2.1. In order to have precise muon information only global reconstructed muons are evaluated.
The analysis processes every global muon in the event. For every global muon matching L1 muons with $\Delta R < 0.2$ and

$$\left| \frac{p_{T_{\text{RECO}}} - p_{T_{\text{L1}}}}{p_{T_{\text{RECO}}}} \right| < 0.5 \tag{4.6}$$

with the transverse momentum of the reconstructed muon $p_{T_{\text{RECO}}}$ and the L1 muon $p_{T_{\text{L1}}}$ are searched for.
The number of L1 muons matched to the global reconstructed muons is shown in figure 4.10.
A very high number of reconstructed muons that can not be matched to a L1 muon is visible. The reconstruction also contains 60666 stand alone muons. These are muons that are measured solely by the muon system and not by the inner tracker. Keeping in

mind, that only up to four L1 muon candidates are created in the global muon trigger (see section 2.3.1), one can assume that many muons do not create a L1 muon. Many L1 muons are created in the forward region due to the pile-up interactions.
887 L1 muons are ambiguous, this translates into 2.2 % of the reconstructed muons. This is the same number as for the 2015 data analysis. It is possible that some of the L1 muons that are not created due to the limitation of the global muon trigger to four muons, would also be ambiguous. Therefore, the number of L1 muon ambiguities is expected to be larger if all L1 muons were created.
However, the L1 muon ambiguity rate is still no reason for concerns even in this high pile-up scenario.

4.3 Impact on MTT concept

As shown in this chapter, the muon ambiguity rate in the L1-Trigger has only a very small impact on the L1-Trigger accept rate. If the HO or MTT system should provide additional information used to reject the low number of L1 muon ambiguities, the systems have to be very efficient in the muon detection. Otherwise, the systems would reject too many L1 muons. The muon detection efficiency of the HO system is O(90 %) [60] mainly due to the fiducial volume of the detector. Therefore, 10 % of the L1 muons could potentially be rejected by HO. A limitation of the ambiguity reduction to the fiducial volume of the HO system is possible. Anyhow, most of the L1 muon ambiguities occur in the sector and wheel gap regions. The HO system has its inactive detector parts in this region [60]. Therefore, it is expected that a limitation of the ambiguity rejection to the fiducial HO volume will greatly decrease the ambiguity rejection capability of HO.
A potential MTT system has thus to detect muons with an efficiency of nearly 100 %. This requirement is unrealistic, since the MTT system would be placed at the HO's position. An increase of the geometrical acceptance is not expected.
A reduction of the tile size and therefore a finer granularity does also not help to significantly reduce critical ambiguities.
Due to the fact that muon ambiguities often have the same position in η and ϕ, a segmented muon trigger can not help at any tile size. Thus, the reduced tile size of the MTT concept is not helpful to reduce the muon ambiguities. An improvement of the L1 muon track matching between different wheels and sectors seems to be a more promising approach.
However, the L1-Trigger including all DT timing information will completely be executed in the service cavern as the HL-LHC runs start. A fast muon trigger might be of help in that case, since very sophisticated algorithms can be run on all agglomerated detector data.

4.4 Summary

The L1 muon ambiguities have been investigated. Even in events containing a sole single muon, muon ambiguities occur at L1. However, the number was found to be too small in order to compromise the L1-Trigger. It was found, that only muon ambiguities that exceed the double muon threshold, while the originating muon does not exceed the single muon threshold, increase the L1-Trigger rate. In these cases the L1 muon ambiguities showed to share their position with the second L1 muon. A discrimination between these L1 muons is therefore impossible using a scintillator-based fast muon trigger. Furthermore, an additional muon trigger would reduce the trigger efficiency, if it is used as veto.
The phase 2 detector will be able to use the full DT and RPC timing information in the L1-Trigger decision. Therefore, it can be expected that the muon ambiguity rate can be reduced compared to the simulations. The necessity of an additional muon trigger detector component is additionally reduced by this fact.
In summary, the application of HO or/and an MTT like system can currently not be recommended for muon ambiguity reduction.

Chapter 5

Redundancy studies

In this chapter the failure of parts of the drift tube (DT) muon system and its impact on the L1 muon trigger is studied. A method is introduced that utilizes data of the hadron outer calorimeter (HO) as redundant information to compensate for these failures.

5.1 DT failure scenarios

As already stated in section 3.3.2, the muon system is likely to suffer from aging and radiation damage.
Thereby, the DT muon system can suffer from various types of failure that can occur within every step of the DT system data processing chain (for details see chapter 2.2.6.1):

- The smallest type of DT failure can be the corruption of a single cell, that can occur everywhere within a DT chamber. The DT system already suffered from this type of failure by now. Most of these failures where repaired during the long shutdown 1 (LS 1). The failure rate of single DT-wires over the first run period of the LHC and the LS 1 is shown in figure 5.1. A small number of failing DT-wires are not expected to influence the muon detection capability due to the DT system's redundancy [40]. A failure of a DT cell can be due to problems with the high voltage supply or a degradation of the anode wire.

- The next possible level of failure is the loss of the bunch and track identifier (BTI). The BTI observes nine DT-wires each to find three or four wires in line that give a signal. If a BTI fails, an adjacent BTI can partially take over the failing BTI's wires. Nonetheless, the data of four wires will not be available for the trigger

chain. The loss of the data of four wires can also occur, if the electronics chip (called MAD chip [80]), that acquires the DT-tube signals, fails.

- A failing track correlator (TRACO) will result in missing data from four BTIs. Thus, the information from $4 \cdot 9 = 36$ wires will be lost. The TRACO combines the data of the inner DT ϕ layer with the outer one.

- The worst failure within one muon station is the failure of the track sorter (TS). The TS combines the data from all TRACOs in the chamber. If the TS fails, the data from the whole DT station is not available for the trigger. This corresponds to the information of 608 – 1408 DT wires depending on the affected station [40]. A failure of the TS can be due to a failure of cooling or the minicrate electronics, that supplies the whole station. The whole CMS detector has 60 muon stations in each layer (station 1–4).

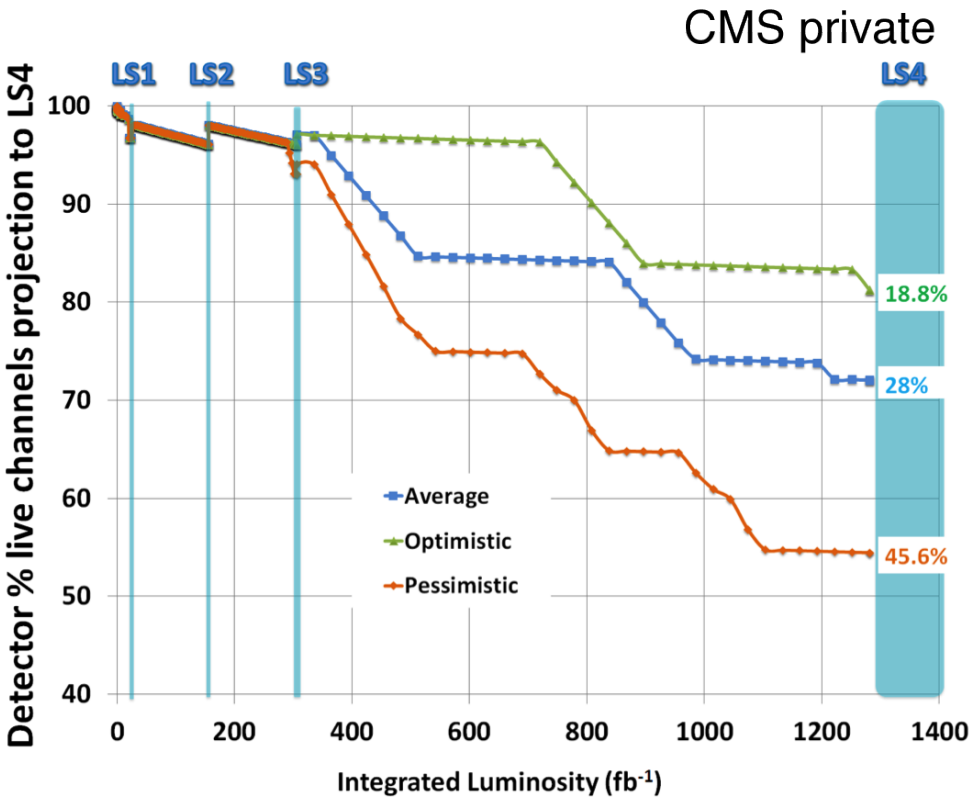

Figure 5.1: Actual and projected failure of single DT-wires (channels) versus the delivered luminosity at CMS [81]. During the long shutdowns (LS 1 – LS 4) parts of the failing DT-wires can be repaired.

The on-chamber electronics that are responsible for the presented failure types all are located within the CMS experimental cavern. Even more, all electronics is placed

within the detector wheels. Thus, in case of a failure of the electronics, a direct intervention is impossible during detector operations. Even a repair during a short accelerator shutdown is unfeasible since the detector wheels have to be moved in most of the cases.
Therefore, it is of vital interest to know about the impact of detector failures in the DT system. Especially the failure of the track sorter (TS) has to be investigated, since it would result in the failure of a whole DT station. A sketch of the relative impact of the discussed failure scenarios is shown in figure 5.2.

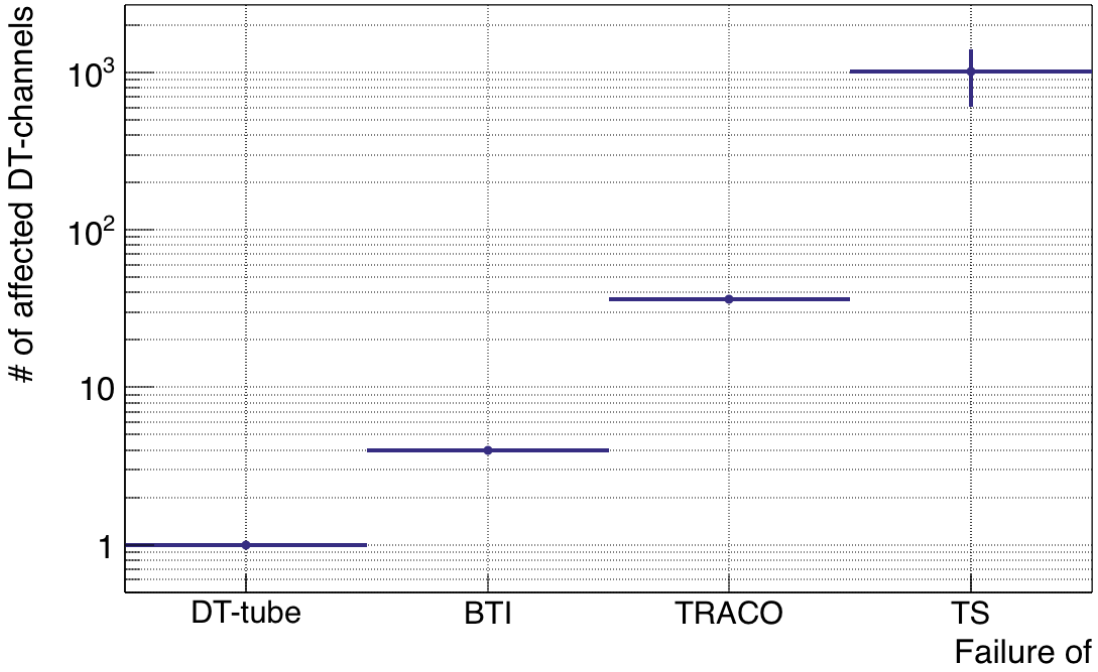

Figure 5.2: Number of affected DT channels in case of a certain DT system failure.

5.2 Failure analysis procedure

The analysis of DT failure events is done based on simulated data. Data events cannot be used for this analysis as they are taken by an almost fully working detector. For an analysis of the impact of failures the same set of events has to be analyzed in the working and the imperfect detector environment, respectively.
A set of 2 million events was produced for each detector failure scenario. The events were produced using CMSSW Version 7.2.3 of the CMS simulation framework [82]. The configuration represents the detector setup during 2015 including the legacy trigger. For the configuration file refer to the appendix.
Each event consists of a muon from a single muon-gun with 3 GeV $< p_T <$ 200 GeV. The muons have positive and negative signs of charge for half of the events each. Additional to the muon, a mean pile-up of 52 interactions from a minimum bias sample

with 13 TeV was mixed into each event with a bunch-crossing spacing of 25 ns. The pile-up yields O(1) additional muon per event in the barrel region. The mixing of the pile-up allows for an analysis of the detector failures in a realistic, noisy environment and represents the maximum expected pile-up until 2018. An almost flat p_T spectrum in the simulated range of the muon gun from 3 GeV $< p_T <$ 200 GeV is e.g. expected for a heavy boson decay such as $W' \rightarrow \mu\nu$ [83].

5.2.1 Generator information handling

The pile-up mixing introduces additional muons in the sample. Due to the structure of the CMSSW pile-up mixing the generator information of the muons from the pile-up interactions is not available. Only the generator information of the muon from the muon-gun is present. Therefore, it is not possible to compare the Level-1-Trigger (L1) information to the generator information of the muons. An alternative information source concerning the generated muons has to be established.
In order to treat the challenge of the missing generator information, two simulation data sets have been created for every type of detector failure using the following steps:

- First of all, a unique generator information of the muons from the muon-gun has been produced (GEN step).

- Afterwards, the full event chain was produced using a fully working detector including simulation, digitization and reconstruction of the event (SIM, DIGI and RECO step). The resulting information of the reconstruction algorithm (RECO step) is known to be very efficient for muons in CMS [8]. This allows to use reconstruction information of the muons in the sample of the fully working detector instead of the missing generator information.

- Alternatively, the event chain mentioned above was produced simulating a detector with failing components in the DT system.

Thereby, both simulations were performed with the same seed for the random number generators. The random number generator seeds are the same for the simulation of the working detector and the detector with failing DT station on an event by event basis. This assures, that the whole event, including the detector response, is exactly the same despite of the impact of the detector failure. The work flow is drafted in figure 5.3.

5.2.1.1 Efficiency

To have an estimate on the precision of the RECO step concerning muon recovery, the efficiency of the recovery of the generated muon is tested. Therefore, the generator information of the muon from the muon-gun is matched to the reconstructed data of the muons in the event. The generator information is matched to a muon if the

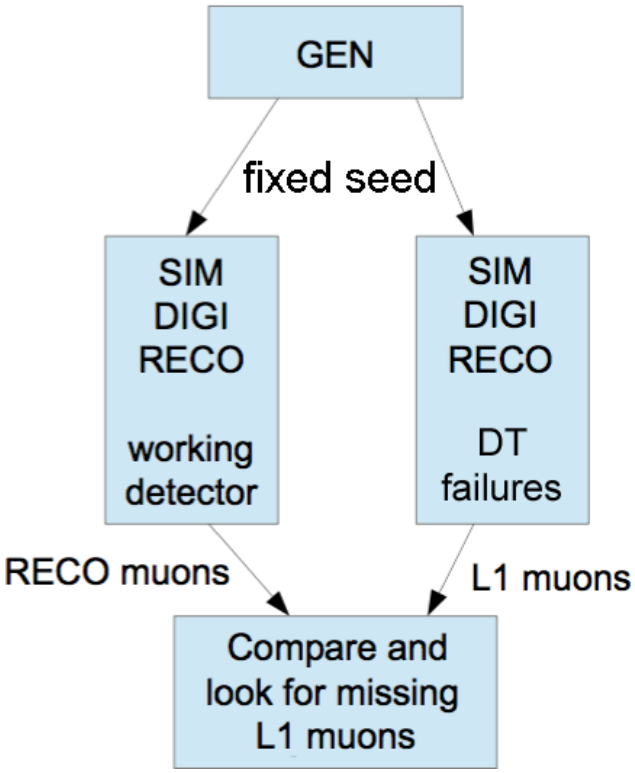

Figure 5.3: Workflow of the failure analysis. The same generator information is used for both samples. One simulated sample contains events in the fully working detector in order to gain the best possible information about the muons in the event. The other sample contains events in CMS with failing detector parts. Comparing the L1 muon information in the second sample with the RECO muon information in the first sample allows for analysis of the inefficiencies.

direction of both muons differs by $\Delta R < 0.2$ at the interaction point and the relative p_T difference is

$$\left| \frac{p_{T_{\text{rec}}} - p_{T_{\text{gen}}}}{p_{T_{\text{gen}}}} \right| < 0.5 \tag{5.1}$$

with the transverse momentum $p_{T_{\text{gen}}}$ of the muon's generator information and the transverse momentum $p_{T_{\text{rec}}}$ of the muon's reconstruction information. This corresponds to the matching criteria used also later on in the analysis code (see section 5.2.3.1).
A subset of 100000 events has been processed. The resulting distributions for p_T, η, ϕ and the muon charge are shown for the generator information and the matched reconstructed muons, respectively in figure 5.4.

As expected, the generated muons are flat in p_T, η, ϕ and the muon charge. The distributions for η, ϕ and the muon charge of the reconstructed muons are flat as well. Only the p_T distribution shows a turn off feature at the upper end of the muons transverse momentum (200 GeV). This is due to the p_T uncertainty on the combined

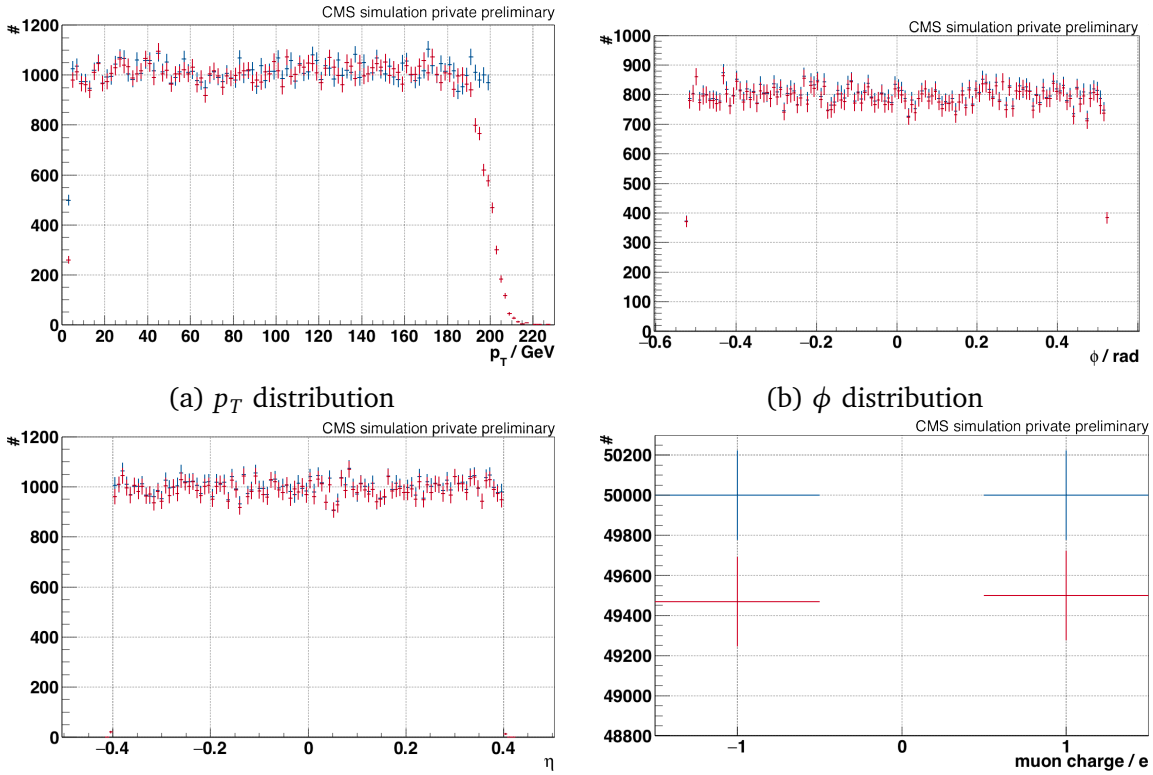

(a) p_T distribution

(b) ϕ distribution

(c) η distribution

(d) charge distribution

Figure 5.4: Distributions of the generated (■ blue colored) and reconstructed muons (■ red colored) from the muon-gun in a sub-sample of 100000 events. All distributions are flat. The p_T distribution shows a turn off feature. Note the offset from zero of the y-axis in the charge distribution. The uncertainties are statistical uncertainties.

measurement of the tracker and the muon system at these energies, of $O(3\ \%)$ [8]. However, the p_T assignment is more precise than the L1 muon p_T resolution. Thus, it can be used in this analysis.
Overall, (99.0 ± 0.3) % of the generated muons from the muon gun are reconstructed within the given cuts. This proves the high accuracy of the reconstruction algorithm. Consequently, it is feasible to use the information of the reconstruction instead of the generator information.

5.2.2 Code changes for failure simulation

The CMSSW code needed changes in order to simulate the failure of DT parts. Normally, the CMSSW framework uses four steps to create a complete event sample, the GEN, SIM, DIGI, and RECO step. During the GEN step, the particles originating from the proton-proton-collision are simulated. The particle's decay and interaction with the detector are simulated in the following SIM step. The detector response is afterwards

simulated during the DIGI step. In the last step - the RECO step - the reconstruction of the particle tracks and of their properties is executed.
The most feasible solution to implement failures is to prevent the detector to digitize the measurements in the DIGI step. In the CMSSW code the simulated analogue DT detector response is digitized in the `DTDigitizer.cc` in the `SimMuon/DTDigitzer` package. This digitization can be inhibited on every signal processing stage corresponding to all presented DT failure scenarios. The inhibition is possible for certain DT-wires, stations, sectors, and wheels. The CMSSW code change that was used in order to simulate a failure, for example, of muon station 2 in sector 1 in wheel 0, is shown in the appendix. Within the `DTDigitizer.cc` an assignment of the simulated hit (`simHit`) to the corresponding detector is performed. The `simHit` and the assigned detector are stored in a `wireMap`. In a next step, the program loops over the complete `wireMap` and calculates the timings of the DTs. These timings are stored together with the detector information in a data format called `DTDigiSimLink` and represent the early step of the DIGI data. By changing the code, the `simHits` for particular DT parts are not pushed into the `wireMap` and are therefore lost in the next step of the algorithm.

5.2.3 Analysis procedure

The failure of a DT muon station 1 and alternatively the failure of a DT muon station 2 were simulated for the sector 1 in the wheels 2-, 1-, and 0 in order to gain a picture of how the failures impact in the whole η range. An extrapolation to the wheels 1 and 2 is allowed due to the symmetric build-up of the CMS detector in η. The simulation of a station 3 or 4 failure has been omitted since the impact of these failures on L1 muon creation is expected to be negligible. The stations 1 and 2 mainly seed the L1 muon creation. Although, the muon stations 3 and 4 are used in the L1-Trigger for track parameter assignments, a failure of these stations will not lead to a missing detection of a muon on level 1 as long as information from the stations 1 and 2 are available.
Each set contains two million events. This results in six million events for a particular wheel. Two million events are simulated for the fully working detector, failing station 1 and failing station 2, respectively. The chosen simulation parameters are shown in table 5.1. The η parameters of the muon-gun were chosen so that the muon-gun fully covers the failing muon station. In order to save computation time and storage the η and ϕ range of the muon-gun covers the stations 1 and 2 so that only three rather than four samples had to be created. Thus, the samples of the fully working detector can be used for comparison to both failure scenarios in a certain wheel.
An event display of the same two events once in a working detector and once in a detector with faulty muon station 2 is shown in figure 5.5.

5.2.3.1 Workflow

In order to analyze the impact of muon station failures on the L1 trigger, the following workflow has been used:
The code compares the sample of the working detector and the sample of the failure

Wheel	2-	1-	0
ϕ range of the muon-gun	-0.52 – 0.52		
η range of the muon-gun	-1.3 – -0.8	-1.0 – -0.3	-0.4 – 0.4
p_T range of the muon-gun	(3 – 200) GeV		
mean pile up	52		

Table 5.1: Simulation parameters for the different scenarios of the DT station failure. For the corresponding wheels the failure of station 1 and station 2 has been simulated separately.

scenario event by event. In a first step the analysis loops over the list of all reconstructed muons in the sample of the working detector. It tries to match the L1 muons from the sample of the working detector and the L1 muons from the sample of the faulty detector to the reconstructed muons.
A match is valid if the L1 muon and the reconstructed muon fall within $\Delta R < 0.2$. Additionally, their p_T values may differ by only

$$\delta p_T = \left| \frac{p_{T_{\text{rec}}} - p_{T_{\text{L1}}}}{p_{T_{\text{rec}}}} \right| < 0.5 \tag{5.2}$$

with the transverse momentum of the reconstructed muon $p_{T_{\text{rec}}}$ and the transverse momentum of the matched L1 muon $p_{T_{\text{L1}}}$. These matching criteria are investigated in section 5.2.3.2.
If more than one L1 muon matches the criteria, the L1 muon with the smallest ΔR is chosen if it also fulfills the p_T criterion.
After the matching a tuple is created. The tuple contains the reconstructed muon, the matched L1 muon from the sample with the working detector, and the L1 muon from the sample with the faulty detector if available.
These tuples can be divided into four categories. The categories are shown in table 5.2. A visualization of the categories is shown in figure 5.6.

	Reconstructed muon has a match of the L1 muon	
Cat. No.	in sample of working detector	in sample of faulty detector
1	yes	yes
2	yes	no
3	no	yes
4	no	no

Table 5.2: Groups of tuples after matching the L1 muons from both samples (working and faulty detector) to the reconstructed muon.

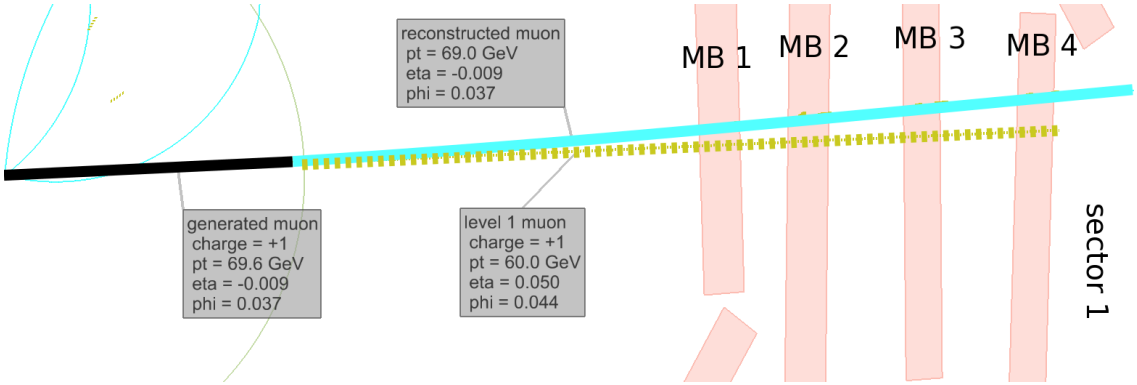

(a) Event from the sample with the fully working detector.

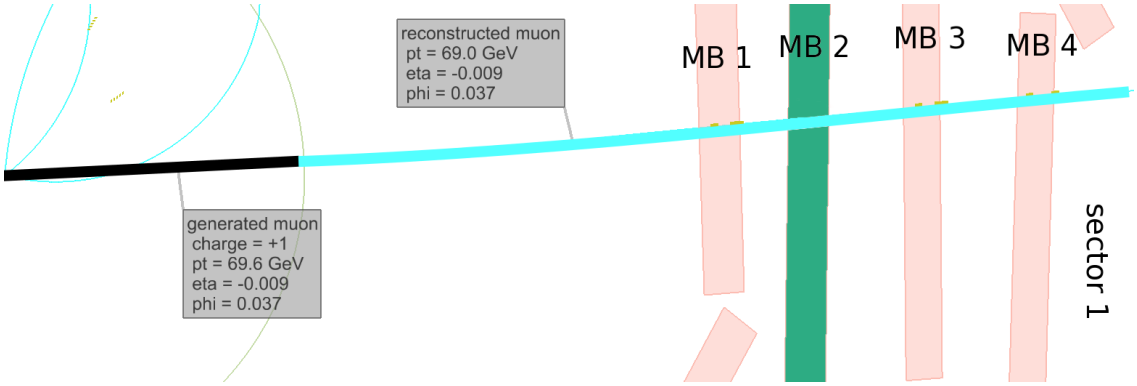

(b) Event from the sample with a faulty muon station 2.

Figure 5.5: Event display of a muon from a muon-gun embedded into pile-up. Figure 5.5a shows the sample with the fully working detector. The sample of figure 5.5b contains a faulty muon station 2 in sector 1. The blue line represents the reconstructed muons. The yellow dotted line represents the Level 1 muon. The green muon station is the failing muon station 2. Calorimeter and tracker entries are not shown.

- In category number one the L1 trigger is able to create a L1 muon independent of the detector failure.
- Category two defines the L1 muon failures due to the detector failure. In this case a L1 muon is detected in the working detector. The not working detector cannot detect the L1 muon anymore.
- In category three the working detector does not see a L1 muon but the faulty detector creates the L1 muon. This can occur, if the missing DT system information leads to a slightly different coordinate of the L1 muon in the detector, such that the L1 muon fits in the matching cone again. Additionally, the L1 trigger has a sorting of muons and can only process four muons (see section 2.3.1). If one L1 muon gets lost, another L1 muon can rise in rank and can be thus created.

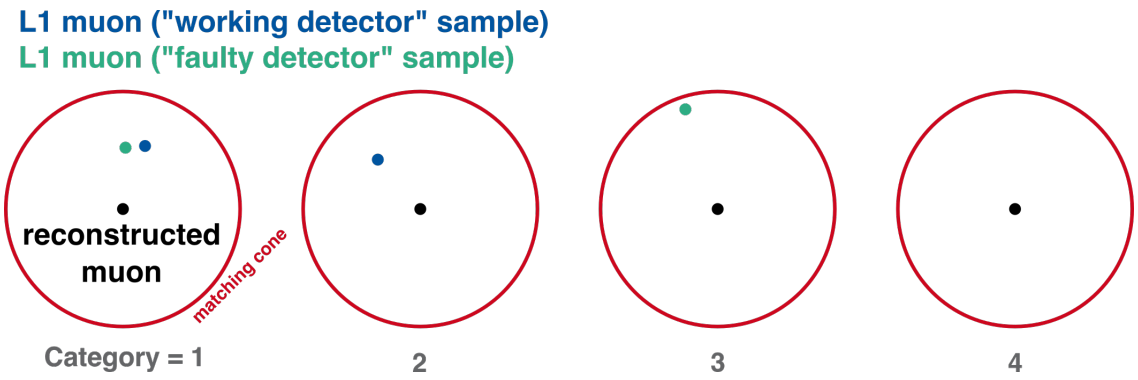

Figure 5.6: Categories of matching with respect to the L1 muons in the samples with the working and faulty detector.

- In the fourth category the detector does not see a L1 muon that matches to the particular reconstructed muon at all. This is due to inefficiencies of the working detector that naturally also show up in the detector with DT failure.

After the matching and grouping, the analysis processes the tuples of category two, since it contains the muons that get lost due to the failure of a DT station. The η and ϕ position is saved. On top of that the algorithm finds the hadron outer calorimeter (HO) tile in the direction of the reconstructed muon. The HO energy is recorded for this muon at the tile that was traversed by the reconstructed muon. Due to the fact that the reconstructed muon does not represent the track of the physical muon exactly, also the highest measured energy of the HO tiles in an area of $3 \cdot 3$ tiles around the central tile is saved. This HO matching gives a first estimate on the capability of the HO to detect the muons that get lost in the L1 trigger due to DT detector failures.

5.2.3.2 Determination of matching criterion

The matching criteria for matching the L1 muons to the reconstructed muons were determined by a parameter scan in the ΔR and $\left|(p_{T_{\text{rec}}} - p_{T_{\text{L1}}})/p_{T_{\text{rec}}}\right|$ phase space.
In a first step, the relative numbers of muons sorted into the different cases are calculated for ΔR values from 0 to 1.0. The p_T difference is restricted to

$$\delta p_T = \left| \frac{p_{T_{\text{rec}}} - p_{T_{\text{L1}}}}{p_{T_{\text{rec}}}} \right| < 0.5. \tag{5.3}$$

during these matchings. Additional to the sorting into the four different cases, the resulting plot distinguishes if the reconstructed muon can be matched to the muon-gun or the pile-up. The resulting plot is shown in figure 5.7.

Starting from $\Delta R = 0$ the number of muons from the muon gun and pile-up in the category one begins to rise sharply. On the other hand, the number of muons in category four decreases. These are mainly correctly associated L1 muons that start to fit into the matching cone as soon as the cone gets larger.

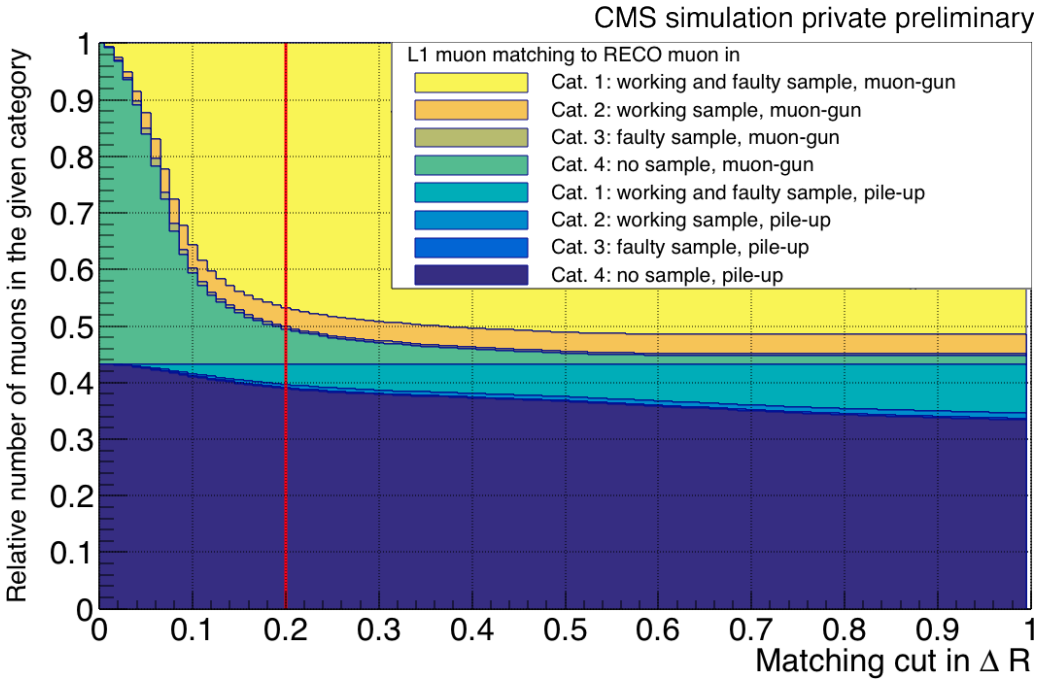

(a) Stacked histogram

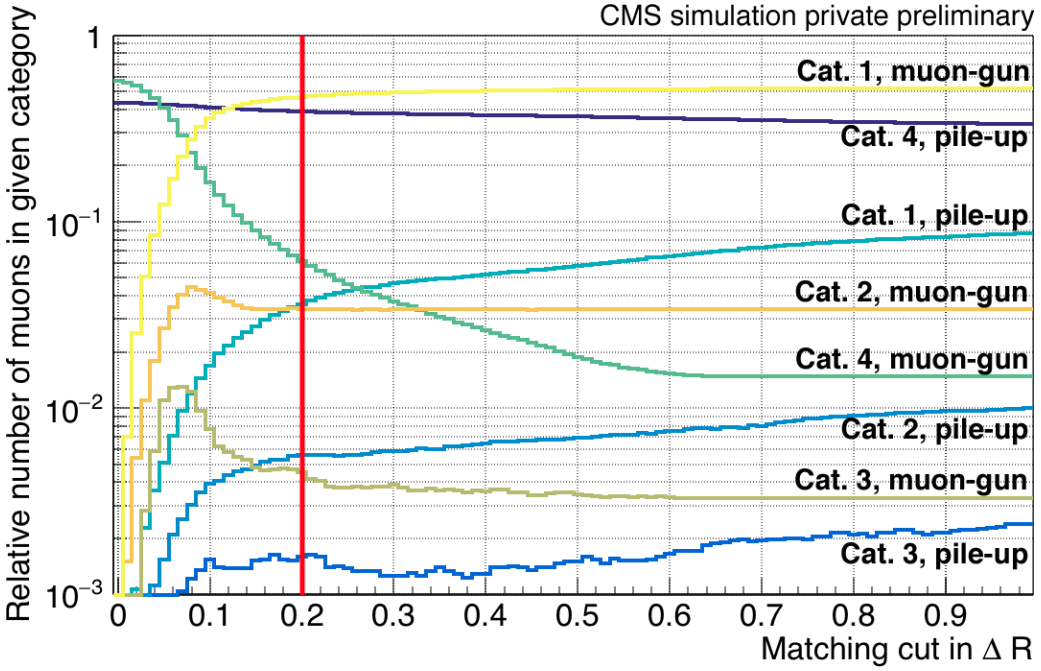

(b) Single contributions

Figure 5.7: Number of muons in the four matching categories keyed by the muons coming from the muon-gun and the muons from the pile-up. The final cut was set to $\Delta R = 0.2$ (red line). About 45 % of the muons originate from pile-up.

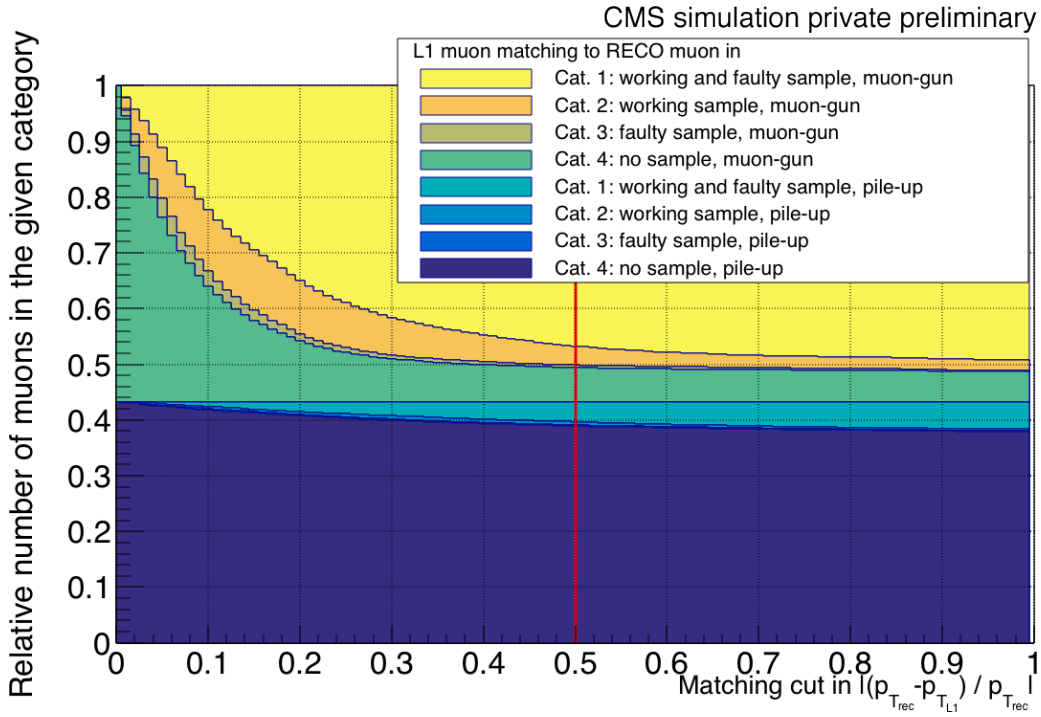

(a) Stacked histogram

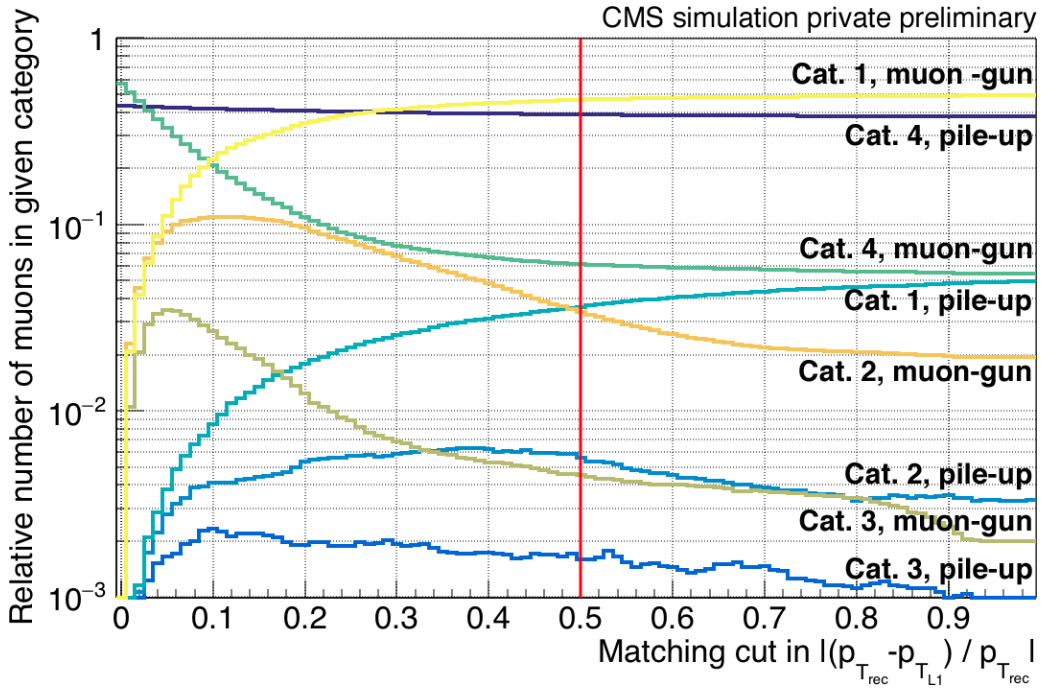

(b) Single contributions

Figure 5.8: Number of muons in the four matching categories keyed by the muons coming from the muon-gun and the muons from the pile-up. The final cut was set to $\delta p_T = \left|\frac{p_{T_{\text{rec}}} - p_{T_{\text{L1}}}}{p_{T_{\text{rec}}}}\right| = 0.5$ (red line). About 45 % of the muons originate from pile-up.

The number of muons from the muon gun in category three increases towards a ΔR value of 0.1. At higher cuts the number decreases again. These are muons where the L1 muon from the sample of the faulty detector is closer to the reconstructed muon than the L1 muon from the sample of the fully working detector. This conclusion can be drawn due to the fact that the number of muons decreases again with higher ΔR cuts. Therefore, a L1 muon in the sample of the working detector has to be present.
The cut value of $\Delta R = 0.2$ was chosen such that most of the muons with a valid L1 muon from both samples are sorted into category one. The number of muons from pile-up in category one increases over the whole parameter range. The slope of this rise changes at $\Delta R = 0.2$. At this point almost all pile-up muons that create a L1 muon are sorted into the categories one to three. For higher ΔR values mainly L1 muons that originate from a different muon are matched. This process naturally continues over the whole parameter range. The fraction of category 2 is stable at this cut for generated and pile-up muons.
The number of muons from pile-up in category 4 is stable in the whole parameter space. Many muons from pile-up have a low transverse momentum. If these muons do not reach the muon system, no L1 muon will be created.

After the ΔR cut was defined, another parameter scan for δp_T values with a fixed $\Delta R = 0.2$ cut has been performed. The categories are again split by the muon sources pile-up and muon-gun. The resulting plot is shown in figure 5.8. Again starting from a δp_T value of 0 the numbers of matched muons in the matching categories one to three increase. This is once more due to the fact, that the muon's δp_T starts to fit into the matching boundaries. Compared to the investigation of the ΔR value, the category three for the muon-gun and the category one for the pile-up behave similar. The slope of the pile-up in category one changes at approximately 0.5.
Nonetheless, the category two for the muon-gun behaves differently. The number of muons in this category increases to a δp_T value of 0.1 and starts to decrease again beyond 0.2. The p_T measurement on level 1 is more precise if more data points are present. Therefore, it is expected that the p_T estimation for the L1 muon in the sample with the faulty detector is more imprecise than the p_T estimation of the L1 muon in the sample of the working detector. By increasing the δp_T cut value, first the L1 muon in the sample of the working detector will be within the cut boundaries while the L1 muon in the sample of the faulty detector is still outside. When the cut is further relaxed, also the L1 muon in the sample of the faulty detector will be within the cut boundaries. Thus, the δp_T cut must not be chosen too tight in order to avoid a false categorization. As a trade-off between these arguments a δp_T value of 0.5 has been chosen. However, the cut values have to be varied to have an estimate on the uncertainty of the cut (see section 5.3.4).

5.3 Failure analysis results

The analysis has been performed for a failure of station 1 and station 2 in sector 1 in the wheels 2-, 1- and 0. The results are presented for the failure of station 1 and station 2 separately.
The relative numbers of L1 muons, that get lost due to DT failures, are calculated. Therefore, the number of L1 muons that are present in the sample with the working detector but missing in the sample with the failing detector part (referred to as additionally missing L1 muon) are normalized to the number of L1 muons from the sample of the working detector, that can be matched to a reconstructed muon.
To make an interpretation of the results more easily, it is important to know the positions of the detector gaps in the η and ϕ view. A schematic of these views is shown in figure 5.9. Straight tracks at positions, that are crucial for the understanding of the analysis results, are plotted.
Two tracks are especially important in the ϕ projection. The track S_1 traverses the station 2 layer at a gap between sector 1 and sector 2. Thus, no information of station 2 will be available for tracks at this ϕ direction. The S_2 trajectory traverses the muon station 3 layer in a gap between sector 1 and sector 12. Station 3 information will not be available for these muons, respectively.
Five tracks are marked out in the η projection. The wheel gap between wheel 0 and wheel 1- is traversed in the region of muon stations for the tracks W_1 (station 2) and W_2 (station 1). No muon station 3 information is available for track W_3 since it traverses the station 3 layer in the wheel 2-/wheel 1- border region. The same border region avoids the muon system to measure a muon on track W_4 in station 2. Muons on the track W_5 are neither measured in station 1 nor in station 4. The muon traverses the gap between wheel 1- and wheel 2- in the station 1 layer. Furthermore, the muon leaves the barrel region before reaching the station 4 plane.
Muons on the highlighted muon tracks are very susceptible for decreasing L1 muon measurement efficiencies in case of a detector failure, since the detector information is reduced for these muons by default.

5.3.1 Failure of an MB DT station 1

The impact of the failure of a complete DT station 1 is investigated for the wheels 2-, 1-, and 0, respectively.

5.3.1.1 Failure in wheel 0

The number of L1 muons that can be matched to a reconstructed muon in the sample of the fully working detector normalized to the number of all reconstructed muons in the fully working detector is shown in figure 5.10. The red rectangle shows the position of the muon station 1 in wheel 0, sector 1. The binning corresponds to the binning of the calorimeter-towers and thus to the size and position of the HO tiles. The muon stations' end in η is at slightly lower values than the end of the HO tile. The

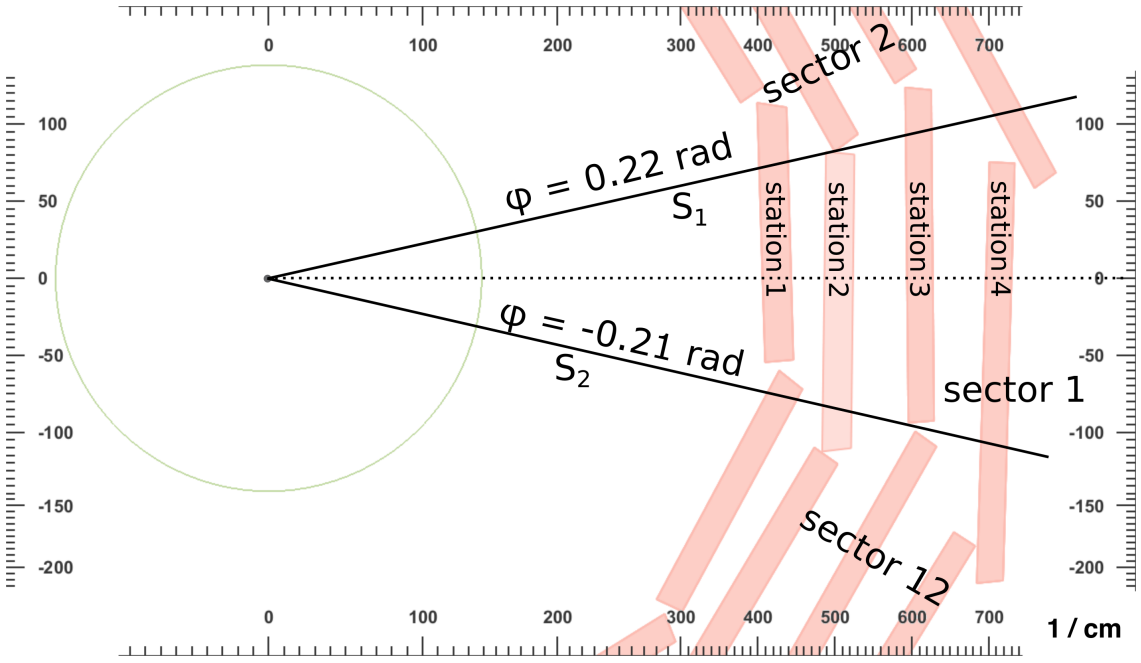

(a) ϕ projection

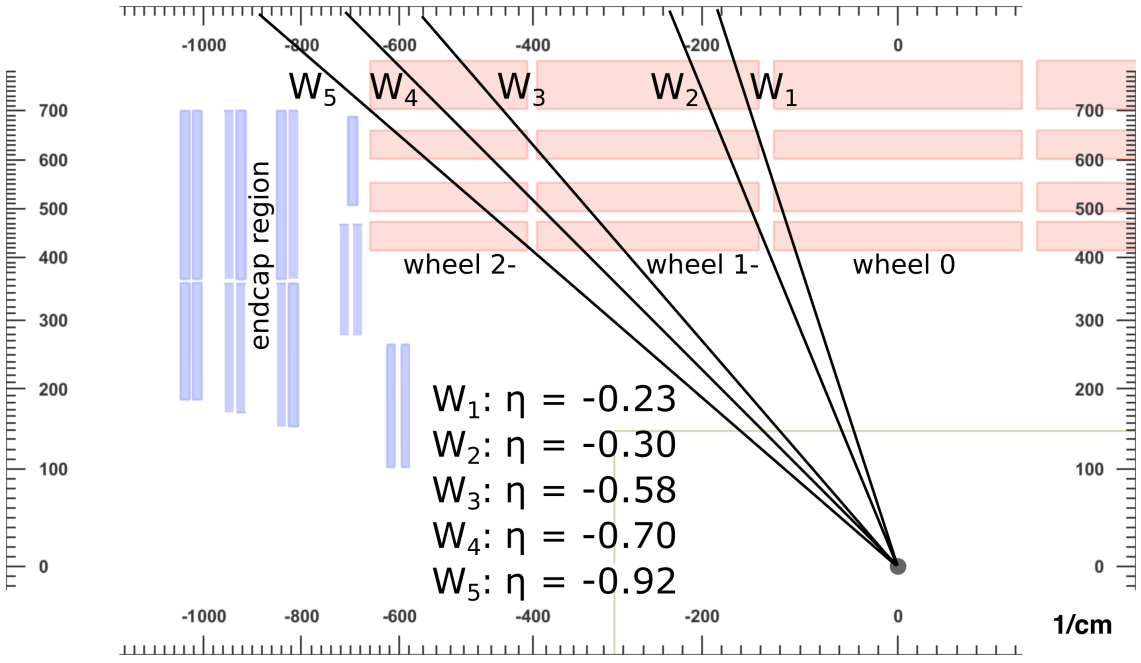

(b) η projection

Figure 5.9: Projections of the detector geometry in ϕ and η. Straight tracks are shown at positions that are crucial for the understanding of the analysis results. The tracks are referred to a S_x and W_x for the discussion of the analysis results. These tracks hit a detector gap in muon station 1 – 3.

difference is marked in figure 5.10. This is due to the fact that the HO tile is closer to the interaction point. The η projection to the wheel gap yields smaller numbers for detector parts (at a fixed z-coordinate) that have a larger distance to the interaction point. For further details please refer to section 2.2.1.

The slightly lower relative numbers of L1 muons matched to the reconstructed muons

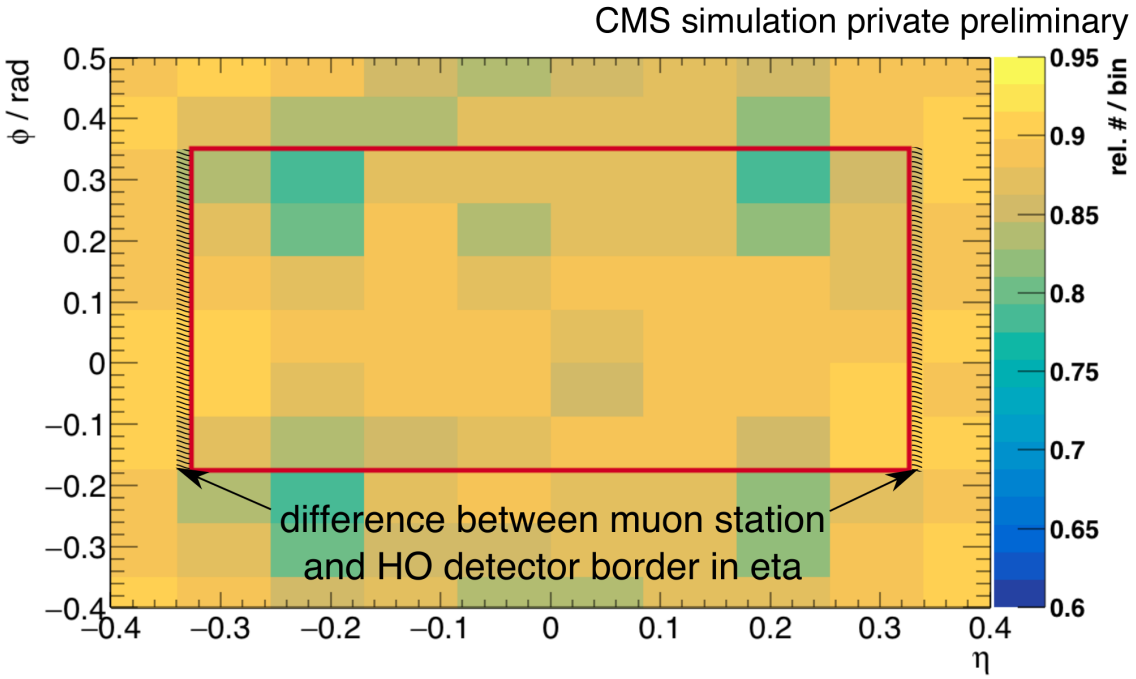

Figure 5.10: Numbers of L1 muons matched to a reconstructed muon normalized to the number of all reconstructed muons per bin in the sample with the fully working detector. The binning corresponds to the binning of the calorimeter-towers. Thus, it also corresponds to the size and position of the HO tiles. The red rectangle represents the position of muon station 1 in wheel 0, sector 1. The coordinates are the direction of the reconstructed muon at the vertex.

at (η, ϕ) = (-0.2, 0.3), (-0.2, -0.2), (0.2, 0.3) and (0.2, -0.2) result from wheel and sector gaps in muon station 1. So at these points only the information of muon station 2, 3 and 4 is present, which leads to a smaller efficiency of the L1 muon recognition. The reconstruction is still efficient at these positions as it also uses tracker data.

At the next step, the number of L1 muons, that can be matched to the reconstructed muons in the sample of the working detector but are missing in the sample of the failing detector, is calculated. These muons are called missing L1 muons in the following. To gain the relative impact of the DT station 1 failure, the number of missing L1 muons is divided by the number of all L1 muons that can be matched to the reconstructed muons in the sample of the working detector (called additional missing L1 muon). This defines the "additional inefficiency", that is introduced by the detector failure additional to the intrinsic detector inefficiency. The resulting plot is shown in figure 5.11.

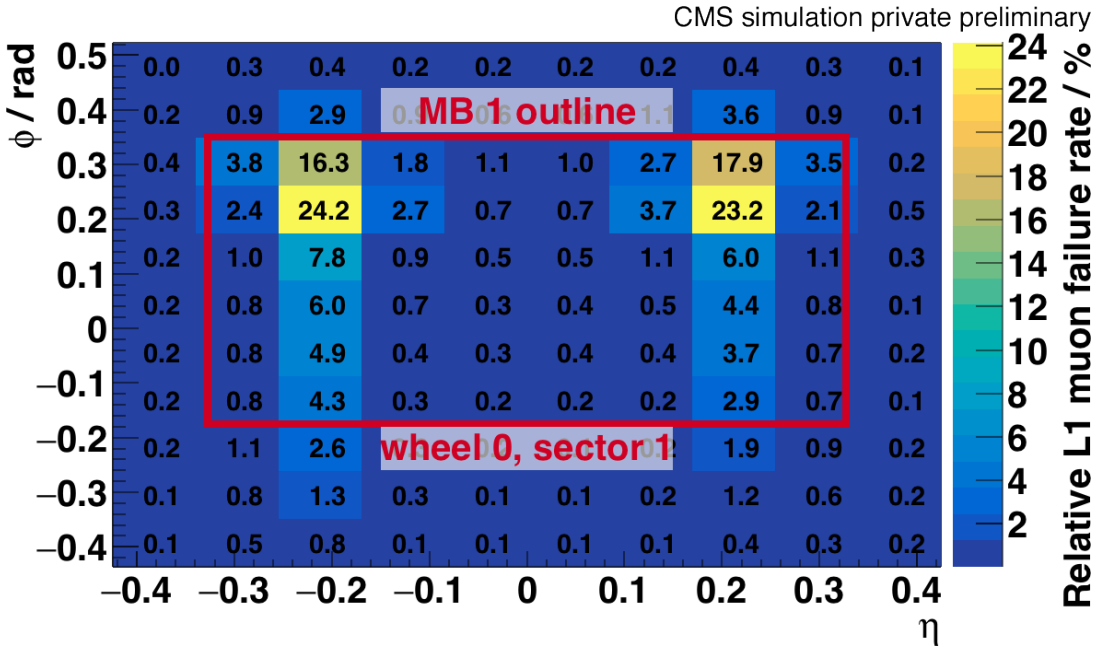

Figure 5.11: Relative number of additional missing L1 muons in case of a failing muon DT station 1 in wheel 0, sector 1. The number of additional missing L1 muons is normalized to the number of all L1 muons that can be matched to a reconstructed muon in the sample of the working detector. The binning corresponds to the binning of the calorimeter-towers/HO tiles. The red rectangle represents the position of the failing DT station. The numbers within the plot represent the relative number of additional missing L1 muons per bin in %.

The additional overall inefficiency for L1 muons in the area of the failing muon station ($\eta = [-0.35, 0.35]$, $\phi = [-0.17, 0.35]$) due to failure of this station is $\bar{\epsilon} = (2.27 \pm 0.02)$ %. The uncertainties are statistical.
The local efficiency drops with respect to the binning of the calorimeter-towers have a maximum of $\epsilon_{\text{local}} = (24.2 \pm 0.4)$ %. This point and the mirrored point in η again correspond to a detector gap and thus an inefficient muon detector in ϕ and η at station 2 (tracks S_1 and W_1 in figure 5.9). A straight muon will also hit station 3 close to its boundary. A track with a small curvature can therefore hit the wheel gaps of both station 2 and station 3.
The higher loss rate at the whole $\eta = \pm 0.2$ slices are also visible in the relative numbers plot (figure 5.11). The fact that these slices extend over the muon station's boundaries is due to the muon-gun p_T with the lower cut at $p_T = 3$ GeV. Therefore, also bent muons, that can hit the gaps in station 2 at very different ϕ projection values, are accounted for. Accordingly, this effect is not visible on the η axis since the muons are not bent in this projection due to the design of the CMS B-field (see section 2.2.5).

5.3.1.2 Failure in wheel 1-

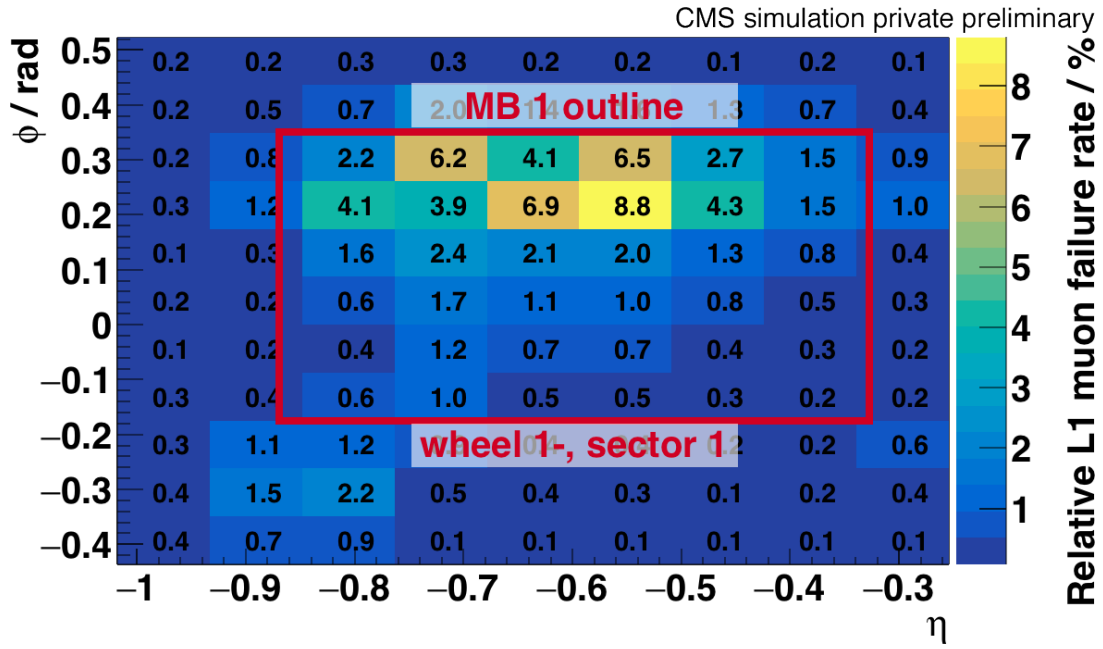

Figure 5.12: Relative number of additional missing L1 muons in case of a failing muon DT station 1 in wheel 1-, sector 1. The number of additional missing L1 muons is normalized to the number of all L1 muons that can be matched to a reconstructed muon in the sample of the working detector. The binning corresponds to the binning of the calorimeter-towers/HO tiles. The red rectangle represents the position of the failing DT station. The numbers within the plot represent the relative number of additional missing L1 muons per bin in %.

The same analysis as described in the section before is executed for station 1 failure in wheel 1-. The plot of the absolute number of additional missing L1 muons is shown in the appendix. The key-plot for the relative number of additionally missing L1 muons is displayed in figure 5.12.
The additional overall inefficiency in the area of the failing muon station is (1.52 ± 0.01) %. The maximal additional local inefficiency is (8.2 ± 0.2) %. Both values are lower compared to the failure of muon station 1 in wheel 0. The maximum value is at a position that corresponds to a straight muon track that hits the wheel gap between the wheels 1- and 2- at the position of station 3 (see figure 5.9b, track W_3). Additionally, the information of station 2 can be missing due to the sector borders at this position (figure 5.9a, track S_1). The impact of a potentially missing information from station 2 is less compared to the scenario in wheel 0. This is due to the fact that the gaps occur between sectors (in ϕ) instead of wheels (in η). The tracks are smeared in ϕ since a p_T-dependent bending to the magnetic field occurs. Therefore, the information of station 2 is more likely to be present.

Generally, the failure rate areas of L1 muons due to gaps in ϕ are less sharp compared to those from gaps in the η projection due to the variable bending of the muon tracks in ϕ.

5.3.1.3 Failure in wheel 2-

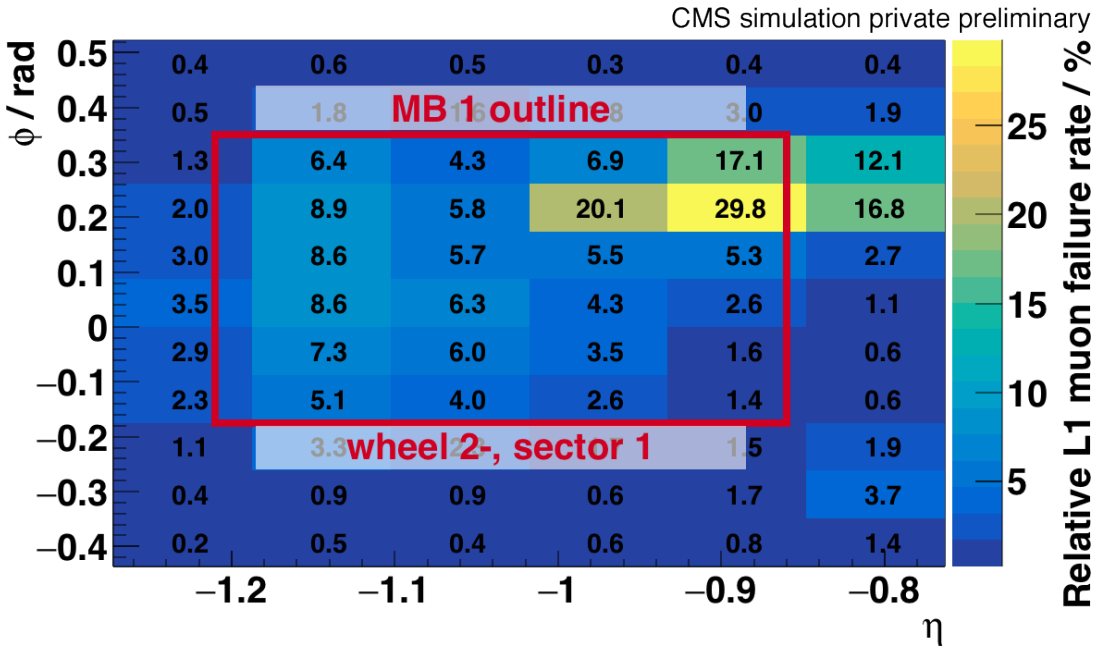

Figure 5.13: Relative number of additional missing L1 muons in case of a failing muon DT station 1 in wheel 2-, sector 1. The number of additional missing L1 muons is normalized to the number of all L1 muons that can be matched to a reconstructed muon in the sample of the working detector. The binning corresponds to the binning of the calorimeter-towers/HO tiles. The red rectangle represents the position of the failing DT station . The numbers within the plot represent the relative number of additional missing L1 muons per bin in %.

For a failure scenario of DT muon station 1, sector 1 in wheel 2- the additional overall inefficiency for L1 muon detection is (4.21 ± 0.02) %. The corresponding plot is shown in figure 5.13.
The additional overall inefficiency is significantly larger compared to the failure scenarios in wheel 0 and wheel 1-. For $\eta < -1.08$ the information of the L1 muon mainly comes from the endcap muon detectors. If the muon station 1 in the barrel region is failing, no information from the barrel muon system is fed into the overlap track finder. This results in a high inefficiency in this region.
The local maximum additional inefficiency is (29.8 ± 0.3) %. At this point the sectors

in ϕ have a gap in station 2 (see figure 5.9a, track S_1). The impact is much higher compared to the other scenarios in this case due to the arguments stated before concerning the overlap to the endcap region.

5.3.2 Failure of an MB DT station 2

The failure of DT station 2 has also been investigated. The same analysis procedure was used as for the analysis of a DT station 1 failure.
The relative additional failure rates are presented for the failure of station 2 in sector 1 in the wheels 0, 1-, and 2-. The resulting plots are shown in figures 5.14, 5.15, and 5.16 respectively.

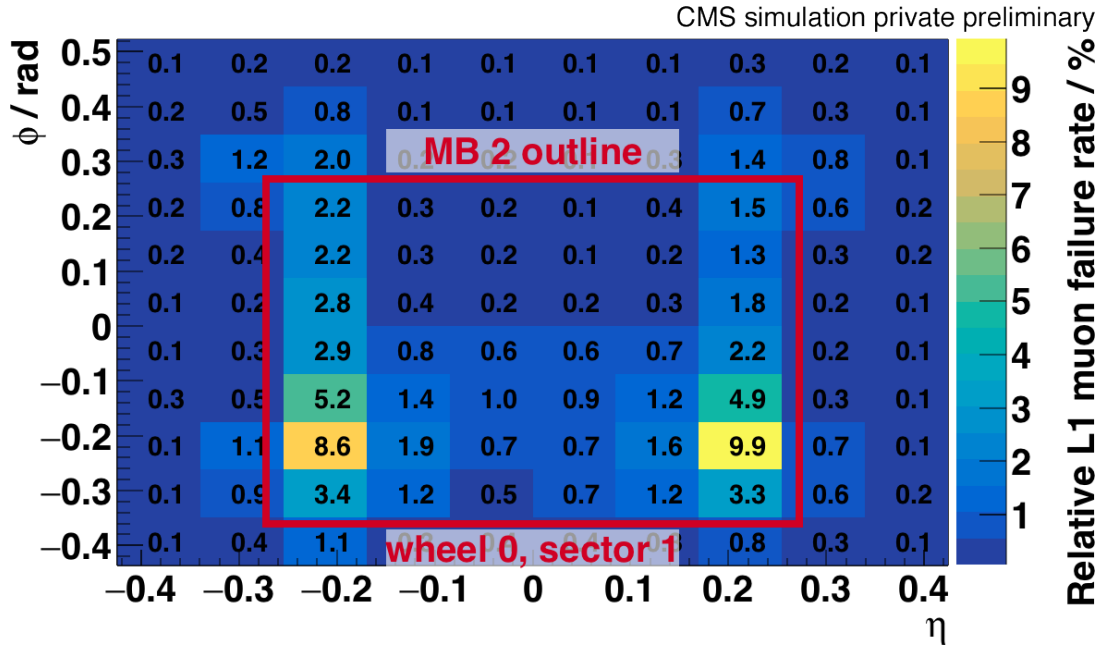

Figure 5.14: Relative number of additional missing L1 muons in case of a failing muon DT station 2 in wheel 0, sector 1. The number of additional missing L1 muons is normalized to the number of all L1 muons that can be matched to a reconstructed muon in the sample of the working detector. The binning corresponds to the binning of the calorimeter-towers/HO tiles. The red rectangle represents the position of the failing DT station. The numbers within the plot represent the relative number of additional missing L1 muons per bin in %.

5.3.2.1 Failure in wheel 0

For wheel 0 overall (1.10 ± 0.02) % additional L1 muon failures occur (see figure 5.14). The maximum local additional failure rate is (9.9 ± 0.3) %. The high local inefficiency

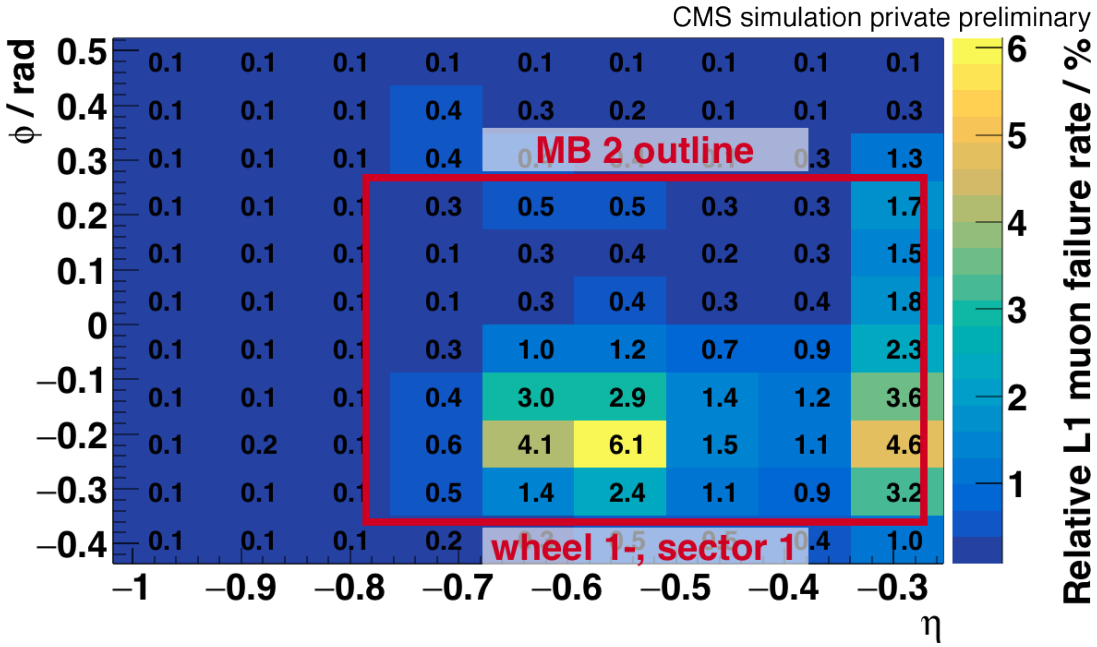

Figure 5.15: Relative number of additional missing L1 muons in case of a failing muon DT station 2 in wheel 1-, sector 1. The number of additional missing L1 muons is normalized to the number of all L1 muons that can be matched to a reconstructed muon in the sample of the working detector. The binning corresponds to the binning of the calorimeter-towers/HO tiles. The red rectangle represents the position of the failing DT station. The numbers within the plot represent the relative number of additional missing L1 muons per bin in %.

is again due to the wheel gap between wheel 0 and wheel 1- in the η projection (see figure 5.9b, track W_2). Additionally, it corresponds to the sector gap between sector 1 and sector 12 in station 1 in the ϕ projection (compare to figure 5.9a, track S_1). The maximal additional failure rate is less compared to a failure of station 1 in the same wheel.
When producing a muon track, beginning with the innermost station, the muon system creates a trajectory of the muon and extrapolates it to the next station. If the information of station 1 is missing, the most precise (in terms of bending) information is not available. If the information of DT station 2 is missing, the information of station 1 can be extrapolated to station 3. Therefore it is more probable that the failure of station 1 leads to missing L1 muons than the failure of station 2.

5.3.2.2 Failure in wheel 1-

Compared to muon station 1, station 2 is positioned at smaller η values in this projection. For this reason the local maximum of the additional failure rate at $\eta = -0.3$ and $\phi = -0.2$ is caused by the blind spot of the muon stations 1 in the wheel gap between

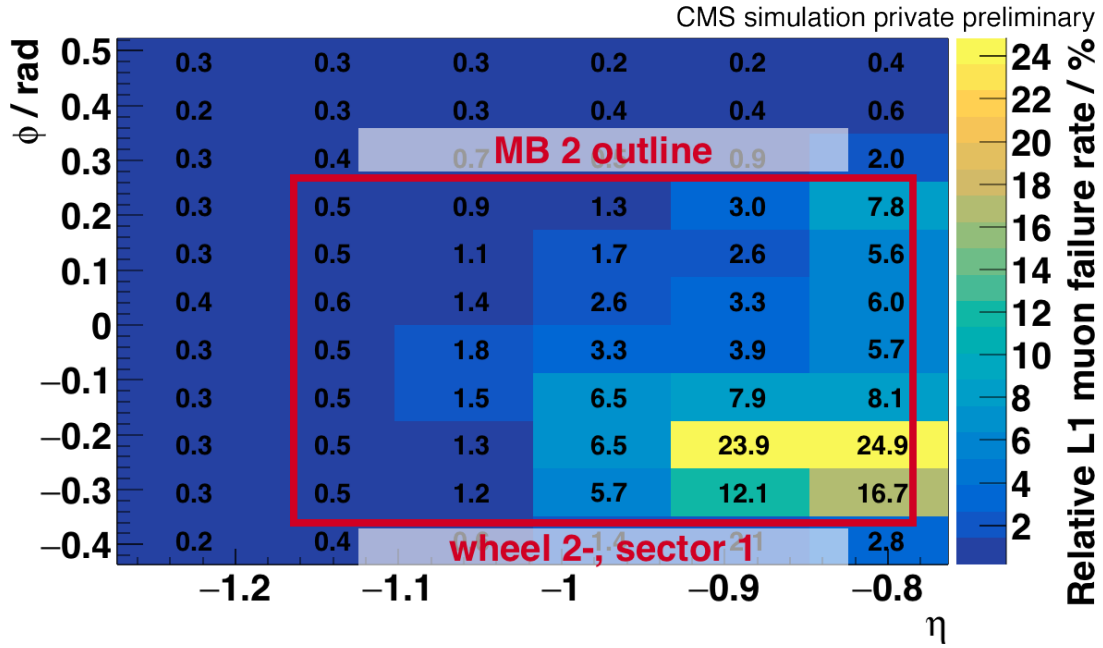

Figure 5.16: Relative number of additional missing L1 muons in case of a failing muon DT station 2 in wheel 2-, sector 1. The number of additional missing L1 muons is normalized to the number of all L1 muons that can be matched to a reconstructed muon in the sample of the working detector. The binning corresponds to the binning of the calorimeter-towers/HO tiles. The red rectangle represents the position of the failing DT station. The numbers within the plot represent the relative number of additional missing L1 muons per bin in %.

wheel 0 and wheel 1. This coincides with the detector gap between sector 1 and 12 in the third muon station (track S_2 and track W_2 in figure 5.9).
The bin maximum of (6.1 ± 0.2) % results also from the detector gap in the ϕ projection in station 3, but also from the gap in the same station between wheel 1- and 2- in the η projection (see figure 5.9b, track W_3).
The failure of station 2 in wheel 1- in sector 1 results in an additional inefficiency of (2.18 ± 0.05) % across the area of the failing station.

5.3.2.3 Failure in wheel 2-

The local efficiency drop for the station 2 failure in wheel 2- is unexpectedly high (see figure 5.16). At the area around $\eta = -0.85$ and $\phi = -0.2$ the failure rate increases up to (24.9 ± 0.4) %. This increase is not very tight but wide-ranging compared to the local failure rate increases observed in the other scenarios. The argument for the ϕ gap between sector 1 and 12 holds valid for the failure in wheel 2-, too. On top of that, at η values of about -0.85, a straight muon track traverses muon station 1 and 2 and does not hit muon station 4 or the muon system of the endcap region (see figure 5.9b,

track W_5). Therefore, taking into account the missing information from station 3 due to the sector borders, only the information of station 1 is present. This is not sufficient to create a L1 muon and yields the unexpectedly high local efficiency drop.
Due to this high lack of muon information, the additional overall inefficiency of (3.85 ± 0.02) is also comparatively large. This setup is a prime example for which the redundancy of HO can help by using the information of station 1 in combination with HO as MIP tag. Such an algorithm has been developed and explained in section 5.4.

5.3.3 Summary of failure rates analysis

The summary of all simulated additional L1 muon detection failure rates is shown in table 5.3. The analysis of L1 muon detection inefficiencies due to a failure of a DT

	Wheel 0		Wheel 1-		Wheel 2-	
	Avg. / %	Peak / %	Avg. / %	Peak / %	Avg. / %	Peak / %
MB 1	2.27 ± 0.02	24.2 ± 0.4	1.52 ± 0.01	8.2 ± 0.2	4.21 ± 0.02	29.8 ± 0.3
MB 2	1.10 ± 0.02	9.9 ± 0.3	2.18 ± 0.05	6.1 ± 0.2	3.85 ± 0.02	24.9 ± 0.4

Table 5.3: Additional failing rates for the detection of L1 muons due to MB DT station failure in sector 1. The maximum local additional inefficiency within the binning of the size of HO tiles and the average additional inefficiency in the area of the failing detector are presented. Local additional inefficiencies above 20 % are highlighted.

MB station reveals a notable impact of this type of detector failure. Although, the RPC detector is fully working in the simulation analyses, the local failure rate for L1 muons due to DT station failure can increase to almost 30 %. Thus, RPC is inefficient in these cases since it does not create own L1 muons. Local hot-spots of increased failure rate always correspond to blind detector spots due to gaps in the detector geometry. At these positions the redundancy of the muon system is partially not given anymore and can result in a loss of L1 muons.
The analysis shows that in the wheels 0 and 2(-) the failure of a DT station can have severe effects. In wheel 2(-) the reduced redundancy due to the overlap of the barrel muon system and the endcap muon system is the most impacting factor.
In order to reduce the inefficiencies and increase the redundancy, an algorithm is introduced that combines the remaining data of the DT stations 1 and 2, as well as HO as MIP tag for muon verification (see section 5.4).

5.3.4 Systematic matching uncertainty

In order to estimate the uncertainty caused by the matching cut criteria for the matching of L1 muons to reconstructed muons (see section 5.2.3.2), the analysis of the missing L1 muon rate is redone with changed matching cuts in station 1, wheel 0. The

applied matching cuts and the results for the additional overall and the maximum local inefficiency are shown table 5.4.

The values for the loose and tight matching criteria where chosen such that they

		Additional inefficiency due to detector failure / %	
$\Delta R <$	$\delta p_T <$	overall	max. local
0.15	0.4	4.08 ± 0.02(stat.)	28.7 ± 0.5(stat.)
0.2	0.5	2.27 ± 0.02(stat.)	24.2 ± 0.4(stat.)
0.3	0.7	2.15 ± 0.01(stat.)	22.7 ± 0.4(stat.)

Table 5.4: Analysis results for different matching cuts in ΔR and δp_T. A loose and a strong cut has been performed in order to estimate the uncertainty arising from the matching cut.

are just sensible for the given matching. At tighter cuts too many L1 muons remain unmatched. At looser cuts too many random L1 muons from a different muon in the event are associated to the wrong reconstructed muon.

The consideration reveals that the systematic uncertainty due to the matching criteria dominates the statistical uncertainties that arise from the event counting. Nonetheless, the matching cut of $\Delta R < 0.15$ is very tight since the binning of an L1 object in η and ϕ is 0.044. Therefore, the tighter tested cut is smaller than four coordinate bins in L1. For this reason more L1 muons do not match the criteria and are considered lost. The looser matching criteria set results in a small variation of the observed failure rates. The rate for the local maximum is about 6 % smaller, the overall rate is 8 % smaller. Consequently the matching criteria selection has an influence on the observed values but do not harm the conclusions drawn from this analysis.

5.3.5 Estimation of HO value for inefficiency recovery

Considering the failure scenario in wheel 0, station 1, sector 1, the additional overall inefficiency due to the detector failure of up to 2.27 % may be acceptable, keeping in mind that this is a failure scenario. Nonetheless, a local additional inefficiency of 24.2 % has a significant impact on the L1 trigger at this position. Consequently, an algorithm to avoid these additional inefficiencies in case of a detector failure is valuable. To make a first estimation if the hadron outer system (HO) and consequently an even better MTT detector can contribute to such an algorithm, the energy deposition of the muons, that get lost in the L1 trigger in the case of muon station failure, in HO is studied. For this purpose, the intersection of the reconstructed muon track with the HO system is calculated and the energy at the corresponding tile and the maximum energy in a $3 \cdot 3$ tile window, respectively, are filled into a histogram.

The histogram for the scenario of DT muon station 1 failure in wheel 0 is shown in figure 5.17. For the single tile efficiency HO is able to detect signals above its MIP threshold of 0.2 GeV for (49.4 ± 0.4) % of the missing L1 muons. In a $3 \cdot 3$ tile area

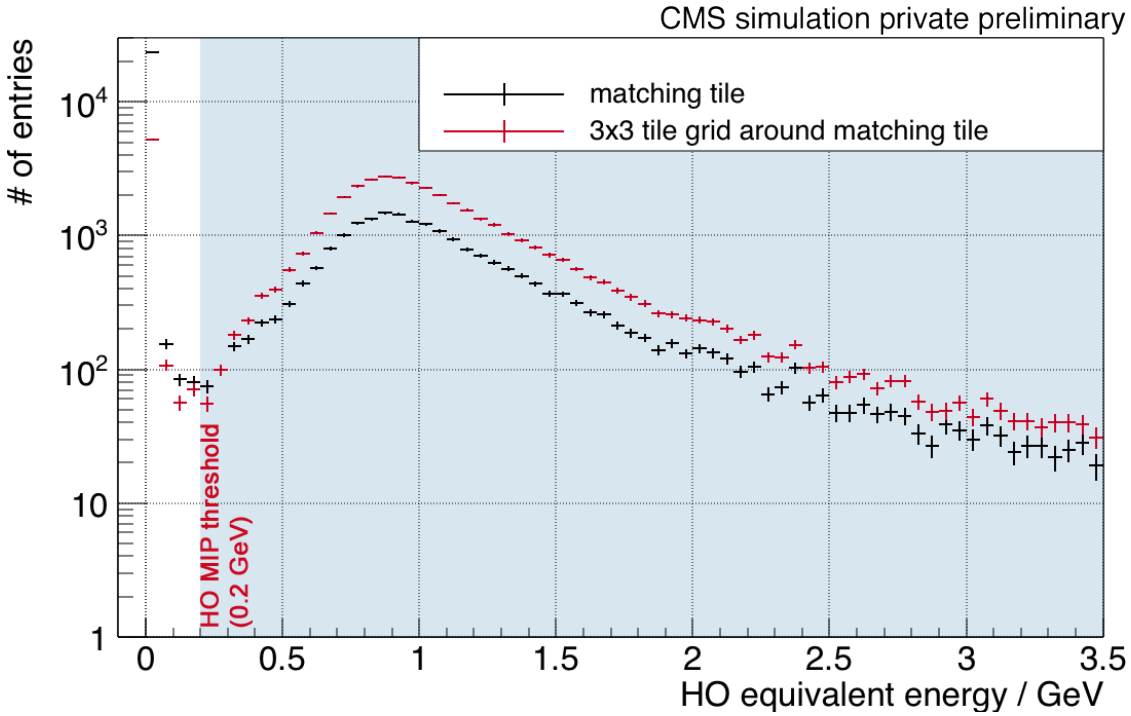

Figure 5.17: Simulated equivalent energy of the HO tile that intersects the reconstructed muon track of muons that experience an L1 failure. The scenario is the failure of DT muon station 1 in wheel 0 at sector 1 (see section 5.3.1.1). The HO energy threshold for MIPs is 0.2 GeV (blue colored area). For the single tile 49.5% of the missing muons are seen by HO, for the $3 \cdot 3$ tile grid 88.5% of the muons are detected by HO.

around the muon's track interception with HO (88.5 ± 0.4) % of the muons show up as MIP signal. The number for the single tile matching is well below the HO geometrical acceptance of $a_{\text{geom}} = (90.5 \pm 0.3)$ % [60]. Nonetheless, the potential matching efficiency for the $3 \cdot 3$ tile area around the muon track is close to the geometrical acceptance. Taking into account HO's muon trigger efficiency of $\epsilon = 97$ % [60] the resulting acceptance of

$$p_{\text{muon trigger}} = a_{\text{geom}} \cdot \epsilon \approx 87.8\% \tag{5.4}$$

compares very well within the uncertainties to the measured potential muon triggering efficiency.
This result highly encourages to further investigate the potential of HO to yield redundancy in case of DT muon station failure. Since HO and a potential MTT are only able to create a muon tag, the muon's p_T, ϕ, and η information has to be extracted from another system. An algorithm to use the HO tag to compensate a muon station 1 or 2 failure, respectively, is presented in the next section 5.4.

5.4 Recovery procedure

To create additional redundancy in the muon system, a scintillator-based muon trigger can be introduced. The concept of a Muon Track fast Tag (MTT, see chapter 3) is such a muon trigger. Also the existing hadron outer calorimeter (HO) represents a scintillator-based detector. Its main purpose as a tail catcher for the calorimeter system can be extended towards a muon trigger system. The basic potential of the HO to detect MIPs and thus muons has been demonstrated in the previous section.
The presented recovery procedure aims to keep the underlying algorithm as robust as possible. Therefore, the algorithm uses only the digitized data of the functioning muon station and combines it with the HO data. HO is used as MIP trigger in order to confirm that the signal measured in the muon station is originating from a physical muon.
The exact procedure is presented exemplary for the failure of DT station MB 2 here. The procedure for the failure of station 1 works in a similar way.
In the case of muon station 2 failure, only the information of muon station 1 is available from the two main track-seeding muon stations in a sector. The information from muon station 1, that can be compared to information from the HO system, is a digitized track within this station. The corresponding data format is called `L1MuDTChambPhContainer` and `L1MuDTChambThContainer`. These containers carry the combined information of the two ϕ layers from the TRACO and the information of the single η layer separately. This information is called ϕ and θ DT trigger primitive (DT TP).
Besides the timing information, the θ DT TP contains information of the entrance point of the measured muon in the muon station in the η projection as local coordinate. Although the drift tubes have a fine resolution (4 cm), the η value in the DT TP is binned into seven η positions only at this stage of readout [84].
The ϕ DT TP also contains timing information. Additionally, two geometrical parameters are stored. The ϕ_{local} angle defines the first intersection point of the muon track with the muon station as local value. The ϕ_{local} variable is stored as number $N_{\phi_{\text{local}}}$ with a binning of 2048. The value of 0 defines the position at which a straight track from the interaction point intersects the muon station perpendicularly.
The second geometrical parameter is the bending angle ϕ_{B}. It is defined as the angle between the muon track within the muon station and the line from the interaction point to the intersection of the beginning of the muon station and the muon track. This definition is feasible due to the fact, that the track of the muon is sufficiently straight within the muon chamber due to the low magnetic field within the station. The ϕ_{B} bending value is stored as $N_{\phi_{\text{B}}}$ number with a binning of 512 and is directly correlated to the muon's p_T. A schematic of both ϕ coordinates of a `L1MuDTChambPhDigi` is shown in figure 5.18.
In principle these DT TPs of the single station can be used to detect muons. In order to gain a reliable measurement of a muon, different tasks have to be performed. A muon measurement needs:

- ϕ coordinate of the muon from the local angle ϕ_{local} (see section 5.4.1)

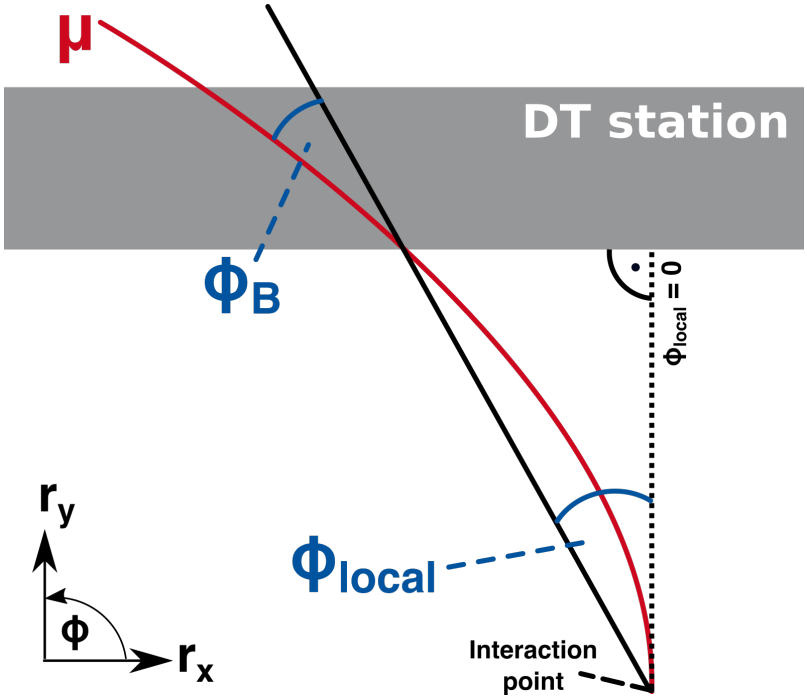

Figure 5.18: Schematic of the geometrical variables of a `L1MuDTChambPhContainer`. The dimensions are not to scale.

- η coordinate of the muon from the `L1MuDTChambThContainer` (see section 5.4.2)
- p_T value gained from the local muon bending ϕ_B (see section 5.4.3)
- MIP tag from HO in order to reject noise (see section 5.4.4)

The steps, that were taken to deal with these tasks, are described in the next sections.

5.4.1 ϕ coordinate definition

The local η and ϕ data of the DT TPs have to be translated to global quantities of the CMS system.
The ϕ value of the DT TP is given relative to the perpendicular intersection of a straight line from the interaction point to the muon chamber with the muon chamber's front side. This information is binned in 2048 values. Therefore, in a first step, the binned value is translated into a radian value with

$$\frac{\phi_{\text{rad}}}{\text{rad}} = \frac{N_{\phi_{\text{local}}}}{2048}. \tag{5.5}$$

Depending on the sector of the DT TP generating station this local value is shifted by

$$\frac{\phi_{\text{shifted}}}{\text{rad}} = \frac{\phi_{\text{rad}}}{\text{rad}} + \frac{2 \cdot \pi}{12} \cdot (n_{\text{station}} - 1) \tag{5.6}$$

with the station number $n_{\text{station}} = [1;12]$. The CMS ϕ coordinate system has a range from $-\pi$ to π. Therefore, values with $\phi_{\text{shifted}} > \pi$ are shifted by -2π. This results in a final translation formula from the local to global coordinates of:

$$\frac{\phi_{\text{global}}}{\text{rad}} = \begin{cases} \frac{\phi_{\text{rad}}}{\text{rad}} + \frac{2\cdot\pi}{12} \cdot (n_{\text{station}} - 1) & , 0 < \frac{\phi_{\text{rad}}}{\text{rad}} + \frac{2\cdot\pi}{12} \cdot (n_{\text{station}} - 1) < \pi \\ \frac{\phi_{\text{rad}}}{\text{rad}} + \frac{2\cdot\pi}{12} \cdot (n_{\text{station}} - 1) - 2\pi & , \pi < \frac{\phi_{\text{rad}}}{\text{rad}} + \frac{2\cdot\pi}{12} \cdot (n_{\text{station}} - 1) < 2\pi \end{cases} \tag{5.7}$$

This represents the global ϕ variable for the track of the muon at the muon station. Furthermore, this coordinate has to be translated to a ϕ coordinate at the interaction point. In order to illustrate the difference please refer to figure 5.18. This correction is obviously depending on the bending angle ϕ_{B} of the muon and consequently on the muon's p_T. A good correction factor is found to be

$$\frac{\phi}{\text{rad}} = \frac{\phi_{\text{global}}}{\text{rad}} - 2 \cdot \frac{N_{\phi_{\text{B}}}}{512} \tag{5.8}$$

with the locally measured bending angle number $N_{\phi_{\text{B}}}$. This value has to be divided by 512 due to its binning.

5.4.2 η coordinate definition

The handling of the local η variable is more difficult. First of all, valid η information for a DT TP does not have to be present at all. In this case, the global η position can only be estimated and set to the η center value of the muon station in which the ϕ DT TPs are created. For a valid `L1MuDtChambThDigi` the η values are binned into 7 bins. For a whole station only one `L1MuDtChambThDigi` is created and contains the information if a muon was measured in every particular bin. Furthermore, it contains the information if three or four DT-wires contribute to the η position measurement. Therefore, the `L1MuDtChambThDigi` returns a seven bin array. If the return value is greater than zero for a particular bin, the center η position of this bin is taken as the muon's η value. If more than one bin has a value greater than 0, it is not clear anymore which combination of η and ϕ values are valid. In this case, all combinations are taken into account. This can be done due to the fact that an HO matching will be performed which can correct the eventual ambiguities (see section 5.4.4).

5.4.3 p_T assignment

In order to assign a p_T value, the local bending angle ϕ_{B} has to be translated. The ϕ_{B} value is the only data available in a DT TP that is correlated with the transverse muon momentum.
An analytical assignment is hardly possible between these two variables. To gain information about the assignment and its uncertainty a simulation of single muons has been performed.
Thereby, the simulated detector properties correspond to the analysis of the DT failure. No pile-up has been mixed to the sample. The muon momentum ranges from

3 GeV $< p_T <$ 100 GeV. At higher transverse muon momentum values than 100 GeV the impact of the muon momentum on the bending angle of the muon in the muon station is expected to be negligible. In sum 600000 events containing only one muon were produced. Half of the muons had a positive charge, the other half had a negative charge. The ϕ range was constrained to sector 1 ($|\phi| < 0.52$). The muons point to wheel 0 ($|\eta| < 0.4$).
The p_T value for each muon is known from generator information. In every event the muon p_T and the simulated bending angle ϕ_B in all four muon stations is stored. For each muon station these values are filled into a two dimensional histogram, shown in figure 5.19 for sector 1 and 2, respectively. The distributions for station 3 and 4 are shown in the appendix.
The bending at station 1 is the strongest of all four stations. For very low muon momenta ($p_T \approx 5$ GeV) it can go up to 0.4 rad. For higher momenta it asymptotically changes towards zero as expected since a muon with a higher energy is less deflected. The two different signs of the bending according to the two muon charges are also expected.
Moving to station 2, the correlation between the bending angle and the muon momentum decreases. The CMS magnetic field vectors have the opposite direction outside the solenoid compared to the vectors within the solenoid (see also section 2.2.5). Therefore, the muon is bent in the opposite direction after leaving the solenoid. With decreasing bending angle also the correlation to the muon momentum decreases.
At station 3 only entries with a bending angle of zero exist. At this position the magnetic field has compensated for the bending from within the solenoid. The DT system sets all bending angles at station 3 to zero. The bending is thus not meaningful at this station.
At station 4 the bending has changed the sign. Nonetheless, the bending is very small and the two muon charges are barely distinguishable since the magnetic field gets weaker at larger distances to the solenoid.
It is obvious that only the information from the stations 1 and 2 can yield reliable p_T information. The p_T assignment and its precision has therefore been quantified for these stations.

In order to obtain a translation formula from ϕ_B to p_T variables and to estimate its uncertainty, histograms for a each p_T slice have been created. A p_T slice has the width of 1 GeV. The data of a p_T slice yields a histogram of bending angles for the certain p_T range. The mean value and the sampling uncertainty are taken from this histogram. More precisely the sampling uncertainty for a single measurement has been used, since the measurement of a particular bending angle will be unique within a DT muon station.
The whole workflow is shown in figure 5.20. The resulting distributions including the uncertainties are shown in figure 5.21.
For small muon momenta, the distinction via the bending angle within a muon station 1 or 2 is possible. As expected the distinction is better in station 1 compared to station 2 due to the larger muon track bending. For larger momenta, the bending angle

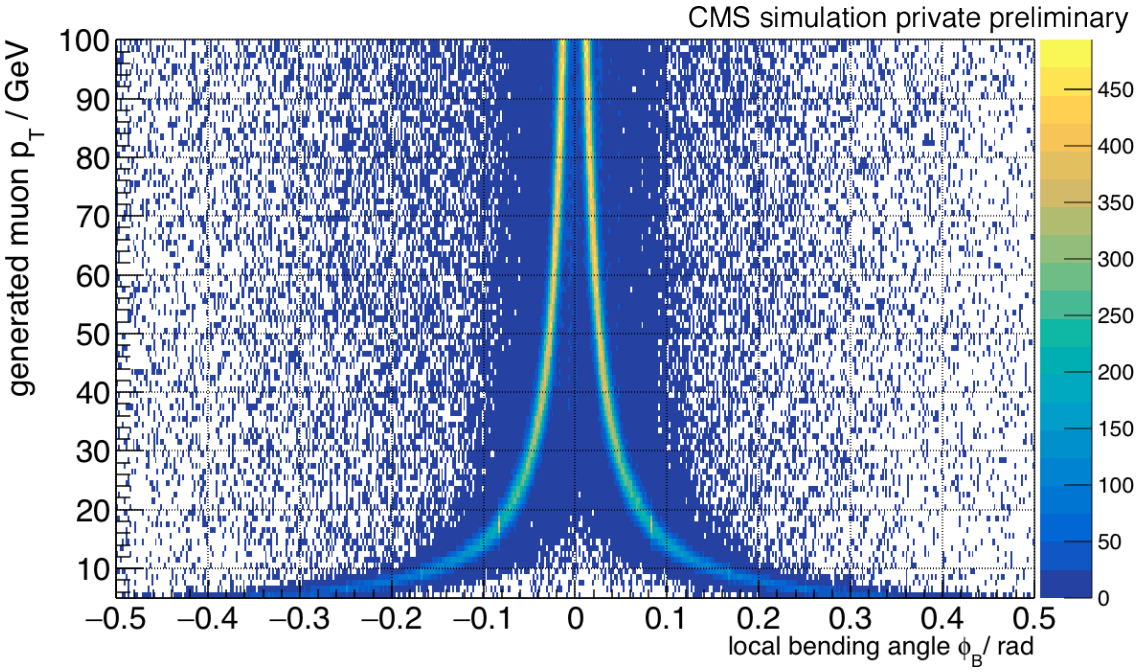

(a) Station 1

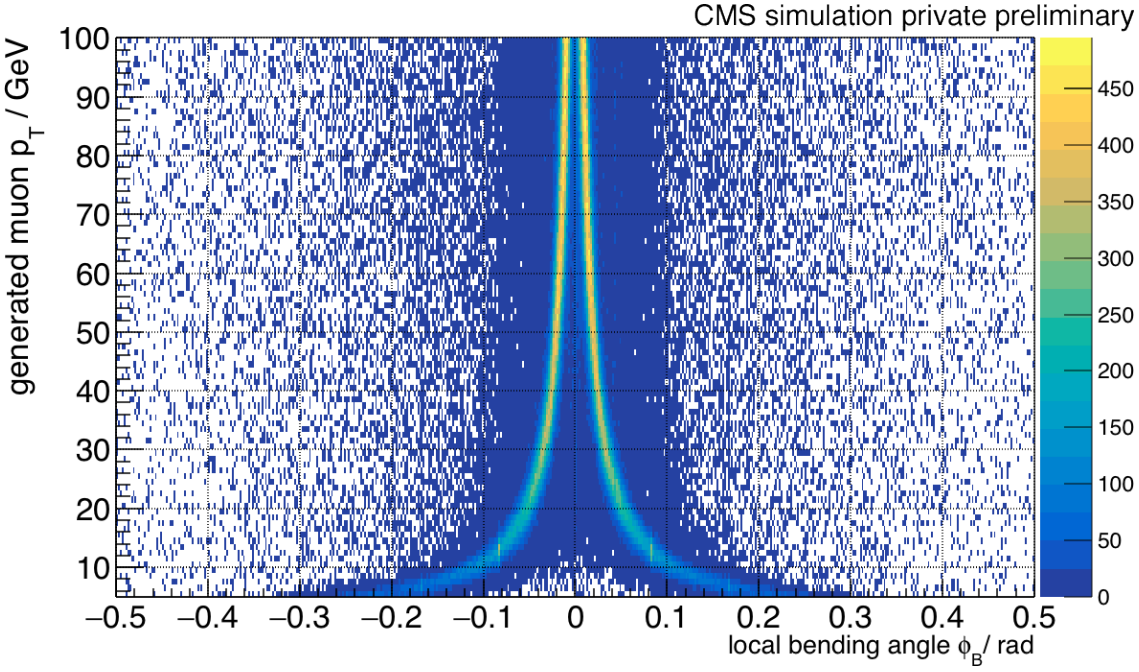

(b) Station 2

Figure 5.19: p_T vs. ϕ_B distribution for single muons at muon stations 1 and 2, respectively. Due to the stronger bending, the distribution is broader for the station closer to the interaction point.

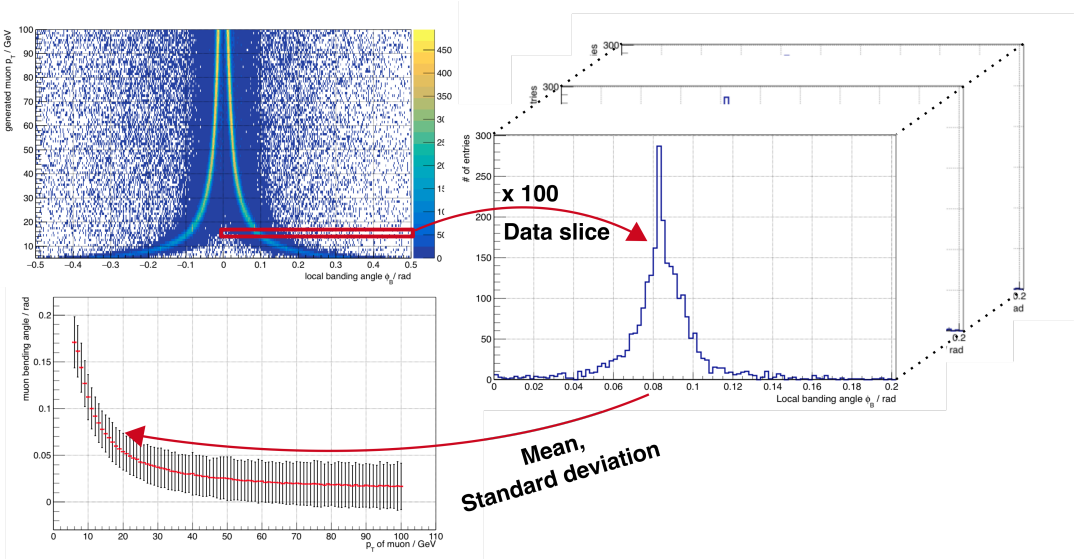

Figure 5.20: Workflow to gain the mean position and the uncertainties of the p_T vs. ϕ_B distribution. The mean and the standard deviation are evaluated from histograms resulting from data slices for every momentum slice.

approaches zero. Thus, a differentiation is not possible above a muon momentum of O(30 GeV).
However, the typical unprescaled L1 single muon thresholds are in the order of 20 GeV and the muon trigger thresholds are kept as low as technically possible in order to avoid the rejection of sensitive data. At higher muon momenta the event will be accepted anyway. The impact of an imprecise muon momentum measurement at high momenta ($p_T > 30$ GeV) on the L1 trigger rate is therefore expected to be negligible. This assumption will be further investigated in section 5.5. Besides the sign, the bending correlation shows no significant difference for μ^+ and μ^-
In a last step, the extracted mean values and uncertainties are plotted. This plot is used to make a generic fit to the data points assuming

$$p_T(\phi_B) = \left(\frac{\text{sign}(q) \cdot a}{\phi_B - b} + c \right) \tag{5.9}$$

with the muon charge q and the local bending angle ϕ_B.
For this fit, the data for both charges are treated separately. It is expected that the muon momentum will be proportional to the inverse bending angle, since a distraction of a charged particle is proportional to its inverse inertia.
The generic fit allows to make a simple conversion between ϕ_B and p_T. The resulting values of the function are shown in table 5.5.
The parameter b is comparatively small. A value of $b \neq 0$ means that the ϕ_B versus $1/p_T$ correlation has an offset from the zero passage. The bending angle is expected to be zero at infinite muon momenta. Therefore, the very small value b is reasonable. The given parameters are used for a direct conversion between ϕ_B and muon p_T.

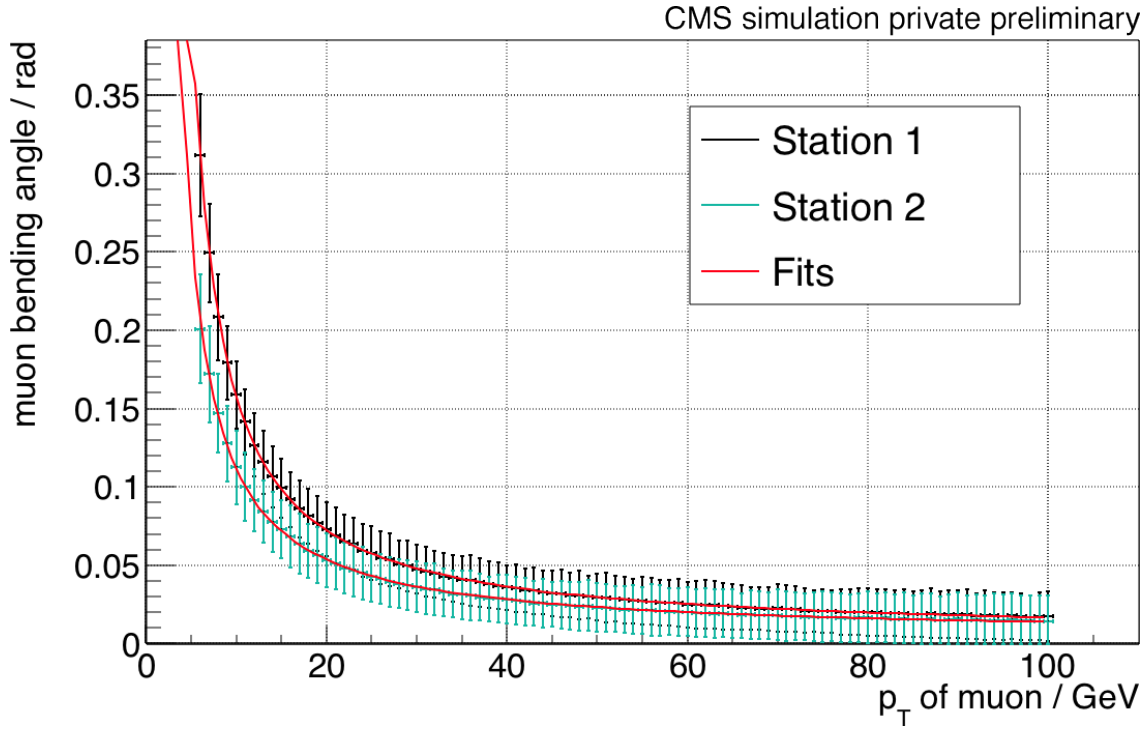

(a) Positive muon charge

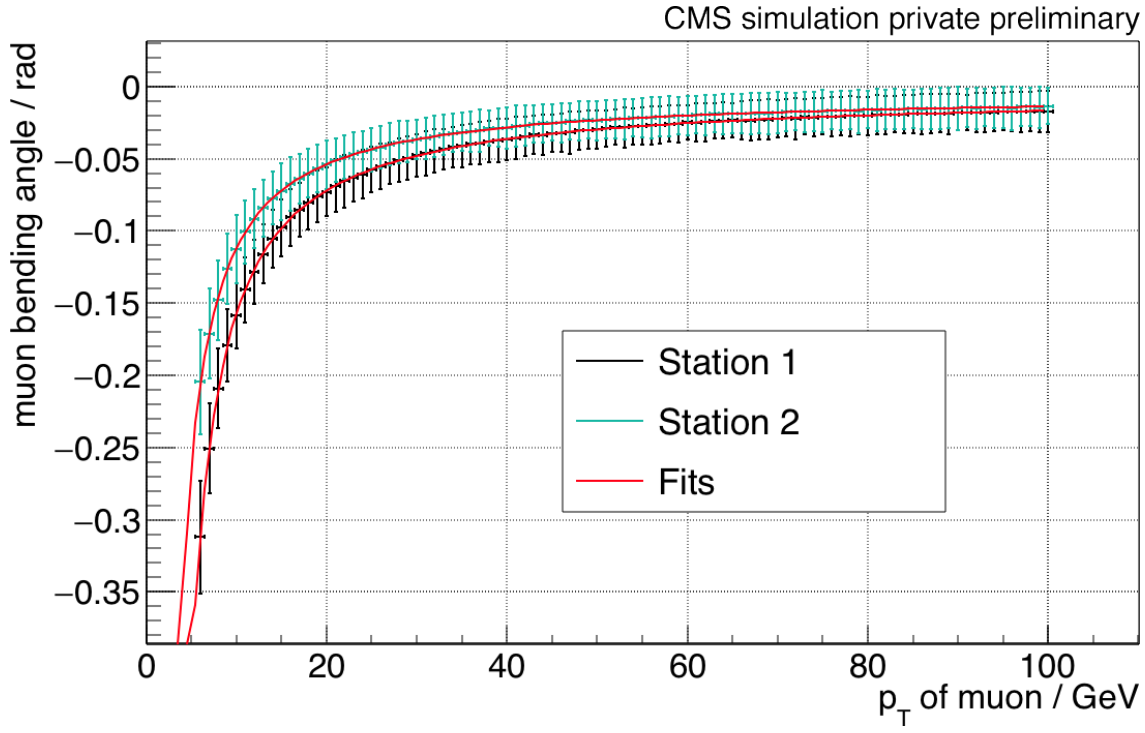

(b) Negative muon charge

Figure 5.21: p_T vs. ϕ_B distribution for single muons at the muon stations 1 and 2 for positive and negative muon charge, respectively. A distinction of p_T values is possible for $p_T < 30$ GeV. At higher p_T values the bending angle stays the same within the standard deviation.

Station	muon charge	Parameter		
		a / GeV	b	c / GeV
1	+	1.16 ± 0.16	$(1.58 \pm 0.34) \cdot 10^{-2}$	2.27 ± 0.86
1	-	1.08 ± 0.16	$(2.01 \pm 0.32) \cdot 10^{-2}$	2.34 ± 0.84
2	+	0.80 ± 0.16	$(1.72 \pm 0.32) \cdot 10^{-2}$	1.84 ± 1.23
2	-	0.79 ± 0.17	$(1.75 \pm 0.34) \cdot 10^{-2}$	1.90 ± 1.25

Table 5.5: Result of the fit of formula 5.9 to the p_T vs. ϕ_B data.

5.4.4 Matching of the muon track to HO

The last point to be handled to create a redundancy between the muon- and the HO-system is the matching of the muon track to the HO tile for the L1 trigger. This matching has to be very time efficient. The whole L1 trigger system has a 3.2 μs latency. The presented matching must consume only a small fraction of this latency (less O(750 ns)). Different to the matching done in section 5.3.5, no reconstructed track information is available. At this point only the information of DT muon station 1 or 2 is helpful for the matching. The ϕ_B, ϕ_{local}, and η variables have to be investigated in a way that a reliable match can be performed.
The η value of the HO tile is easy to determine. Since the muon track in the η projection is a straight line starting from the interaction point, the η value of the muon station will be the same as the η value of the HO tile. However, due to a different binning in DT η and HO η adjacent tiles in η will have to be taken into account when providing the MIP tag. The HO system does not use the geometrical η variable but uses a binned iη counting (see section 2.2.4.1). Starting from $\eta = 0$ the tiles are counted from -1 to -15 for negative wheel numbers and from 1 to 15 for positive wheel numbers. The measured η value of the DT muon station has therefore to be translated into the iη counting. This is solved by calculating

$$\mathrm{i}\eta_{\mathrm{unshifted}} = \frac{(\eta + 15 \cdot s)}{s} \tag{5.10}$$

with the HO tile size s in η direction

$$s = \frac{2\pi}{72} \tag{5.11}$$

and the direction of the muon η.
The value $\mathrm{i}\eta_{\mathrm{unshifted}}$ is then cut to an integer. Afterwards a shift is applied resulting in

$$\mathrm{i}\eta = \begin{cases} \mathrm{i}\eta_{\mathrm{unshifted}} & , \mathrm{i}\eta_{\mathrm{unshifted}} < 0 \\ \mathrm{i}\eta_{\mathrm{unshifted}} + 1 & , \mathrm{i}\eta_{\mathrm{unshifted}} \geq 0 \end{cases} \tag{5.12}$$

The calculation translates the η value to an iη value omitting $\mathrm{i}\eta = 0$. $\mathrm{i}\eta = 0$ is not assigned as there is no central HO tile in η in the center of wheel 0.

The matching of the muon track in ϕ is more complex. The matching depends on the ϕ position and the bending of the muon track. In order to take into account the CMS magnetic field, a parameterization study has been performed.
The study is based on the same single muon-gun dataset as in the section before. For different extrapolation methods the measured muon track is extrapolated from the DT muon station to the HO tile. The two different extrapolation methods between DT and HO are tested. After the presentation of the extrapolation methods the efficiency determination for the muon matching is shown.

5.4.4.1 Linear extrapolation

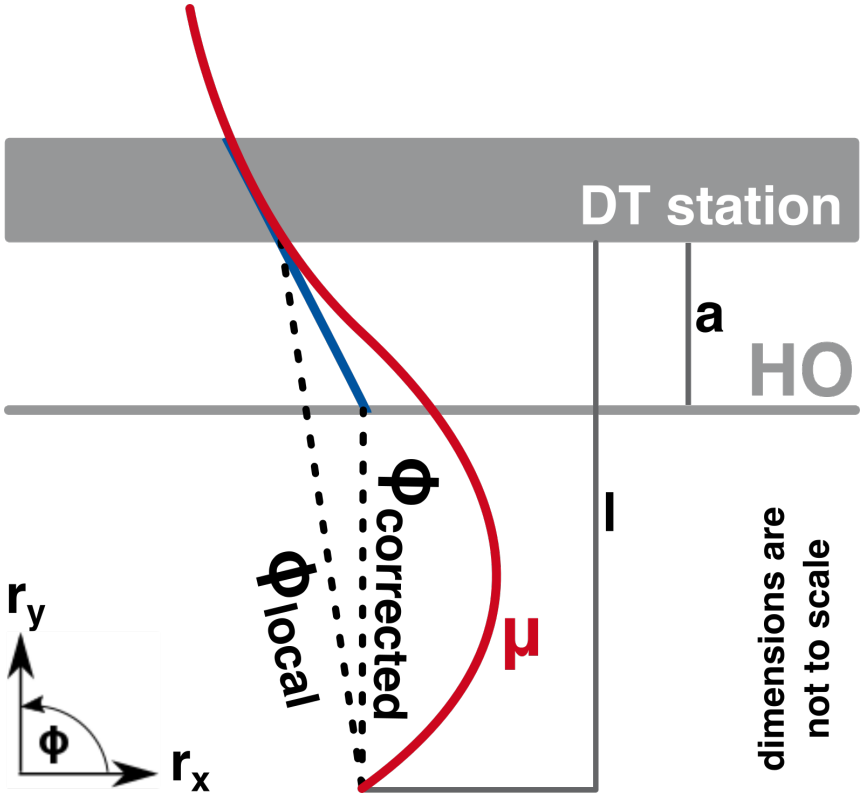

Figure 5.22: Principle of a linear extrapolation from a muon station to HO. The extrapolated ϕ position at HO is closer to the real intersection point compared to the ϕ_{local} value at the muon station.

The first extrapolation method is a simple linear extrapolation. The extrapolation is illustrated in figure 5.22. The ϕ value of the muon at the muon station is shifted closer to the intersection between HO and the muon track. The correction formula for the local ϕ position is

$$\tan(\phi_{\text{corrected}}) = \frac{l \cdot \tan(\phi_{\text{local}}) - a \cdot \tan(\phi_{\text{local}} + \phi_{\text{B}})}{l - a} \tag{5.13}$$

with the distance between interaction point and muon station l and the effective distance between muon station and HO, a.
The muon track is not expected to be straight between HO and the muon stations, since there is a notable magnetic field left in the return iron yokes. The extrapolation was therefore tested with different effective parameters a.

5.4.4.2 Circular extrapolation

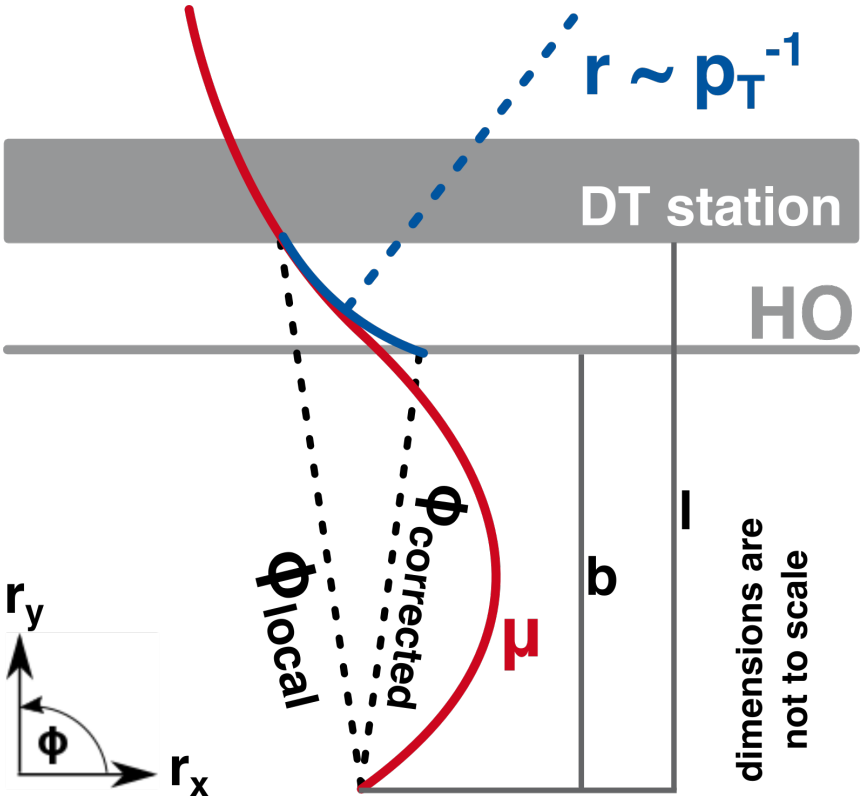

Figure 5.23: Principle of a circular extrapolation from a muon station to HO. The extrapolated ϕ position at HO is closer to the real intersection point compared to the ϕ_{local} value at the muon station.

The second type of extrapolation utilizes the fact that a charged particle propagates on a circular trajectory in a homogeneous magnetic field. The circular extrapolation is also an approximate extrapolation that will need effective values, as the CMS magnetic field is not homogeneous outside the solenoid. The principle of the circular extrapolation is shown in figure 5.23.
For the circular extrapolation, the muon p_T is determined using the ϕ_{B} value of the DT TP as described in section 5.4.3. The radius of the circular track of the muon is calculated using

$$\frac{r}{\text{m}} = \frac{p_T}{0.3 \cdot B_{\text{eff}}} \cdot \frac{\text{T}}{\text{GeV}} \tag{5.14}$$

with the effective magnetic field B_{eff} and the transverse muon momentum p_T. This circle is then extrapolated from the muon chamber to the HO system. The resulting corrected muon angle is

$$\tan(\phi_{\text{corrected}}) = \frac{r \cdot \cos\left(\arcsin\left(\frac{b-l}{r} - \sin(\phi_{\text{local}} + \phi_{\text{B}})\right)\right) + l \cdot \tan(\phi_{\text{local}}) - r \cdot \cos(\phi_{\text{local}} + \phi_{\text{B}})}{b} \tag{5.15}$$

with the distance b from the interaction point to the HO system and the distance l from the interaction point to the muon station. Due to the complex magnetic field outside the solenoid an effective value for the field and for the distance between muon station and HO system is used.

5.4.4.3 Test of extrapolation methods

The same single μ events without pile-up as in section 5.4.3 were used in order to quantify the matching of the muon track in HO. In each event the position of the muon at HO, that is extrapolated from the muon system, is registered. Additionally, the position iϕ of the HO tile with the highest measured energy within the event is stored (see section 2.2.4.1 for the HO coordinate system). Since there are no other particles, the HO tile with the highest energy entry will be considered as the tile that has been crossed by the muon unless no HO tile has been hit by the muon. In this case a random HO tile will be the tile with the highest energy entry. The resulting plot is shown in figure 5.24a exemplary for the uncorrected ϕ_{local} position at muon station 1.

At the local positions of $\phi_{\text{local}} = -10°$ and 20° the borders of the muon station 1 to the sectors 12 and 2 are visible. At these positions no DT TP is generated and therefore no entry into the histogram is created. A second feature are small randomly spread entries at all positions. These result from events in which a DT TP is present but the muon did not hit an HO tile. To avoid that feature, an energy threshold of 0.2 GeV is required. Only HO entries above this threshold account for the histogram. This threshold removes the noisy entries, as demonstrated in figure 5.24b.

After adding the energy threshold a clear correlation between HO tile number of the tile with the highest measured energy and the local entrance angle at the muon station is visible.

This view does allow for an analysis of the matching methods between HO and the muon stations. In order to define a quality criterion, again slices of the y-axis are created for every bin similar to the first step described in figure 5.20. The resulting histograms show the quality of the matching. In an ideal case, the histograms for two adjacent iϕ slices should not overlap. An example of the resulting histograms is shown in figure 5.25.

To define a matching efficiency the regions are split into 5° regions. Every region is corresponding to the HO tile at this position (e.g. i$\phi = 71$ for $-10° < \phi < -5°$...). For the efficiency the number of entries of the certain iϕ-slice within the 5° window is normalized to the number of entries in the histogram for a certain iϕ-slice.

The efficiency is determined for all six tile slices in ϕ direction in sector 1. A list of the tested effective parameters of distance between muon station and HO as well as the

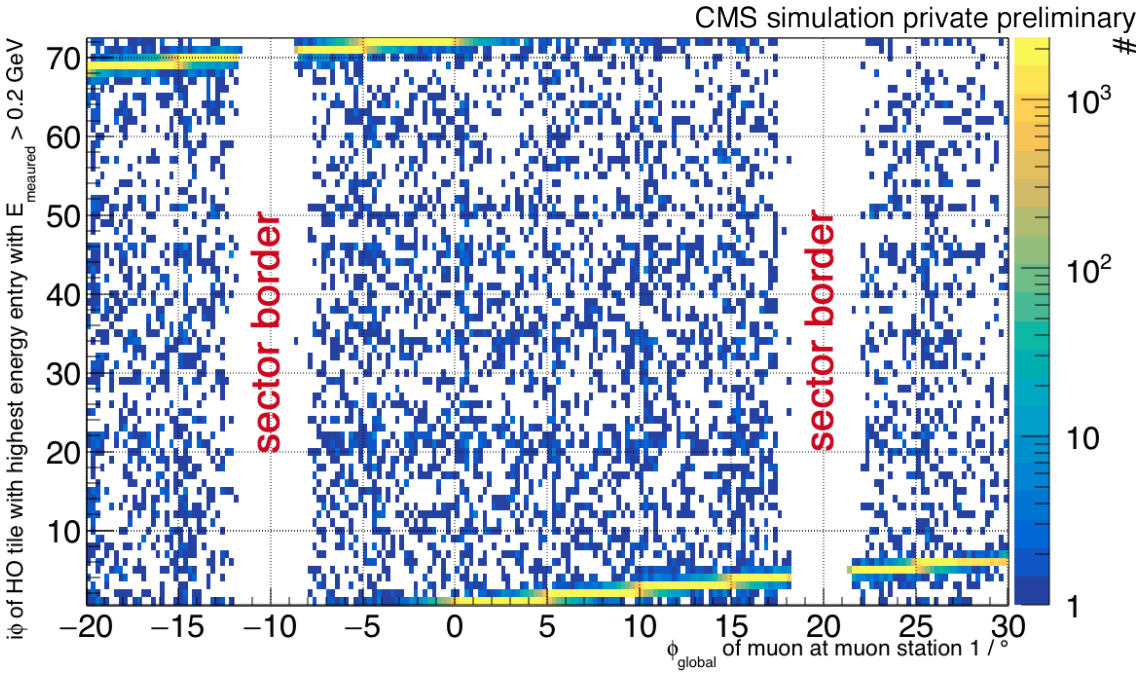

(a) no energy cut

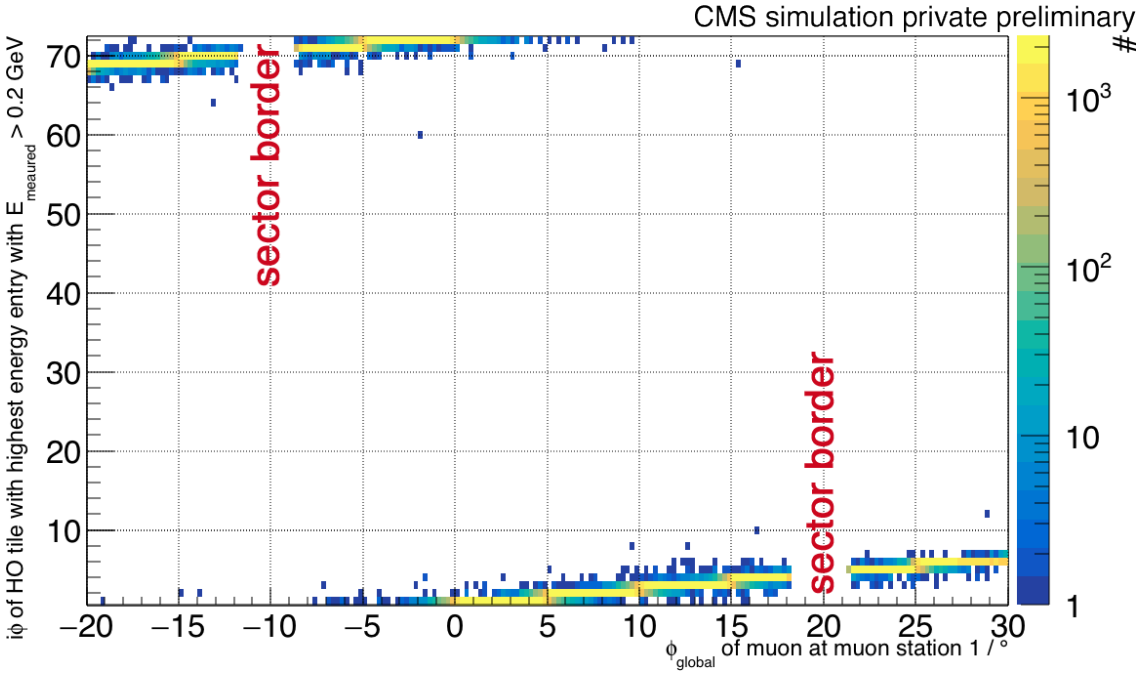

(b) 0.2 GeV energy cut

Figure 5.24: iϕ position of the HO tile with the highest energy entry vs. the measured ϕ_{global} position at the muon station 1 with and without applied cut on the HO tile energy of 0.2 GeV.

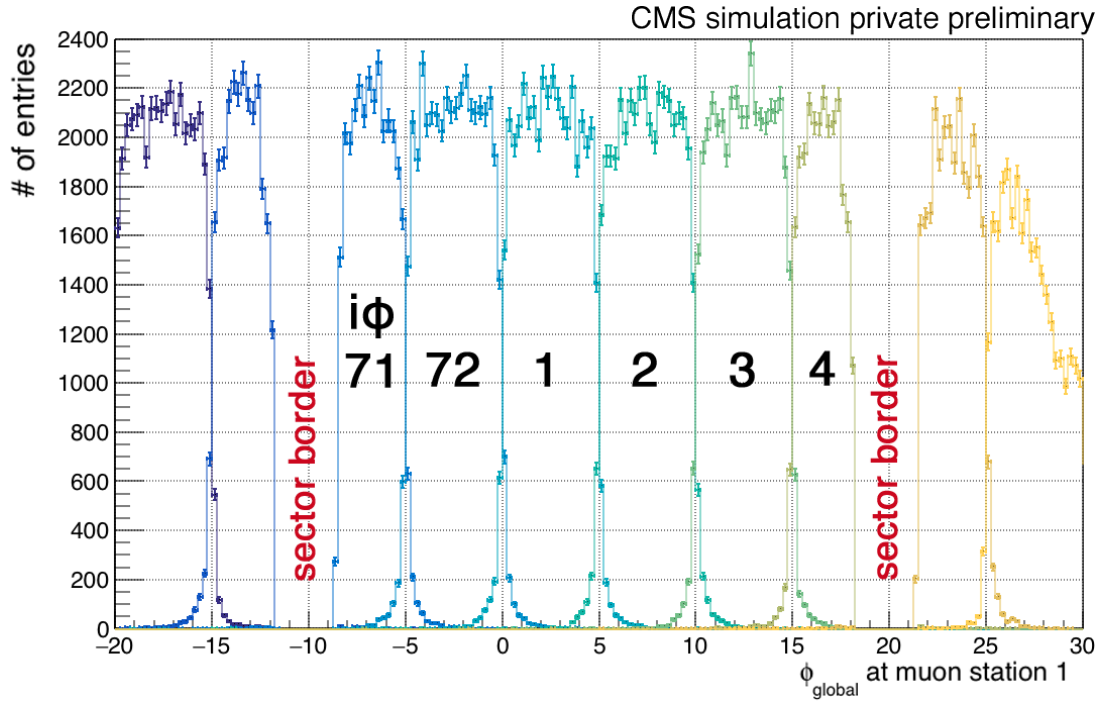

Figure 5.25: Histograms of the ϕ_{global} position measured at DT muon station 1 in the case that an HO tile at a certain iϕ position is the tile with the highest energy. In the overlap region between the histograms a distinct assignment of a ϕ_{global} position to an HO iϕ position is impossible.

magnetic field is given in table 5.6a. The resulting matching efficiency is also shown in table 5.6a as a weighted mean from all six distributions.

The matching efficiency without any correction - thus taking the uncorrected ϕ_{global} variable for the match to the HO tile - is 92.04% ± 0.06% for a match from station 1 to HO. The uncertainty is a statistical uncertainty.

The matching efficiencies (DT MB station 1 → HO) of the best tested parameters for the linear and circular extrapolation of 93.64% ± 0.05% and 93.63% ± 0.05%, respectively, are comparable within the uncertainties. For simplicity reasons the linear extrapolation with an effective distance $a = 25$ cm has been chosen. Using the extrapolation the matching efficiency increases by 1.6 percentage points. The fact that the extrapolation does not have a huge impact arises from the fact that the muon station 1 is very close to the HO tiles. Additionally, the tracks of muons with high p_T ∼100 GeV are almost straight on the distances between muon station and HO as they have a track radius of O(100 m) (see formula 5.14).

For the matching of the muon track to HO at station 2, the extrapolation is tested with different parameters. The tested parameters and the resulting matching efficiencies are shown in table 5.6b.

The increase from 85.0% to 88.3% using the linear extrapolation method with an effective distance $a = 50$ cm between DT MB 2 and HO is larger than the achieved

Extrapolation type	distance $a = l - b$	Magnetic field B	matching efficiency
None	–	–	$\left(92.04^{+0.06}_{-0.06}\right)\%$
Circular	30 cm	1 T	$\left(93.36^{+0.05}_{-0.05}\right)\%$
Circular	20 cm	1 T	$\left(93.61^{+0.05}_{-0.05}\right)\%$
Circular	10 cm	1 T	$\left(93.06^{+0.05}_{-0.05}\right)\%$
Circular	30 cm	2 T	$\left(93.36^{+0.05}_{-0.05}\right)\%$
Circular	20 cm	2 T	$\left(93.63^{+0.05}_{-0.05}\right)\%$
Linear	20 cm	–	$\left(93.61^{+0.05}_{-0.05}\right)\%$
Linear	25 cm	–	$\left(93.64^{+0.05}_{-0.05}\right)\%$
Linear	30 cm	–	$\left(93.40^{+0.05}_{-0.05}\right)\%$
Linear	35 cm	–	$\left(93.03^{+0.05}_{-0.05}\right)\%$
Linear	50 cm	–	$\left(91.21^{+0.06}_{-0.06}\right)\%$

(a) DT MB 1 to HO

Extrapolation type	distance $a = l - b$	Magnetic field B	matching efficiency
None	–	–	$\left(84.99^{+0.08}_{-0.08}\right)\%$
Circular	30 cm	1 T	$\left(87.26^{+0.07}_{-0.07}\right)\%$
Circular	20 cm	1 T	$\left(86.67^{+0.07}_{-0.07}\right)\%$
Circular	50 cm	0.5 T	$\left(82.45^{+0.08}_{-0.08}\right)\%$
Linear	30 cm	–	$\left(87.26^{+0.07}_{-0.07}\right)\%$
Linear	35 cm	–	$\left(87.48^{+0.07}_{-0.07}\right)\%$
Linear	50 cm	–	$\left(88.33^{+0.07}_{-0.07}\right)\%$
Linear	60 cm	–	$\left(83.47^{+0.08}_{-0.08}\right)\%$

(b) DT MB 2 to HO

Table 5.6: Tested effective values for distance a between muon station and HO as well as the magnetic field B for the extrapolation from muon station 1 and 2. The uncertainties are statistical uncertainties.

increase for the extrapolation from DT MB 1. This is reasonable keeping in mind that the deflection of the muon will be larger at DT MB 2. Therefore, a larger potential to increase the matching efficiency is present. The lower matching efficiency from MB 2 compared to MB 1 can also be explained by the larger distraction due to the larger distance.
The effective value for the distance $a = 50$ cm is smaller than the real distance of about 1 m in the detector.

Applying the linear extrapolation with an effective distance $a = 25$ cm (MB station 1) and $a = 50$ cm (MB station 2), defines the matching of the muon track to HO with DT TP data. This allows to use the HO MIP tag as confirmation of the DT TP data in order to distinguish noise and signal in the muon station.

5.4.5 Workflow of redundant L1 muon creation

Using the η and ϕ coordinates (see sections 5.4.1 and 5.4.2), the p_T assignment (see section 5.4.3), and the matching to HO (see section 5.4.4), a low quality type of L1 muon (called L1-HO muon) can be created that is helpful in the case of DT MB failure. The workflow on how to create this type of low-level L1 muons is described in this section. The description refers to the failure of DT MB 2. The workflow for the failure of DT MB 1 is similar except for the fact, that the information of the other remaining DT MB is used.
For each event, L1-HO muon candidates are created in the wheel and sector of the DT MB failure. It is not necessary to create L1-HO muons in other wheels or sectors, since the DT system works normally there.
In order to gain L1-HO muon candidates, the list of all DT TPs in the event is iterated. Only the DT TPs of the corresponding muon station 1 are used. If only a DT TP containing η information (θ DT TP) is available for the particular station, no L1-HO muon candidate will be created, because the availability of a DT TP with ϕ information is essential in order to determine a p_T value.
If a DT TP with ϕ information (ϕ DT TP) is present, at first a check is executed if a θ DT TP is also available for the station. If no θ DT TP is present, the η value of the L1-HO muon will be set to the center of the corresponding wheel.
If an θ DT TP is available, the η position is defined as described in section 5.4.1. Afterwards the ϕ and p_T values are also calculated from the ϕ DT TP as discussed.
In a next step, a quality value is assigned to the L1-HO muon candidates depending on the matching to HO. Therefore, the HO tile is calculated at which the muon passage is expected due to the extrapolation of the muon track (see section 5.4.4 for the matching). If the expected tile has an energy entry above the MIP threshold of 0.2 GeV, the quality is set to the maximum value 7. If the exact HO tile does not show an energy value above the threshold, the adjacent tiles in η are checked. If one of these two tiles has a sufficient energy value, the quality of the L1-HO muon candidate is set to 6.
Only L1-HO muon candidates with a quality code of 6 or 7 are accepted in the further process in order to keep the number of resulting fake L1-HO muons as low as possible. Nonetheless, more qualities are available. They can be used to include more L1-HO muon candidates with a less precise matching in the algorithm. The other qualities are:

- If the HO tile with a measured energy > 0.2 GeV, that is closest to the expected HO tile, is at the correct iϕ but at a wrong iη with an iη value within the observed wheel, the quality is set to 5.

- If no η information is available but the expected ϕ matches to an HO MIP signal within the wheel, the quality is 4.
- If the expected η coincides with an HO signal but the iϕ is off by one, the quality is 3.
- If iη and iϕ differ by one each, the quality is 2.
- A quality of 1 is assigned to L1-HO muon candidates that are off by one iϕ and have an iη within the wheel.
- 0 quality is assigned to L1-HO muon candidates that do not have an iη assignment and have an iϕ assignment that is off by one iϕ.

A sample distribution of the difference between the expected HO tile passage position of the muon and the next HO tile with an energy above 0.2 GeV is shown in figure 5.26. The corresponding qualities for each tile are also shown there.
As stated before, only the L1-HO muon candidates with a quality of 6 or 7 are accepted

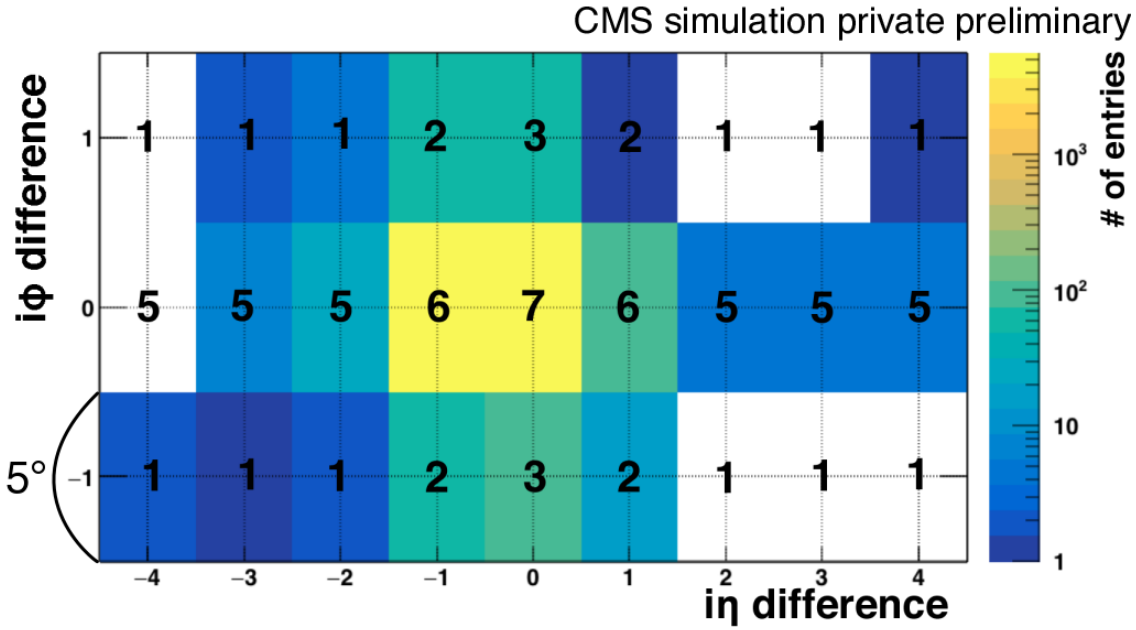

Figure 5.26: Difference between the position of the expected passage of the muon through HO and the nearest HO tile with a measured energy above the MIP threshold of 0.2 GeV. Half of the muons have a negative charge, the other half has a positive charge. The numbers within the plot represent the assigned qualities for the resulting L1-HO muon candidates. These quality values are only valid if the nearest HO tile with an energy above threshold is within the same wheel and sector as the expected passage point. Otherwise no L1-HO muon candidate is created.

as L1-HO muons. The nearest reconstructed muon in the event is matched to the L1-HO muon corresponding to the matching done for the DT MB station failure impact study ($\Delta R < 0.2$, $\delta p_T < 0.5$).
In events with L1 muon detection inefficiency, by definition, the reconstructed muon has a match to an L1 muon in the sample of the working detector but no match to an L1 muon in the sample of the failing DT MB station. The created L1-HO muon is then compared to the matched L1 muon from the sample of the working detector in terms of η, ϕ, and p_T. This will give information on the data quality of the L1-HO muons as well as on the recovery efficiency by comparing to the absolute number of lost L1 muons.
To determine the number of additional L1-HO muons that are introduced by fake L1-HO muons, also events without L1 muon inefficiency have been investigated. Here the number of L1-HO muons that are created and can not be matched to an L1 muon is registered (see section 5.5.3).

5.5 Recovery procedure results

Corresponding to the presented workflow in the section before, an analysis has been performed on how many of the muons that get lost due to DT MB failure (see sections 5.2 and 5.3) can be recovered using the information of the remaining DT MB 1/2 combined with HO.
The same dataset was used as in the DT station failure analysis (see section 5.3). The events in the dataset each contain a muon from a muon gun with a flat p_T spectrum ranging from 3 GeV – 200 GeV. Half of the muons from the muon gun carry a negative charge, half of the muons carry a positive charge. Additionally, 52 pile-up interactions are merged into each event in average. These pile-up interactions origin from a minimum bias sample. The trigger is the legacy trigger. As already stated, an almost flat p_T spectrum in the simulated range of the muon gun from 3 GeV $< p_T <$ 200 GeV is e.g. expected for a heavy *W'* boson decay [83]. The influence of a steeply falling transverse muon momentum spectrum on the recovery efficiency is discussed in section 5.5.2.

5.5.1 Recovery efficiency

At first the recovery efficiency of the presented approach is investigated. For the analysis of the introduced fake L1-HO muons please refer to section 5.5.3. The results for wheel 0 regarding station 1 or 2 failure are presented in detail. Special features for DT failures in wheel 1- and 2- are also discussed. For the remaining results, please refer to the appendix.

5.5.1.1 Wheel 0

Station 2 Failure The position of the reconstructed muons corresponding to the recovered additional missing L1 muons due to failure of DT MB 2 in wheel 0 are shown

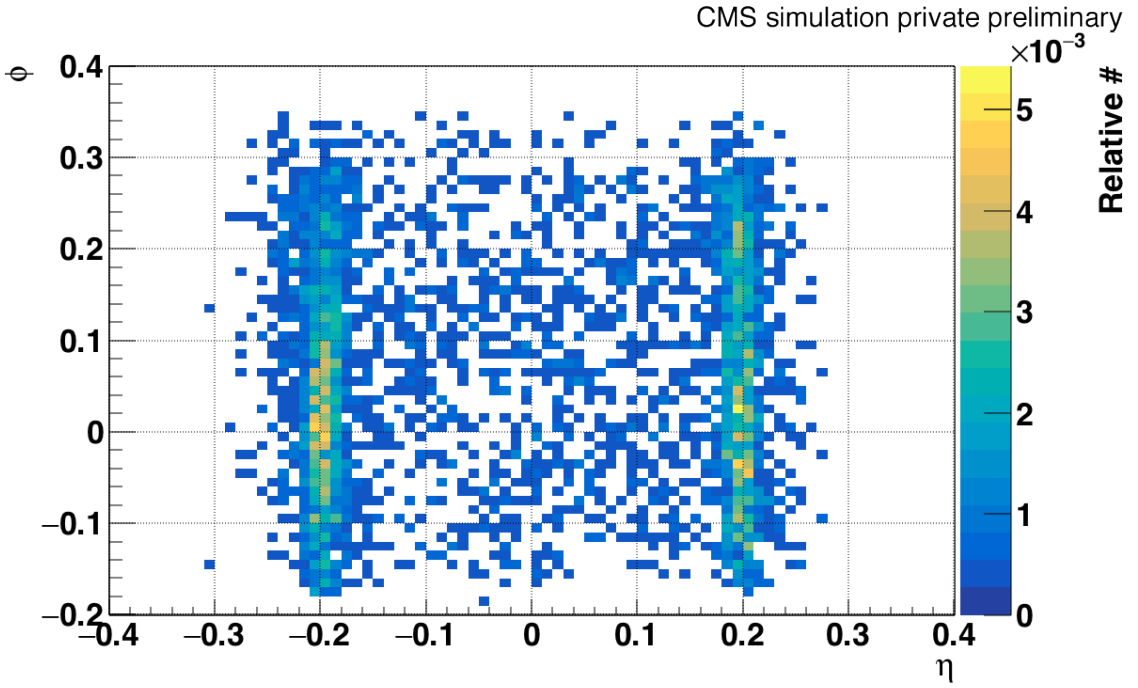

Figure 5.27: Reconstructed η-ϕ coordinates of the position of all reconstructed muons, that are matched to an L1-HO muon. The muons are not detected in case of DT MB 2 failure in wheel 0, but are recovered as L1-HO muon.

in figure 5.27.

Obviously, most recoveries are made in the region of the wheel gaps. Within the remaining area of wheel 0 the recovered L1-HO muons seem to be equally distributed. (34.4±0.6) % of the additional missing L1 muons due to MB station 2 failure can be recovered with the method described in the sections before. If no MIP tag was requested (36.4 ± 0.6) % of the additional missing L1 muons would be recovered. Anyway, it is not recommended to use no MIP tag, as it introduces many fake L1-HO muons. This will be discussed later in section 5.5.3.

Due to the asymmetric detector setup in the ϕ-projection (see figure 5.9a), only 30.9 % of the additional missing L1 muons are observed in the sample including a μ^+ gun. The part of the sample including a μ^- gun contains 69.1 % of the additionally missing L1 muons. Both sub-samples have the same size of 1 million events. The absolute numbers are summarized in table 5.7.

The absolute number of recovered L1-HO muons is nearly the same in the sub-sample with the μ^+ gun and in the sub-sample with the μ^- gun. The L1-HO muon recovery does not prefer any muon charge since the setup of a single muon station and the HO tiles is symmetric in ϕ. The algorithm results in a recovery rate of (53.7 ± 1.3) % for the μ^+ gun sub-sample and (25.7 ± 0.6) % for the μ^- sub-sample.

In order to determine the precision of the recovery, the correlation between the ϕ and η-coordinates of the matched reconstructed muon and the recovered L1-HO muon is investigated. The correlation plots are shown in figure 5.28.

Sample	No. of failures	No. of recoveries	Recoveries / %
μ^+	3220	1730	53.7 ± 1.3
μ^-	7206	1852	25.7 ± 0.6
full	10426	3582	34.4 ± 0.6

Table 5.7: Absolute and relative numbers for the recovery of inefficiencies due to a failure of DT MB station 2 in wheel 0.

The ϕ-correlation (see figure 5.28a) obtains a good recovery of the ϕ-coordinate. The correlation factor

$$\rho(\phi_{\mathrm{L1}}, \phi_{\mathrm{RECO}}) = \frac{\sum_{i=1}^{n} \left(\phi_{\mathrm{L1}i} - \overline{\phi_{\mathrm{L1}}}\right)\left(\phi_{\mathrm{RECO}i} - \overline{\phi_{\mathrm{RECO}}}\right)}{\sqrt{\sum_{i=1}^{n} \left(\phi_{\mathrm{L1}i} - \overline{\phi_{\mathrm{L1}}}\right)^2 \cdot \sum_{i=1}^{n} \left(\phi_{\mathrm{RECO}i} - \overline{\phi_{\mathrm{RECO}}}\right)^2}} \tag{5.16}$$

with the coordinate of the recovered L1-HO muon ϕ_{L1} and the coordinate of the corresponding reconstructed muon ϕ_{RECO} is 0.93. Thus, the correlation is very good.
The correlation for the ϕ-coordinate is plausible since the entrance position of the muon in MB station 1 can be measured precisely.

The correlation of the η-coordinate (see figure 5.28b) shows a very coarse binning for the L1-HO muon's η coordinate. As described before, the η-coordinate, though also measured quite precisely, is only available as data binned by seven divisions in the L1 trigger. Besides of this, the correlation of the η-coordinates is also very good. Furthermore, the binning of the η-coordinates from MB 1 information ($\Delta\eta = 0.93$) is only twice as large as the normal L1 η binning ($\Delta\eta = 0.44$).

Due to the applied p_T thresholds in the L1 trigger, the measurement of the muon momentum is even more crucial than the muon coordinates. The procedure was described in section 5.4.3. The resulting correlation plot comparing the recovered L1-HO muon p_T and the p_T of the lost L1 muon is shown in figure 5.29. This plot allows to draw direct conclusions about the L1 trigger rate since the trigger rate is depending on the p_T thresholds. A plot of the correlation between p_T of the L1-HO muon and p_T of the corresponding reconstructed muon, that has the same structure, is shown in the appendix (figure 8).
The binning corresponds to the binning of the L1 p_T information. A correlation between the values can be observed. The bin with most entries is the upper right one for $p_T = 140$ GeV. Here many of the muons with a transverse momentum of 140 GeV $< p_T < 200$ GeV accumulate.
Assuming a trigger threshold of 20 GeV for the single muon trigger, a number of muons will not pass the trigger due to a mismeasured, too low momentum. These muons are located in the lower right red rectangle. In this sample 8.9 % of the recovered L1-HO muons will not exceed the trigger threshold although the original L1 muon, that is lost

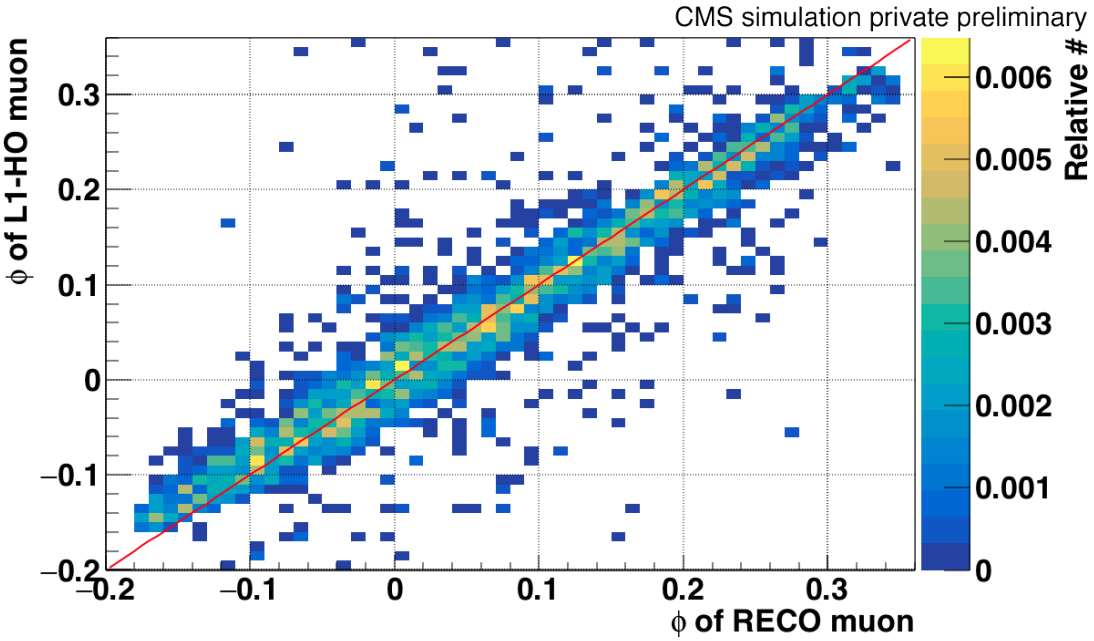

(a) ϕ correlation

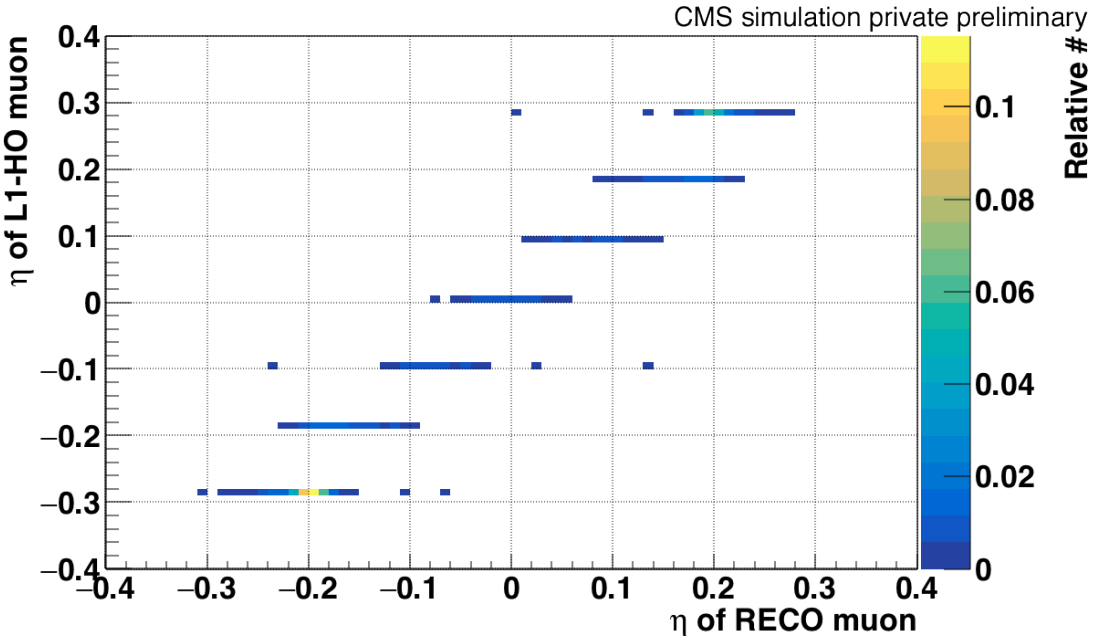

(b) η correlation

Figure 5.28: Correlation plots for the coordinates ϕ (top) and η (bottom) of the recovered L1-HO muon (coordinates from presented algorithm) and the corresponding matched reconstructed muon (reconstructed coordinates) for the failure of DT MB station 2 in wheel 0.

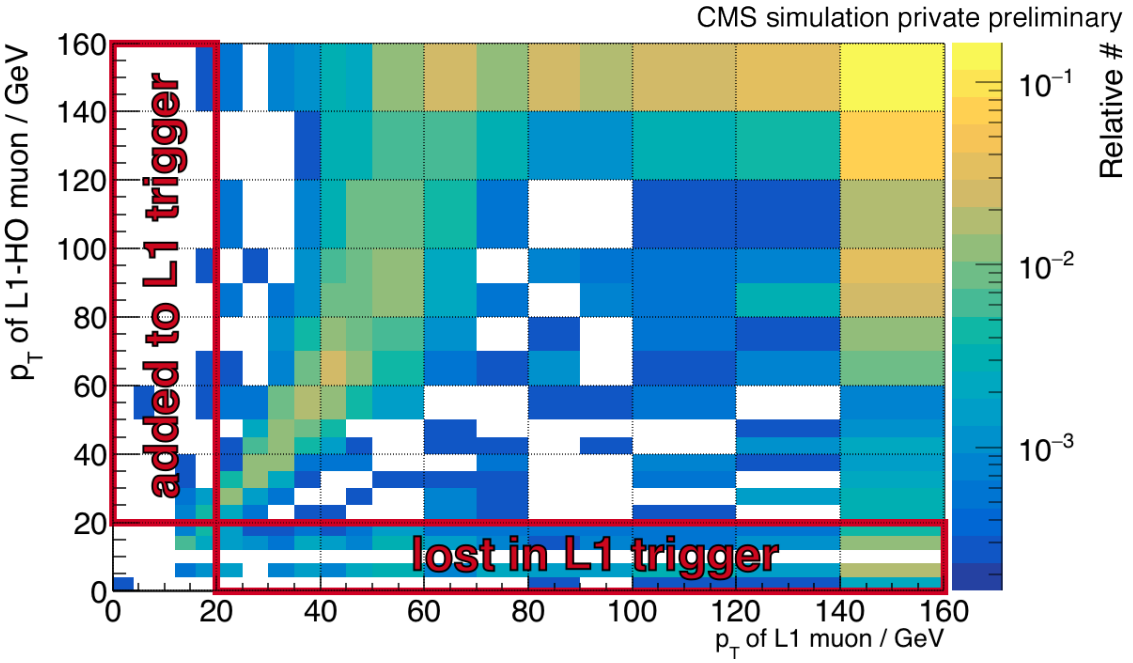

Figure 5.29: Correlation plot of the L1 transverse muon momentum p_T of the L1 muon from the sample with the fully working detector, that is not present in the sample with the detector failure of DT MB station 2 in wheel 0, and the transverse muon momentum of the corresponding matched L1-HO muon that is generated with the information of DT MB station 1 and HO as MIP tag. The binning corresponds to the p_T binning in L1. The bins above 140 GeV are overflow bins.

due to the detector failure, would have exceeded the threshold. Nonetheless, these muons do not have a problematic impact on the trigger, as they simply do not activate it. On the other hand, these muons can not be accounted for the number of recovered muons. The recovery efficiency thereby decreases to 31.2 %.
Also the implemented method assigns too high p_T values to a small number of muons. They are located in the upper left rectangle in figure 5.29. Here, the L1 trigger will give an L1 accept, although the original L1 muon would not have exceeded the trigger threshold. However, the number of 33 muons that fulfill this criterion (corresponding to 0.9 % of the recovered L1-HO muons) is well below of the number of lost L1 muons. Thus, these muons will not compromise the L1 trigger's capacity.

All in all the method can recover a significant number of L1 muons that get lost due to a DT MB station 2 failure. The position and transverse momentum estimate is sufficient. Furthermore, after an L1 accept the HLT will perform a much more precise track reconstruction using the information of the tracker allowing for a correction of the method's uncertainties.

Station 1 failure The L1 muon recovery in case of station 1 failure is expected to be strongly reduced compared to the recovery for station 2 failure. On the one hand, more L1 muons will be missing due to the failure of the most crucial station 1. On the other hand, the extrapolation of the track to HO and the p_T assignment are expected to be less accurate.

The positions of the reconstructed muons, that are assigned to the L1-HO muons, are shown in figure 5.30.
As for the recovery of L1 muons lost due to station 2 failure, most L1-HO muons are at

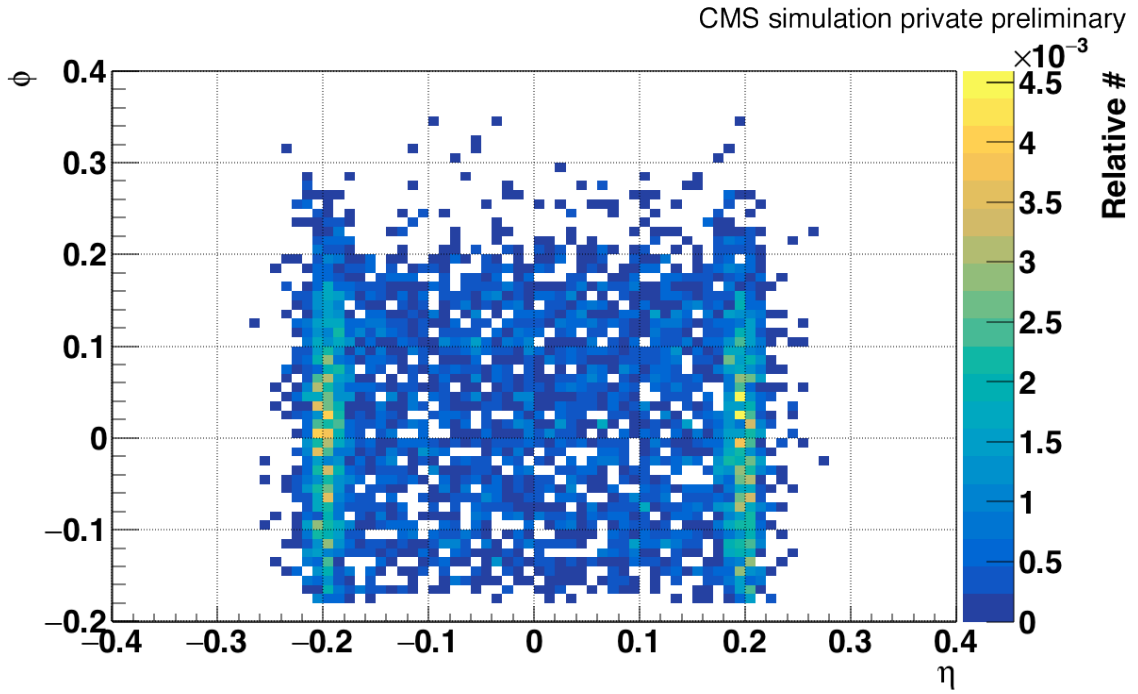

Figure 5.30: η-ϕ coordinates of the position of the reconstructed muon that is matched to an L1 muon. The muon is not detected in case of DT MB 1 failure in wheel 0 but has been recovered as L1-HO muon.

the position of the wheel gaps. In addition to that, the remaining recovered L1 muons are equally distributed within wheel 0.
Compared to the failure of station 2 the positions of the recovered L1 muons are now shifted to lower ϕ values. This is due to the fact that DT MB station 2 is positioned at smaller ϕ coordinates.

The resulting ϕ and η coordinate correlations between the recovered position and the matched L1-HO muon position are shown in figure 5.31.
The distribution for the ϕ coordinates still shows a correlation (see figure 5.31a). However, the distribution is much more smeared compared to the distribution for the recovery of DT MB 2 failures (figure 5.28a). The position measurement itself in station 2 is as accurate as in station 1. But the correction of the position due to the bending

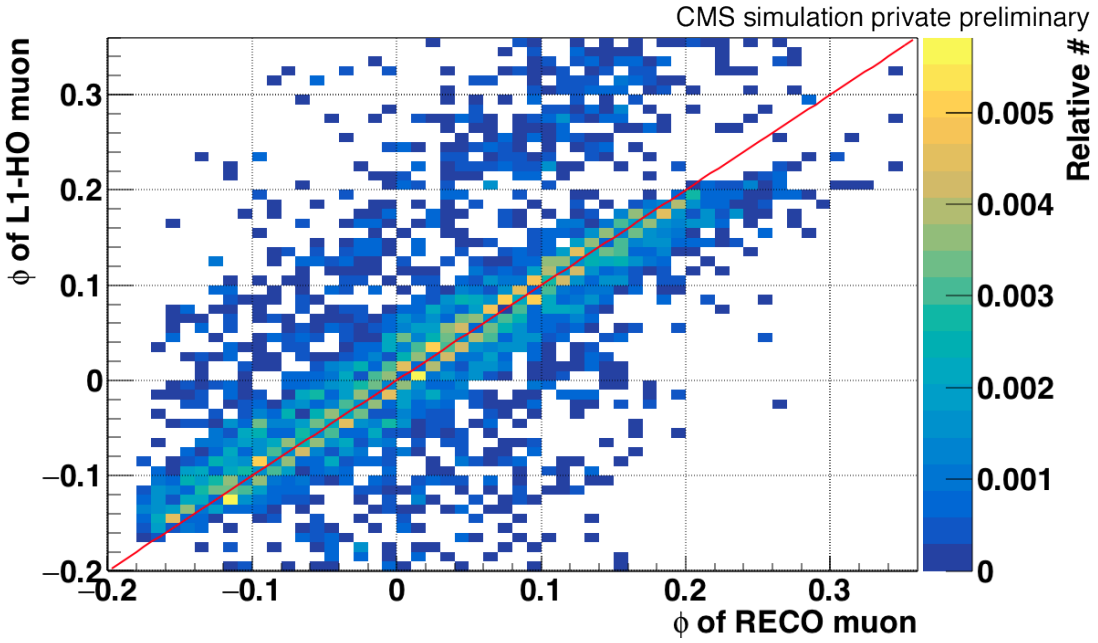

(a) ϕ correlation

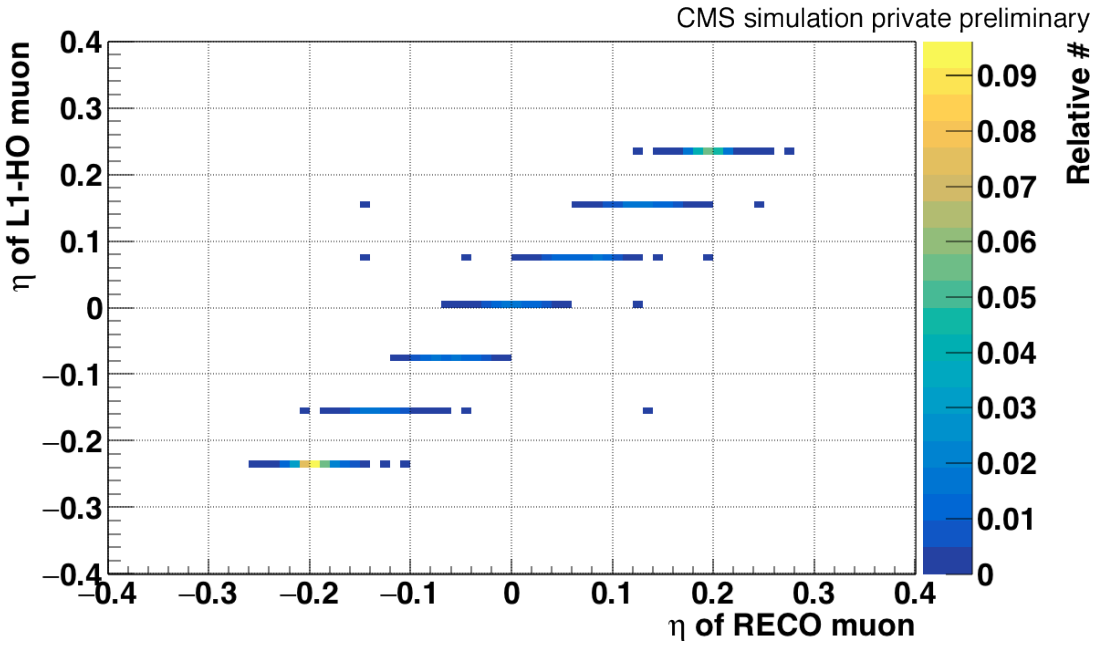

(b) η correlation

Figure 5.31: Correlation plots for the coordinates ϕ (top) and η (bottom) of the recovered L1-HO muon (coordinates from presented algorithm) and the corresponding matched reconstructed muon (reconstructed coordinates) for the failure of DT MB station 1 in wheel 0.

includes the worse bending angle measurement at this station. The correlation factor (see formula 5.16) is

$$\rho(\phi_{\mathrm{L1}}, \phi_{\mathrm{RECO}}) \approx 0.73 \tag{5.17}$$

which reveals the expected reduced correlation due to the smaller bending angles in station 2 and the resulting smaller p_T-resolution.
Still, the η correlation (see figure 5.31b) seems to be fine besides the constraints due to the poor binning of the η values discussed in the paragraph before.

The determination quality of the p_T values is revealed in the corresponding correlation plot in figure 5.32.
As expected, the p_T correlation is broader than for station 1 information. Especially,

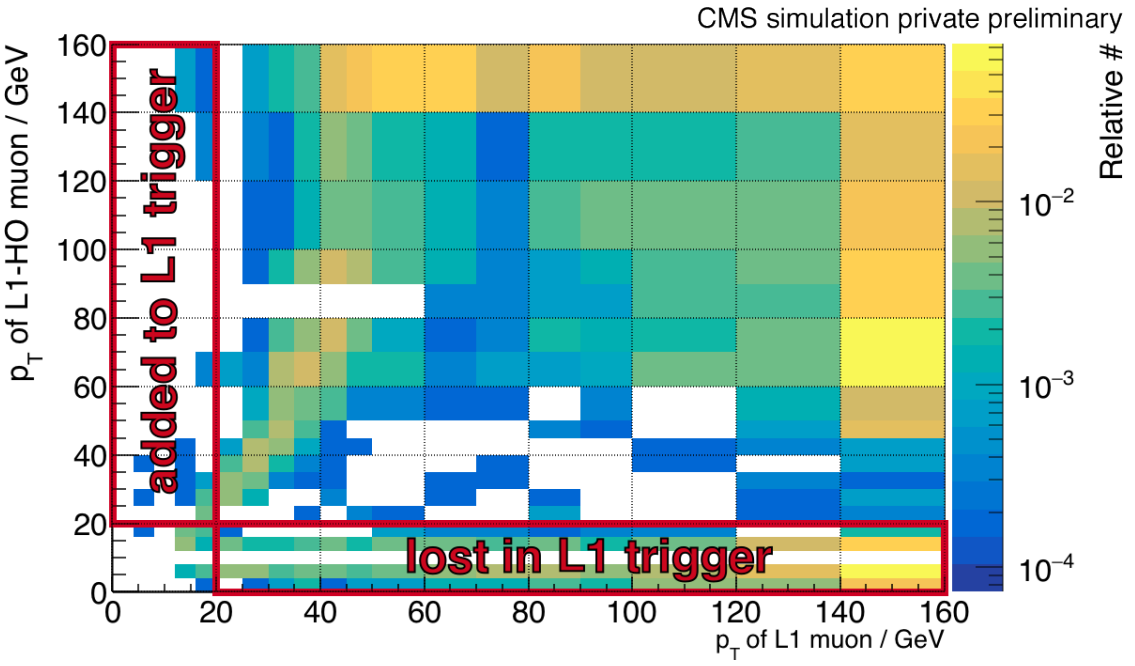

Figure 5.32: Correlation plot of the L1 transverse muon momentum p_T of the L1 muon from the sample with the fully working detector, that is not present in the sample with the detector failure of DT MB station 1 in wheel 0, and the transverse muon momentum of the corresponding matched L1-HO muon that is generated with the information of DT MB station 2 and HO as MIP tag. The binning corresponds to the p_T binning in L1. The bins above 140 GeV are overflow bins.

many muons are detected as low energy muons. This is also reflected in the number of L1-HO muons that do not account for a 20 GeV single muon trigger although they should due to the momentum value of the original L1 muon. In this sample 25.7 % of the L1-HO muons do fulfill this criterion.
The fraction of L1-HO muons falsely exceeding the trigger threshold is 1.0 %.

Using the information of DT MB station 2 and the HO MIP tag, 14.4 % of the additional missing L1 muons can be recovered overall. 10.7 % of the muons are recovered. This value is corrected for the muons that have an assigned p_T value below 20 GeV.
A charge asymmetry is visible for recovery of the missing L1 muons due to DT MB 1 station failure, too. The sub-sample containing a μ^+ gun yields 13.0 % recovered L1-HO muons. The fraction of recovered L1-HO muons for the sub-sample containing the μ^- is 16.1 %. The absolute numbers are summarized in table 5.8.

As expected, the recovery using information of DT MB 2 is less accurate and effective

Sample	No. of failures	No. of recoveries	Recoveries / %
μ^+	18711	2438	13.0 ± 0.3
μ^-	15089	2426	16.1 ± 0.3
full	33800	4864	14.4 ± 0.2

Table 5.8: Absolute and relative numbers for the recovery of L1 muon detection inefficiencies, that are due to a failure of DT MB station 1 in wheel 0.

compared to the recovery using DT MB 1. The poor ϕ assignment accuracy and the broad p_T distribution question the application of this method in the L1 trigger for DT MB 1 failure.

5.5.1.2 Wheel 1-

The distributions for the η, ϕ, and p_T correlation for the recovery of the failure of DT MB station 1 or 2 in wheel 1- are similar to those of the corresponding stations in wheel 0. Therefore, the distributions are only shown in the appendix. In order to quantify the recovery capability of the described approach, the number of recovered L1-HO muons can be used. They are displayed in table 5.9b for the failure of station 2.
The relative number for the recovery of L1 muon detection inefficiencies caused by the failure of station 2 in wheel 1- is less compared to the number in the same station at wheel 0. Muon tracks traversing muon station 2 in wheel 0 will always traverse the station 1 layer outside a wheel gap in η. In wheel 1- the muons may traverse the muon station layer 1 in a wheel gap on their track to station 2. In these cases a recovery of L1 muons with station 1 is impossible.
The numbers for the failure of station 1 are shown in table 5.9a. The fraction of recovered L1 muons drops by a factor of four compared to the recovery in wheel 0. This can be attributed to the fact that the area of station 2, that can contribute to the recovery of L1 muons lost due to station 1 failure, is smaller compared to wheel 0. The muons, that can potentially be recovered, have to fulfill two criteria. On the one hand, they have to pass station 1 – otherwise no information would be missing and thus no L1 muon can get lost. On the other hand, they have to pass station 2. The η range at

Sample	No. of failures	No. of recoveries	Recoveries / %
μ^+	14131	304	2.2 ± 0.1
μ^-	13332	334	2.5 ± 0.1
full	27463	638	2.3 ± 0.1

(a) station 1 failure

Sample	No. of failures	No. of recoveries	Recoveries / %
μ^+	3859	970	25.1 ± 0.8
μ^-	6103	1069	17.5 ± 0.5
full	9962	2039	20.5 ± 0.5

(b) station 2 failure

Table 5.9: Absolute and relative numbers for the recovery of L1 muon detection inefficiencies, that are due to a failure of DT MB station 1 and 2 in wheel 1-.

which both criteria are fulfilled is smaller in wheel 1- than in wheel 0.

5.5.1.3 Wheel 2-

The number of recoveries using data of station 1 in wheel 2- is shown in table 5.10b. The fraction of L1 muons that can be recovered using data from DT MB station 1 in wheel 2- and the HO MIP tag is larger compared to those in wheel 0 and 1-. This is due to the fact that the station failure of a DT MB 2 has a higher impact on the resulting L1 muon inefficiency (see section 5.3.1.3). It is very likely that no information is available from station 3 and 4. Therefore, the combination of station 1 and 2 data is crucial. The loss of data in station 2 results in many muons that create good data in station 1 but are not created as L1 muons due to a mismatch in the overlap region between wheel and endcap. These muons can be recovered by the presented algorithm with a high quality due to the precise muon measurement in station 1.
The number of recoveries in case of station 1 failure is shown in table 5.10a. The number of recovered L1-HO muons is again smaller compared to those in wheel 1-. The same argument as for the decreased recovery capability in wheel 1- compared to wheel 0 holds. The area at which the muon passes station 1 and 2 is again smaller.

5.5.2 Influence of the muon momentum spectrum

The recovery procedure has been tested for events containing a single muon gun with a flat p_T spectrum ranging from 3 GeV to 200 GeV and 52 pile-up interactions in average.

Sample	No. of failures	No. of recoveries	Recoveries / %
μ^+	36616	432	1.2 ± 0.1
μ^-	41609	545	1.3 ± 0.1
full	78225	977	1.2 ± 0.1

(a) station 1 failure

Sample	No. of failures	No. of recoveries	Recoveries / %
μ^+	4863	2931	60.3 ± 1.1
μ^-	11322	3593	31.7 ± 0.6
full	16185	6524	40.3 ± 0.5

(b) station 2 failure

Table 5.10: Absolute and relative numbers for the recovery of L1 muon detection inefficiencies, that are due to a failure of DT MB station 1 and 2 in wheel 2-.

In order to determine the influence of a falling muon p_T spectrum on the recovery, the p_T correlation distribution for the recovery in case of a MB 2 station failure in wheel 0, sector 1 (see section 5.5.1.1) has been reweighed.
Therefore, a single muon p_T distribution was utilized that was created by the MUSiC group of the III. Physics Institute A, RWTH Aachen University [85]. The distribution contains the reconstructed p_T information of muons in events that

- were measured with a detector that was fully operational (certified good),
- that pass the single or double muon trigger of the HLT,
- are without fake missing transverse energy due to detector noise, cosmic rays, and beam-halo.

An integrated luminosity of 19.7 fb^{-1} from 2016 data was accounted for the distribution. For a more detailed description of the event selection refer to [86]. The spectrum of the used distribution is exponentially falling for transverse muon momenta up to 200 GeV and represents the muon spectrum that is expected from minimum bias events.
Using the p_T distribution, each entry in the p_T correlation plot has been reweighed. Therefore, the muon p_T of the reconstructed muon that is matched to the L1 muon in the sample of the working detector is used. The weight of an entry in the correlation plot is thereby the number of muons in the corresponding bin in the single muon p_T distribution. Thus, entries from muons with a lower p_T value have a larger weight than muons with a higher p_T value. The weight for transverse muon momenta below 30 GeV were extrapolated exponentially from the data points between 30 GeV –

200 GeV as the distribution shows a turn on feature below 30 GeV due to the applied cuts.

The resulting p_T correlation plot is shown in figure 5.33. As expected, the bin con-

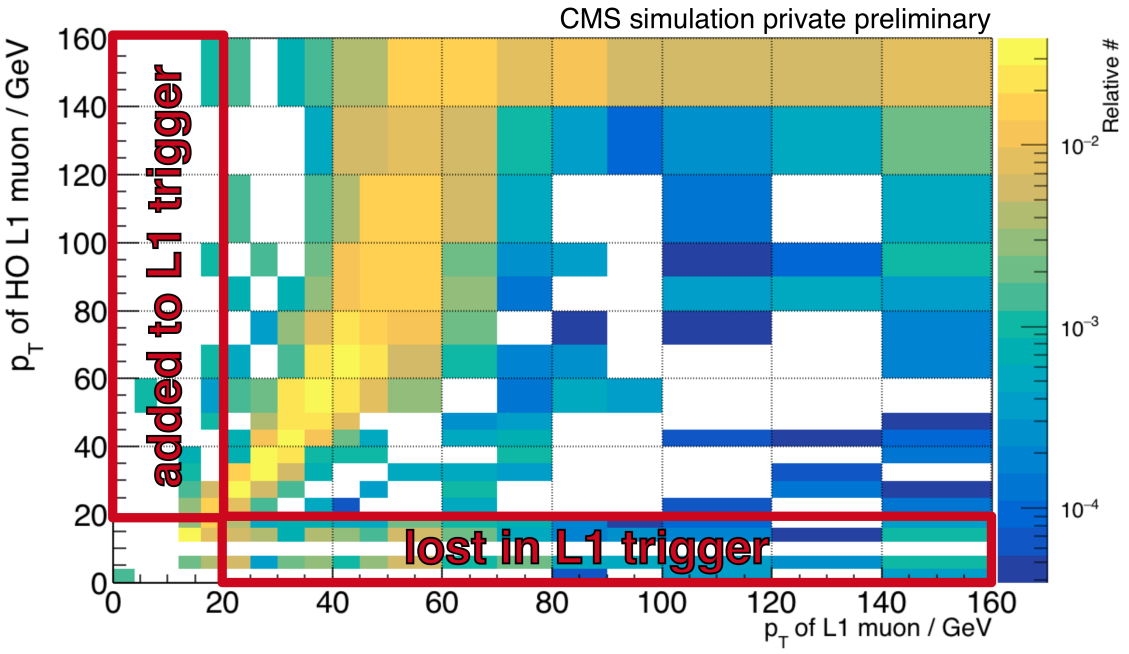

Figure 5.33: Correlation plot of the L1 transverse muon momentum p_T of the L1 muon from the sample with the fully working detector, that is not present in the sample with the detector failure of DT MB station 2 in wheel 0, and the transverse muon momentum of the corresponding matched L1-HO muon that is generated with the information of DT MB station 1 and HO as MIP tag. The binning corresponds to the p_T binning in L1. The bins above 140 GeV are overflow bins. The bins are reweighed following an exponentially falling muon p_T spectrum.

tent in lower p_T bins is much larger compared to the original distribution (see figure 5.29). On the one hand, the relative number of muons that are lost in the L1 trigger due to a measured p_T value below 20 GeV (lower right rectangle) is smaller (6.8 %) than the same number in the original distribution (8.9 %). This is mainly due to muons with a reconstructed $p_T > 140$ GeV that had an assigned HO-L1 transverse momentum of $p_T < 20$ GeV. As these muons are now less weighted, the fraction of recovered HO-L1 muons that will not exceed the trigger threshold although the original L1 muon, that is lost due to detector failure, would have exceeded the threshold, is reduced.
On the other hand, the number of HO-L1 muons that exceed the trigger threshold of 20 GeV although the original L1 muon did not exceed it, is increased (3.3 %) compared to the original p_T correlation distribution (0.9 %). Anyhow, the changes in the presented relative numbers are small with respect to the drastic change of the muon mo-

mentum spectrum (flat/exponentially falling). Furthermore, the number of L1 muons that are lost in the L1 trigger due to mismeasurements is still well greater than the number of HO-L1 muons that are added to the L1 trigger due to a p_T mismeasurement.

5.5.3 Fake L1-HO muons

After the discussion of the recovery efficiency gained by the introduced algorithm, also the number of falsely created L1-HO muons has to be discussed. L1-HO muons generated by the algorithm, that can be matched

1. neither to a reconstructed muon
2. nor to an existing L1 muon

within the matching criteria applied in the recovery efficiency analysis ($\Delta R < 0.2$, $\delta p_T < 0.5$), are called fake L1-HO muons. These muons are created due to an arbitrary coincidence of a DT TP and an HO MIP signal or by muons that are undetected at L1 and in the reconstruction.
In order to analyze the impact of fake L1-HO muons on the L1 trigger occupancy, the p_T distribution of the fake L1-HO muons created in the samples, that are used for the redundancy studies presented in this chapter, is investigated. The p_T distribution of the fake L1-HO muons generated during the L1 muon recovery in wheel 0 based on DT MB station 1 data is shown in figure 5.34.
The algorithm additionally introduces $3.8 \cdot 10^{-4}$ fake L1-HO muons per event on average at station 1 in wheel 0. Assuming a single muon trigger threshold of 20 GeV, only 5.5 % of these fake L1-HO muons will pass the threshold and therefore create an L1 accept. Even with a trigger threshold of 10 GeV only 11.9 % of the fake L1-HO muons exceed the trigger threshold. Compared to the muons, that can not be recovered, the number of fake L1-HO muons is small (11.0 %). These numbers translate into an additional trigger rate of 0.8 kHz for an assumed trigger threshold of 20 GeV. Though the additional rate is not negligible, the additional rate can be compensated for by reducing bandwidth from other triggers as the overall L1 trigger rate is O(100 kHz). This tradeoff is of course only acceptable in case of a failure scenario.
If no HO MIP tag was requested in order to create a L1-HO muon, the algorithm would introduce $7.4 \cdot 10^{-4}$ fake L1-HO muons per event on average at station 1 in wheel 0. 9.4 % of these fake L1-HO muons would exceed a 20 GeV trigger threshold resulting in an additional L1 trigger rate of 2.8 kHz (see figure 15 in the appendix for the corresponding distribution). Consequently, the use of HO for MIP identification is strongly encouraged in the L1-HO muon creation algorithm.
The number of fake L1-HO muons in case of DT MB station 1 failure in wheel 0 is even smaller. $1.5 \cdot 10^{-4}$ fake L1-HO muons are created per event on average of which 15.5 % pass a 20 GeV trigger threshold. The fraction of L1-HO muons that are created due to a muon that is undetected in L1 and in the reconstruction will be smaller, due to the less accurate matching of the muon track between the muon station and HO, leading

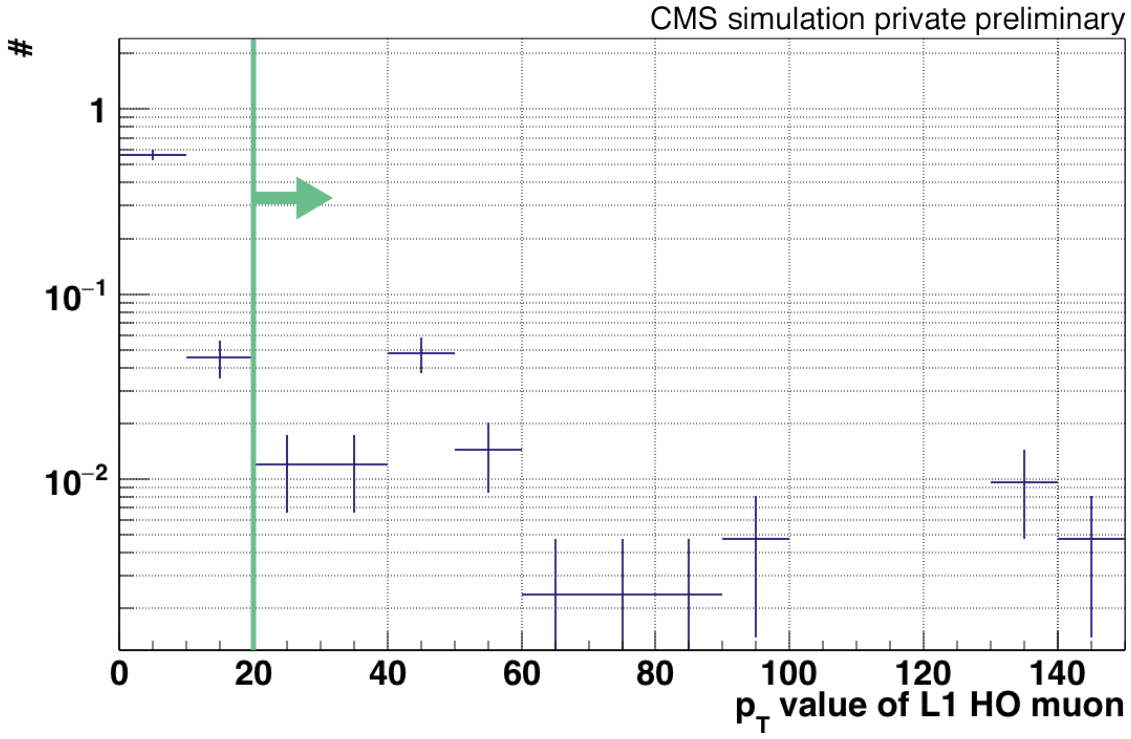

Figure 5.34: Relative p_T distribution of fake L1-HO muons. The green line shows a single muon trigger threshold of 20 GeV. The fake L1-HO muons are created during the recovery procedure of L1 muons that are lost due to a failure of station 2 in sector 1 in wheel 0.

to a smaller number of fake L1-HO muons.
The p_T distributions of the fake L1-HO muons for station 2 failure in the wheels 1- and 2- are shown in figure 5.35.
The p_T distributions of the fake L1-HO muons in wheel 1- and 2- show a similar behavior as in wheel 0. However, the absolute number of fake L1-HO muons is slightly larger. In wheel 1- in $4.3 \cdot 10^{-4}$ of the events a fake L1-HO muon is created (13.2 % passing a 20 GeV threshold). The algorithm generates fake L1-HO muons in $4.1 \cdot 10^{-4}$ of the events (2.7 % passing a 20 GeV threshold) in wheel 2-.
The HO system has a higher occupancy in the wheels 1- and 2- compared to wheel 0. Therefore, a coincidence between a DT TP and an HO TP is more likely. The number of fake L1-HO muons, that pass the muon trigger threshold of 20 GeV, is in the same order of magnitude in all wheels.
The absolute numbers of fake L1-HO muons is shown in table 5.11.

5.6 Single DT-wire failure

As described at the beginning of this chapter, also the degradation of single DT-wires has occurred and will also occur in future. Therefore, the impact of this single DT-wire

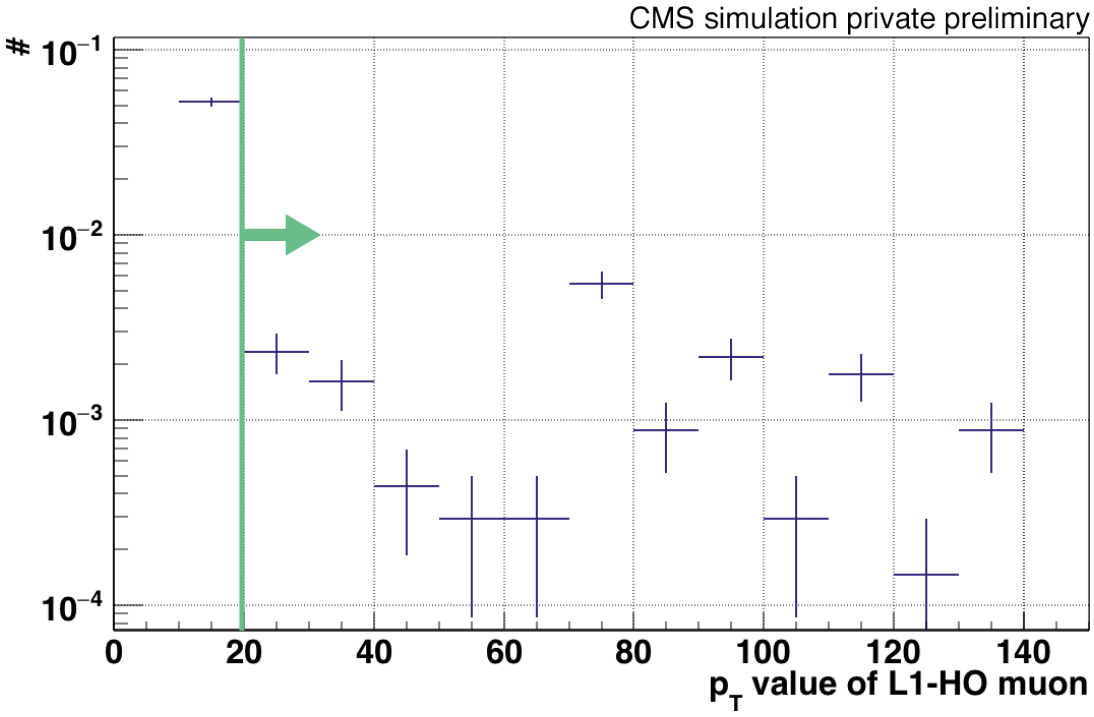

(a) Wheel 1-

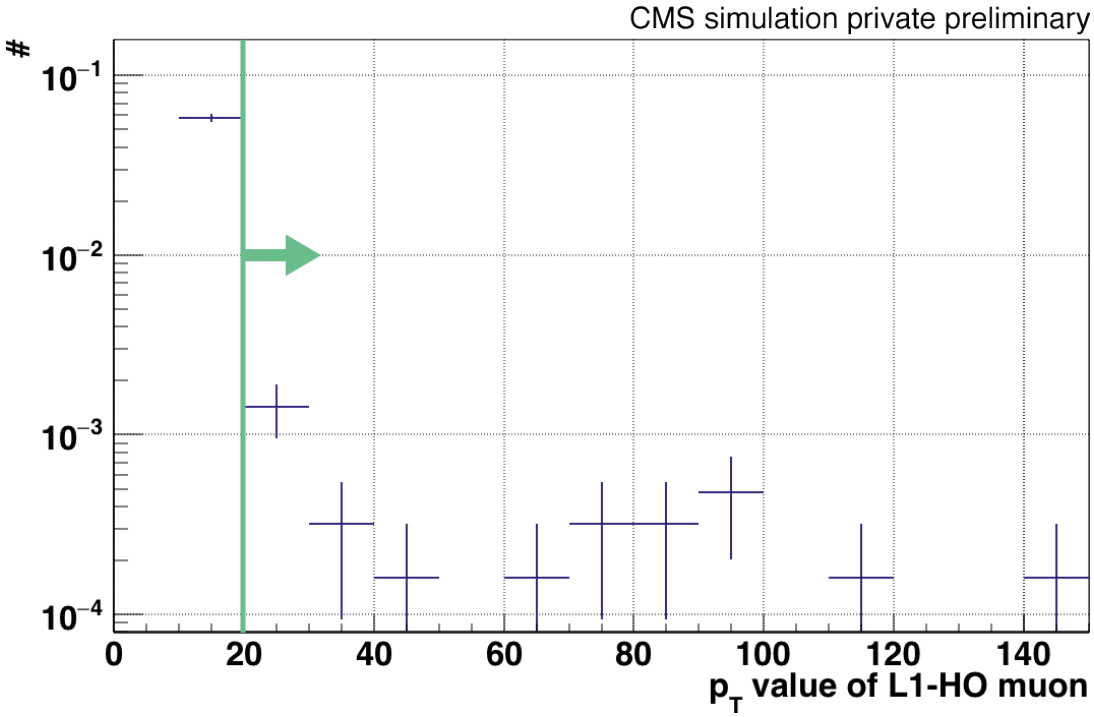

(b) Wheel 2-

Figure 5.35: Relative p_T distributions of fake L1-HO muons. The green line represents a single muon trigger threshold of 20 GeV. The fake L1-HO muons are created during the recovery of L1 muons that are lost due to a failure of station 2 in sector 1 in the wheels 1- and 2-.

Wheel	No. of fake L1-HO muons	
	overall	exceeding 20 GeV
0	756	42
1-	303	47
2-	856	113

Table 5.11: Number of fake HO-L1 muons in 2 million events per wheel each for DT MB station 2 failure.

failure was also analyzed. The analysis procedure is the same compared to the analysis of the DT station failure (see 5.2). The changed code is shown in in the appendix. The percentage of DT-wires that fail is individually fixed in each simulation sample. However, the particular failing wires are selected randomly for each event.
The used samples contain 24000 events each including a single muon-gun with a p_T range of 3 GeV to 200 GeV and 52 mean pile-up. The muon-gun covers the full ϕ range. In the η projection the gun points to $-0.8 < \eta < 0.8$ in order to cover the whole barrel region. The sample of the fully working detector contains 48389 L1 muons. The simulation uses the legacy trigger.
The resulting number of failing L1 muons due to failure of random DT-wires as a function of the amount of DT wires switched off is shown in figure 5.36.
Obviously, the failure of up to 10 % of the DT-wires is not crucial if they are randomly distributed. From these DT-wire failure rates on, the number of missing L1 muons increases significantly. The sharp rise ends at about 60 % failing DT-wires. At this point $\sim$ 21 % L1 muons are not detected anymore. These L1 muons correspond to the L1 muons that are detected by DT only. The DT system is inoperative at this fraction of failing wires. RPC detected L1 muons are still present. These numbers show the great redundancy of the DT and the RPC system in the L1 trigger that has been observed before [87]. Each subsystem is able to create L1 muons on its own. If both systems measure an L1 muon, the information can be used for a more precise measurement of the L1 muon.
Consequently, the introduction of the upgraded muon trigger will not change this behavior since the RPC system has to create the L1 muons on it self, if too many DT wires are inoperative.
Resultantly, the current failure rates of DT-wires are not a reason for concerns. Nevertheless, the high expected DT failure rates until LS 4 (18.8 % - 45.6 %, see also figure 5.1) will have an impact on the DT L1 muon triggering capability. This will be the case even if the RPC system would not show any degradation.
The use of HO or an HO like system in these cases is not analyzed in this thesis. Anyhow, the potential of such systems to compensate for those DT failures can be questioned. In case of single DT-wire failures, the information in all stations will be degraded. Therefore, a simple muon tag might not be sufficient to gain information for the η, ϕ, and p_T values of the muon.

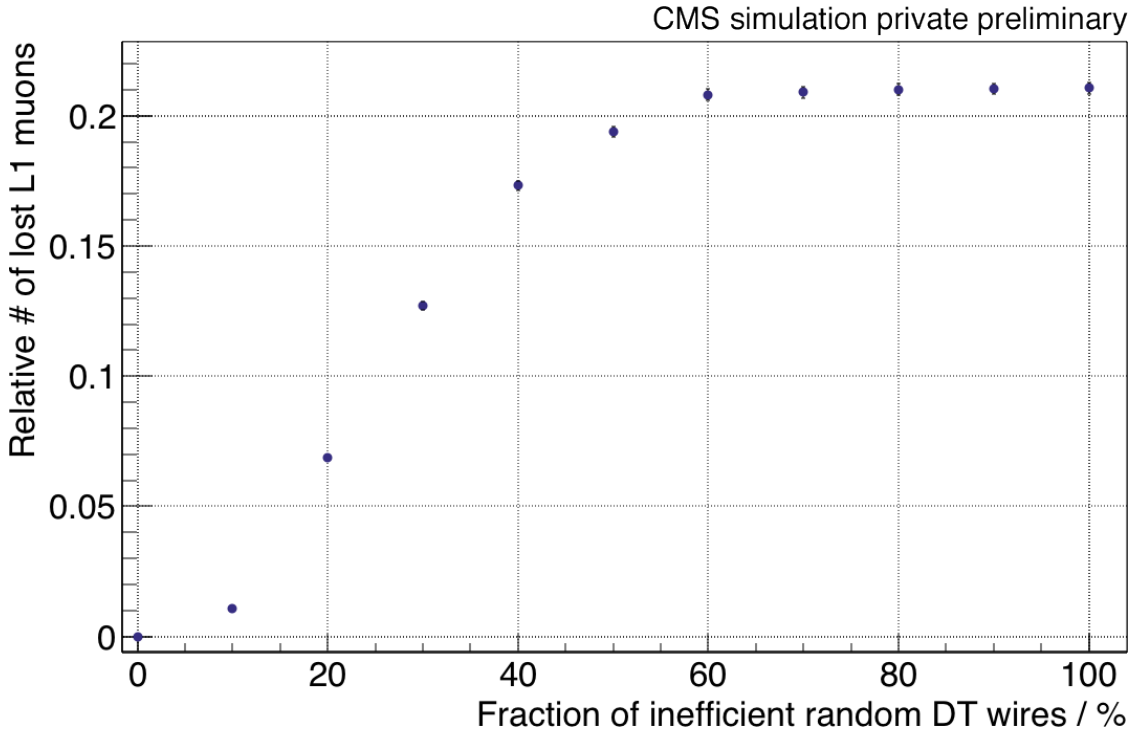

Figure 5.36: Number of L1 muons that are not created due to single DT-wire failure by the percentage of failing DT-wires. The relative number is normalized to the number of L1 muons that are created with a fully working DT and RPC system. The CSC system is not accounted for as the muons of the sample are only present in the barrel region.

Chapter 6

Efficiency Studies

The previous chapter concentrated on the efficiency losses in the L1 muon recognition due to detector failures. It was shown, that the combination of DT muon station 1 information and hadron outer calorimeter (HO) information can contribute to the L1 muon recognition in case of a detector failure. This redundancy potential is now investigated in this chapter with respect to muon measurement inefficiencies that are present in the fully operational detector. Therefore, the muon system efficiency to detect muons in the Level-1 trigger (L1) is investigated in this chapter. Particularly, the DT trigger primitive (TP) generation efficiency and the DT-track-finder (DTTF) efficiency are analyzed. The investigation utilizes the legacy trigger. However, the conclusions can also be drawn for the upgraded muon trigger since the combination of HO and DT without RPC is investigated.
The DT TPs are the information of a muon track (direction and bending angle) within a DT station. These are forwarded to the DTTF that combines the information of the four muon stations per sector and assigns a measurement quality, η, ϕ, and p_T values to the muon track (see also 2.2.6.1).
After the analysis of the efficiency drops within the detector geometry, the potential of the HO system to compensate for these inefficiencies together with the DT MB 1 stations is investigated.

6.1 HO in the DT muon trigger

The failure of parts of the muon system is an interesting field of application for the hadron outer calorimeter (HO) as redundancy system (see chapter 5). In addition, inefficiencies in the current, fully operational detector can yield a scope for HO usage. The muon system's inefficiencies originate from the structure of the detector. Espe-

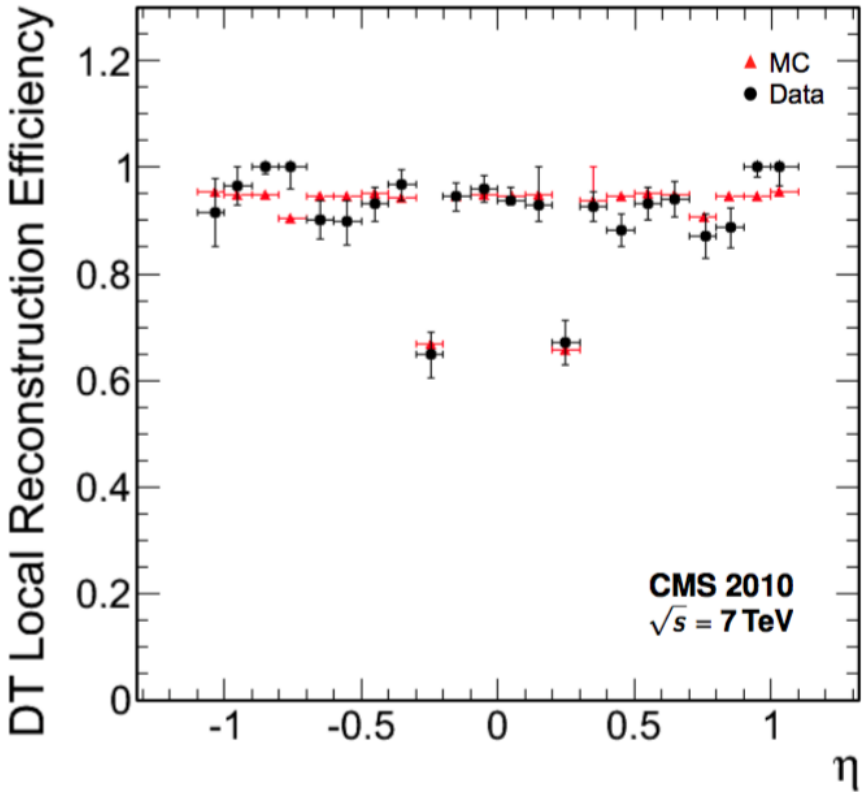

Figure 6.1: Simulated (MC) and measured DT local efficiency depending on the η position [39]. The local efficiency significantly drops at the wheel border between wheel 0 and 1±. The DT local efficiency was simulated and measured by filtering for events with a J/ψ or a Z boson decaying into muon pairs.

cially at the wheel borders the efficiency can drop. A plot of the local reconstruction efficiency of the DT muon system averaged over all 12 stations is shown in figure 6.1. The local reconstruction efficiency corresponds to the efficiency of the DT muon system to create a DT TP within a certain station.
The local reconstruction efficiency for the DT system is known to drop locally to 70 % within a 0.1 η bin [39] during the first LHC run. Besides these areas the local reconstruction efficiency is 95 %. The efficiency is expected to be similar during the second run. The efficiency drop occurs in the region of the wheel transition from wheel 0 to wheel 1±. Due to the fact that the HO system and the muon system have their unequipped wheel gaps at different positions in the η projection, HO can potentially provide redundancy in these cases.
The impact of the local reconstruction efficiency on the drift tube track finder (DTTF) and thus on an early stage of the L1 muon detection and the potential of HO to provide redundancy is investigated in this chapter.

6.2 DT efficiency analysis setup

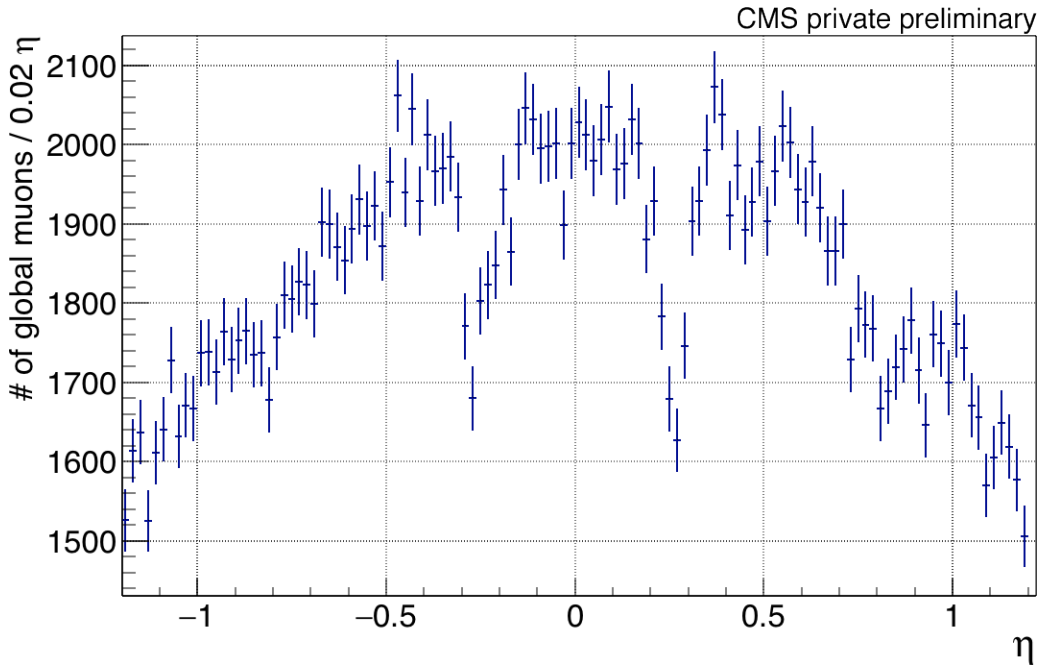

Figure 6.2: η distribution of all global muons with $p_T > 14$ GeV in the used $Z \to \mu\mu$ event sample. The local drop in the number of global muons at $\eta = \pm 0.3$ is due to the wheel border between the wheels 0 an 1±.

Since no artificial detector failure is investigated, the local efficiency decline of the DT system can be investigated using data.
In this analysis a subset from data taken in 2015 is used. The data events contain a $Z \to \mu\mu$ decay from the data taking period 2015D. The criteria for the $Z \to \mu\mu$ decay on the muons (μ_1, μ_2) are

$$M_{\text{inv}}(\mu_1, \mu_2) > 30 \text{ GeV} \tag{6.1}$$

with the invariant mass of the two muons $M_{\text{inv}}(\mu_1, \mu_2)$. One muon (called μ_1) has to fulfill the following criteria:

- Transverse muon momentum $p_T > 10$ GeV
- Pseudorapidity $\left|\eta_\mu\right| < 2.4$
- μ_1 has to be measured in the muon system as well as in the trigger system.
- The muon's track distance to the primary vertex has to be smaller than 2 cm.

The other muon (μ_2) only has to have a transverse momentum $p_T > 20$ GeV.
All muon combinations within an event are tested for the presented criteria. If a pair of muons fulfills the criteria, the event is selected as $Z \to \mu\mu$ event.

The preselected sample contains 2027225 events. CMSSW Vers. 7.4.14 was utilized for processing data using the global tag associated to the sample[1].
For each event only global muons with a $p_T > 14$ GeV are investigated to keep the impact of multiple scattering low and to get precise muon information. The η distribution of all investigated muons is shown in figure 6.2.
Obviously, there are enough muons passing the p_T criterion in every bin in order to perform a statistically significant analysis. The local drop in the number of global muons is related to the wheel borders between the wheels 0 and 1±.
As shown in chapter 5, only the information of muon station 1 is precise enough to yield information about the muon p_T. Therefore, the presented efficiencies always refer to efficiencies at muon station 2. Then, in case of an inefficiency in station 2, muon station 1 can still yield information.
A matching of the trigger data of the DT TPs, DTTF tracks and HO MIP tags ($E_{\text{meas.}} > 0.2$ GeV) as well as the reconstructed track segments[2] to the global muons is performed. The matching utilizes a matching cone of $\Delta R < 0.2$. The reconstructed track segment represents a track segment of three to four DT wires in a DT station that were crossed by a muon. Thus, if a reconstructed track segment can be matched to a reconstructed muon, the corresponding station was potentially able to detect the muon. Anyhow, this information can only be used offline.

6.2.1 DT TP efficiency analysis

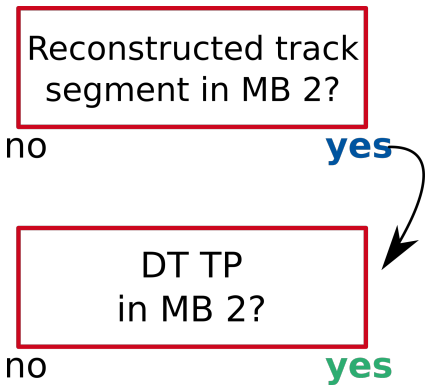

Figure 6.3: Decision path for the DT TP efficiency plot (see figure 6.4). Every muon track (reconstructed muon) is filtered by the decision path criteria. The number of tracks fulfilling the whole chain up to the green "yes" is normalized to the number of tracks that fulfill all criteria up to the blue "yes".

The efficiency is determined that a potentially measurable muon leads to a DT TP in station 2. The efficiency is calculated by normalizing the number of matched DT TPs at station 2 to the number of matched `DTRecSegment4D` at station 2 in each bin. A

[1] `74X_dataRun2_Prompt_v4`
[2] The data class of the reconstructed track segment is the `DTRecSegment4D`

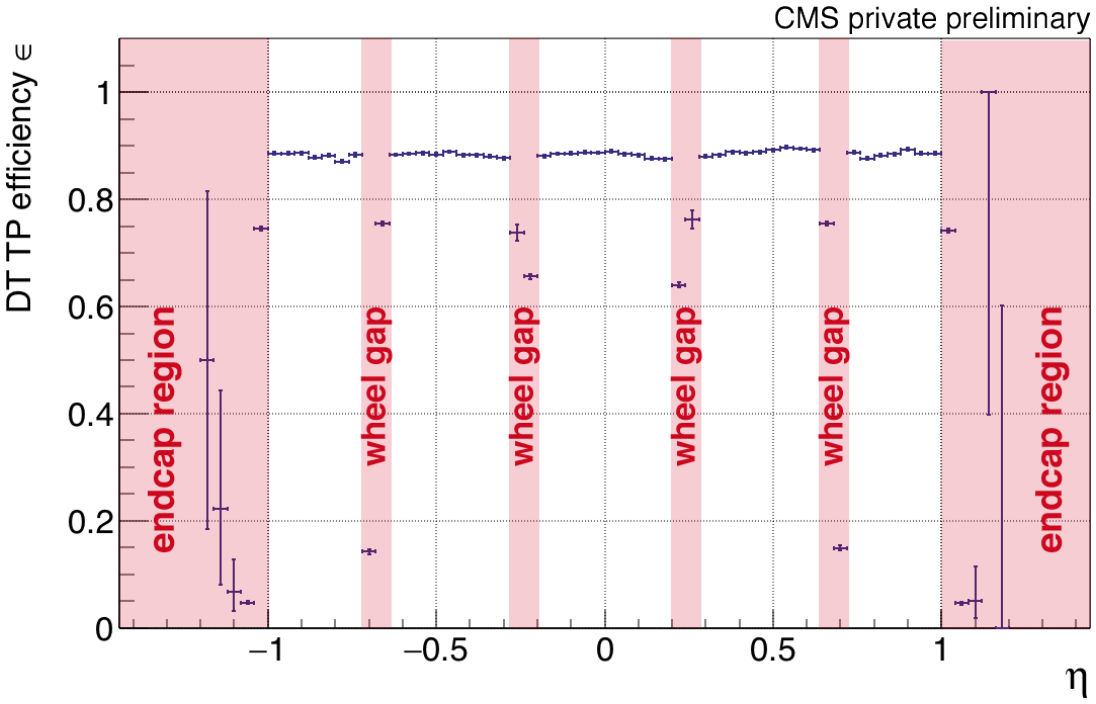

Figure 6.4: DT TP generation efficiency depending on the detector position in η in muon station 2. The efficiency is normalized to the number of available reconstructed track segments in each bin and is averaged over all 12 stations and μ^+, μ^-.

sketch of the underlying decision tree is shown in figure 6.3 and will be extended step by step in the next sections. The distribution is shown in figure 6.4. 698463 global muons passed the momentum cut and can be matched to a reconstructed track segment in station 2. The distribution is averaged over all 12 sectors and both signs of muon charge.

The distribution is symmetric towards $\eta = 0$ as it is expected due to the symmetric setup of the CMS detector. Within the wheels the DT TP generation efficiency is constant at the order of 90%. In the transition region between wheel 0 and 1± ($\eta \approx \pm 0.2$) the efficiency drops to 65%. This efficiency decrease is very sharp because the wheel gap is relatively small in the muon track's coordinate system. The gap for this track between wheels 1± and 2± is larger. This is reflected by the larger efficiency reduction at these positions ($\eta \approx \pm 0.7$) down to $\sim$ 15%. At the end of the barrel region ($\eta \approx \pm 1.1$) the efficiency also drops sharply due to the ending of the barrel muon detectors. No statistics is available for large absolute η values ($|\eta| > 1.1$).

The discussed distribution can be qualitatively compared to the distribution shown in the chapter's introduction 6.1, that shows the same behavior. However, the efficiency reduction between wheel 2± and 1± is not visible there. This is due to the larger binning in the introduction plot.

Please note that the investigated efficiency is a local efficiency of station 2. The ef-

ficiency to create a DTTF track and a L1 muon using DT data or DT and RPC data, respectively, is larger.

6.2.2 DTTF track efficiency analysis

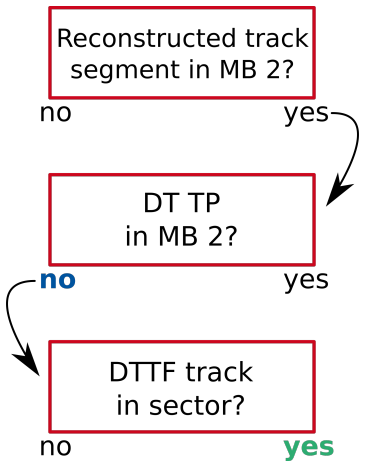

Figure 6.5: Decision path for the DTTF efficiency plot (see figure 6.6). Every muon track is filtered by the decision path criteria. The number of tracks fulfilling the whole chain up to the green "yes" is normalized to the number of tracks that fulfill all criteria up to the blue "no".

From the hardware point of view, the DT muon system generates the DT TPs inside the muon station in the experimental cavern. Therefore, in the current setup, a redundancy using HO cannot be built at this level of data. The created DT TPs are processed in the service cavern in order to create DTTF tracks. At this point, HO data can be combined with the DT data. Therefore, the DTTF efficiency has been investigated, too. The DT track finder (DTTF) combines the DT TPs of all four muon stations and creates DTTF tracks from them.
To analyze the DTTF, the tracks with a missing DT TP in station 2 are further processed. In this case the DT MB station 2 did not create a DT TP although it was fully operational. In order to determine if the missing DT TP in station 2 contributes to a missing DTTF track, the number of missing DT TPs in station 2 coinciding with a missing DTTF track is normalized to the number of reconstructed muon tracks with missing DT TP in station 2 (see figure 6.5). The resulting efficiency is shown in figure 6.6.
The DTTF efficiency in case of a missing DT TP in station 2 drops to $\sim$ 75% in the wheel gaps between wheel 0 and 1$\pm$. Moreover, the efficiency drop is broader in η compared to the DT TP efficiency (figure 6.4). This is due to the fact that the wheel gap of DT station 2 and the wheel gap of DT stations 1, 3, and 4, respectively are all at different η positions. The missing DT TP in station 2 is a prerequisite for this efficiency. However, another missing DT TP in one of the remaining three stations is very likely in order to lead to a missing DTTF track. Therefore, this area is broadened.

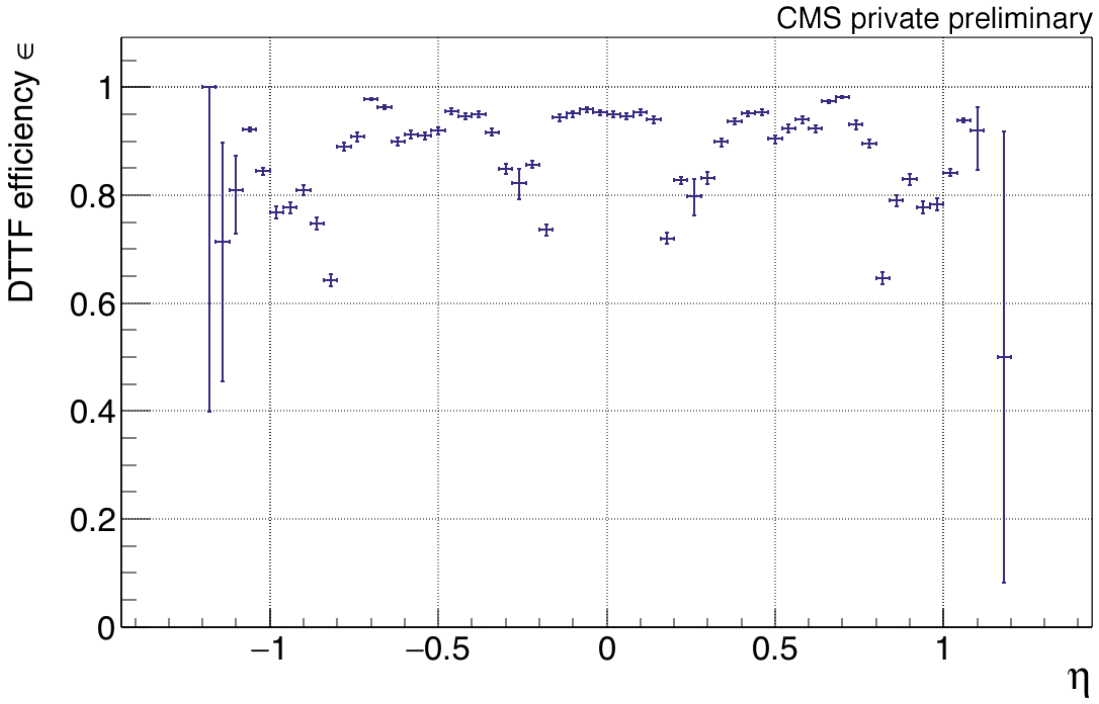

Figure 6.6: DTTF track generation efficiency depending on the detector position in η in station 2. The efficiency is normalized to the number of muon tracks with a missing DT TP in station 2 in each bin.

The potential of HO to reduce the efficiency drop of the DTTF in case of a missing DT TP in station 2 is investigated in the next section.

6.3 HO redundancy potential

The HO system's redundancy potential is investigated in two different scopes. In the first scope the redundancy potential of HO (or MTT) is investigated to recover DTTF tracks. As described before, this redundancy can be created with the current CMS setup since the DT TPs are generated in the experimental cavern and then forwarded to the service cavern. Here HO MIP data and DT TPs can be combined. The service cavern contains the trigger logic as well as the readout electronics that is not mounted on the detector directly. Other than the cavern that houses the CMS detector, the service cavern is always accessible.
The second scope is the DT TP generation redundancy. The CMS detector will receive major upgrades for the phase two runs in 2025. One of the upgrades is the transmission of DT timing information to the service cavern and the generation of TPs there. This will become possible due to the improvements of bandwidth in the optical data transmission achieved over the last years [53]. A DT TP generation in the service cavern allows for a combination of HO and DT timing information in order to create redundancy at the level of DT TP generation and thus before the DTTF.

6.3.1 DTTF track generation redundancy

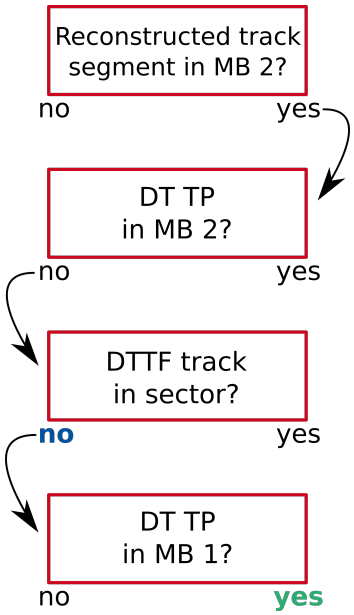

Figure 6.7: Decision tree for the plot of the local DT TP availability in MB 1 in case of a DTTF track and DT TP MB 2 (see figure 6.8). Every muon track is filtered by the decision tree criteria. The number of tracks fulfilling the whole chain up to the green "yes" is normalized to the number of tracks that fulfill all criteria up to the blue "no".

A reduction of the DTTF track efficiency has been shown in the previous section. In order to estimate the potential of HO to provide redundancy, the reconstructed muon tracks without a matched DTTF track have been investigated further.

6.3.1.1 DT TP in station 1

As already discussed in chapter 5 the muon system needs to provide DT TPs from station 1[3] that can be combined with an HO MIP tag. Therefore, it is first checked if a DT TP is present in station 1 in these cases. The frequency of occurrence is shown in figure 6.8. The number of reconstructed muon tracks that fulfill all criteria for the DTTF inefficiency and additionally have a valid DT TP in station 1 have been normalized to the number of muon tracks with missing DTTF and a missing DT TP in station 2 (see figure 6.7).
In most areas of the detector's barrel region in only 20% of the cases with a missing DTTF track and a missing DT TP in station 2 a DT TP in station 1 is available. However, the availability of a DT TP in station 1 is a prerequisite to use HO as backup system. The low frequency of occurrence can be explained with the fact that a DT TP in station 1 mostly will lead to a DTTF track even if no DT TP is present in station 2. If a DTTF

[3]In the presented discussion of an efficiency drop at station 2

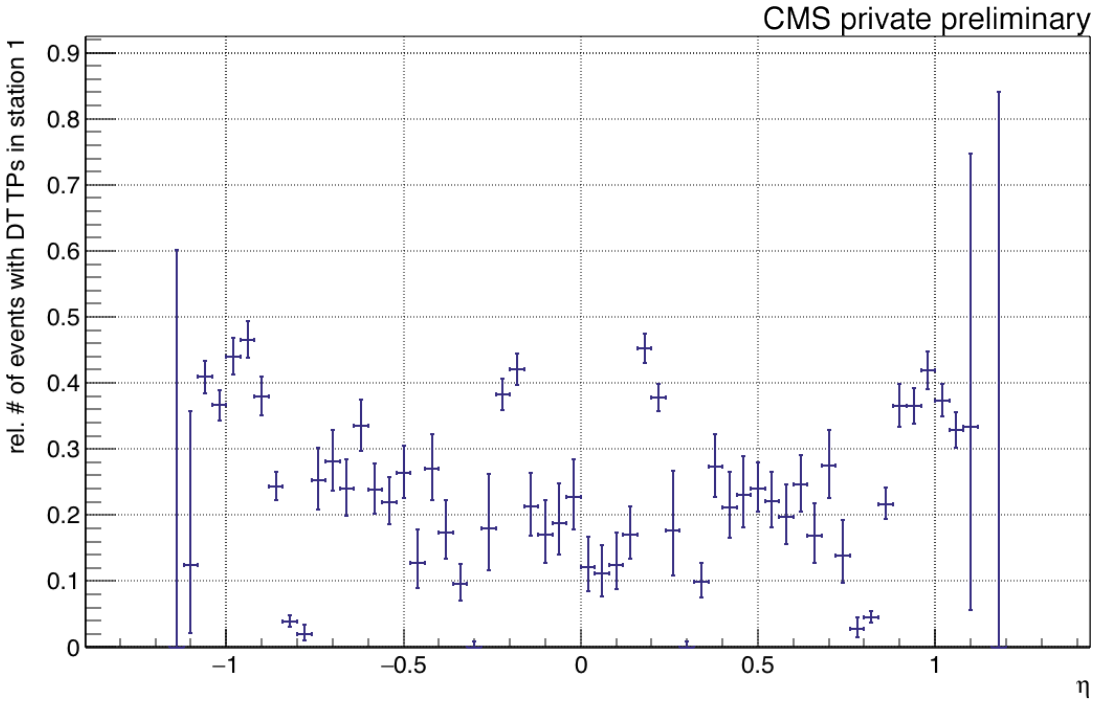

Figure 6.8: Local availability of a DT TP in station 1 in case of a missing DT TP in station 2 coinciding with a missing DTTF track. The number of available DT TPs in station 1 in case of a missing DT TP in station 2 coinciding with a missing DTTF track is normalized to the number of missing DTTF tracks coinciding with a missing DT TP in station 2 in each bin. This represents the upper limit of cases in which the HO system can provide redundancy.

track is present no backup system is needed.
Nonetheless, the frequency of occurrence is at O(40%) in the wheel gap regions between the wheel 0 and 1±.

6.3.1.2 HO MIP tag

The next prerequisite to provide redundancy is the existence of an HO MIP tag. In order to investigate the HO MIP tag, a MIP tag is required to be within a cone of $\Delta R < 0.2$ around the track of the investigated global muon. The HO MIP tag efficiency is shown for the case of a missing DTTF track coinciding with a missing DT TP in station 2 and a present DT TP from station 1 (referred to as recoverable track). The corresponding plot is shown in figure 6.10. The efficiency represents the fraction of valid HO MIP tags in case of a recoverable track (see also figure 6.9). The HO efficiency for recoverable tracks ϵ_{HO} is

$$\epsilon_{\mathrm{HO}} = \left(94.48^{+0.43}_{-0.40}\right)\ \%. \tag{6.2}$$

This value is larger than the geometrical coverage of HO [60] of

$$\epsilon_{\mathrm{HO,geometrical}} = (90.5 \pm 0.3)\ \%. \tag{6.3}$$

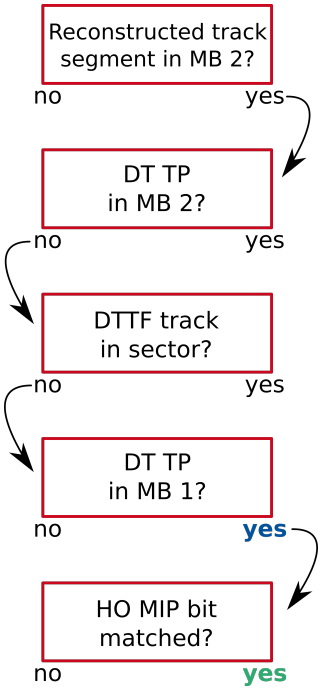

Figure 6.9: Decision path for the plot of the HO MIP tag efficiency in case of a recoverable event (see figure 6.10). Every muon track is filtered by the decision path criteria. The number of tracks fulfilling the whole chain up to the green "yes" is normalized to the number of tracks that fulfill all criteria up to the blue "yes".

This is plausible since the tracks that contribute to the HO efficiency for recoverable tracks contain a DT TP at station 1. Since DT muon station 1 and the HO system are placed very close to each other, the muon has a high probability to also create a MIP tag in the HO system.

6.3.1.3 DTTF HO redundancy

As the uncertainty bars indicate, the absolute number of muon tracks, that are classified as recoverable track, is low anyway. Only 3046 of the 698463 considered muons are marked as recoverable. This translates into

$$p_{\text{recoverable}} = (0.43 \pm 0.01)\ \% \tag{6.4}$$

of the muons that create a reconstructed track segment. Nonetheless, the HO can be matched to the DT TP in station 1 with a very high efficiency in these cases. The DTTF track efficiency is now shown considering that HO recovers all recoverable tracks that have a matched HO MIP tag in figure 6.11. As expected, the overall improvement is low. However, the DTTF efficiency can be improved from 70 % to 85 % in the wheel gap between wheel 0 and wheel 1±. If a link between HO and the DT TPs is established in

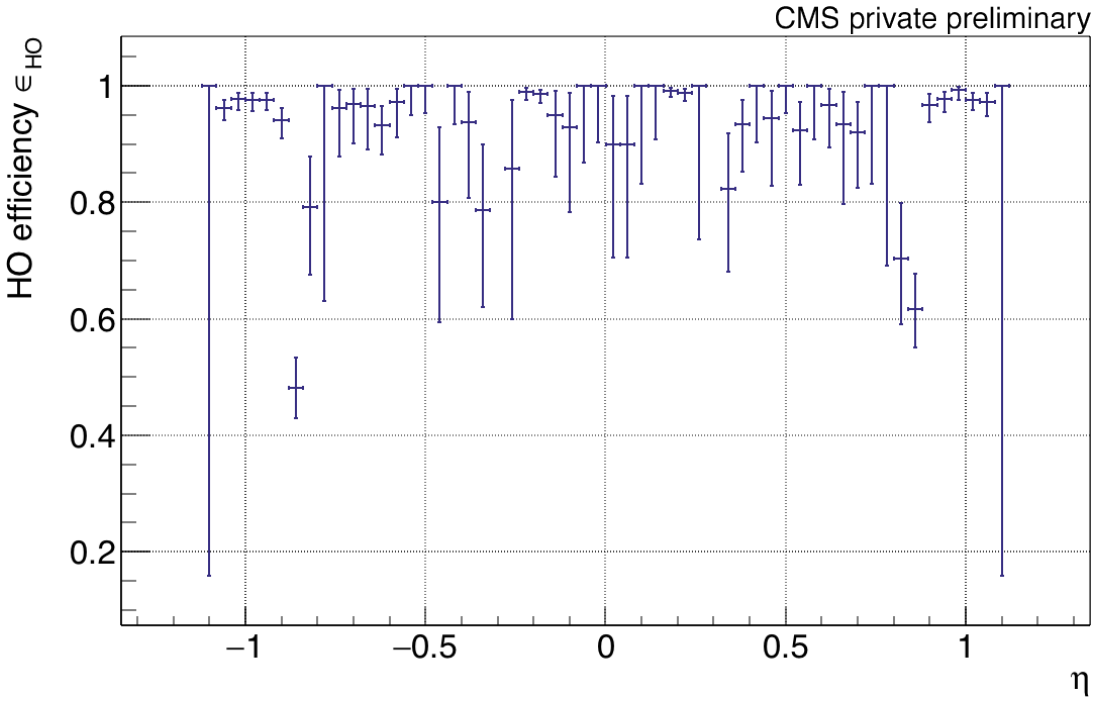

Figure 6.10: HO MIP tag efficiency for the case of DTTF track inefficiency coinciding with a DT TP station 2 inefficiency and a present DT TP from station 1 (recoverable event). An HO MIP tag accounts for the efficiency if it is present within a $\Delta R < 0.2$ around the reconstructed muon that is matched to the DT TP.

the service cavern, the HO can contribute to a better DTTF track generation efficiency, since it will not veto other muon data and therefore will not decrease efficiency.

6.3.2 DT TP generation redundancy

The DT TP generation will be done in the service cavern in phase 2 of the LHC running from 2025 on. Here the HO MIP information can be combined with the timing information of the DTs. This could allow to recover DT TPs that are not created due to a low quality in DT timing measurement. Assuming that the integration of HO MIP data would always recover the inefficient DT TPs, yields an upper threshold for the provided redundancy. The resulting efficiency is shown in figure 6.12. Therefore, the distribution of the DT TP efficiency in station 2 (see also figure 6.4) is used (labeled DT only). If an HO MIP tag is available in case of a DT TP inefficiency in station 2 the track accounts also for the combined efficiency (HO+DT).
The DT TP efficiency potentially increases from $\sim$ 90 % to $\sim$ 99 % by including the HO MIP tag into the DT TP generation. Especially, the combined HO+DT TP efficiency in the wheel gap regions is large due to the offset of the η positions of the HO system and muon station 2.
The exact technical design of such a combination of HO and DT timing data needs to

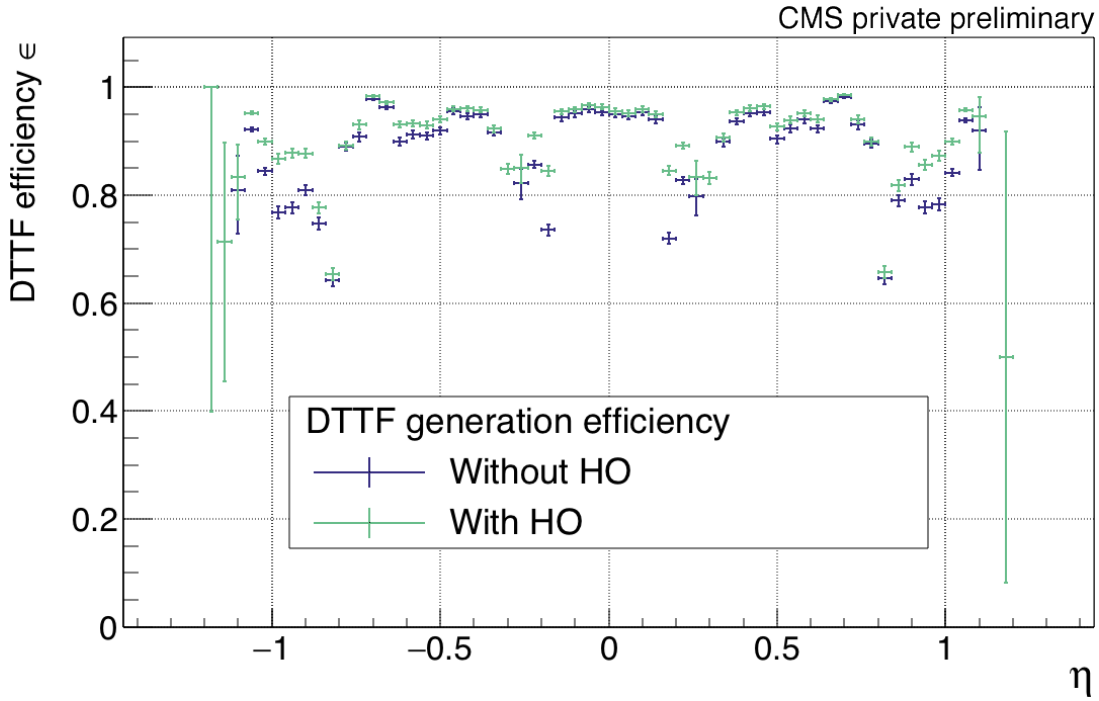

Figure 6.11: DTTF track efficiency as shown in figure 6.6. The added data points show the DTTF efficiency in the case that the addition of HO data into the DTTF can recover all recoverable tracks that have a matching HO MIP tag.

be developed and depends strongly on the constantly evolving changes planned during preparation of the phase 2 run. This design will also be responsible for the final redundancy that the HO system could provide. In any case a combination of HO data with DT data is an interesting field of application with a high potential.

6.4 Potential of an MTT with finer granularity and better timing

The potential of the existing HO detector has been demonstrated with data in this chapter. The MTT concept foresees a scintillator-based detector with a better spatial resolution and potentially an improved time resolution.
However, a better time resolution compared to the HO system is not necessary for the presented scope. The width of the HO detector signal is $\sim$ 50 ns and its time resolution is well below the LHC clock cycle [73]. Thus, the HO time resolution is sufficient to make a timing on event to event basis. The HO time resolution is even compatible with the time resolution of the DT muon detector. Therefore, an even better timing resolution can not provide additional benefit.
The limiting factor for a feasible spatial resolution is the resolution of the DT TP positions. A variation of the HO matching cone size and the resulting number of matches

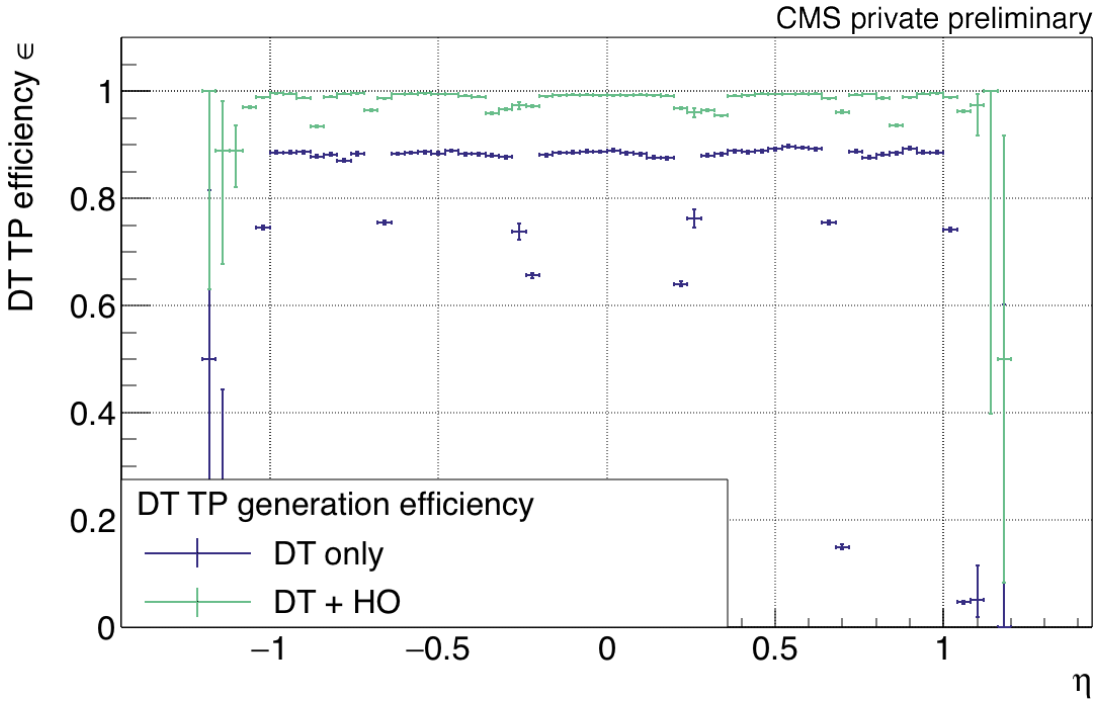

Figure 6.12: DT TP generation efficiency in station 2 in 2015D data and the ideal case with an HO tag leading to a recovery of the DT TP efficiency if a matching HO tag is present in the data. This defines the upper threshold of the redundancy potential.

between HO and the muon track can yield information if a finer granularity results in a better redundancy.
The number of matches between HO and the muon track is shown in figure 6.13. Only tracks that do not result in a DT TP in muon station 2 are considered. These tracks do potentially need an HO MIP tag in order to regain the muon information.
The number of matches significantly drops when the matching cone has a size of $\Delta R < 0.15$ or tighter. The granularity of the HO system is $\Delta\eta \cdot \Delta\phi = 0.087 \cdot 0.087$. Therefore, an impact on the number of matching HO MIP tags should only be visible at a matching cone size of 0.05 if it was due to the HO granularity as the maximum distance between the center of an HO tile and a muon track can be

$$\Delta R_{\text{max}} = \sqrt{\left(\frac{0.087}{2}\right)^2 + \left(\frac{0.087}{2}\right)^2} \approx 0.061. \tag{6.5}$$

Obviously, the matching between HO and the muon track needs to take into account adjacent HO tiles, too. Consequently, a finer granularity is not feasible in this sense.
Anyway, the HO matching efficiency is very high. Considering the costs for an MTT upgrade, the cost-benefit ratio is questionable as long as a working HO system exists.

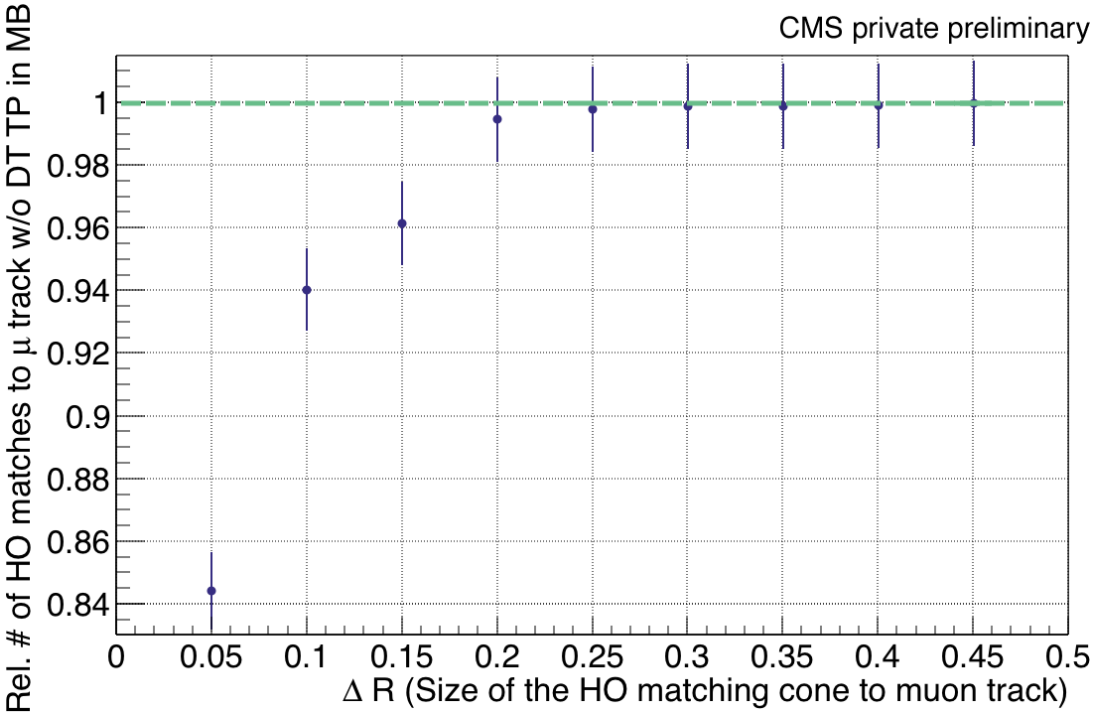

Figure 6.13: Number of matches of HO MIP tags to the muon track in the case of a missing DT TP in muon station 2 relative to the size of the matching cone. The green line shows the number of muon tracks with a missing DT TP in muon station 2.

Chapter 7

Conclusion and deduction

7.1 Conclusion

Three different possible application scenarios for a scintillator-based muon trigger have been investigated in the previous chapters. The analyses were all conducted with focus on the usability and necessity of such a muon trigger in order to solve challenges in the presented scenarios.

The impact of muon ambiguities showed to be unproblematic for the Level-1-Trigger (L1-Trigger) even at the high luminosities of the HL-LHC (see chapter 4). Although muon ambiguities occur on L1 during muon recognition, the number of additional L1-Trigger accepts is very low ($< 10^{-5}$). The use of a muon trigger detector such as HO would introduce a smaller efficiency of L1 muon detection. This trade-off is too large compared to the benefits of a reduction of the anyway unproblematic muon ambiguity rate.
Therefore, the use of HO or an HO-like system is not convenient in this scope.

The second analysis (chapter 5) concentrated on the impact of DT station failure on the L1 muon measurement. It became obvious, that the failure of a DT muon station 1 or 2 has significant impact on the L1 muon efficiency in the area of these stations. A local loss of up to 30 % of the L1 muons has to be expected.
Due to the results of this analysis, an algorithm has been introduced, allowing to recover parts of these former lost L1 muons. This algorithm combines the information of the muon station 1 or 2 and of the HO system as MIP tagger. The combination has been chosen to be comparatively simple in order to allow for a fast implementation into the existing firmware in the service cavern in case of a muon station failure.

The analysis of the recovered L1 muons (L1-HO muons) demonstrated the capability to locally recover up to 40 % of the L1 muons that are lost due to a DT station failure. The resulting η, ϕ, and p_T variables are accurate compared to those of the L1 muons, that were lost due to the detector failure. Thereby, the implementation of the algorithm introduces a notable but manageable amount of noise.
However, the efficiency and accuracy of the algorithm are better in the case of DT muon station 2 failure compared to the failure in station 1.
The impact of randomly failing DT wires was also investigated. The L1 muon detection efficiency decreases from 100 % to 75 % with 0 % to 60 % failing DT wires. At 60 % failing DT wires the DT system is inoperative. The remaining muons are created by the RPC system alone.

In the third analysis (see chapter 6) the DT trigger primitive (TP) creation efficiency showed a lack of efficiency in the wheel gaps with a locally reduced efficiency of 20 % – 70 %. Since the DT TP generation is performed in the experimental cavern nowadays, a scintillator-based muon tagger system can not provide help to reduce the inefficiency. Starting in 2023, the DT TP generation will be executed in the service cavern. The potential application of HO or an HO like system has been presented in this case.
Additionally, the DTTF track production efficiency has been investigated. The HO system was found to be potentially helpful for 0.5 % of the muons. The application of HO in the DTTF could yield an efficiency increase from 70 % to 85 % in the wheel gaps.
As the introduction of HO in the DT track finder would not reduce the DTTF efficiency, since HO would only be used in cases where the normal DTTF algorithm fails, HO can be considered as valuable in this case.

7.2 Studies' impact on the MTT-concept

The implementation of a detector according to the concept of the Muon Track fast Tag (MTT), was also studied. The similarity of the hadron outer calorimeter (HO) and the MTT detector was utilized. The MTT detector can thereby offer an improved time and spatial resolution.
The potential of the HO detector was shown for the use as redundancy system in a failure scenario of a DT station. Also a backup for the DTTF production and a potential assistance for the DT TP production in a phase 2 CMS detector is feasible.
However, the better timing resolution of the MTT detector cannot provide additional benefit in the presented cases. The MTT timing precision has to allow an assignment to the bunch-crossings. This is also provided by the HO system [88].
The spatial resolution of the MTT detector can be improved in both directions (η, ϕ) compared to HO. A finer η resolution does not seem useful, since the assignment of an η position from the data of a single DT station in L1 is very coarse. The presented redundancy algorithm has to take into account more than one HO tile in η anyway.
Also the ϕ projection of muon tracks from a muon station to the HO system has a resolution that does not indicate the need of an improved resolution in the redundancy

algorithm. However, if used as additional system in the DT TP generation in a phase 2 scenario, more precise ϕ information from a muon trigger might be helpful. This depends on the application of HO or MTT as simple muon identification tag or if it is also used to improve the muon momentum resolution.
All in all, an urgent need to exchange the HO system with the MTT detector has not been found. Nonetheless, the MTT concept may provide help in future scenarios. Furthermore, it is a veritable backup solution if any problems with the HO system occur and a new detector becomes necessary.

7.3 The use of HO in the present muon trigger system

As shown in the analyses, the HO system can provide redundancy in case of DT station failure and can be helpful in the DTTF track creation. Supported by these studies, the HO data is now fed into a joint muon trigger system combining the trigger primitives (TPs) of DT, RPC, and HO. The module combining this data is called TwinMux [89] and creates so-called super primitives from this data. The super primitives are used to build muon tracks in the L1-Trigger. The combination of this data was only possible by efforts to upgrade HO with silicon photomultipliers (SiPM) [73] and building a connection between HO and the TwinMux in hard- and firmware. The performed upgrade work is presented in the next chapter.

Chapter 8

The hadron outer calorimeter as part of the muon trigger

Supported by the studies presented in chapters 5 and 6, the hadron outer calorimeter (HO) data is forwarded to a new muon trigger, that can combine drift tube (DT), resistive plate chamber (RPC) and HO data. The upgrade process towards this combined muon trigger, that the author contributed to, is presented in this chapter.

8.1 Concept of the combined muon trigger

The sector collectors (see section 2.2.6.1) of the DT muon system were positioned in the service cavern instead of the experimental cavern [90] during the long shutdown 1 (LS1, 2012 – 2014). This relocation allows to combine the trigger primitives created by the DT stations with RPC and HO data. The resulting super primitives can then be used in the barrel muon track finder (BMTF) that combines the tracks from different sectors.
A new hardware component in the Level-1 (L1) muon trigger - the TwinMux - will fulfill this task. The TwinMux is a data concentrator and fan-out card that receives the trigger primitives of DT, RPC and HO in one sector within one wheel. The DT data of each station is transmitted via eight Low Voltage Differential Signaling (LVDS) lines at 480 Mb/s to one TwinMux - allowing for 80 bit per bunch-crossing of net data. The RPC data is transmitted by five gigabit optical links (GOL) with a bandwidth of 1.6 Gb/s each [89]. The HO system uses three GOL for the transmission of the data to one TwinMux. The HO data is routed via the RPC system and then transmitted to the TwinMux using the GOLs. A schematic of the TwinMux integration with DT and RPC data is shown in figure 8.1. In a first step, the DT and RPC data is combined to gain a

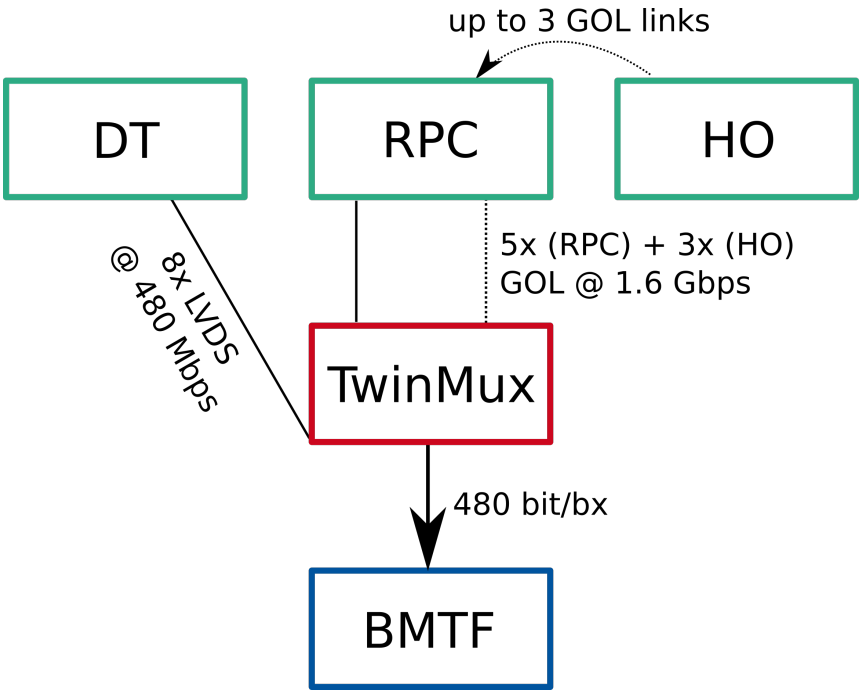

Figure 8.1: Schematic of the TwinMux integration with DT, HO, and RPC data. The HO data is fed into the TwinMux using the same transmission technique as RPC but only using three GOLs. The TwinMux outputs 480 bit per bunch-crossing (bx)

higher efficiency and quality of the track data in the BMTF. This allows for a better p_T assignment and thus a higher rate reduction in the BMTF. The HO system is currently kept as backup and is planned to be also used in the trigger in 2017. Here HO can provide additional information similar as shown in the presented algorithm for DT failure compensation in chapter 5.

8.2 Hadron outer calorimeter history

The hadron outer calorimeter (HO) was originally equipped with hybrid photo detectors (HPDs) for the light readout. HPDs are photo detectors that are based on a conventional photo-cathode to convert photons into a measurable charge. The electrons, that are knocked out of the cathode, are accelerated in an electrical field towards an avalanche photo-diode (APD). Within the APD, an avalanche is started yielding an amplification of O(2000). The accelerating electrical field within the HPD needs a supply voltage of O(10 kV) [91].
The HO setup using HPDs was found to allow for a trigger efficiency of 90 % of minimum ionizing particles (MIP) [34].
The signal and pedestal distributions for the HPD channels in wheel 2 of the CMS

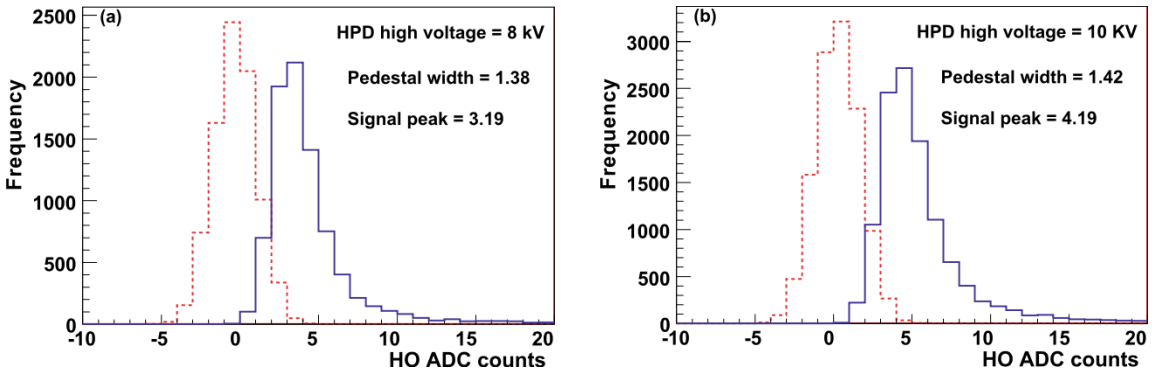

(a) 8 kV supply voltage (b) 10 kV supply voltage

Figure 8.2: HO ADC counts for signal (blue line) and pedestal (red dashed line) for a cosmic muon measurement of the HPD equipped HO in wheel 2 of the CMS detector [34]. For lower supply voltages (left, 8 kV) the separation between signal and pedestal is reduced compared to higher supply voltages (right, 10 kV).

detector are shown in figure 8.2 for a cosmic muon measurement. By increasing the supply voltage from 8 kV to 10 kV the mean MIP signal height increases by 31 %. The mean signal is 2.3 times larger than the pedestal width for 8 kV supply voltage. For 10 kV supply voltage, the value increases to 2.9. The separation between signal and pedestal is reduced for lower supply voltages.

During the first full CMS detector test with a magnetic field of 3.8 T, the fringe field directly outside the solenoid has been found to be 0.02 T at wheel 0 and 0.2 T at higher wheel numbers. This fringe field resulted in an increased discharge rate of the HPDs. During the run, the discharge rate increased further. By the end of the run, 14 of 132 HPD channels had to be switched off due to the discharge. The other channels were supplied with decreased voltage leading to a reduced detection efficiency for MIPs [92].

During the winter shutdown 2008/2009, the HPDs with the highest noise rates have been replaced by new HPDs. After the replacement 96 % of the channels were operative. However, due to the performance issues the HPDs were replaced by Silicon Photomultipliers (SiPM) until 2014. Therewith, HO follows the MTT concept (see chapter 3). SiPMs are arrays of parallel APDs that yield a linear gain of $O(10^6)$ at low light fluxes [93] (see section 3.2.1).

8.3 SiPM upgrade work

The high noise rate and the resulting reduced MIP detection efficiency required the exchange of the HPDs by SiPMs. Besides the fact that SiPMs are insensitive to magnetic fields [94], SiPMs need a significantly lower bias voltage compared to HPDs

(O(100 V)). As test setup $\sim$ 5 % of the channels were equipped with SiPMs [73] in 2009. These channels showed a convincingly good performance. Hence, the remaining channels were exchanged during the first long shutdown (LS1).
Beforehand, several types of SiPMs from different manufacturers had been tested. Finally, Hamamatsu MPPCs have been chosen with a detector size of $(3 \cdot 3)$ mm^2 and a cell pitch of 50 μm [95], [38]. SiPMs irradiated with $3 \cdot 10^{10}$cm^{-2} protons were found to be fully operational. However, the dark rate count increased due to added crystal lattice impurities in the SiPM. In turn, this dark count rate reduced by a factor of 2 after 100 days of annealing at room temperature [96]. Therefore, the SiPMs are currently expected to function over the full HO detector lifetime including HL-LHC runtime.

The exchange was performed using "drop in" replacement modules. Except for the missing high voltage connection, these readout modules (RMs), that contain the electronics and SiPMs, have the same size and connectors as the former HPD modules. This allows to simply remove the old module and plug in the new one. A picture of the replacement RMs is shown in figure 8.3.
The readout modules direct the light of one HO tile to one SiPM each using a so-called

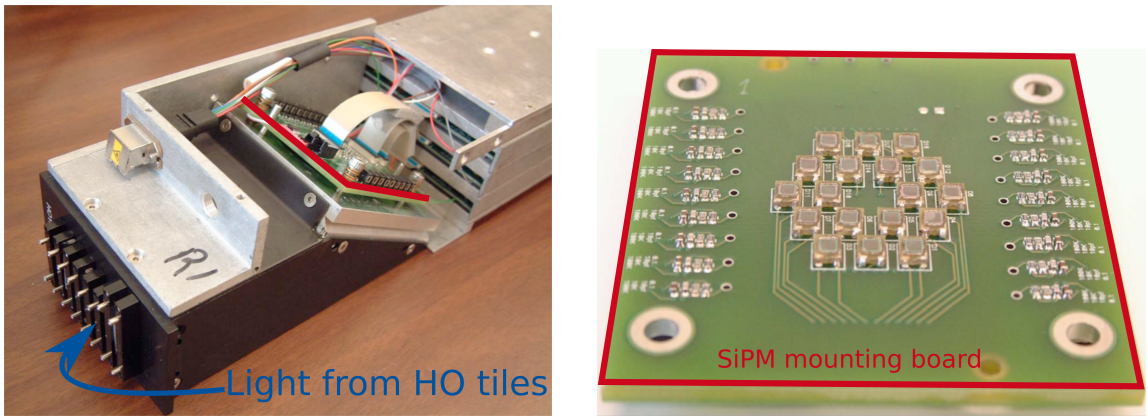

(a) Readout Module (b) SiPM mounting board

Figure 8.3: Picture of a readout module (RM) containing SiPMs, adapted from [95]. The optical cables, that carry the light from the scintillator bars, can be connected to the black left side (a). The so-called optical decoder unit between fibers and SiPM mounting board directs the light of one HO tile coming from four optical fibers to one SiPM. The SiPM mounting board is equipped with 18 SiPMs (b). The SiPM charge signals are digitized in 25 ns steps on an ADC board within the RM.

optical decoder unit (ODU). The charge signal of every SiPM is digitized in 25 ns bins using an 8-bit QIE (Charge Integrator and Encoder – A charge integrating amplitude to digital converter).
The mounting of the light fibers on the SiPMs in the ODU is done using direct coupling in the wheels 1± and 2±. Here, four fibers and one calibration fiber with a diameter

of 1 mm each have to match to a sensitive SiPM area of $(3 \cdot 3)$ mm^2. The mounting of the light fibers at wheel 0 cannot be done directly. At wheel 0 two layers of scintillator are stacked each providing four light fibers. Eight fibers and one calibration fiber with a diameter of 1 mm do not fit directly on the SiPM's sensitive area. Therefore, a so-called light mixer is positioned between light fibers and the SiPM. The light mixer is a cone with a diffuse reflective coating reducing the diameter of the illuminated area from 3.6 mm to 2.9 mm [97]. A light mixer was not necessary before. The light mixer is simply placed between fibers and SiPMs within the RM. As they are mounted on the RM, they are intrinsically installed during the RM exchange. A schematic of the light mixer and a projection onto the SiPM are shown in figure 8.4.

The light mixer introduces a loss of 20 % to 40 % in light intensity [97]. However,

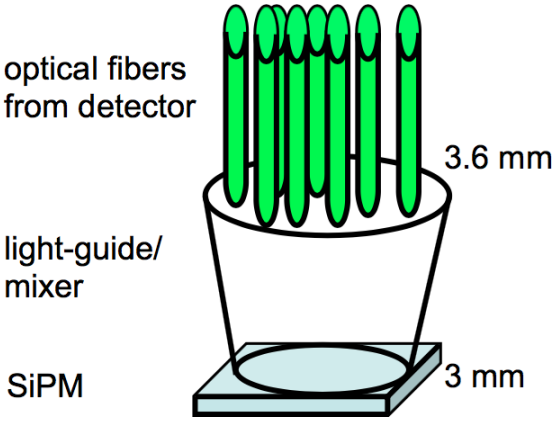

(a) Light mixer scheme

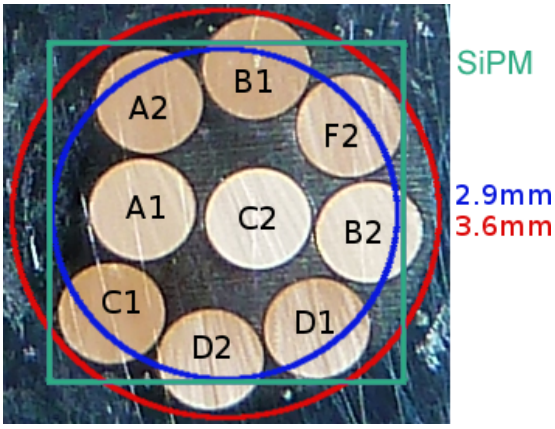

(b) Projection of the cone diameters on the SiPM area

Figure 8.4: Scheme of a light mixer reducing the size of the combined light spots from a diameter of 3.6 mm to 2.9 mm, adapted from [97]. 8 HO fibers + 1 calibration fiber (A1 – F2) need to fit to the SiPM size of 3 mm.

this can be corrected for using a channel-by-channel calibration, which is a standard procedure to compensate for inhomogeneities in the whole light guiding setup.

8.3.1 SiPM upgrade commissioning

After the installation of SiPMs, all channels have been commissioned in terms of temperature, gain, operation voltage stability, and MIP identification efficiency.

8.3.1.1 Temperature stability

The temperature of the SiPMs is stabilized using a water cooling circuit on the back of the mounting of the RMs together with peltier elements placed on the back of the SiPM mounting board. This stabilization is crucial for the performance of SiPMs since their

operating parameters strongly depend on the temperature. The same regulation electronics can be used that was implemented for HPD operation. In order to determine the temperature stability, the desired temperature was set to a fixed value in the room temperature regime. Afterwards, the temperatures at the SiPMs were measured over a period of about one month. The resulting plot is shown in figure 8.5. The temperature

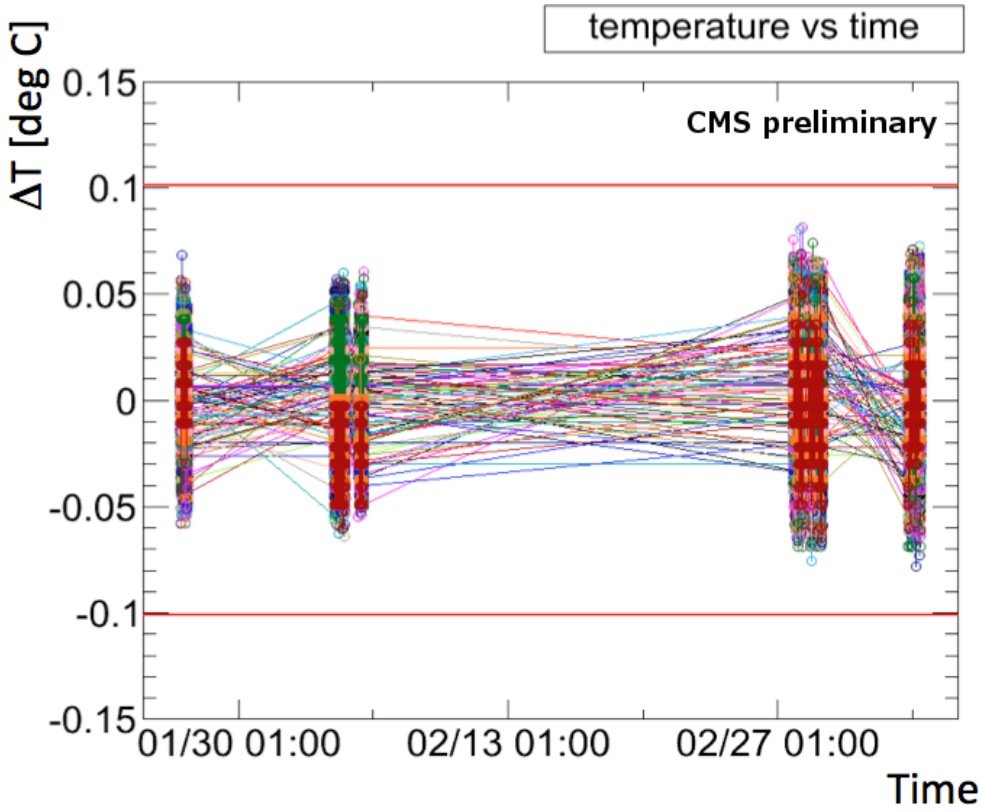

Figure 8.5: Temperature curve for all installed RMs over a time of one month in 2014 [98]. The temperature is stable within 0.1 °C. The connection lines between the six data-points per RM do not represent an extrapolation.

was found to be stable within 0.1 °C at every measurement point [98]. This ensures a proper function in terms of temperature.

8.3.1.2 Gain stability

In a next step, the gain variations for different SiPMs over six runs (from February to March 2014) have been investigated. The gain was measured by applying LED light pulses. These pulses are directed on the SiPMs via the calibration fiber. Due to the fact that the SiPM yields almost the same charge per hit cell, the gain can be measured by obtaining the mean measured value and the signal width. The gain g does not depend

on the number of photons per light pulse when using

$$\frac{\sigma^2}{m} = \frac{\left(\sqrt{N} \cdot g\right)^2}{N \cdot g} = \frac{N \cdot g^2}{N \cdot g} = g \tag{8.1}$$

with the mean signal height m, the signal width σ. The relative gain variations over the six runs for all SiPMs is shown in figure 8.6. The width of the relative gain variation

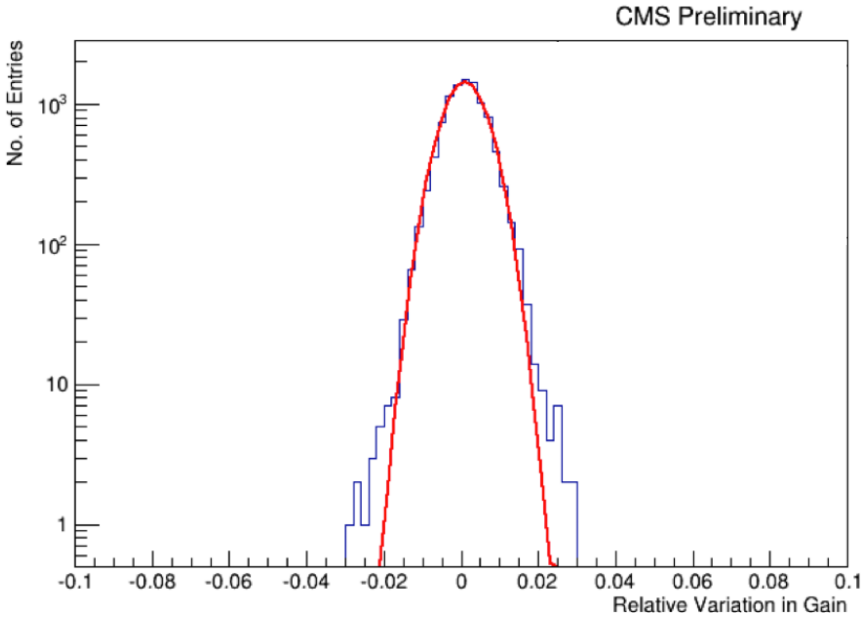

Figure 8.6: Relative gain variations for all SiPM channels of HO over six runs adapted from [98]. The maximum variation is 3 %.

distribution is 0.6 % [98]. The complete distribution is within 3 %. The gain variation is independent of the coupling (direct or light mixer) of the fibers to the SiPMs. Thus, the gain variation is sufficiently small for a proper HO usage.

8.3.1.3 Breakdown voltage stability

In a last step, the breakdown voltage stability of the SiPMs was measured. The breakdown voltage defines the working point of the SiPM [99]. The variation of the breakdown voltage is contained within 50 mV over the month of measurement [98]. This very stable behavior is directly correlated with the stable behavior of the temperature control.

8.3.1.4 MIP identification capability

The working parameters of the SiPMs have been checked and found to be very stable. In a next step, the MIP identification efficiency has been investigated.

This test was performed using atmospheric muons that traverse the CMS detector. These muons have been tagged by the muon system. The track was extrapolated to the HO tiles and the measured energy at these tiles was recorded.
The distribution of the measured energy is a landau distribution for each tile [100]. This distribution is shifted to higher most probable values (MPVs) for vertical HO tiles. Here the cosmic muons pass the tile almost in their complete width leading to a higher energy loss. These shifts are corrected geometrically by calculating the track length within the tile. This correction allows to compare the measured MPVs at different ϕ positions. The corrected mean MPVs for all iϕ positions is shown in figure 8.7. See section 2.2.4.1 for the iϕ counting of HO tiles.
The tiles show a mean MPV of between 60 to 100 ADC counts. The relative deviation

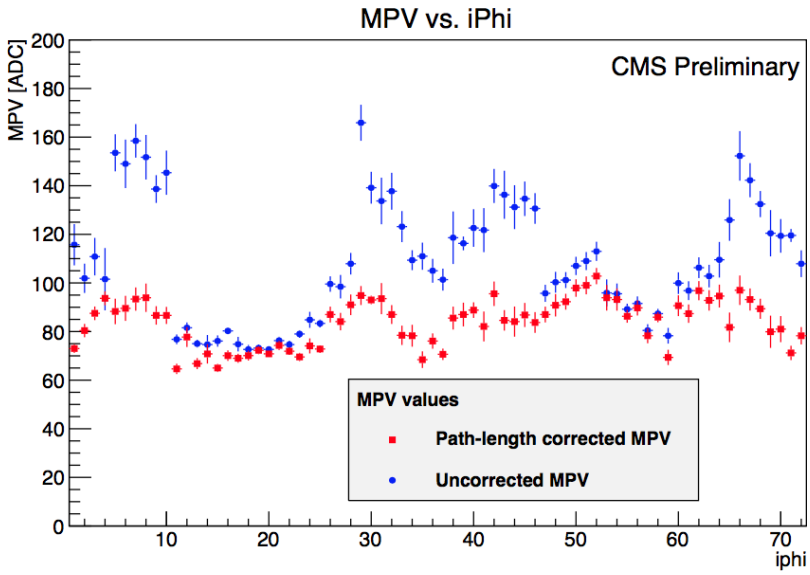

Figure 8.7: Mean most probable value for all tiles within one iϕ slice measured with cosmic muons with and without correction due to different path-lengths through an HO tile [101]. The variation of the values after correction is mainly due to the different light transmitting fiber lengths.

is due to the position of the readout modules. This is expected as the light transmitting fibers have different lengths for tiles at different iϕ positions. Thus, the attenuation is different, too. These variations can be corrected for with a calibration.
A measurement of the SiPM signals in HO shows the good separation between pedestal and signal (see figure 8.8).

With the presented investigations, the good functioning of the upgraded HO system has been proven. The SiPM equipped HO was consequently applied in the data taking of 2015 and 2016. Furthermore, the SiPM integration and reliable HO system performance allow to integrate the HO signals in the TwinMux.

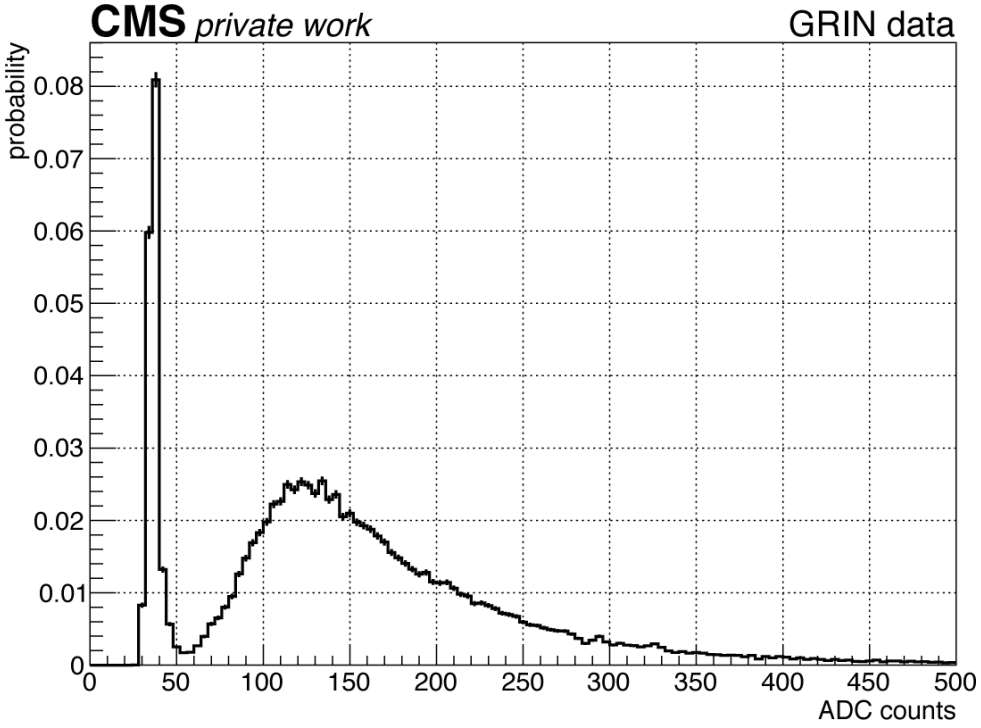

Figure 8.8: HO SiPM signal in ADC counts from tiles with muon transition [60]. A clear separation between pedestal and signal is visible. The MIP signal purity and efficiency are $\sim$ 97 % each for a threshold of 54 ADC counts.

8.4 HO TwinMux integration

Since the HO is ready for use, the integration of HO into the TwinMux and therefore a combined muon trigger is possible. This section describes the technical steps that have been performed by the hadron calorimeter group and the author in order to prepare the application of HO in the TwinMux. The hardware connection has been established. Unless otherwise noted, the presented technical steps are finished and checked for proper operation.
In order to execute the HO integration into TwinMux, four main steps had to be taken.

- In a first step, the fibers between the HO detector in the experimental cavern and the HO logic in the service cavern had to be rearranged in order to use the HO information in the following steps (see section 8.4.1).

- In a second step, the cables between HO and RPC, that are transmitting the data to TwinMux, had to be plugged. Therefore, a cable mapping had to be created (see section 8.4.2).

- Additionally, the output firmware of the HO side had to be written and installed (see section 8.4.3).

- In a last step, the transmission of the HO data to the RPC, that transmits the data to TwinMux, had to be synchronized (see section 8.4.4).

- In order to save the TwinMux input in a CMSSW data format, the HO input data words have to be unpacked. This step is not necessary to test if the connection between HO and TwinMux is established (see section 8.4.5). The unpacking is not implemented yet (December 2016).

A picture of the tasks that had to be fulfilled is shown in figure 8.9. The HO data, that is

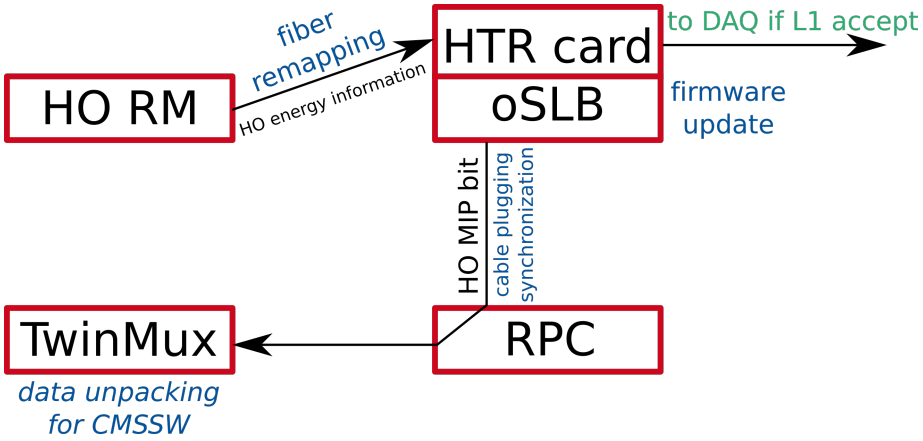

Figure 8.9: Data chain of the HO data from the HO readout modules (RM) towards the TwinMux. The tasks that had to be finished in order to receive MIP bits in the TwinMux are shown in blue color. The unpacking of the data is not necessary to receive data in TwinMux. However, it is needed to work with the HO MIP bits in the offline event sample. The data is transmitted via the RPC system since cables were already present between oSLB and RPC. Additionally, the reception protocol in TwinMux for data coming from RPC is already implemented.

transmitted to the TwinMux, consists of one bit per HO tile. The bit is set to 1 if HO has measured a MIP in the tile. If HO measured too much or less energy than expected for a MIP, the bit is set to 0. A valid MIP signal is currently defined as a measured HO SiPM signal from 40 to 200 ADC counts[1]. Hardware constraints of the GOL connections do not allow for more than one bit per tile. Future developments might allow for two bits per HO tile. In this case, an additional differentiation between no signal and large signals would be introduced.

8.4.1 HO internal fiber rerouting

Before connecting HO and TwinMux various tasks concerning the data processing from the HO tiles to the HO readout in the service cavern had to be resolved.

[1] http://cmsonline.cern.ch/cms-elog/956930

As explained in section 2.2.4.1, the data containing the measured energies from three HO tiles is transmitted via one fiber from the readout boxes (RBX) to the HCal trigger and readout (HTR) cards that process the data in case of an L1 accept. Furthermore, the HTR cards check if a MIP signal was measured during each bunch-crossing for every tile and transmit this data via the optical serial link boards (oSLB) to the RPC system, that then forwards this information to the TwinMux via gigabit optical links (GOL).
Each HTR card can accept 16 fibers - 8 fibers in a “top” and “bottom” called input each - from the RBXs and therefore the information of 48 tiles at maximum. Four HTR cards aggregate the information of one sector in all wheels.
The mapping of the tiles that are transmitted via one fiber from the RBX to the HTR cards is shown in figure 8.10.
The data fed to the HTR cards can be rerouted by replugging the single optical fibers

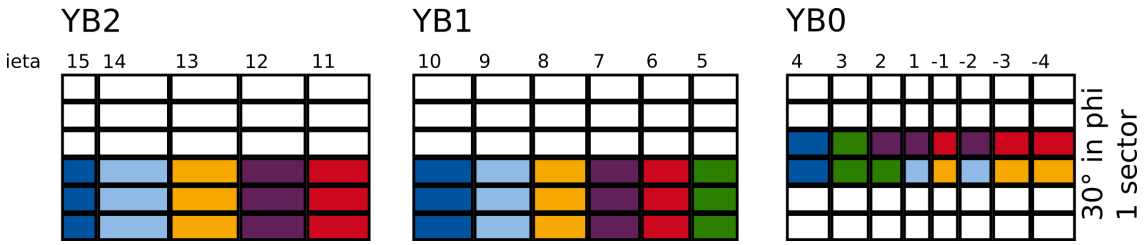

Figure 8.10: Mapping of HO tile information to the optical fibers that transmit data from the RBXs to the HTR cards. One particular color within a wheel (YB) corresponds to the HO tile MIP information on one optical fiber. The information of up to three HO tiles are transmitted by one optical fiber. The pattern is repeated in the white areas. YB 2- and YB 1- have the same but mirrored mapping, respectively.

in the service cavern. During this process the information of the three tiles in one fiber can not be rearranged. The former mapping of the HO tile information to the HTR cards is shown in figure 8.11 for a single sector.
As a consequence of the asymmetric mapping from the HO tile data to single fibers in

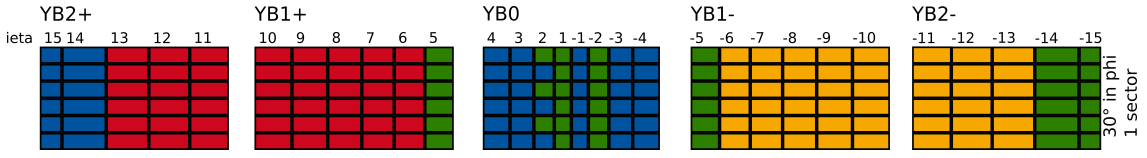

Figure 8.11: Mapping of the HO tile information to a certain HTR card before replugging. The information of the tiles with the same color are all routed to the same HTR card in a particular sector. The mapping scheme is the same for all sectors.

wheel 0, the mapping to the HTR cards is also asymmetric there. However, since the data was only used in the case of an L1 accept, the specific mapping had no influence

on the further processing.
Now, as the HO information is also directed into the TwinMux, the mapping faced different constraints:

- Each HTR card has three oSLB outputs.
- One oSLB output can transfer the MIP data of 24 tiles per bunch-crossing at maximum.
- Every sector within one wheel is equipped with one TwinMux. Therefore, the information of a complete sector has to be transferred to five different TwinMux according to the five wheels.
- One TwinMux can receive the data from up to five oSLBs.

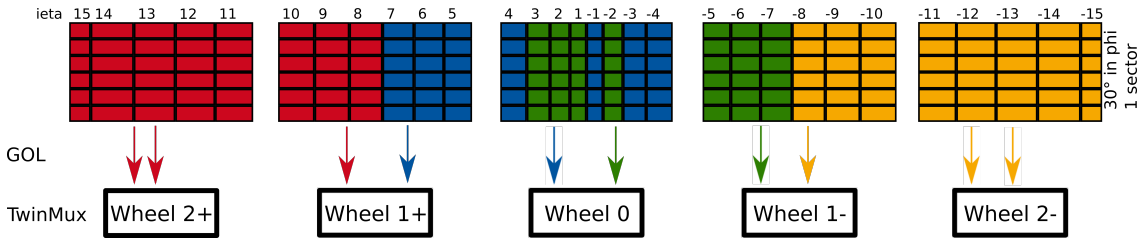

Figure 8.12: Mapping of the HO tile information to a certain HTR card after rearrangement. The information of the tiles with the same color are all routed to the same HTR card. The layout is the same for each sector. Every arrow symbolizes one gigabit optical link (GOL) occupying one oSLB on the HTR card. Not more than three oSLB per HTR card are used. No GOL is carrying more than 24 HO tile MIP information bits.

With the knowledge of these constraints, it becomes obvious that the former mapping from the HO tiles to the TwinMux was not suitable. The data from four different wheels was fed into one HTR card (HTR card corresponding to the green color in figure 8.11). This HTR card would thus need to output the MIP data to four different TwinMux. This is impossible because the HTR card has only three different oSLB outputs.
A change of the fiber mapping had to be executed. This remapping was done in the patch panel in front of the HTR cards by replugging the optical fibers. The rearranged mapping is shown in figure 8.12.
After remapping, the presented constraints are now fulfilled. Even though the mapping is not completely symmetric, the maximum number of outputs per HTR card is now reduced to three. A picture of the open patch panel is shown in figure 8.13.
As soon as the cables were replugged, the fibers could be connected from the oSLBs to the TwinMux side.

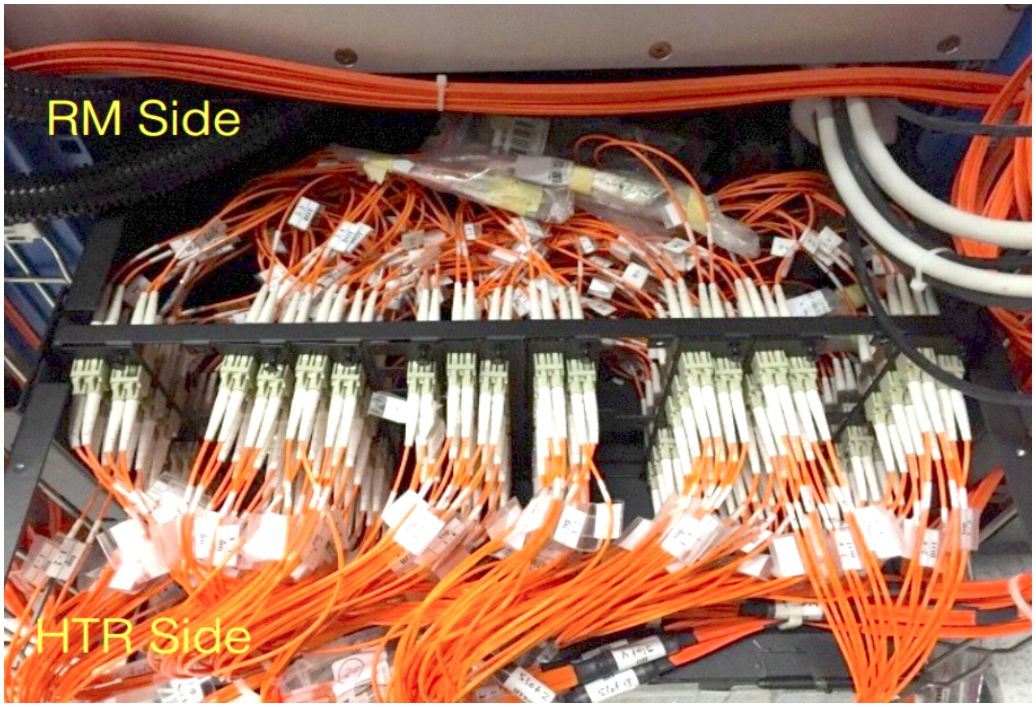

Figure 8.13: Picture of the patch panel during fiber replugging [102]. The cables on the upper side arrive from the readout boxes (RM Side) in the experimental cavern. The patched cables on the lower side are routed to the HTR cards.

8.4.2 Cabling between HO and TwinMux

During the setup of the CMS detector, optical fibers between the crates carrying HO and RPC hardware were already foreseen. Consequently, fibers were routed between HO and RPC. These fibers transmit the signals of the oSLB to RPC. The RPC system then transmits the HO data together with the RPC data using GOL to the TwinMux.
All cables on the HO side have been plugged in first. In order to have a correct mapping on the RPC side, a map of the cables' labels and the corresponding oSLB has been created. Using this map, the cables can be plugged in on the RPC side. By the time of the writing of this thesis (December 2016), the cables of sector 4 in the wheel 2 and 1 have been already plugged in on RPC side. Even though not all cables have been integrated in yet, this allows for a test of the full data processing chain. The remaining cables are going to be plugged during the technical stop in winter 2016/2017.

8.4.3 oSLB firmware upgrade

After the installation of the transmission fibers from the HO HTR cards to the TwinMux, the firmware of the oSLB had to be adapted in order to reflect the presented, updated mapping. Therefore, a map had to be created that reflects which oSLB on which HTR card outputs a certain MIP bit. Since one oSLB can output up to 24 MIP bits per bunch-crossing, the order of these MIP bits in the oSLB signal had to be defined, too.

As the mapping of the HO MIP data to the 16 fibers that go into an HTR card is known

fiber	ch 2		ch 0		ch 1	
top	eta	phi	eta	phi	eta	phi
1	-15	6	-15	5	-15	4
2	-14	4	-14	6	-14	5
3	-13	6	-13	5	-13	4
4	-12	4	-12	6	-12	5
5	-11	6	-11	5	-11	4
6	-10	4	-10	6	-10	5
7	-9	6	-9	5	-9	4
8	-8	4	-8	6	-8	5
bottom	eta	phi	eta	phi	eta	phi
1	-15	3	-15	2	-15	1
2	-14	1	-14	3	-14	2
3	-13	3	-13	2	-13	1
4	-12	1	-12	3	-12	2
5	-11	3	-11	2	-11	1
6	-10	1	-10	3	-10	2
7	-9	3	-9	2	-9	1
8	-8	1	-8	3	-8	2

Table 8.1: Excerpt of the mapping table for the mapping of the HO tile information to the 16 fibers that are directed to an HTR card (here HTR card no. 18). The HTR card has two inputs (top and bottom). Each input carries 8 optical fibers. Every fiber carries the data of three HO tiles (ch 0, 1, 2). This information is then used for the mapping to the oSLBs. For a better understanding, three data points are colored in this input table as well as in the output table 8.2.

(see table 8.1), this information can be used to create a table for the oSLB output (see table 8.2).

The update of the HTR firmware using the new maps was done externally at Boston University. The new firmware is installed on all HTR cards (version 0x90)[2].

The implemented mapping was checked. For that purpose, the oSLB outputs were fed into another HTR card in a test setup. By installing the firmware for the different HTR cards in the test setup, the output for every HTR card was checked. The mapping was found to be correct.

[2] http://physics.bu.edu/~wusx/download/oslb/

bit no.	oSLB 1	oSLB 2	oSLB 3
1	T1-2	B1-2	T6-0
2	T1-0	B1-0	T6-1
3	T1-1	B1-1	T6-2
4	T2-0	B2-0	T7-2
5	T2-1	B2-1	T7-0
6	T2-2	B2-2	T7-1
7	T3-2	B3-2	T8-0
8	T3-0	B3-0	T8-1
9	T3-1	B3-1	T8-2
10	T4-0	B4-0	B6-0
11	T4-1	B4-1	B6-1
12	T4-2	B4-2	B6-2
13	T5-2	B5-2	B7-2
14	T5-0	B5-0	B7-0
15	T5-1	B5-1	B7-1
16			B8-0
17			B8-1
18			B8-2

Table 8.2: Excerpt of the mapping table for the mapping of the HTR card inputs to the three oSLBs. The encoding at a certain bit position represents the input in the HTR card that is used in this bit. T1-2 is the input at the top input of the HTR card in fiber 1 at channel 2. For a better understanding, three positions are colored in this table as well as in table 8.1. One so-called data word contains the bits of an oSLB output column plus bunch-crossing information as well as a parity bit.

With the update of the HTR firmware and the plugging of the cables (section 8.4.2) the link is finished on the HO side. As a last step, the data that is transmitted, has to be received in the RPC for further transmission to TwinMux.

8.4.4 HO-RPC-TwinMux synchronization

Since the gigabit optical link is also used by RPC, the reception protocol for the bit stream (called data words) is already implemented in TwinMux. Thus, the transmission of HO data from RPC to TwinMux is implemented by default.
Nonetheless, the link between HO and RPC needs to be synchronized. A single oSLB

outputs 32 bits per bunch-crossing. The first 24 bits contain the HO MIP bits. The next four bits contain the bunch-crossing numbering. The last four bits are used as error test code. The last of the four bits is a parity bit.
For synchronization, the bunch-crossing number of the oSLB data is used to align HO data with RPC data on RPC side. The bunch-crossing counting within the oSLB firmware was found to be correct [3]. An update of the reception side in RPC will need a new alignment test.
By reading the input of the TwinMux locally, a check can be performed if data is arriving. This check has been performed and showed non-zero MIP bits arriving in TwinMux. A snapshot of the output is shown in figure 8.14. This test proves, that the signal

```
[143]  603aac302c3c3c3c     HO WORD
wheel, sector : 2, 4
mip : 0
mip : 1
mip : 1
mip : 0
mip : 1
mip : 0
```

Figure 8.14: Screenshot of an HO data word for wheel 2, sector 4 received in TwinMux. The data word is locally unpacked. The unpacking of the data words into a CMSSW event format including HO tile ID for a certain MIP bit is in preparation.

transmission between HO and TwinMux is working. As soon as the bunch-crossing counting is checked for the new RPC reception protocol update, HO is ready for use in L1.

8.4.5 HO unpacking and processing

In order to have HO-TwinMux information also available in the CMSSW event data format, the data words have to be unpacked. The unpacking is not needed in order to verify that data is arriving at the TwinMux. However, it is needed in order to save the TwinMux HO data in the CMSSW event data format. The unpacking also uses the mapping table for the mapping of the HTR card inputs to the oSLB shown in the section before (see table 8.2).
The unpacker as well as an oSLB emulator for the CMSSW framework is currently being written[4]. Afterwards the data quality management (DQM) of CMS will implement quality checks for this link. A check of the HO impact on the muon triggering capability will be performed using combined DT and HO data.

[3] http://cmsonline.cern.ch/cms-elog/960013
[4] https://github.com/cms-sw/cmssw/blob/1e4dfc5c2ee9eeb4050c06316b4fb9d61acb5e03/EventFilter/L1TXRawToDigi/plugins/L1TTwinMuxRawToDigi.cc

8.4.6 Résumé of the HO-TwinMux link status

The TwinMux link from HO has been established from the hardware point of view in sector 4 in the wheels 1 and 2. The full hardware and firmware setup is installed on HO side. The cables that still have to be plugged in at the RPC/TwinMux side will be installed during the LHC end-of-year technical stop 2016/2017.
The firmware of the HO HTR cards was updated in order to reflect the new fiber mapping. The output of the oSLBs had been verified. MIP bits were received in the TwinMux.
The reception firmware of the oSLB data words is currently finalized in order to save the TwinMux input in a CMSSW event data format. A DQM of the HO data in TwinMux is currently developed and will conclude the HO-TwinMux integration. A test of the HO influence on the super primitive creation in the wheel gap regions similar to the analysis shown in chapter 6 is planned during the first half of 2017.

Chapter 9

Summary and Outlook

The application of scintillator-based fast muon triggers in CMS was investigated in this thesis. The introduction of a new fast muon trigger is motivated by future challenges that come up with improvements of the LHC when the luminosity will be increased up to and beyond $5 \cdot 10^{34}\text{cm}^{-2}\text{s}^{-1}$. Furthermore, the CMS detector components will suffer from aging and radiation damage which will effect their efficiency. Therefore, two approaches have been presented. The existing hadron outer calorimeter (HO), that is able to measure minimum ionizing particles (MIP) and was beforehand only used as a "tail-catcher" of the hadronic calorimeter, and the concept of a Muon Track fast Tag (MTT). Both are based on a readout by silicon photomultipliers (SiPM).
The development towards the MTT detector and the evolving field of application was presented. The different investigations concerning scintillator type, size, and wrapping as well as SiPM property analyses have been introduced. The current focus of application was discussed, namely in cases of muon ambiguities and muon system inefficiencies.
Afterwards, three different studies, based on the discussed focus of a scintillator-based fast muon trigger, have been presented. The analyses of muon ambiguities, detector failures, and efficiency decrease due to a lack of geometric acceptance in the drift-tube (DT) system were conducted with respect to the application of HO as supportive muon trigger. An extrapolation of these results towards the concept of MTT was performed exploiting the similarity of HO and MTT.
The studies unveiled, that a scintillator-based fast muon trigger is not crucial for the reduction of muon ambiguities.
However, a support by HO was affirmed in the cases of DT detector failures and to reduce geometric and intrinsic DT inefficiencies. It was shown, that the failure of a whole DT station 2 could lead to losing up to ∼25 % of the L1 muons locally. An algorithm, that combines HO MIP information with the remaining DT station 1 infor-

mation, is thereby able to recover $\sim$ 40 % of these L1 muons. Thus, HO proved to be very helpful in this scenario. The ϕ, η, and p_T resolution of these recoveries faced to be sufficiently precise. The algorithms, that obtain these variables were developed and discussed extensively.
The reduction of intrinsic DT muon system inefficiencies in the DT track finder (DTTF) showed to be at the level of $\sim$ 1 % only, assuming a fully working detector. However, since the HO system would not veto any of the DTTF tracks, it is expected to be still supportive in this case, especially in the wheel gap regions.
Furthermore, a large potential of the HO system was shown, when HO data is combined with DT data during the trigger primitive (TP) generation. The combination can potentially increase the DT TP generation efficiency from 70 % to 95 % in the wheel gap regions. Overall, an efficiency increase from 90 % to 99 % could be reached. This scenario becomes possible with the phase 2 of LHC (in 2025) when the TP generation will be centrally done in the service cavern rather than the experimental cavern.
The concept of an MTT with a finer granularity and a potential better time resolution would yield no further improvement in the scope of all these studies. Consequently, it is advised to keep the MTT detector concept as a backup solution for the case of a potential renewal. A direct exchange of HO with an MTT is currently not foreseen.
Supported by the presented studies, the implementation of the HO MIP signal into a muon trigger (TwinMux), that combines DT, RPC, and HO data, was brought forward. After the upgrade of the HO system with SiPMs the steps towards the HO integration have been presented. The HO system is now fully equipped to feed MIP data to the TwinMux. Consequently, the steps have been taken to prepare the HO data inclusion e.g. in case of a DT detector failure.

Concerning a reduction of intrinsic muon system inefficiencies, after a concluded intensive data quality test, the HO signal will be first used in local runs and will be combined with DT data there. The corresponding algorithm is currently under developed and needs to be verified, before it is installed in the BMTF. The capability of HO to gain efficiency in the muon trigger has to be analyzed with these local run data. Afterwards, a full integration of HO into the TwinMux algorithm is planned. The analysis of the full run data will then conclude the HO-TwinMux integration, that was initiated with the support of the presented analyses.

Glossary

ADC	Amplitude to Digital Converter
BMTF	Barrel Muon Track Finder
BSM	Beyond Standard Model
BTI	Bunch and Track Identifier
bx	bunch-crossing
CERN	European Organization for Nuclear Research
CMS	Compact Muon Solenoid
CSC	Cathode Strip Chamber
DQM	Data Quality Management
DT	Drift Tube
DTTF	Drift Tube Track Finder
EB	Electromagnetic calorimeter in the Barrel region
ECal	Electromagnetic Calorimeter
EE	Electromagnetic calorimeter in the Endcap region
GOL	Gigabit Optical Link
HB	Hadronic calorimeter in the Barrel region
HCal	Hadronic Calorimeter
HE	Hadronic calorimeter in the Endcap region
HF	Hadronic calorimeter in the Forward region
HL-LHC	High Luminosity - Large Hadron Collider
HLT	High Level Trigger
HO	Hadron Outer calorimeter
HPD	Hybrid Photo Detector
HTR	HCal Trigger and Readout card
L1-HO muon	L1 muon backup created by HO and one DT station

L1	Level-1
LEP	Large Electron Positron collider
LHC	Large Hadron Collider
LS	Long Shutdown
LVDS	Low Voltage Differential Signal
MB	Muon stations in the Barrel region
MIP	Minimum Ionizing Particle
MPV	Most Probable Value
MTT	Muon Track fast Tag
ODU	Optical Decoder Unit
oSLB	Optical Serial Link Board
QIE	Charge Integrating ADC
RBX	Readout Box
RM	Readout Module
RPC	Resistive Plate Chamber
S/B	Signal to Background ratio
SiPM	Silicon Photomultiplier
TP	Trigger Primitive
TRACO	Track Correlator
TS	Track Sorter
WLS	Wavelength Shifting fiber
YB	CMS detector ring

References

[1] R. Garoby. „Upgrade issues for the CERN accelerator complex“. In: *Proc. EPAC*. Vol. 8. 2008, p. 3734.

[2] S. Chatrchyan et al. „Observation of a new boson at a mass of 125 GeV with the CMS experiment at the LHC“. In: *Physics Letters B* 716.1 (2012), pp. 30–61.

[3] G. Aad et al. „Observation of a new particle in the search for the Standard Model Higgs boson with the ATLAS detector at the LHC“. In: *Physics Letters B* 716.1 (2012), pp. 1–29.

[4] S. Chatrchyan et al. „Search for supersymmetry in hadronic final states with missing transverse energy using the variables α T and b-quark multiplicity in pp collisions at $\sqrt{s} = 8$ TeV“. In: *The European Physical Journal C* 73.9 (2013), pp. 1–31.

[5] 2016. URL: https://twiki.cern.ch/twiki/bin/view/CMSPublic/LumiPublicResults#Luminosity_versus_day.

[6] T. Reis. „Searches for new massive resonances decaying to leptons at CMS“. In: *Particle Physics at the Year of Centenary of Bruno Pontecorvo - Proceedings of the Sixteenth Lomonosov Conference on Elementary Particle Physics*. Ed. by A. Studenikin. 2015, pp. 160–163.

[7] CMS Collaboration. „Search for narrow resonances in dilepton mass spectra in proton-proton collisions at sqrt (s)= 13 TeV and combination with 8 TeV data“. In: *arXiv preprint arXiv:1609.05391* (2016).

[8] CMS Collaboration. „Performance of CMS muon reconstruction in pp collision events at $\sqrt{s} = 7$ TeV“. In: *Journal of Instrumentation* 7.10 (2012), P10002.

[9] A. A. Drozdetskiy. „The standard model higgs boson discovery potential in the decay channel H→ZZ→4μ with the CMS detector“. PhD thesis. University of Florida, 2007.

[10] L. Thomas. „Searches for BSM physics in dilepton, multilepton, and lepton+ MET final states at CMS“. In: *CMS-CR-2016-137*. 2016.

[11] CMS collaboration. „Projected Performance of an Upgraded CMS Detector at the LHC and HL-LHC: Contribution to the Snowmass Process“. In: *arXiv preprint arXiv:1307.7135* (2013).

[12] G. Apollinari. „High Luminosity Large Hadron Collider HL-LHC“. In: *CERN Yellow Reports* 5.1 (2016).

[13] S. Mersi et al. „CMS Tracker layout studies for HL-LHC“. In: *Physics Procedia* 37 (2012), pp. 1070–1078.

[14] S. Myers and E. Picasso. „The design, construction and commissioning of the CERN large Electron–Positron collider“. In: *Contemporary Physics* 31.6 (1990), pp. 387–403. DOI: 10.1080/00107519008213789. eprint: http://dx.doi.org/10.1080/00107519008213789. URL: http://dx.doi.org/10.1080/00107519008213789.

[15] O. Brüning et al. „LHC design report (Volume I, The@ LHC main ring)“. In: *Reports-CERN* (2004).

[16] L. Evans and P. Bryant. „LHC Machine“. In: *Journal of Instrumentation* 3.08 (2008), S08001.

[17] D. Iwanenko and I. Pomeranchuk. „On the Maximal Energy Attainable in a Betatron“. In: *Phys. Rev.* 65 (11-12 June 1944), pp. 343–343. DOI: 10.1103/PhysRev.65.343. URL: http://link.aps.org/doi/10.1103/PhysRev.65.343.

[18] H. Winick and S. Doniach. *Synchrotron radiation research*. Ed. by Plenus Press New York. Springer Science & Business Media, 2012.

[19] A. Airapetian et al. *ATLAS detector and physics performance*. CERN-LHCC-99-015. ATLAS-TDR-015, 1999.

[20] F. Carminati et al. „ALICE: Physics performance report, volume I“. In: *Journal of Physics G: Nuclear and Particle Physics* 30.11 (2004), p. 1517.

[21] S. Cadeddu et al. „LHCb reoptimized detector design and performance“. In: *LHCb-TDR-009* (2003).

[22] CMS Collaboration. „CMS physics technical design report, volume II: physics performance“. In: *Journal of Physics G: Nuclear and Particle Physics* 34.6 (2007), p. 995.

[23] CMS Collaboration. „The CMS experiment at the CERN LHC“. In: *Journal of Instrumentation* 3.08 (2008), S08004.

[24] T. Sakuma and T. McCauley. „Detector and Event Visualization with SketchUp at the CMS Experiment“. In: *Journal of Physics: Conference Series*. Vol. 513. 2. IOP Publishing. 2014, p. 022032.

[25] T. Lenzi and G. De Lentdecker. „Development and Study of Different Muon Track Reconstruction Algorithms for the Level-1 Trigger for the CMS Muon Upgrade with GEM Detectors“. In: *arXiv preprint arXiv:1306.0858* (2013).

[26] CMS Collaboration. „Performance of the CMS Level-1 trigger during commissioning with cosmic ray muons and LHC beams“. In: *Journal of Instrumentation* 5.03 (2010), T03002.

[27] T. Speer et al. „Track reconstruction in the CMS tracker“. In: *Nuclear Instruments and Methods in Physics Research Section A: Accelerators, Spectrometers, Detectors and Associated Equipment* 559.1 (2006), pp. 143–147.

[28] V. Veszpremi for the CMS Collaboration. „Operation and performance of the CMS tracker“. In: *Journal of Instrumentation* 9.03 (2014), p. C03005.

[29] A. Tricomi. „Upgrade of the CMS tracker“. In: *Journal of Instrumentation* 9.03 (2014), p. C03041.

[30] CMS Collaboration. *The CMS Electromagnetic Calorimeter Technical Design Report*. CERN/LHCC, 1997.

[31] R.-Y. Zhu et al. „A study on the properties of lead tungstate crystals“. In: *Nuclear Instruments and Methods in Physics Research Section A: Accelerators, Spectrometers, Detectors and Associated Equipment* 376.3 (1996), pp. 319–334.

[32] S. Abdullin et al. „Design, performance, and calibration of CMS hadron-barrel calorimeter wedges“. In: *The European Physical Journal C* 55.1 (May 2008), pp. 159–171.

[33] N. D. Giokaris et al. „Study of dose-rate effects en the radiation damage of polymer-based SCSN23, SCSNSl, SCSNSl+Y7, SCSNSl+YS and 3HF scintillators“. In: *Radiat. Phys. Chem.* 41.1/2 (1993), pp. 315–320.

[34] S. Abdullin et al. „Design, performance, and calibration of the CMS hadron-outer calorimeter“. In: *The European Physics Journal C* 57.3 (2008), pp. 653–663.

[35] Saint-Gobain Crystals. „BC400, BC-404, BC-408, BC-412, BC-416: premium plastic scintillators“. In: *Saint-Gobain Crystals, Nemours* (2005).

[36] C. Albajar et al. „Conceptual design of an improved CMS RPC Muon Trigger using the Hadron Outer scintillators“. In: *Nuclear Instruments and Methods in Physics Research Section A: Accelerators, Spectrometers, Detectors and Associated Equipment* 545.1 (2005), pp. 97–113.

[37] J. Freeman. „Silicon photomultipliers for the CMS hadron calorimeter“. In: *Nuclear Instruments and Methods in Physics Research Section A: Accelerators, Spectrometers, Detectors and Associated Equipment* 617.1 (2010), pp. 393–395.

[38] A. Heering et al. „Performance of Silicon Photomultiplers with the CMS HCAL Front-End Electronics“. In: *Nuclear Instruments and Methods in Physics Research Section A: Accelerators, Spectrometers, Detectors and Associated Equipment* 576.2 (2007), pp. 341–349.

[39] CMS Collaboration. „The performance of the CMS muon detector in proton–proton collisions at s = $\sqrt{7}$ TeV at the LHC“. In: *Journal of Instrumentation* 8.11 (2013), P11002.

[40] CMS Collaboration. „The muon project technical design report“. In: *CERN/LHCC* 32.404 (1997), p. 1997.

[41] CMS Collaboration. „Performance of the CMS drift tube chambers with cosmic rays“. In: *Journal of Instrumentation* 5.03 (2010), T03015.

[42] R. Martinelli et al. *Design of the Track Correlator for the DTBX Trigger*. CMS NOTE 1999/007. Feb. 1999.

[43] CMS Collaboration. „The TriDAS Project Technical Design Report, Volume 1: The Trigger Systems“. In: *LHCC* (Dec. 2000).

[44] G. Pugliese. „The RPC system for the CMS experiment“. In: *2006 IEEE Nuclear Science Symposium Conference Record*. Vol. 2. IEEE. 2006, pp. 822–826.

[45] F. Thyssen. „Performance of the Resistive Plate Chambers in the CMS experiment“. In: *Journal of Instrumentation* 7.01 (Jan. 2012), p. C01104.

[46] B. Mandelli et al. „Systematic study of RPC performances in polluted or varying gas mixture compositions: An online monitor system for the RPC gas mixture at LHC“. In: *Nuclear Science Symposium and Medical Imaging Conference (NSS/MIC), 2012 IEEE*. IEEE. Apr. 2012, pp. 1135–1140.

[47] M. Felcini. „The trigger system of the CMS experiment“. In: *Nuclear Instruments and Methods in Physics Research Section A: Accelerators, Spectrometers, Detectors and Associated Equipment* 598.1 (Jan. 2009), pp. 312–316.

[48] CMS Collaboration. „The CMS trigger system“. In: *arXiv preprint arXiv:1609.02366* (2016).

[49] A. Tapper et al. „Revised CMS Global Calorimeter Trigger Functionality & Algorithms“. In: *Proceedings of the 12th Workshop on Electronics for LHC and Future Experiments*. Vol. 204. 2006.

[50] Manfred Jeitler et al. „Upgrade of the CMS Global Muon Trigger“. In: *IEEE Transactions on Nuclear Science* 62.3 (June 2015), pp. 1104–1109.

[51] M. Jeitler and CMS collaboration. „The upgrade of the CMS trigger system“. In: *Journal of Instrumentation* 9.08 (2014), p. C08002. URL: http://stacks.iop.org/1748-0221/9/i=08/a=C08002.

[52] V. Gori. „The CMS High Level Trigger“. In: *International Journal of Modern Physics: Conference Series*. Vol. 31. World Scientific. 2014, p. 1460297.

[53] CMS Collaboration. „Technical Proposal for the Phase-II Upgrade of the Compact Muon Solenoid“. In: *CERN-LHCC-2015-010, LHCC-P-008* (2015).

[54] A. Montanari et. al. *Muon Trigger Upgrade at SLHC: Muon Track fast Tag*. CMS Internal Note. Oct. 2007.

[55] 2016. URL: https://indico.cern.ch/event/76076/contributions/2090880/attachments/1051701/1499532/papacz_CMS_week_20091208.pdf.

[56] 2016. URL: http://indico.cern.ch/event/67916/contributions/2074157/attachments/1022854/1456252/mtt_activity_aachen_200910.pdf.

[57] N. Otte et al. „The SiPM—a new photon detector for PET“. In: *Nuclear Physics B-Proceedings Supplements* 150 (2006), pp. 417–420.

[58] P. Maanen. „Simulationsstudien für das MTT-System bei CMS“. MA thesis. III. Physikalisches Insitut B, RWTH Aachen University, Nov. 2012.

[59] S. Weingarten. *Prototypdetektoren für das geplante Upgradeprojekt Muon Track Fast Tag am CMS-Experiment*. Springer Fachmedien Wiesbaden, 2015.

[60] Y. Erdogan. „Conceptual investigations of a trigger extension for muons from pp collisions in the CMS experiment“. PhD thesis. III. Physikalisches Insitut B, RWTH Aachen University, 2014.

[61] T. Radermacher. *Optimierung der Kopplung zwischen Silizium-Photomultipliern und ein Szintillationsmaterial an einem Prototyp-Detektormodul für das CMS-Experiment*. Bachelor thesis, III. Physikalisches Institut B, RWTH Aachen University. 2012.

[62] P. Papacz. *Optimisation of the Particle Detection Efficiency for Scintillation Detectors with SiPM Readout*. Diploma thesis, III. Physikalisches Institut A, RWTH Aachen University. Mar. 2010.

[63] F. Scheuch. *Measurements of a detector prototype with direct SiPM read-out and comparison with simulated data*. Bachelor thesis, III. Physikalisches Institut A, RWTH Aachen University. Aug. 2010.

[64] J. Rennefeld. *Studien zur Eignung von Silizium Photomultipliern für den Einsatz im erweiterten CMS Detektor am SLHC*. Diploma thesis. Feb. 2010.

[65] L. S. Weinstock. „Development of front-end electronics for detectors with SiPM readout“. MA thesis. III. Physikalisches Insitut B, RWTH Aachen University, Sept. 2014.

[66] J.-F. Schulte. *Studies of SiPM properties using an integrating sphere*. Bachelor thesis, III. Physikalisches Institut A, RWTH Aachen University. Mar. 2010.

[67] F. Scheuch. „Measurement and simulation of electrical properties of SiPM photon detectors“. MA thesis. III. Physikalisches Insitut A, RWTH Aachen University, Nov. 2012.

[68] F. Scheuch. „Electrical characterization and simulation of SiPMs“. In: *Nuclear Instruments and Methods in Physics Research A* 787 (2015), pp. 340–343.

[69] *Organic Scintillation Materials*. Data sheet. Saint-Gobain Crystals, Jan. 2015.

[70] CMS Collaboration. „The Hadron Calorimeter Project Technical Design Report“. In: *CERN/LHCC* 31 (1997).

[71] CMS Collaboration. *CMS Phase II Upgrade Scope Document*. Sept. 2015.

[72] T. Szczęśniak. „Time Resolution of Scintillation Detectors Based on SiPM in Comparison to Photomultipliers“. In: *Nuclear Science Symposium Conference Record* (2010), pp. 1728–1735.

[73] J. Anderson et al. „Upgrade of the CMS Hadron Outer Calorimeter with SIPMs“. In: *Physics Procedia* 37.72–78 (2012).

[74] The ATLAS and CMS Collaborations. *Expected pile-up values at the HL-LHC*. ATL-UPGRADE-PUB-2013-014. 2013.

[75] CMS Collaboration. „CMS Technical Design Report for the Muon Endcap GEM Upgrade“. In: *CMS-TDR-013* (2015).

[76] A. Fagot et al. „R&D towards the CMS RPC Phase-2 upgrade“. In: *Journal of Instrumentation* 11.09 (2016), p. C09017.

[77] CMS Collaboration. *A proposed DT-seeded Muon Track Trigger for the HL-LHC*. CMS Performance Note. May 2015.

[78] D. Haitz. *Analyse von $Z \rightarrow \mu^+ \mu^-$+Jet Ereignissen und Kalibration der Jet-Energieskala des CMS-Detektors*. Diploma thesis, Fakultät für Physik des Karlsruher Instituts für Technologie (KIT). 2013.

[79] CMS Collaboration. „CMS Luminosity Measurement for the 2015 Data Taking Period“. In: *CMS Physics Analysis Summary CMS-PAS-LUM-15-001* (Mar. 2016).

[80] F. Gonella and M. Pegoraro. *The MAD, a Full Custom ASIC for the CMS Barrel Muon Chambers Front End Electronics*. CERN, 2001.

[81] *Daniel Francois Teyssier, private communication, 2016*.

[82] C. Rovelli. „The detailed simulation of the CMS detector“. In: *CMS CR-2007/082*. 2007.

[83] S. Chatrchyan et al. „Search for leptonic decays of W' bosons in pp collisions at $\sqrt{s} = 7$ TeV“. In: *Journal of High Energy Physics* 2012.8 (2012), pp. 1–33.

[84] 2016. URL: https://github.com/cms-sw/cmssw/blob/CMSSW_9_0_X/L1Trigger/DTTriggerServerTheta/src/DTChambThSegm.cc.

[85] D. Duchardt private communication 2017. URL: https://cms-project-music.web.cern.ch/cms-project-music.

[86] D. Duchardt. „MUSiC: A Model Unspecific Search for New Physics Based on $\sqrt{s} = 8$ TeV CMS Data“. PhD thesis. III. Physikalisches Insitut A, RWTH Aachen University, 2017, to be published.

[87] A. O. M. Iorio. „Study of the RPC Level-1 trigger efficiency in the compact muon solenoid at LHC with cosmic ray data“. In: *Nuclear Instruments and Methods in Physics Research Section A: Accelerators, Spectrometers, Detectors and Associated Equipment* 661 (2012), S27–S29.

[88] A. Künsken. „Studies on the use of the CMS Outer Hadron Calorimeter in the Level-1 Muon Trigger“. PhD thesis. RWTH Aachen University, 2017, to be published.

[89] A. Triossi et al. „A New Data Concentrator for the CMS Muon Barrel Track Finder“. In: *Proceedings of Technology and Instrumentation in Particle Physics 2014 (TIPP2014)*. Vol. 1. Amsterdam, the Netherlands., 2014, p. 412.

[90] Á. Navarro-Tobar and C. Fernández-Bedoya. „CMS DT upgrade: the sector collector relocation“. In: *Journal of Instrumentation* 11.02 (2016), p. C02046.

[91] G. Anzivino et al. „Review of the hybrid photo diode tube (HPD) an advanced light detector for physics“. In: *Nuclear Instruments and Methods in Physics Research Section A: Accelerators, Spectrometers, Detectors and Associated Equipment* 365.1 (1995), pp. 76–82.

[92] CMS Collaboration. „Commissioning of the CMS experiment and the cosmic run at four tesla“. In: *Journal of Instrumentation* 3.03 (Mar. 2010), T03001.

[93] P. Buzhan et al. „Silicon photomultiplier and its possible applications“. In: *Nuclear Instruments and Methods in Physics Research Section A: Accelerators, Spectrometers, Detectors and Associated Equipment* 501.1 (2003), pp. 48–52.

[94] R. Hawkes et al. „Silicon Photomultiplier Performance Tests in Magnetic Resonance Pulsed Fields“. In: *2007 IEEE Nuclear Science Symposium Conference Record*. Vol. 5. 2007, pp. 3400–3403.

[95] A. Heering et al. „Large-Area SiPMs for the CMS Hadron Outer Calorimeter“. In: *2007 IEEE Nuclear Science Symposium Conference Record*. Vol. 2. IEEE. 2007, pp. 1545–1550.

[96] P. Bohn et al. „Radiation Damage Studies of Silicon Photomultipliers“. In: *Nuclear Instruments and Methods in Physics Research Section A: Accelerators, Spectrometers, Detectors and Associated Equipment* 598.3 (2009), pp. 722–736.

[97] A. Lobanov et al. *SiPM Light Mixers for CMS HO Upgrade*. Tech. rep. DESY CMS Group, 2011.

[98] A. Künsken et al. „SiPM Operational Experience in Outer HCAL in CMS“. In: *arXiv preprint arXiv:1408.5709* (Aug. 2014).

[99] Simon M. Sze, Kwok K. Ng. *Physics of Semiconductor Devices*. Vol. 3. John Wiley & sons, Nov. 2006.

[100] E. Ney and D. Thon. „Scintillation Counting of Cosmic-Ray Particles“. In: *Physical Review* 81.6 (1951), p. 1068.

[101] A. Lobanov. „The CMS Outer HCAL SiPM Upgrade“. In: *Journal of Physics: Conference Series*. Vol. 587. 1. 2015, p. 012005.

[102] *Pooja Saxena, private communication, 2016*.

Appendix

```
import FWCore.ParameterSet.Config as cms

process = cms.Process('HLT')
process.load('Configuration.StandardSequences.Services_cff')
process.load('SimGeneral.HepPDTESSource.pythiapdt_cfi')
process.load('FWCore.MessageService.MessageLogger_cfi')
process.load('Configuration.EventContent.EventContent_cff')
process.load('SimGeneral.MixingModule.mix_POISSON_average_cfi')
process.load('Configuration.Geometry.GeometryExtended2015Reco_cff')
process.load('Configuration.Geometry.GeometryExtended2015_cff')
process.load('Configuration.StandardSequences.
   MagneticField_38T_PostLS1_cff')
process.load('Configuration.StandardSequences.Generator_cff')
process.load('IOMC.EventVertexGenerators.
   VtxSmearedRealistic8TeVCollision_cfi')
process.load('GeneratorInterface.Core.genFilterSummary_cff')
process.load('Configuration.StandardSequences.SimIdeal_cff')
process.load('Configuration.StandardSequences.Digi_cff')
process.load('Configuration.StandardSequences.SimL1Emulator_cff')
process.load('Configuration.StandardSequences.DigiToRaw_cff')
process.load('HLTrigger.Configuration.HLT_GRun_cff')
process.load('Configuration.StandardSequences.RawToDigi_cff')
process.load('Configuration.StandardSequences.L1Reco_cff')
process.load('Configuration.StandardSequences.Reconstruction_cff')
process.load('CommonTools.ParticleFlow.EITopPAG_cff')
process.load('Configuration.StandardSequences.EndOfProcess_cff')
process.load('Configuration.StandardSequences.
   FrontierConditions_GlobalTag_condDBv2_cff')

process.mix.input.nbPileupEvents.averageNumber = cms.double
   (52.000000)
process.mix.bunchspace = cms.int32(25)
process.mix.minBunch = cms.int32(-12)
process.mix.maxBunch = cms.int32(3)
process.mix.input.fileNames = readFiles
process.genstepfilter.triggerConditions=cms.vstring("generation_step
   ")
from Configuration.AlCa.GlobalTag_condDBv2 import GlobalTag
process.GlobalTag = GlobalTag(process.GlobalTag, 'PHYS14_25_V1', '')

process.generator = cms.EDProducer("FlatRandomPtGunProducer",
  PGunParameters = cms.PSet(
        MinPt  = cms.double(3.),
        MaxPt  = cms.double(200.),
        PartID = cms.vint32(13),
        MaxPhi = cms.double(3.141/6),
        MinPhi = cms.double(-3.141/6),
        MaxEta = cms.double(.4),
        MinEta = cms.double(-.4)
    ),
       AddAntiParticle = cms.bool(False),
       firstRun = cms.untracked.uint32(1)
)
...
```

Figure 1: Excerpts of the configuration file for the failure samples.

```
164   //************ 2 ***************
165
166   // These are sorted by DetId, i.e. by layer and then by wire #
167   //  map<DTDetId, vector<const PSimHit*> > wireMap;
168   DTWireIdMap wireMap;
169
170   for(MixCollection<PSimHit>::MixItr simHit = simHits->begin();
171       simHit != simHits->end(); simHit++){
172
173     // Create the id of the wire, the simHits in the DT known also
          the wireId
174     DTWireId wireId( (*simHit).detUnitId() );
175
176     // The newly implemented code lines
177     if(wireId.wheel() == 0 && wireId.sector() == 1 && wireId.station() == 2)
          continue;
178
179     // Fill the map
180     wireMap[wireId].push_back(&(*simHit));
181   }
182
183   pair<float,bool> time(0.,false);
```

Figure 2: Code snippet of the `DTDigitizer.cc` from the package `SimMuon/DTDigitzer` within `CMSSW_7_2_3`. The blue colored lines were added in order to simulate DT station failure. This failure can be simulated for different sets of wheels, sectors, stations and wires.

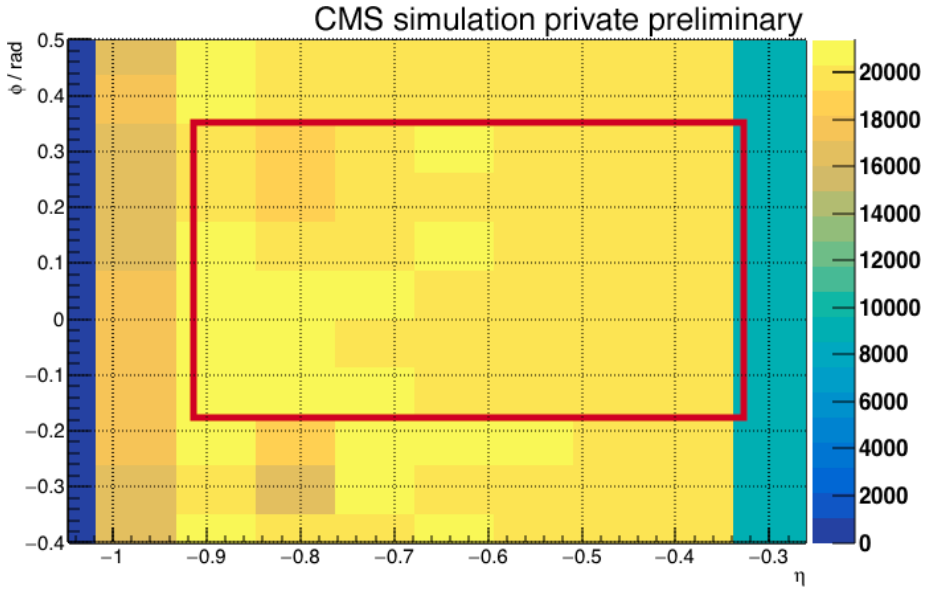

(a) Wheel 1-

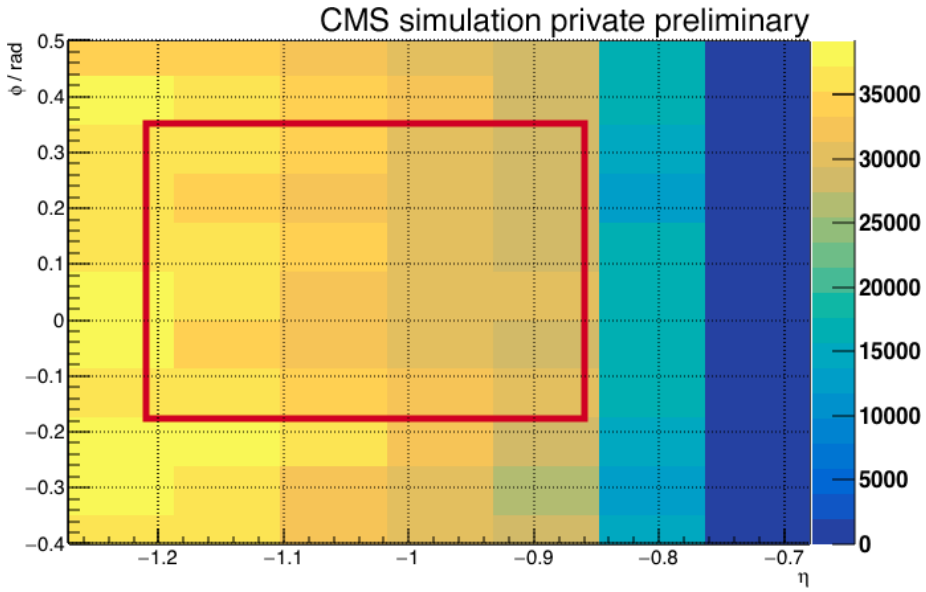

(b) Wheel 2-

Figure 3: Absolute numbers of L1 muons matched to a reconstructed muon in the sample with the fully working detector. The binning corresponds to the binning of the calorimeter-towers. Thus, it also corresponds to the size and position of the HO tiles. The red rectangle shows the position of muon station 1 in sector 1.

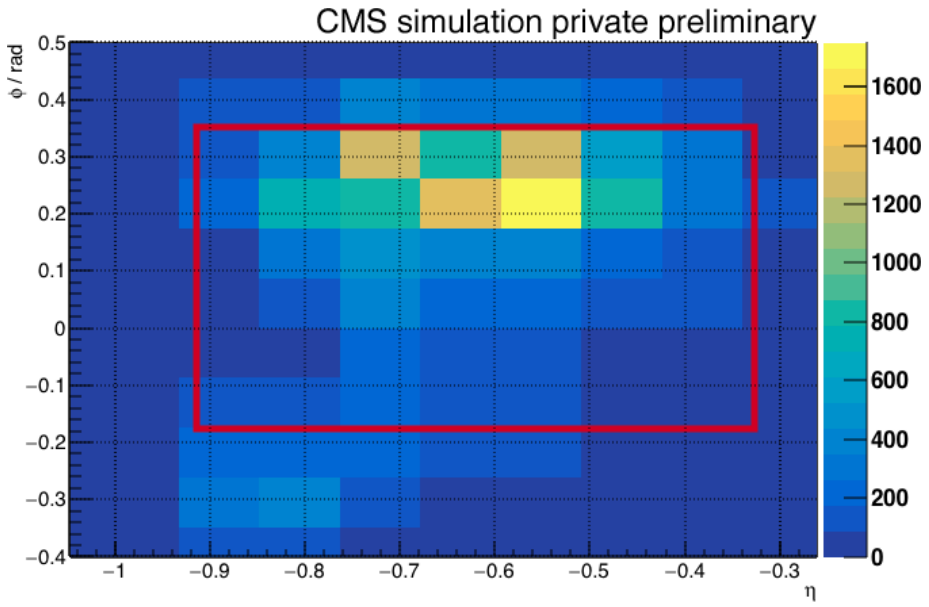

(a) Wheel 1-

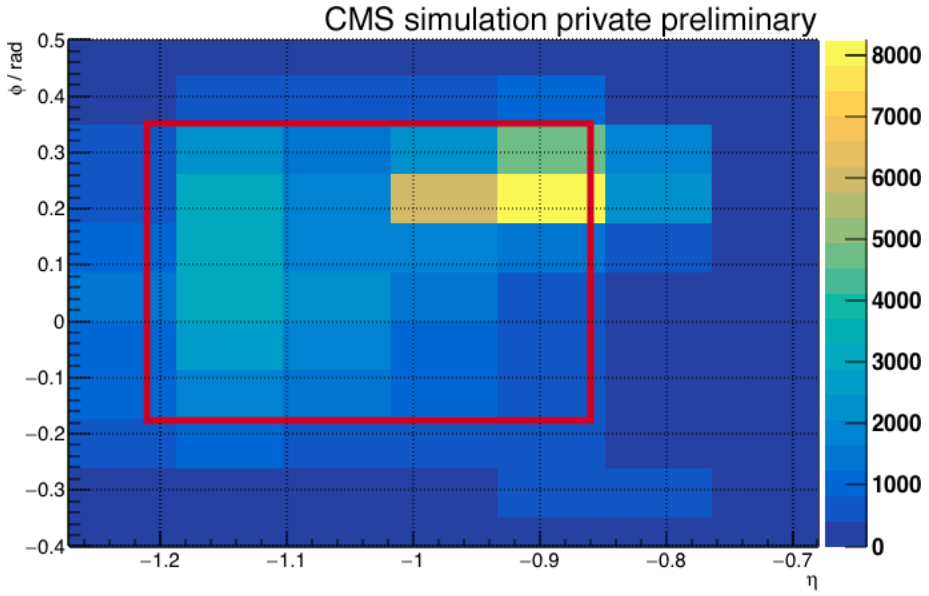

(b) Wheel 2-

Figure 4: Absolute numbers of L1 muons that can be matched to a reconstructed muon in the sample with the fully working detector but are missing in the sample of the erroneous detector. The binning corresponds to the binning of the calorimeter-towers. Thus, it also corresponds to the size and position of the HO tiles. The red rectangle shows the position of the failing muon DT station 1 in sector 1.

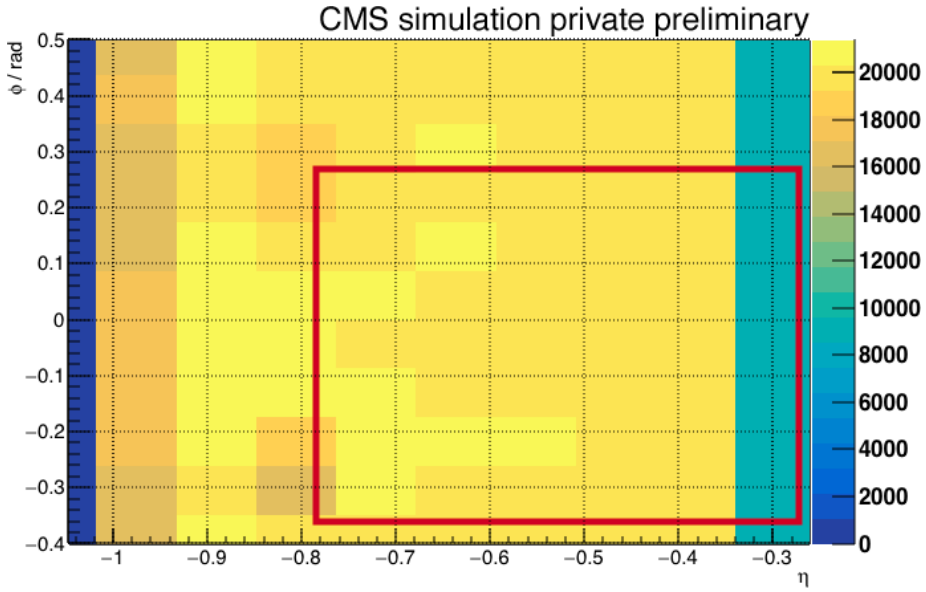

(a) Wheel 1-

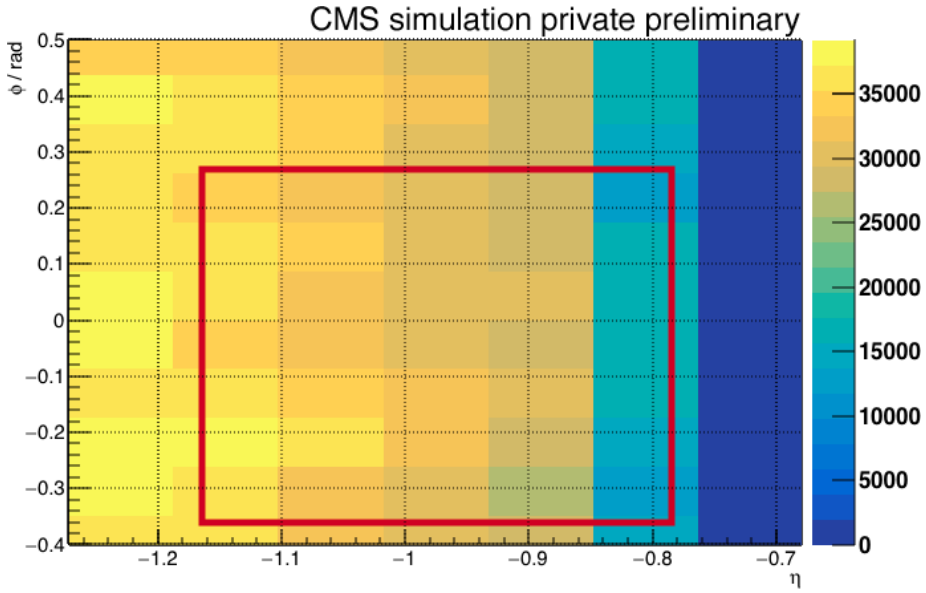

(b) Wheel 2-

Figure 5: Absolute numbers of L1 muons matched to a reconstructed muon in the sample with the fully working detector. The binning corresponds to the binning of the calorimeter-towers. Thus, it also corresponds to the size and position of the HO tiles. The red rectangle shows the position of muon station 2 in sector 1.

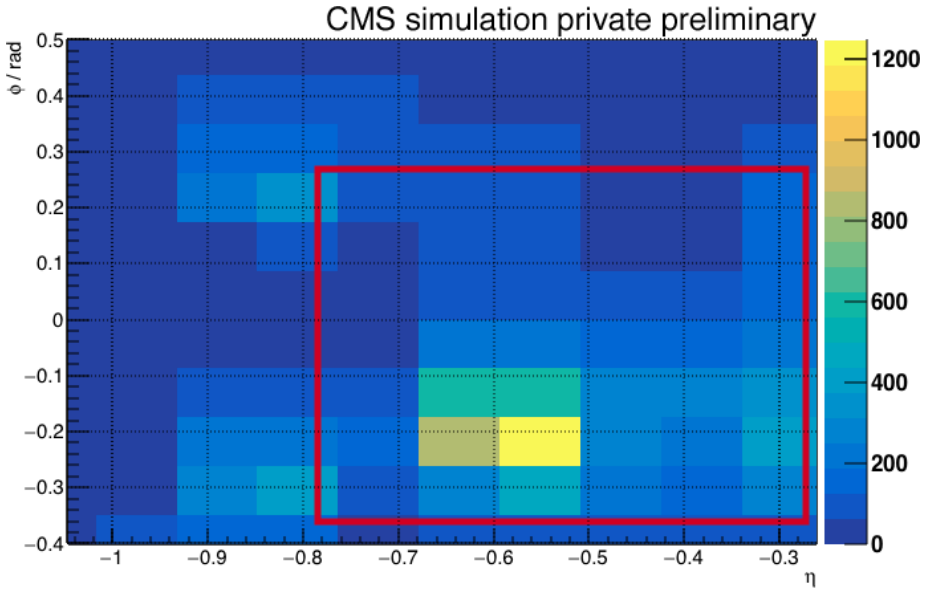

(a) Wheel 1-

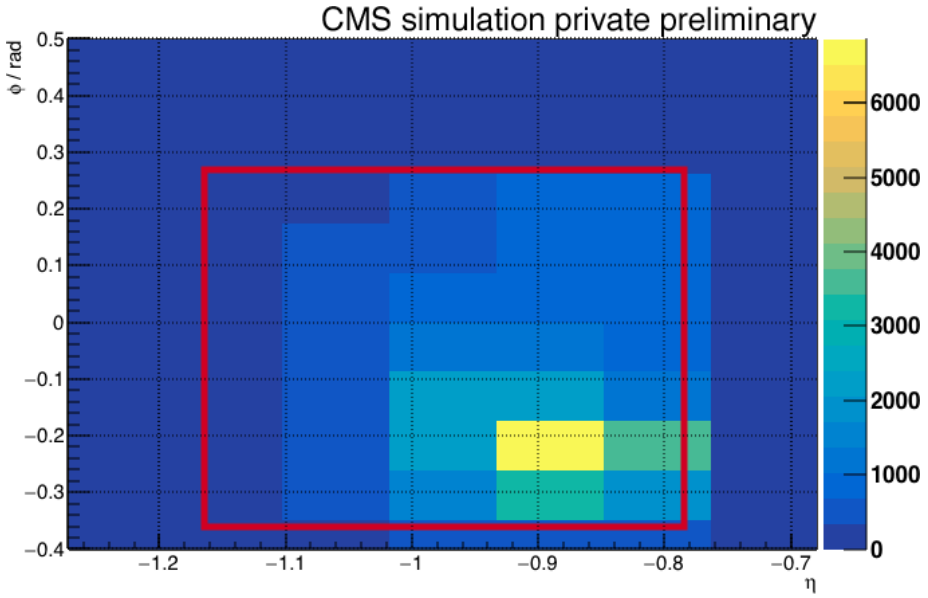

(b) Wheel 2-

Figure 6: Absolute numbers of L1 muons that can be matched to a reconstructed muon in the sample with the fully working detector but are missing in the sample of the erroneous detector. The binning corresponds to the binning of the calorimeter-towers. Thus, it also corresponds to the size and position of the HO tiles. The red rectangle shows the position of the failing muon DT station 2 in sector 1.

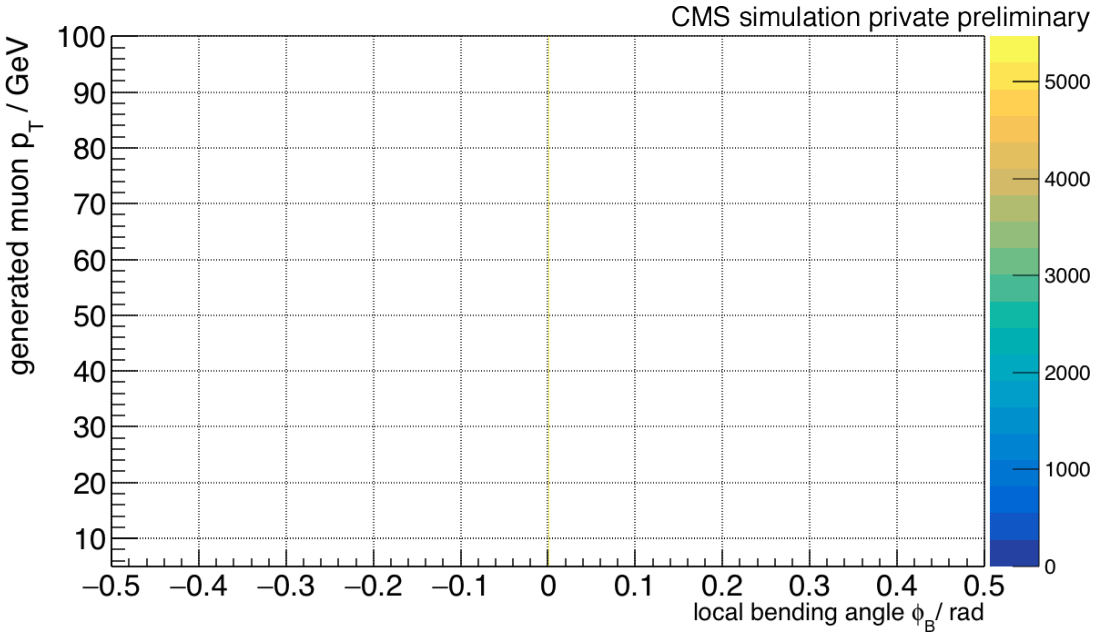

(a) Station 3

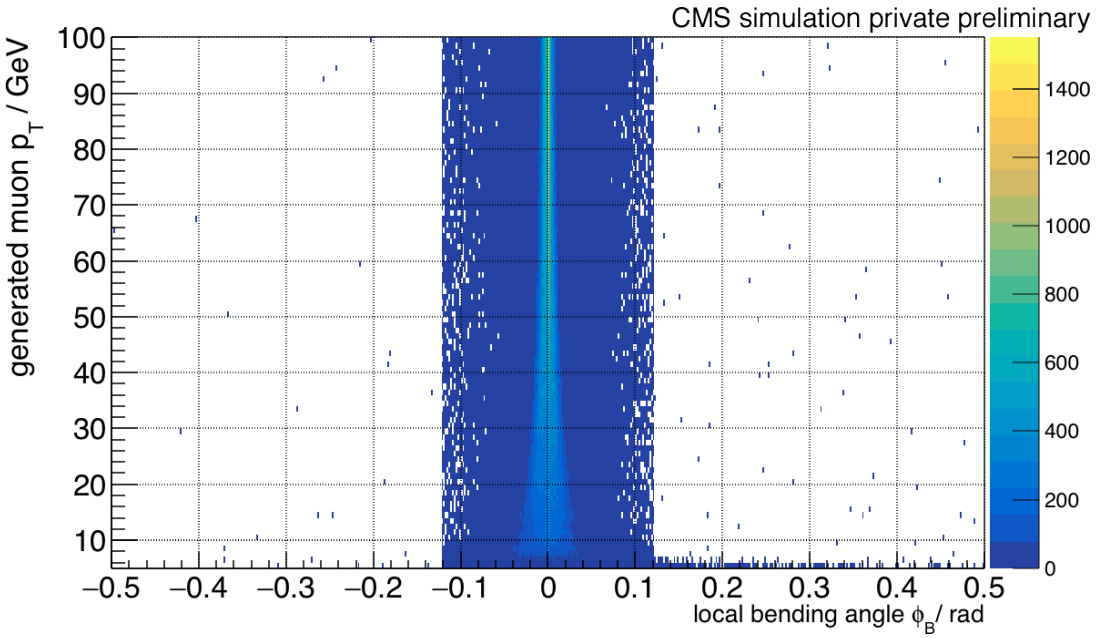

(b) Station 4

Figure 7: p_T vs. ϕ_B distribution for single muons at muon stations 3 and 4, respectively.

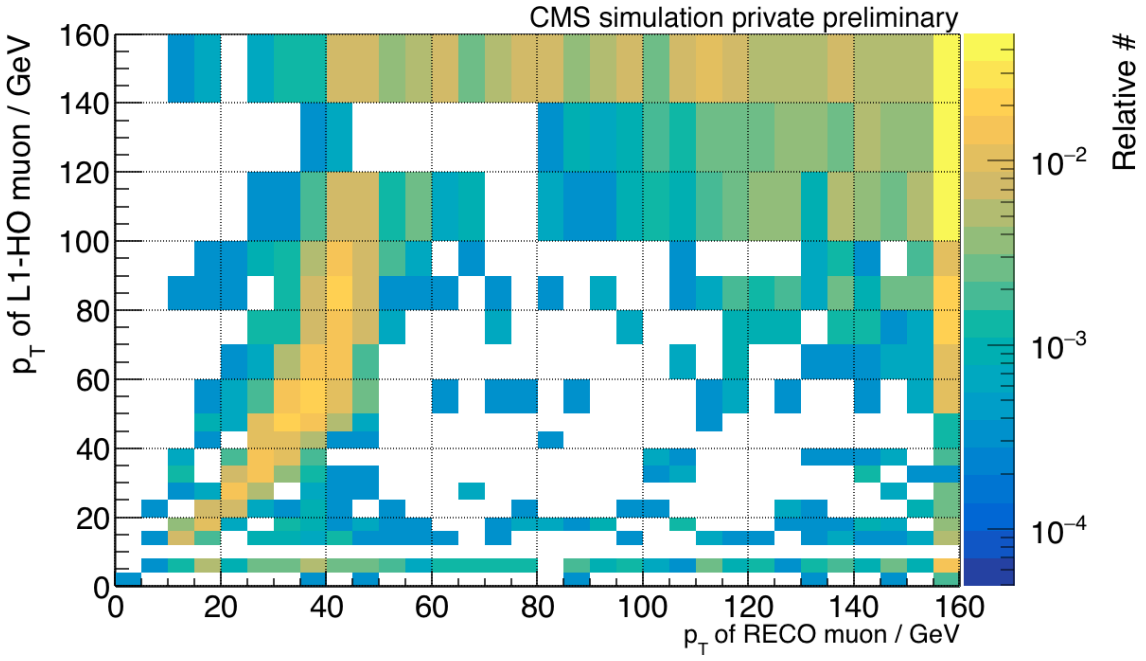

Figure 8: Correlation plot of the transverse muon momentum p_T of the reconstructed muon, that is matched to the recovered L1-HO muon, and the recovered L1-HO muon using the information of DT MB station 1 and HO as MIP tag.

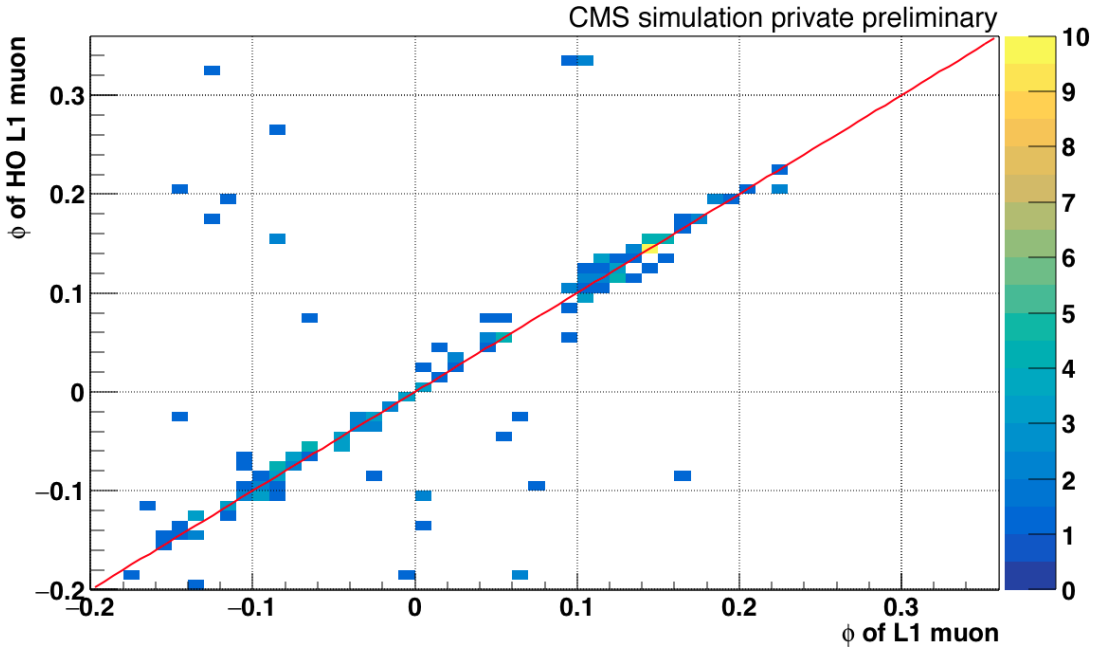

(a) Failure of DT MB station 1

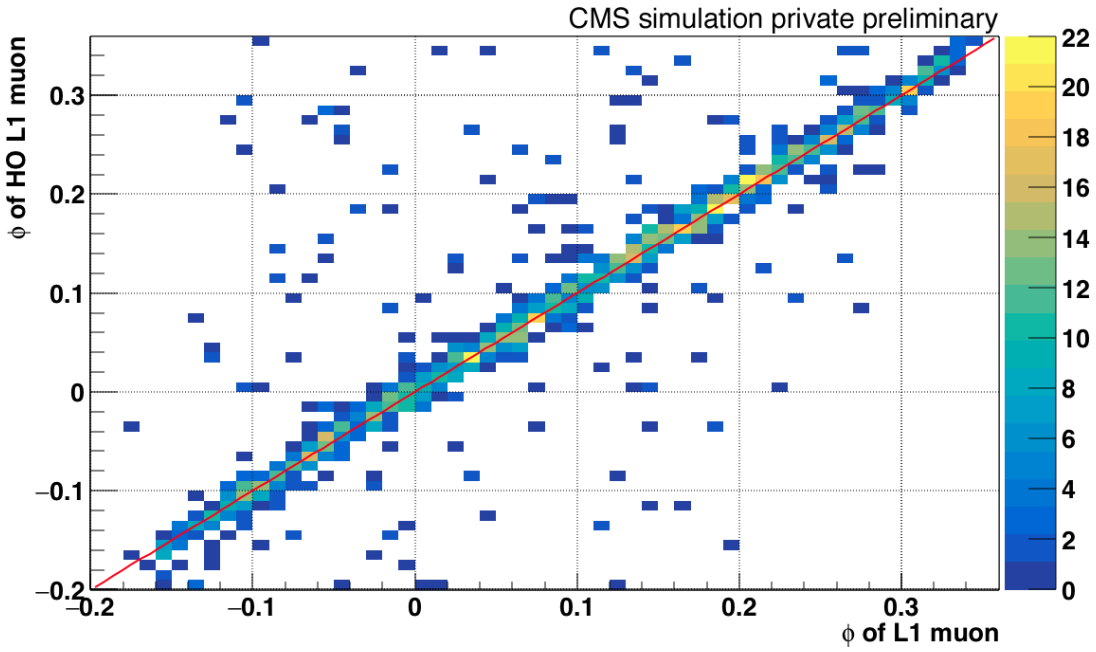

(b) Failure of DT MB station 2

Figure 9: Correlation plots for the ϕ coordinate of the recovered L1 muon (called L1 HO muon) and the corresponding reconstructed muon for the failure of DT MB 1/2 in wheel 1-.

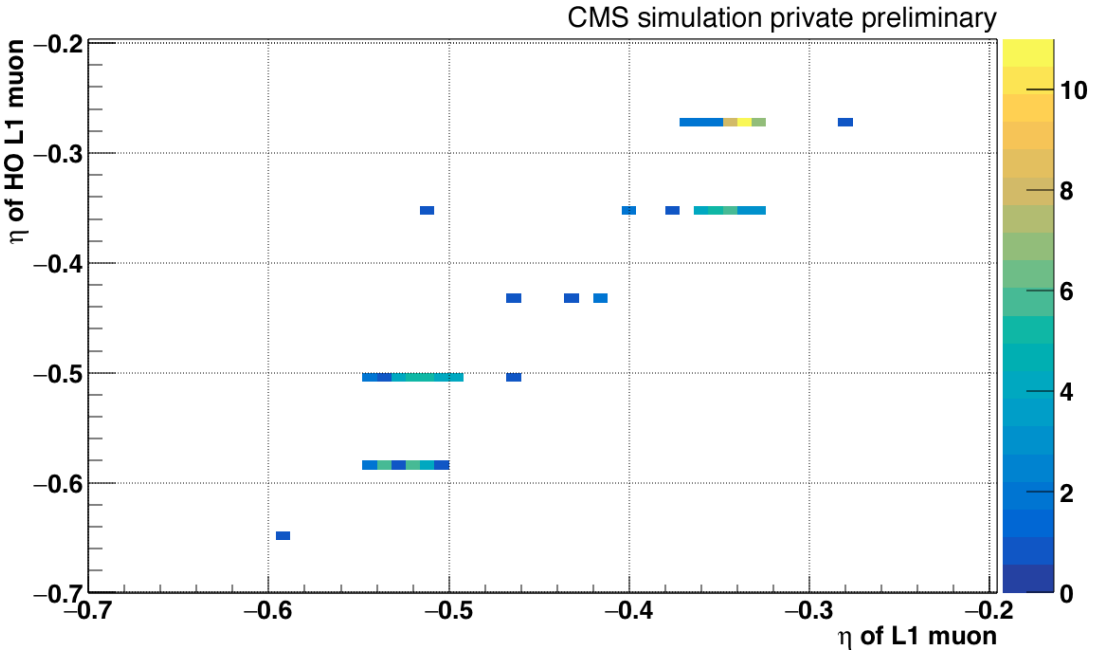

(a) Failure of DT MB station 1

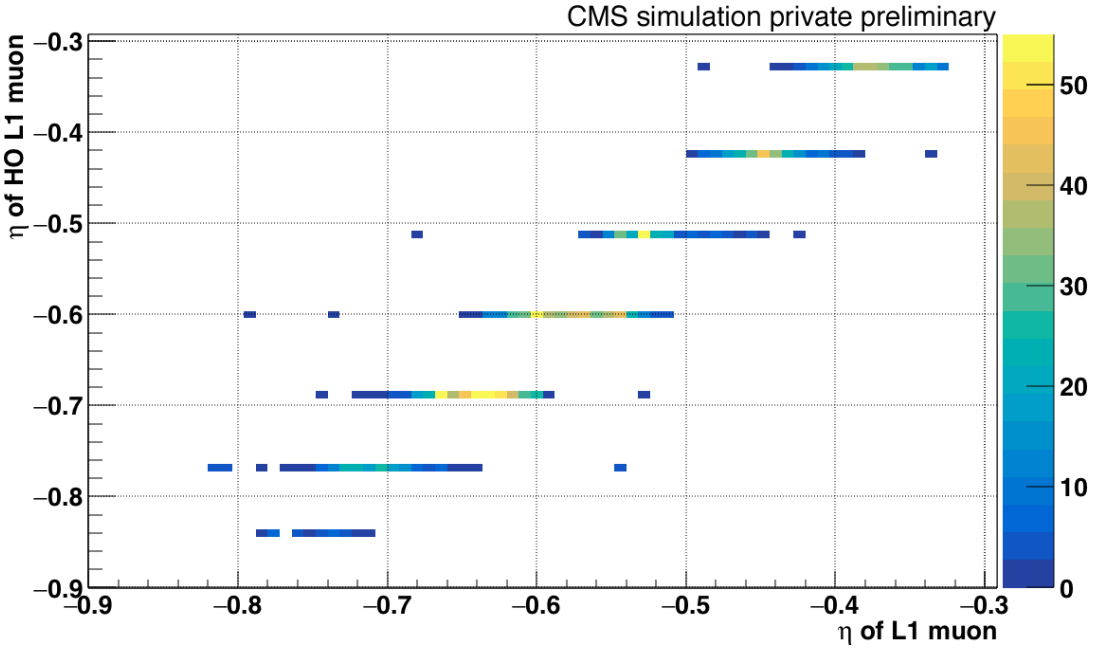

(b) Failure of DT MB station 2

Figure 10: Correlation plots for the η coordinate of the recovered L1 muon (called L1 HO muon) and the corresponding reconstructed muon for the failure of DT MB 1/2 in wheel 1-.

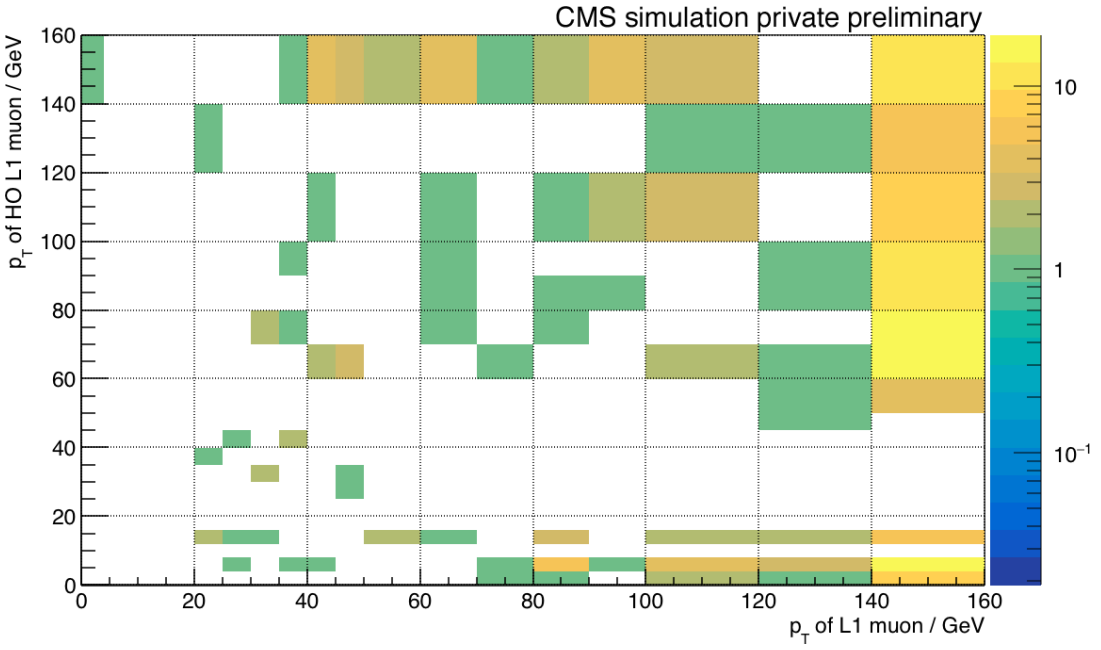

(a) Failure of DT MB station 1

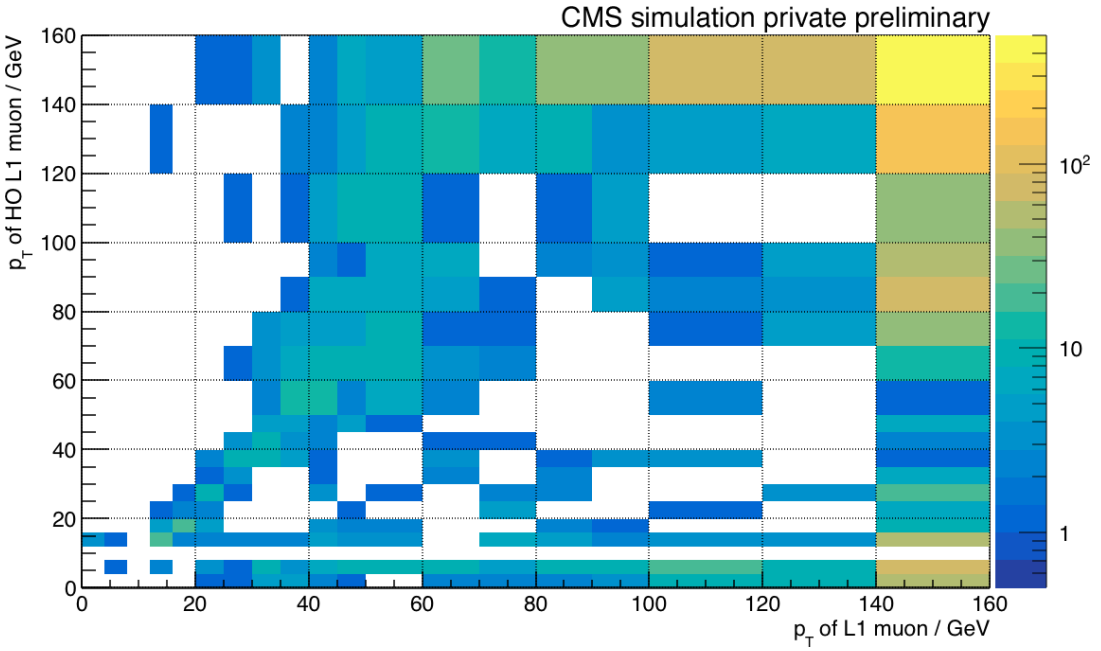

(b) Failure of DT MB station 2

Figure 11: Correlation plots for the p_T value of the recovered L1 muon (called L1 HO muon) and the corresponding L1 muon for the failure of DT MB 1/2 in wheel 1-.

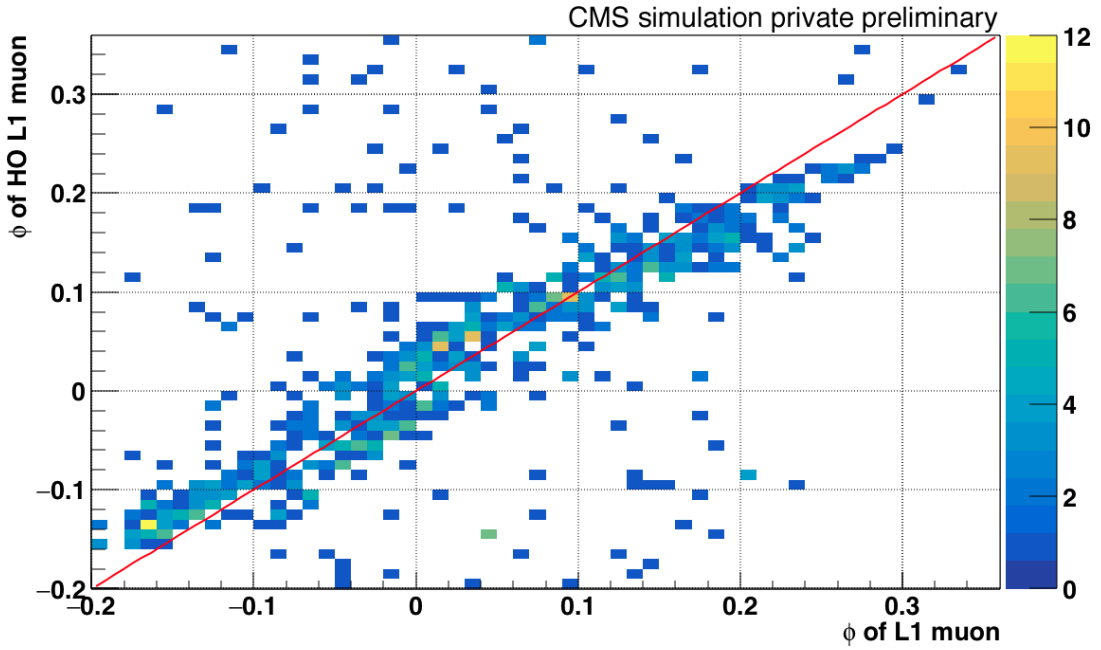

(a) Failure of DT MB station 1

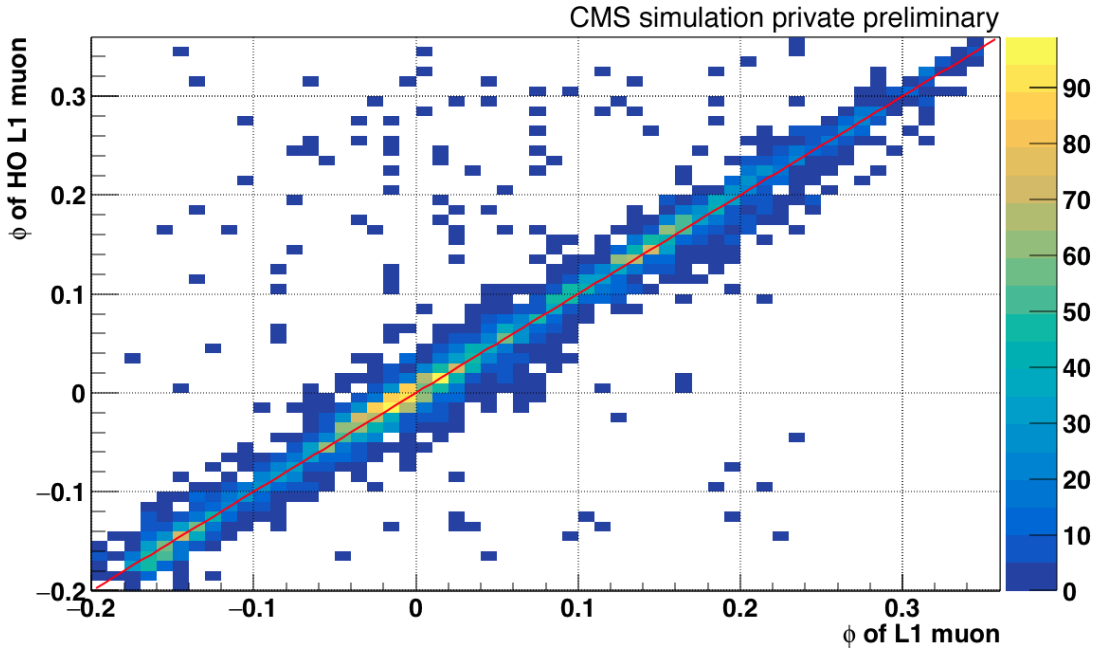

(b) Failure of DT MB station 2

Figure 12: Correlation plots for the ϕ coordinate of the recovered L1 muon (called L1 HO muon) and the corresponding reconstructed muon for the failure of DT MB 1/2 in wheel 2-.

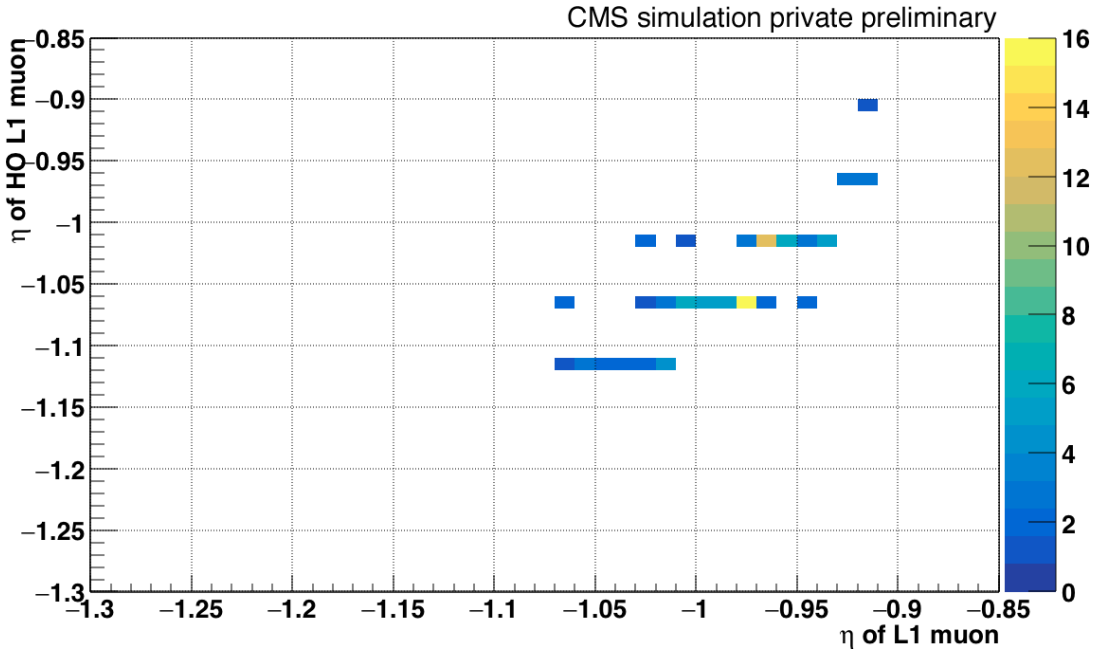

(a) Failure of DT MB station 1

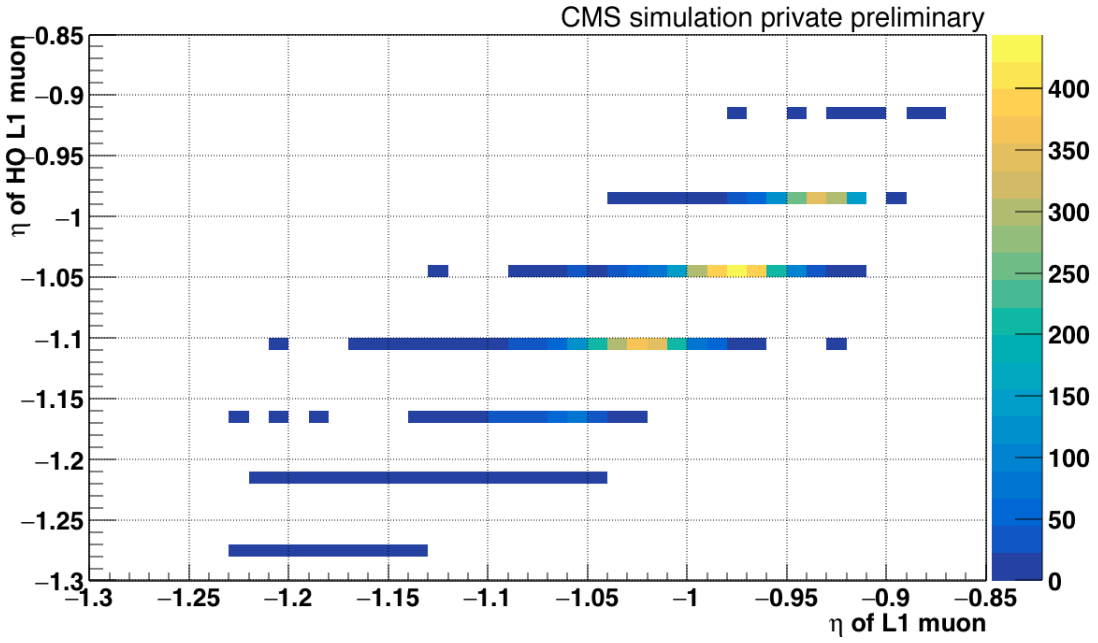

(b) Failure of DT MB station 2

Figure 13: Correlation plots for the η coordinate of the recovered L1 muon (called L1 HO muon) and the corresponding reconstructed muon for the failure of DT MB 1/2 in wheel 2-.

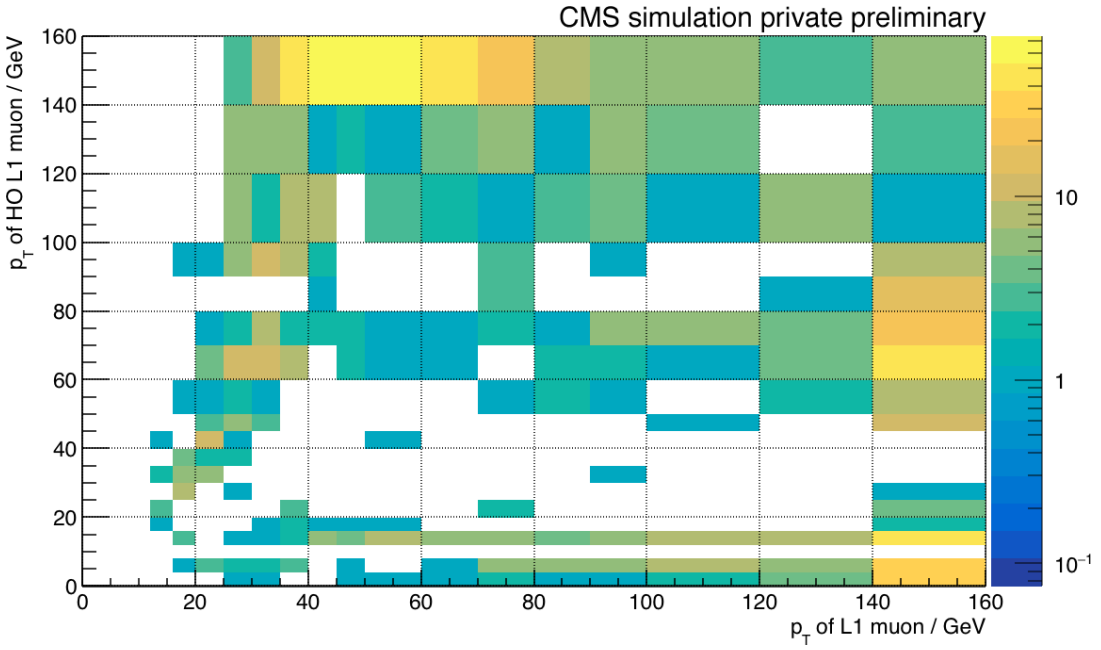

(a) Failure of DT MB station 1

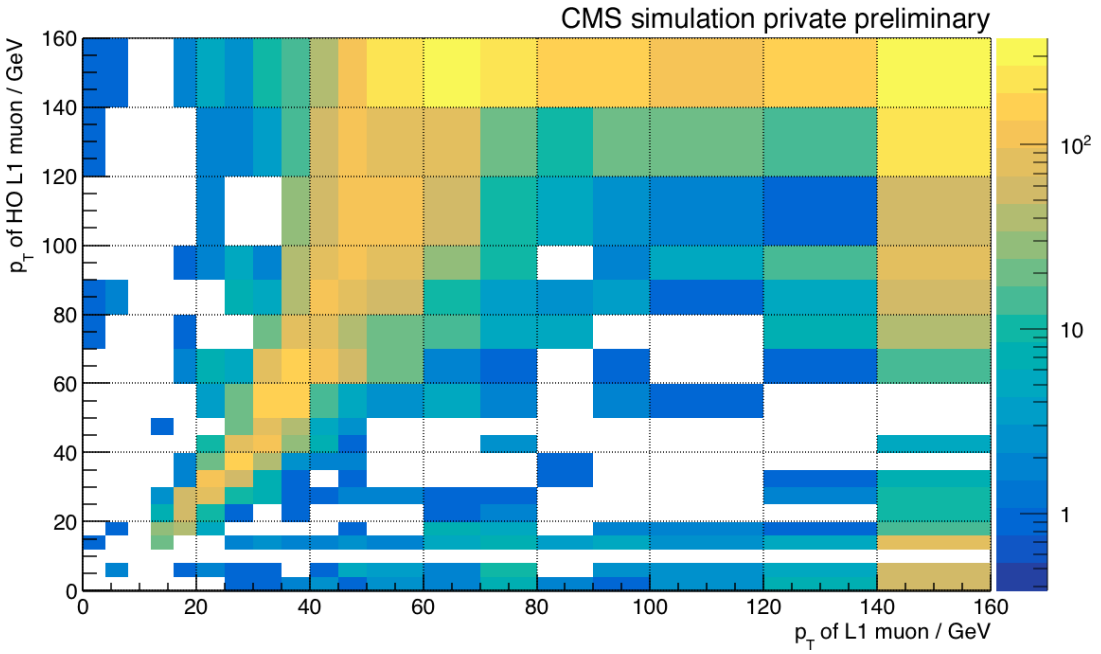

(b) Failure of DT MB station 2

Figure 14: Correlation plots for the p_T value of the recovered L1 muon (called L1 HO muon) and the corresponding L1 muon for the failure of DT MB 1/2 in wheel 2-.

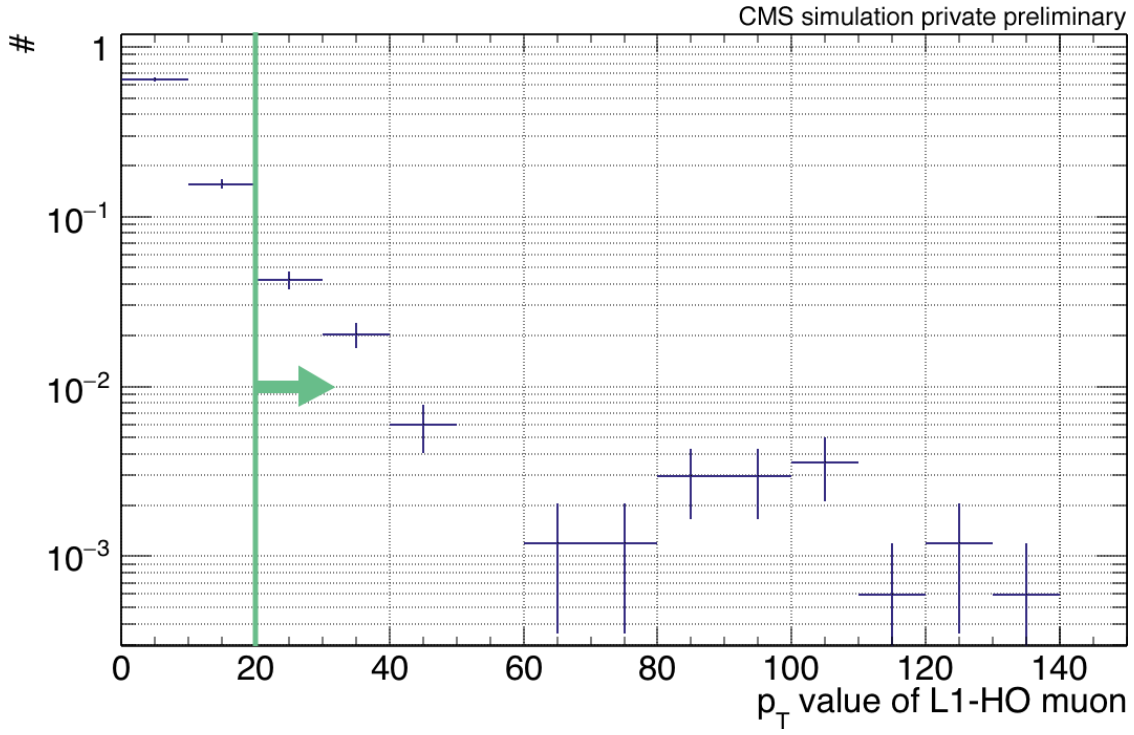

Figure 15: Relative p_T distribution of fake L1-HO muons when no MIP tag is required in order to create a L1-HO muon. The green line shows a single muon trigger threshold of 20 GeV. The fake L1-HO muons are created during the recovery procedure of L1 muons that are lost due to a failure of station 2 in sector 1 in wheel 0.

```
164   //************ 2 ***************
165
166   // These are sorted by DetId, i.e. by layer and then by wire #
167   //  map<DTDetId, vector<const PSimHit*> > wireMap;
168   DTWireIdMap wireMap;
169
170   for(MixCollection<PSimHit>::MixItr simHit = simHits->begin();
171       simHit != simHits->end(); simHit++){
172
173     // Create the id of the wire, the simHits in the DT known also
          the wireId
174     DTWireId wireId( (*simHit).detUnitId() );
175
176     // The newly implemented code line
177     if(rand() % 100 < failurePercentage) continue;
178
179     // Fill the map
180     wireMap[wireId].push_back(&(*simHit));
181   }
182
183   pair<float,bool> time(0.,false);
```

Figure 16: Code snippet of the `DTDigitizer.cc` from the package `SimMuon/DTDigitzer` within CMSSW Vers. 7.2.3. The blue colored line was added in order to simulate single DT-wire failure. The percentage of the failing wires can be changed by changing the `failurePercentage` value.

Danksagung

Mein Dank gilt Herrn Prof. Dr. Thomas Hebbeker für seine Bereitschaft mir die Mitarbeit an seinem Institut und in diesem spannenden Themenfeld zu ermöglichen. Zudem danke ich für die damit verbundene Bereitschaft als Berichter tätig zu sein. Dieser Dank gilt auch PD Dr. Oliver Pooth, der diese Aufgabe ebenfalls übernommen hat.

Im Folgenden will ich weitere Personen und Gruppen erwähnen, es aber bei einem großen Dank am Ende belassen, um den Leser nicht mit unendlichen Varianten des Danksagens zu ermüden.

In den langen Jahren meiner Tätigkeit am III. Physikalischen Institut A der RWTH Aachen University, die - mit der Bachelorarbeit im Jahr 2010 begonnen - mit der Promotion nun einen Abschluss findet, hat mir Dr. Markus Merschmeyer stets mit Rat und Tat zur Seite gestanden. Dies trotz der großen Fülle an Verwaltungsaufgaben zu leisten ist bei Weitem keine Selbstverständlichkeit.
Im Rahmen der Anfertigung der Dissertation habe ich eng mit der MTT Gruppe der beiden III. Physikalischen Institute zusammengearbeitet. Die konstruktive Kritik und die hilfreichen Hinweise haben maßgeblich zum Erfolg dieser Arbeit beigetragen.
Auch im Büro und unter den „Hallenbewohnern“ wurden Diskussionen, Anregungen und Kritik ausgetauscht. Die gute persönliche Atmosphäre in der Halle hat dabei wesentlich dazu beigetragen jede (im Zweifel im Nachhinein auch noch so unsinnige) Frage diskutieren zu können. An dieser Stelle sei besonders Dr. Tim Niggemann erwähnt, der als Bürokollege besonders für Programmierfragen stets ein offenes Ohr hatte.
In der Halle ist Dr. Karl ein ewiges Mysterium und ein fleißiger Kollege. Wenn die Überlegungen und Analysen den Kopf zum Platzen zu bringen drohten, hat er stets zu einer willkommenen Ablenkung beigetragen.
Neben den Kollegen und Freunden am Institut war mir meine Familie auch immer eine Stütze. Dies gilt nicht nur finanziell, sondern auch besonders persönlich (und manchmal antreibend). Ich freue mich daher die Frage „Wann gibst du denn endlich ab?“ in Zukunft mit einem „Hab ich schon gemacht!“ beantworten zu können.
Eine weitere Person, die meinen Weg als Physiker und persönlich immer begleitet hat, ist Andreas Künsken. Unsere Wege sind auf dem Weg bis zur Promotion in der Ele-

mentarteilchenphysik parallel verlaufen - von der ersten Vorlesung an. Nicht nur die Zusammenarbeit der beiden III. Physikalischen Institute in der MTT Gruppe hat von dieser Freundschaft außerordentlich profitiert.
Zu guter Letzt sei hier die Bischöfliche Studienförderung Cusanuswerk e.V. erwähnt. Seit dem März 2014 hat mich das Bundesministerium für Bildung und Forschung über diese Stiftung mit einem Stipendium unterstützt. Zusätzlich zur finanziellen Unterstützung hat mir das Cusanuswerk mit vielen Veranstaltungen den Horizont über die Welt der Teilchenphysik hinaus eröffnet. Die vielen Begegnungen mit so unterschiedlichen Menschen verschiedenster Fachrichtungen und persönlicher Meinungen, die alle der Respekt und das Interesse am Gegenüber verbindet, haben mich tief beeindruckt und geprägt.

Sollten Sie sich als Leser zu jedem neuen Abschnitt doch ein kleines „Danke“ vorgestellt haben, verstehen Sie sicherlich, warum ich bisher darauf verzichtet habe. Daher sei es an dieser Stelle nun allen Genannten und (den hoffentlich wenigen) versehentlich nicht Genannten gesagt:

Vielen Dank!